QUANTIFYING THE EFFECTS OF SOIL AND PLANT CHARACTERISTICS ON RADIOCAESIUM UPTAKE

A GLOBAL PERSPECTIVE

Margot Vanheukelom

Supervisor:
Prof. Erik Smolders

Co-supervisors:
Dr. Lieve Sweeck
Dr. Talal Almahayni

Members of the Examination Committee:
Prof. Christine Kirschhock (chair)
Prof. Roel Merckx
Prof. Jan Elsen
Prof. Bruno Delvaux
Dr. Liesbeth Van Laer

Dissertation presented in partial fulfilment of the requirements for the degree of Doctor of Bioscience Engineering (PhD)

November 2024

Doctoraatsproefschrift nr. 1987 aan de faculteit Bio-ingenieurswetenschappen van de KU Leuven.

© 2024 Margot Vanheukelom
Uitgegeven in eigen beheer, Margot Vanheukelom, Polderstraat 20, 3051 Sint-Joris-Weert.

Alle rechten voorbehouden. Niets uit deze uitgave mag worden vermenigvuldigd en/of openbaar gemaakt worden door middel van druk, fotokopie, microfilm, elektronisch of op welke andere wijze ook zonder voorafgaandelijke schriftelijke toestemming van de uitgever.

All rights reserved. No part of the publication may be reproduced in any form by print, photoprint, microfilm, electronic or any other means without written permission from the publisher.

Acknowledgments

Mijn mama vertelde me dat dit het belangrijkste deel van het manuscript is. En ze had gelijk; ik zou een heel boek kunnen schrijven over hoe dankbaar ik ben voor al jullie steun, inspiratie en de kansen die ik heb gekregen.

Allereerst wil ik mijn begeleider Erik bedanken. Ik heb ontzettend veel van je geleerd, zowel academisch als persoonlijk: dat ik mag zijn wie ik ben. Ik begon met een enorm enthousiasme aan dit doctoraat, en ik ben je dankbaar hoe je daarin meeging: mijn enthousiasme stimuleren en weer aanwakkeren als het wat afnam. Je gaf me veel vrijheid, maar ook deadlines wanneer ik die nodig had. Bedankt dat je de afgelopen jaren het beste uit me hebt gehaald.

Ik wil graag mijn SCK-mentor Lieve bedanken. Zij gaf me de kans om dit avontuur aan te gaan. Tijdens mijn masterproef liet ze mijn nieuwsgierigheid naar het onderwerp en het onderzoek groeien en vertrouwde ze erop dat ik dit doctoraat zou voltooien. Ze zou tevreden geweest zijn.

I would like to thank my SCK co-mentor Talal. Thank you for your critical eye and for playing devil's advocate. I feel I have grown and become more down-to-earth thanks to you.

Bedankt Mara, Mark, Pieter en Nina voor jullie inzet, geduld, en enthousiasme. Ik ben trots op jullie en tevreden met ons werk. Ik ben niet altijd de beste mentor geweest, maar heb geleerd uit mijn fouten: dat duidelijke communicatie en structuur essentieel zijn als mentor.

Verder wil ik graag Roel bedanken. Jij hebt mijn interesse voor dit onderzoek gewekt door mij als bachelorstudent uit te nodigen op de doctoraatsverdediging van Shinichiro Uematsu. Van jou heb ik geleerd om uit de geschoolde bubbel te stappen en naar de echte wereld met reële problemen te kijken. Bedankt voor die onvergetelijke reis naar Kenia om 80 kg (!) bodem te verzamelen op Mount Elgon en terug naar België te brengen. Wat een gek idee! Toch bleef je het avontuur toejuichen, geweldig!

Bedankt Jan, om die pot experimenten met kleien voor mijn masterproef mogelijk te maken. Dankzij jou brachten bedrijven Vandersanden en Wienerberger tot wel 500 kg klei naar het SCK-laboratorium, kon ik met Nancy samenwerken en leerde ik over kleimineralen.

Bedankt Nancy, om me vanaf het begin te helpen met staalvoorbereiding en mineralen te zoeken in klei- en bodemstalen. Het mineralogielab was een

afgelegen plekje op de campus, maar als jij er was, zat ik er graag en voelde het als een bezoek aan een vriendin.

May, mijn superheld!!! Ik heb zoveel van jou geleerd en bewonder je leergierigheid en positiviteit. Samenwerken met jou gaf altijd een gevoel van zekerheid, en je herinnerde je details van experimenten uit het verre verleden. Ik bewonder je toewijding en het vertrouwen dat iedereen in je stelt.

Axel, Robin, en Jean, bedankt om er altijd te zijn in de BIS-groep. Bedankt om de deur steeds open te houden, advies te geven, en te helpen waar jullie konden. Toen ik na mijn ski-ongeluk met een kapotte knie thuis zat, stelden jullie me gerust dat ik op jullie kon rekenen voor het grote potexperiment. Samen lopen in de Molse bossen tijdens pauzes vond ik geweldig.

Kristin, Karla, Lore, Simon, Dries, Karlien, en Uldeen, bedankt voor jullie hulp, flexibiliteit, en advies. Jullie zijn onmisbaar om alles in goede banen te leiden en ik ben dankbaar dat ik steeds op jullie kan rekenen.

Bedankt Jos, om mijn klankbord te zijn. Ik ben dromerig, en ik bewonder hoe jij dromen tastbaar en praktisch kunt maken. Van jou heb ik geleerd helder en concreet te denken.

Bedankt Hildegarde, om me een duwtje in de rug te geven, mij te vergeven en te inspireren. Ik vind je een ongelooflijk sterk persoon en bewonder je eerlijkheid en drijfveer.

Bedankt Gerd, om me met open armen in de groep te ontvangen. Ik bewonder je eindeloze energie en enthousiasme, die aanstekelijk werken. Jij hebt me geleerd dat een positieve houding cruciaal is in internationale samenwerkingen en dat je zo een groep bij elkaar houdt.

I would like to thank my colleagues from the IAEA D15019 CRP group. We have learned so much from each other’s research and insights, and I thoroughly enjoyed our presentations and discussions. Meeting a group of people studying similar topics has been of great inspiration to me.

Een grote dankjewel aan iedereen die zich voor me openstelde en er voor me was tijdens dit doctoraatsavontuur. Jullie hebben me veel geleerd en dit gaf me energie. Rudy, Gregory, Danny, Eric, Stijn, Elodie, Lander, merci!

Special thanks to my British research superstars whom I deeply admire: Nick, Neil, Brenda, and Joanne. You have helped me greatly in chasing my dream of building a big database.

Thank you, dear colleagues in the Soil and Water Management group. You made me feel part of a close-knit circle of friends in which I thrived. Thank you for lifting my spirits during stressful moments, for lending a listening ear, and for adding joy to metal meetings and seminars. I am grateful that you made those congresses in Glasgow and Lyon a little more fun, the relaxing coffee breaks, TGIFs, beer tastings, weekends away, and celebrations. Thanks to the running group for getting some fresh air in the forest through all four seasons, and to the gym bros and bras who made working out together a great support for my recovery. Thank you for the memorable ski trips. Go muddy giants!!

My thanks go as well to colleagues in the Biosphere Impact Studies group. Thank you for always being open to questions and for sharing your advice. I appreciated our congress trip to Oslo and the gala dinner at the opera house.

Bedankt aan mijn vrienden, die toevallig ook doctoreren, om regelmatig samen te gaan lunchen. Ik vond het heerlijk om mijn hart bij jullie te luchten en te horen dat het voor jullie soms ook moeilijk was. Ik vond het fijn om die mijlpalen samen te vieren.

Bedankt aan mijn vrienden en vriendinnen. De laatste jaren heb ik minder van me laten horen, maar jullie zijn er altijd voor me geweest. Bedankt voor het luisterend oor, een schouder om op te leunen, jullie advies en geruststelling, en voor de avonturen en plezier die we hebben gedeeld. Onze gezellige avonden, wandelingen, etentjes, en heerlijke weekends zijn onvergetelijk.

Thanks to everyone who inspired me along the way: inspiration has been the driving force behind my PhD, giving me energy and motivation throughout this journey.

Ik wil graag mijn twee lieve grote broers en hun partners bedanken. Jullie zijn mijn warme familie, onder jullie vleugels voel ik me veilig en kan ik mijn ongefilterde zelf zijn. Het doet me deugd dat jullie trots op me zijn en ik kijk naar jullie op.

Als laatste wil ik graag mijn mama en papa bedanken. Ik vind niet de juiste woorden om uit te drukken hoe gelukkig ik ben dat ik in dit nestje ben opgegroeid: als een prinses, zonder zorgen en met grote dromen. Jullie hebben me alles gegeven waar ik met oneindige tevredenheid op terugkijk. Bedankt voor jullie steun, kansen, troost, zorg, en geruststelling. Ik kan nog steeds niet bevatten hoe onvoorwaardelijk jullie liefde is voor ons.

Mijn lieve Jasper, bedankt dat ik de afgelopen jaren fouten mocht maken, mocht groeien, en dat je met me meeging door die laatste loodjes. Ik ben klaar voor ons volgende avontuur!

Summary

In case of nuclear accidents, radiocaesium (^{134}Cs and ^{137}Cs) can be released into the environment, contaminating agricultural soils and entering the food chain via plant uptake. This is because Cs exhibits similar biochemical behavior to the plant nutrient potassium (K). Radiocaesium is strongly adsorbed onto the weathered edges of micaceous clay minerals, such as illite, and this limits its transfer to the food chain. The soil-to-plant transfer of radiocaesium is expressed as the concentration ratio (CR), i.e., the ratio of the radiocaesium concentration in the plant material to that in the soil, and that CR value is key in environmental impact assessments after nuclear accidents. After the Chornobyl and Fukushima accidents, many CR observations were gathered and models were developed to predict the CR of radiocaesium in soils. However, these models used for impact assessments were based on data from the affected regions with limited diversity in soil characteristics. It has never been verified whether these models can be used to predict soil radiocaesium bioavailability on a global scale. Nuclear energy is expanding in the world and it is logical that emergency planning requires information on radiocaesium soil-to-plant transfer. This research was set up to explore and understand the soil properties affecting radiocaesium bioavailability globally. The central hypothesis was that radiocaesium sorption is affected by the clay mineralogy in soils and that information on clay mineralogy can be linked with other globally available soil information to improve predictions of radiocaesium bioavailability on a global scale.

This study started by collecting existing information on radiocaesium CRs from the literature in a systematic way, creating a comprehensive and harmonized database with 8,837 records from 142 studies. It showed that CRs ranged over seven orders of magnitude between 2.8 10^{-5} to 3.8 10^{2} kg kg^{-1}. The highest CRs were observed in soils originating from tropical climates and organic soils, and the lowest in soils temperate climates. However, data from tropical (N = 404) and arid (N = 47) regions were limited. Statistical analyses revealed that random variation of the studies, soil properties, and plant species were the main factors influencing CR. When comparing models, semi-mechanistic models outperformed machine learning models on small datasets (N <200), while machine learning models were superior with larger datasets. A global radiocaesium transfer map was created with a machine learning model and global soil data, identifying highly weathered and organic soils as

the most vulnerable. However, the map was based on a limited dataset (*N* = 513) and the residual error showed that the 95% confidence intervals of CRs were still larger than two orders of magnitude. The key missing variables in the global soil maps are the soil exchangeable K content and the soil mineralogy.

In a second step, it was experimentally investigated to what extent clay mineralogy affects the bioavailability of ^{137}Cs. This was first explored with plant substrates based on a mixture of pure sand with ten different clay minerals. The clays were mixed with sand in single and double clay doses, spiked with ^{137}Cs, and grown with grass in a greenhouse experiment. The CR generally decreased with increasing clay dose, but the CRs varied two orders of magnitude depending on the type of clay and exchangeable K content. The CR was highest for clays with little ^{137}Cs specific sites, such as expanding clay (smectite) and where the exchangeable K content was low compared to the other clays. The CR was well predicted from the soil solution ^{137}Cs and K concentrations (R^2 = 0.72 for log transformed CRs), corroborating earlier findings in natural soils. The CR (log-transformed) was statistically unrelated to total clay mineral content or 1:1 and 2:1:1 type clay mineral content, while it significantly decreased with increasing 2:1 clay mineral content (R^2 = 0.32). A multiple regression model with four different X-ray diffraction (XRD) based clay mineral groups yielded the strongest predictive power (R^2 = 0.79). We concluded that XRD quantification is valuable for describing ^{137}Cs bioavailability in clay-sand mixtures with contrasting properties.

The follow-up experimental study identified if similar trends of mineralogy are true in natural soil. The ^{137}Cs bioavailability was studied in soils from contrasting parent materials and weathering stages. Two soil sequences from Kenya (*N* = 6) and the Philippines (*N* = 6) were sampled, representing different weathering stages affecting soil mineralogy. In addition, other soils (*N* = 26) with contrasting soil properties, including Andosols and Ferralsols, were included in the collection. A greenhouse experiment was set up with these soils. A subset of the soils was fertilized with K to investigate its effect on ^{137}Cs CR reduction. The soils were characterized, including mineralogy by XRD, spiked with ^{137}Cs and grown with grass. The CRs varied four orders of magnitude among soils. It was highest in tropical Ferralsols (47 kg kg^{-1}) due to the low ^{137}Cs interception potential of kaolinite clay and the low exchangeable potassium in these soils. The semi-mechanistic ^{137}Cs transfer model, mainly calibrated to temperate soils, poorly predicted the underlying

processes in highly weathered tropical soils but, due to compensatory effects of the ^{137}Cs adsorption and available K in soils, still reasonably well predicted the ^{137}Cs bioavailability (i.e., $^{10}log(CR)$) across all soils ($R^2 = 0.78$).

Finally, experimental work was devoted to ^{137}Cs adsorption (not bioavailability) in soils as affected by the clay mineralogy in soils of contrasting weathering stages. The clay and silt fractions were isolated from 24 soils from contrasting weathering stages. The ^{137}Cs adsorption was measured as the Radiocaesium Interception Potential (RIP), for all bulk soil samples and in their corresponding clay (0–2 µm) and silt (2–50 µm) fractions, along with XRD analysis of the mineralogy of these fractions. Results showed that the RIP in these soils was unrelated to the soil clay content (p >0.05), well in contrast with the general concept of models that propose that the clay fraction in the soil is key to predicting a CR value. Instead, soil mineralogy, particularly illite content, explained the soil RIP. In some soils, a significant portion of the RIP was found in the silt fraction (>50%). Moreover, the RIP of the isolated clay fraction could be larger than the RIP of soil, likely due to the clay isolation procedure, which released K from clay mineral interlayers, increasing frayed edge sites, and caused disaggregation of clay minerals, increasing the clay content. This showed that studying isolated components of soil does not necessarily represent intact soils in the field.

Overall, this research emphasizes the importance of considering soil mineralogy when predicting radiocaesium bioavailability, thereby enhancing the effectiveness of radiocaesium impact assessments on a global scale. This work showed that, besides peat soils, highly weathered soils are most vulnerable to radiocaesium transfer with CR values exceeding 10 kg kg^{-1}, i.e., plants concentrate radiocaesium from such soils. This also means that emergency planning around new nuclear installations in tropical regions, often dominated by highly weathered soils, requires specific attention to food chain risks. Collating all RIP data showed that soil mineralogy greatly improved RIP predictions compared to predictions based on standard soil properties such as clay and organic matter content. However, it was demonstrated that the standard soil properties, complemented with soil classification according to the World Reference Base (WRB) are almost as strong predictors as soil mineralogy. The effects of soil structure and mineralogy on radiocaesium bioavailability in field conditions need further study, particularly in tropical regions where the long-term fate of radiocaesium remains largely unknown.

Samenvatting

Bij nucleaire ongelukken kan radiocesium (^{134}Cs en ^{137}Cs) in het milieu vrijkomen, landbouwgrond verontreinigen en via de opname door planten in de voedselketen terechtkomen. Dit komt doordat Cs een gelijkaardig biochemisch gedrag vertoont als het nutriënt kalium (K). Radiocesium wordt sterk adsorbeert aan de verweerde randen van kleimineralen, zoals illiet, en dit belet de overdracht in de voedselketen. De overdracht van radiocesium van bodem naar plant wordt uitgedrukt als een concentratieratio (CR), dat is de verhouding tussen de radiocesiumconcentratie in het plantmateriaal en die in de bodem. Die CR-waarde is essentieel bij de impactanalyses na nucleaire ongelukken. Na de ongelukken in Tsjernobyl en Fukushima werden veel CR-waarnemingen verzameld en modellen ontwikkeld om de CR's van radiocesium in de bodem te voorspellen. Deze modellen die gebruikt werden voor impactanalyses, waren echter gebaseerd op gegevens uit de getroffen regio's met een beperkte diversiteit in bodemkenmerken. Er is nooit onderzocht of deze modellen gebruikt kunnen worden om de biobeschikbaarheid van radiocesium op wereldwijde schaal te voorspellen. Kernenergie breidt zich wereldwijd uit en bijgevolg is er voor het plannen van noodsituaties informatie nodig over de overdracht van radiocesium van bodem naar plant op wereldwijde schaal. Dit onderzoek werd verricht om de bodemeigenschappen die de biobeschikbaarheid van radiocesium op wereldschaal beïnvloeden, te onderzoeken en te begrijpen. De belangrijkste hypothese was dat adsorptie van radiocesium wordt beïnvloed door de kleimineralogie in bodems. Informatie over deze kleimineralogie kan dan worden gekoppeld aan andere wereldwijd beschikbare bodeminformatie om de biobeschikbaarheid van radiocesium op wereldschaal beter te voorspellen.

Dit onderzoek begon met het systematisch verzamelen van bestaande informatie over CR's van radiocesium uit de literatuur, waardoor een uitgebreide en geharmoniseerde databank werd gemaakt met 8837 rijen gegevens uit 142 verschillende studies. Hieruit bleek dat de CR's over zeven orden van grootte varieerden van $2.8\ 10^{-5}$ tot $3.8\ 10^{2}$ kg kg^{-1}. De hoogste CR's werden waargenomen in bodems uit tropische klimaten en organische bodems, en de laagste in bodems uit gematigde klimaten. De gegevens uit tropische (N = 404) en aride (N = 47) gebieden waren echter wel beperkt. Statistische analyses toonden aan dat de willekeurige variatie van de verschillende studies, de bodemeigenschappen en plantensoorten de

belangrijkste factoren waren die de CR's beïnvloedden. De semi-mechanistische modellen presteerden beter dan machinelearningmodellen als een beperkt aantal gegevens beschikbaar waren (*N* <200), terwijl machinelearningmodellen beter werkten bij grotere aantallen. Er werd een wereldkaart gemaakt van de bodem-naar-plantoverdracht van radiocesium met behulp van machinelearningmodellen en wereldwijde bodeminformatie. Daarbij werden sterk verweerde en organische bodems aangewezen als het meest risicovol. De kaart was echter gebaseerd op een beperkte verzameling gegevens (*N* = 513) en de resterende fout toonde aan dat de 95% betrouwbaarheidsintervallen van de CR's nog steeds groter waren dan twee orden van grootte. De belangrijkste ontbrekende variabelen in de wereldwijde bodemkaarten zijn het uitwisselbare K-gehalte en de mineralogie van de bodem.

In een tweede stap werd experimenteel onderzocht in welke mate mineralogie de biobeschikbaarheid van ^{137}Cs beïnvloedde. Dit werd eerst onderzocht met plantensubstraten gemaakt van een mengsel van puur zand met tien verschillende kleisoorten. De kleien werden gemengd met zand in enkele en dubbele kleidoseringen, ^{137}Cs werd toegevoegd en er werd gras in gekweekt in een groeikamer. De CR nam over het algemeen af naarmate de kleidosis toenam, maar de CR's varieerde twee orden van grootte afhankelijk van het type klei en het uitwisselbare K-gehalte. De CR was het hoogst voor klei met weinig ^{137}Cs-specifieke adsorptiesites zoals zwellende klei (smectiet) en klei waarvan het uitwisselbare K-gehalte laag was, vergeleken met de andere kleisoorten. De CR werd goed voorspeld op basis van de ^{137}Cs- en K-concentraties in de bodemoplossing (R^2 = 0,72 voor log-getransformeerde CR), wat eerdere bevindingen in natuurlijke bodems bevestigt. De CR (log-getransformeerd) was statistisch niet gerelateerd aan het totale gehalte aan kleimineralen of het gehalte aan kleimineralen van het type 1:1 en 2:1:1, terwijl het significant afnam met een toenemend gehalte aan kleimineralen van het type 2:1 (R^2 = 0,32). Een meervoudig regressiemodel met vier verschillende kleimineraalgroepen, gebaseerd op X-stralendiffractie (XRD), leverde het sterkste voorspellende model op (R^2 = 0,79). We concludeerden dat XRD-kwantificering waardevol is voor het beschrijven van de biobeschikbaarheid van ^{137}Cs in klei-zandmengsels met contrasterende eigenschappen.

Het experimentele vervolgonderzoek identificeerde of soortgelijke trends van mineralogie waar zijn in natuurlijke bodems. De biobeschikbaarheid van ^{137}Cs in bodems van diverse moedermaterialen en verweringsstadia. Twee

bodemsequenties uit Kenia (*N* = 6) en de Filipijnen (*N* = 6) werden verzameld om de verschillende verweringsstadia te vertegenwoordigen die de bodemmineralogie beïnvloedden. Ook andere bodems (*N* = 26) met contrasterende bodemeigenschappen werden verzameld, zoals Andosols en Ferralsols. Er werd een experiment opgezet met deze bodems in de groeikamer. Een deel van de bodems werd bemest met K om het effect op de afname van de ^{137}Cs-CR te onderzoeken. De bodems werden gekarakteriseerd. Zo werd de mineralogie door XRD gemeten. Daarnaast werd er ^{137}Cs aan de bodems toegevoegd en werd er gras op gekweekt. De CR's varieerde vier orden van grootte tussen de bodems. De CR was het hoogst in tropische Ferralsol (47 kg kg^{-1}) vanwege de lage ^{137}Cs-selectieve adsorptie van kaolinietklei en de lage dosering uitwisselbare K in deze bodems. Er werd een semi-mechanistisch ^{137}Cs-overdrachtsmodel aangewend, dat voornamelijk gekalibreerd was voor gematigde bodems die gedomineerd worden door verweerde mica mineralen. Het model voorspelde de onderliggende processen in sterk verweerde tropische bodems slecht, maar door compenserende effecten van de ^{137}Cs-adsorptie en beschikbare K in bodems, voorspelde het nog steeds redelijk goed de biobeschikbaarheid van ^{137}Cs (^{10}log(CR)) in alle bodems (R^2 = 0,78).

Ten slotte werd er experimenteel onderzoek gedaan naar ^{137}Cs-adsorptie (niet biobeschikbaarheid) beïnvloed door de kleimineralogie in bodems van verschillende verweringsstadia. De klei- en leemfracties werden geïsoleerd uit 24 bodems uit verschillende verweringsstadia. De ^{137}Cs-adsorptie werd gemeten als het Radiocesium-Interceptiepotentieel (RIP), voor alle bulk bodemstalen en in de bijbehorende klei- (0–2 µm) en leemfracties (2–50 µm), samen met XRD-analyses van de mineralogie van deze fracties. De resultaten toonden aan dat het RIP in deze bodems niet gerelateerd was aan het kleigehalte (p >0,05), dit in tegenstelling tot het algemene concept van modellen die stellen dat de kleifractie in de bodem de belangrijkste voorspeller is van een CR-waarde. In plaats daarvan verklaarde de mineralogie van de bodem, met name het illietgehalte, de RIP van de bodem. In sommige bodems werd een aanzienlijk deel van het RIP gevonden in de leemfractie (>50%). Bovendien kon de RIP van de geïsoleerde kleifractie groter zijn dan de RIP van de bodem, waarschijnlijk als gevolg van de klei-isolatie procedure, waarbij K vrijkwam uit de kleiminerale tussenlagen, waardoor de gerafelde randen toenamen en waarbij het scheiden van kleimineralen uit de bodem het kleigehalte verhoogde. Dit toonde aan dat het bestuderen van geïsoleerde

bodemcomponenten niet noodzakelijkerwijs een intacte bodem in het veld weerspiegelt.

Over het algemeen benadrukt dit onderzoek het belang van de mineralogie van bodems bij het voorspellen van de biobeschikbaarheid van radiocesium, waardoor de doeltreffendheid van de impactanalyses van radiocesium op wereldwijde schaal wordt verbeterd. Dit onderzoek toont aan dat, naast veenbodems, sterk verweerde bodems het meest kwetsbaar zijn voor de overdracht van radiocesium met CR-waarden van meer dan 10 kg kg^{-1}. Dit wil zeggen dat planten radiocesium uit dergelijke bodems ophopen. Bijgevolg vereisen noodplannen rond nieuwe nucleaire installaties in tropische gebieden specifieke aandacht voor de risico's van de voedselketen. Het samenvoegen van alle RIP-gegevens toonde aan dat bodemmineralogie de RIP-voorspellingen sterk verbeterde in vergelijking met voorspellingen op basis van standaard bodemeigenschappen zoals klei en organische stofgehalte. Er werd echter aangetoond dat de standaard bodemeigenschappen, aangevuld met bodemclassificatie volgens de World Reference Base (WRB), bijna even sterke voorspellers zijn als bodemmineralogie. De effecten van bodemstructuur en mineralogie op de biobeschikbaarheid van radiocesium in veldomstandigheden moeten verder onderzocht worden, vooral in tropische gebieden waar de gevolgen van radiocesium op lange termijn nog grotendeels onbekend zijn.

Popular summary

Nuclear energy is growing worldwide and is logically not without environmental risk. It is, therefore, crucial to assess the risks of potential nuclear accidents and how to mitigate their impact on agriculture at a global scale. A major concern is radiocaesium, a radioactive element that is released during nuclear accidents, such as those at Chornobyl and Fukushima. Radiocaesium can contaminate soil and enter the food chain by mimicking potassium, an essential plant nutrient. This radiocaesium contamination can persist for decades because the radioactive half-life of radiocaesium is 30 years. Clay minerals in soils can retain radiocaesium so that less radiocaesium is transferred from the soil to the plant. To what extent radiocaesium is retained in soil depends on the type of clay mineral. Scientists have developed models to calculate the transfer of radiocaesium from the soil to edible crops. These models have been calibrated to data from the Chornobyl and Fukushima-affected regions; these have soils with similar clay mineral types. This raises the question: can these models predict radiocaesium transfer to plants from soils with different mineralogies worldwide?

First, a systematic review was conducted, yielding a harmonized database on radiocaesium transfer from soil to plants covering various climates and soils. The results revealed that soils from tropical areas were underrepresented but that these soils yield much higher radiocaesium transfer to crops than soils from temperate areas, highlighting the need for more diverse data from soils from tropical areas. While traditional mechanistic models worked well for smaller datasets, artificial intelligence models proved to be more effective when handling larger datasets. We conducted greenhouse experiments to gain further insights into the role of clay mineralogy in soils on the bioavailability of radiocaesium in soil. Results showed that radiocaesium availability to plants varied over two orders of magnitude depending on the clay mineralogy at equal clay content. For example, soils from tropical climates with highly weathered clays retain less radiocaesium, and low potassium contents in these soils allow plants to take up more radiocaesium. These findings counter previous assumptions of models that mineral soils are much less vulnerable than peat soils. The results also show that soil mineralogy can be incorporated into models to better predict radiocaesium transfer in soils around the world. Soil mineralogy is not known at a global

scale with high resolution. However, this research has shown that the standard soil properties complemented with soil classification can improve the predictions.

Vulgariserende samenvatting

Kernenergie neemt wereldwijd toe en is logischerwijs niet zonder milieurisico. Het is daarom van cruciaal belang om de risico's van mogelijke nucleaire ongelukken te evalueren en de impact ervan op de landbouw wereldwijd te beperken. Een groot probleem is radiocesium, een radioactief element dat vrijkomt bij kernongevallen, zoals die in Tsjernobyl en Fukushima. Radiocesium kan de bodem verontreinigen en in de voedselketen terechtkomen doordat het kalium nabootst, een essentiële voedingsstof voor planten. Deze verontreiniging met radiocesium kan tientallen jaren aanhouden vanwege de lange, radioactieve halfwaardetijd van radiocesium. Die bedraagt namelijk 30 jaar. Kleimineralen in de bodem kunnen radiocesium vasthouden, zodat er minder radiocesium van de bodem naar de plant wordt overgedragen. In welke mate radiocesium wordt vastgehouden in de bodem hangt af van het type kleimineraal. Wetenschappers hebben modellen ontwikkeld om de overdracht van radiocesium van de bodem naar eetbare gewassen te berekenen. Deze modellen zijn gekalibreerd aan de hand van gegevens uit de gebieden rond Tsjernobyl en Fukushima. Beide getroffen gebieden hebben bodems met vergelijkbare types kleimineralen. Maar kunnen deze modellen de overdracht van radiocesium voorspellen naar planten vanuit bodems met verschillende mineralogieën overal ter wereld?

Eerst werd er een systematisch onderzoek uitgevoerd, dat een eenduidige databank opleverde over de overdracht van radiocesium van de bodem naar planten die verschillende klimaten en bodems omvatte. De resultaten toonden aan dat bodems uit tropische gebieden onvoldoende vertegenwoordigd waren, maar dat deze bodems een veel hogere radiocesiumoverdracht naar gewassen geven dan bodems uit gematigde gebieden. Dit benadrukt de noodzaak van meer diverse gegevens van bodems uit tropische gebieden. Terwijl traditionele mechanistische modellen goed werkten voor kleine verzamelingen van gegevens, bleken artificiële-intelligentiemodellen effectiever te zijn bij het verwerken van grotere verzamelingen van gegevens. We voerden experimenten uit in een groeikamer om meer inzicht te krijgen in de rol van kleimineralen op de biobeschikbaarheid van radiocesium in de bodem. De resultaten toonden aan dat de beschikbaarheid van radiocesium voor planten meer dan twee orden van grootte varieerde, afhankelijk van de kleimineralogie bij een gelijk kleigehalte. Zo houden bodems uit tropische klimaten met sterk verweerde klei minder radiocesium vast en zorgen lage

kaliumgehaltes in deze bodems ervoor dat planten meer radiocesium kunnen opnemen. Deze bevindingen weerleggen eerdere aannames van modellen dat minerale bodems veel minder kwetsbaar zijn dan veenbodems. De resultaten laten ook zien dat bodemmineralogie kan worden geïntegreerd in modellen om de overdracht van radiocesium in bodems over de hele wereld beter te voorspellen. Bodemmineralogie is niet overal even welbekend. Dit onderzoek heeft echter aangetoond dat standaard bodemeigenschappen in combinatie met bodemclassificatie de voorspellingen kunnen verbeteren.

List of abbreviations

1:1 clay	clay minerals with layers of one tetrahedral sheet and one octahedral sheet (g 100 g^{-1})
a	mineral phases that appear amorphous on XRD pattern (g 100 g^{-1})
Al-2:1 clay	aluminum-rich clay minerals with layers of two tetrahedral sheets enclosing one octahedral sheet (g 100 g^{-1})
AlOx	aluminum (oxy-)hydroxides (g 100 g^{-1})
Amp	amphibole (g 100 g^{-1})
ANOVA	one-way analysis of variance
Ant	anatase (g 100 g^{-1})
Cal	calcite (g 100 g^{-1})
CEC	cation exchange capacity ($cmol_c$ kg^{-1})
CF	plant concentration factor (L kg^{-1})
CR	radiocaesium soil-to-plant concentration ratio (kg kg^{-1})
CR_{agg}	aggregated radiocaesium soil-to-plant concentration ratio (m^2 kg^{-1})
CV	coefficient of variation
Dol	dolomite (g 100 g^{-1})
FAO	Food and Agriculture Organization of the United Nations
Fe-2:1 clay	iron-rich clay minerals with layers of two tetrahedral sheets enclosing one octahedral sheet (g 100 g^{-1})
Fe-2:1:1 clay	iron-rich clay minerals with layers of two tetrahedral sheets enclosing one octahedral sheet and an interlayer hydroxide sheet (g 100 g^{-1})
FeOx	iron (oxy-)hydroxides (g 100 g^{-1})
FES	frayed edge site
Fsp	feldspar (g 100 g^{-1})
GM	geometric mean
IAEA	International Atomic Energy Agency
IUR	International Union of Radioecologists
K_c	selectivity coefficient
K_D	solid-liquid distribution coefficient (L kg^{-1})
LD	laser diffraction
LOI	loss-on-ignition
MAFF	Ministry of Agriculture, Forestry and Fisheries of Japan

Mg-2:1:1 clay	magnesium-rich clay minerals with layers of two tetrahedral sheets enclosing one octahedral sheet and an interlayer hydroxide sheet (g 100 g^{-1})
mica	mica (e.g., muscovite) (g 100 g^{-1})
Ms	muscovite (g 100 g^{-1})
N	number of observations
n	number of replicates
NARO	National Agriculture and Food Research Organization of Japan
N_{ref}	number of references
Po	pyrrhotite (g 100 g^{-1})
Px	pyroxene (g 100 g^{-1})
Qtz	quartz (g 100 g^{-1})
REML	restricted maximum likelihood
RES	regular exchange site
RIP	radiocaesium interception potential (mmol kg^{-1})
RIP_{clay}	radiocaesium interception potential in the clay fraction (mmol kg^{-1} clay)
RIP_{sand}	radiocaesium interception potential in the sand fraction (mmol kg^{-1} sand)
RIP_{silt}	radiocaesium interception potential in the silt fraction (mmol kg^{-1} silt)
RIP_{soil}	radiocaesium interception potential in the soil (mmol kg^{-1} soil)
RMSE	root mean square error
SD	standard deviation
SE	standard error
SOC	soil organic carbon content (g 100 g^{-1} soil)
SOM	soil organic matter content (g 100 g^{-1} soil)
WI	weathering index of the soil
XRD	X-ray diffraction
ZnO	zincite (g 100 g^{-1})

Table of contents

Acknowledgments I

Summary V

Samenvatting IX

Popular summary XIII

Vulgariserende samenvatting XV

List of abbreviations XVII

Table of contents XIX

Chapter 1 The fate of radiocaesium in the soil-plant system 1

Chapter 2 A database for predicting radiocaesium soil-to-plant transfer on a global scale 31

Chapter 3 Quantitative clay mineralogy predicts radiocaesium bioavailability to ryegrass grown on clay-sand mixtures 57

Chapter 4 Highly weathered mineral soils have highest transfer risk of radiocaesium contamination after a nuclear accident: a global soil-plant study 79

Chapter 5 The clay mineralogy rather than the clay content determines radiocaesium adsorption in soils 101

Chapter 6 Advancing global radiocaesium soil-to-plant transfer predictions: Feasibility, modeling, mapping, and future challenges 121

Bibliography 141

Supplementary information 157

Project output 291

Chapter 1
The fate of radiocaesium in the soil-plant system

Today, we face big challenges in securing a sustainable energy supply while mitigating climate change. Nuclear energy is seen as a potential solution, offering low-emission electricity that could complement renewable sources such as wind and solar in the transition to net-zero emissions. Several countries such as Canada, China, Finland, India, Japan, Romania, the Russian Federation, the United Kingdom, and the United States are exploring or have implemented nuclear reactors in cogeneration mode for district heating, hydrogen production, and other applications as strategy for climate change mitigation (IAEA, 2024). Energy security and price increases underscore the need for diversification of energy sources away from fossil fuels, requiring an evaluation of the role of nuclear in future energy mix. Public concerns regarding nuclear incidents drive decision-makers to re-evaluate and strengthen nuclear safety and emergency preparedness (IEA, 2022).

The demand for electricity continues to increase worldwide, driving countries such as Chile, Ghana, and Pakistan to explore nuclear energy, while others, including South Africa, Turkey, and the United Arab Emirates, are considering expanding their existing nuclear power capacities (IAEA, 2021a). In addition, countries such as Egypt, Kenya, Morocco, Niger, Nigeria, and Sudan, amongst others, have been working with the International Atomic Energy Agency (IAEA) to assess their readiness for launching nuclear programs. However, a critical question arises: Are these countries prepared to manage the potential consequences of nuclear accidents?

Neutron-induced nuclear fission of uranium-235 generates radioactive by-products, and when these radionuclides are released into the terrestrial environment, radioactive caesium and strontium are most of the concern because of their high production yields and physiochemical properties (Davis, 1961). These anthropogenic radionuclides can be taken up by living organisms, leading to internal exposure to ionizing radiation. This thesis focuses on the fate of radioactive caesium in the terrestrial environment, as its dynamics can vary significantly across different regions.

In this manuscript, radioactive caesium or radiocaesium refers to the isotopes ^{134}Cs and ^{137}Cs. The half-life of ^{134}Cs is about 2 years, while that of ^{137}Cs is 30 years (Davis, 1961). Both isotopes decay by releasing beta particles and gamma radiation. For instance, ^{137}Cs decays to meta-stable barium-137

(^{137}Ba) through the emission of 511 keV beta particles, followed by 662 keV gamma rays as it stabilizes into non-radioactive ^{137}Ba. Additionally, ^{137}Cs can decay directly into stable ^{137}Ba by emitting a higher energy beta particle of 1,180 keV. In the case of ^{134}Cs, beta particles of 83–683 keV and gamma radiation of 473–1,367 keV are released as it decays into stable barium-134 (Davis, 1961). Despite differences in their decay processes, ^{134}Cs and ^{137}Cs have a similar fate in the environment.

Since nuclear weapons testing began in 1945, the fate of radiocaesium in terrestrial environments has been extensively studied (e.g., Davis, 1961). However, it was the large-scale nuclear accidents at Chornobyl in 1986 and at Fukushima in 2011 that highlighted the severe and widespread consequences of radiocaesium contamination. The Chornobyl accident resulted in transboundary contamination across Europe, with radionuclides deposited in many neighboring countries. In contrast, at Fukushima, approximately 80% of the atmospheric radionuclides were deposited into the ocean, limiting the contamination of land (Steinhauser et al., 2014 and references therein).

Following a nuclear accident, the release of radionuclides poses health risks to organisms, including humans. These risks can manifest through external exposure, internal exposure from inhaling radionuclides, and internal exposure through the consumption of contaminated food. Of these pathways, ingesting contaminated food becomes the most critical route of exposure in the long-term aftermath of a nuclear accident. Exclusion zones were established around the Chornobyl and Fukushima nuclear power plants, where residents were evacuated, and areas with the highest radiation levels (>1,480 kBq m^{-2}) were contained (Figure 1.1). The contaminated area in Europe covered 29,400 km^2 (2,940,000 ha), while in Japan it covered 1,700 km^2 (170,000 ha). In Belarus, the country most severely affected by Chornobyl, the contaminated areas consisted of 43% agricultural land, 39% forests, and 2% rivers and lakes. In Japan, over 75% of the contaminated land was forested, <10% rice paddy fields, <10% other agricultural areas and <5% urban areas.

The socioeconomic consequences of large-scale nuclear accidents are profound and long-lasting. Several countermeasures have been implemented to mitigate these consequences (Beresford et al., 2016 and references therein). At the food safety level, permissible levels of radionuclide concentrations in agricultural products have been defined. For land

management, soil remediation strategies, including deep plowing, applying mineral fertilizers, and soil excavation, have been tested and have been adopted. In the aftermath of Chornobyl, it was predicted that remediation efforts would be necessary in inhabited areas until at least 2045. Restrictions remain in place for animal production systems in parts of Scandinavia, even after almost 40 years after the accident.

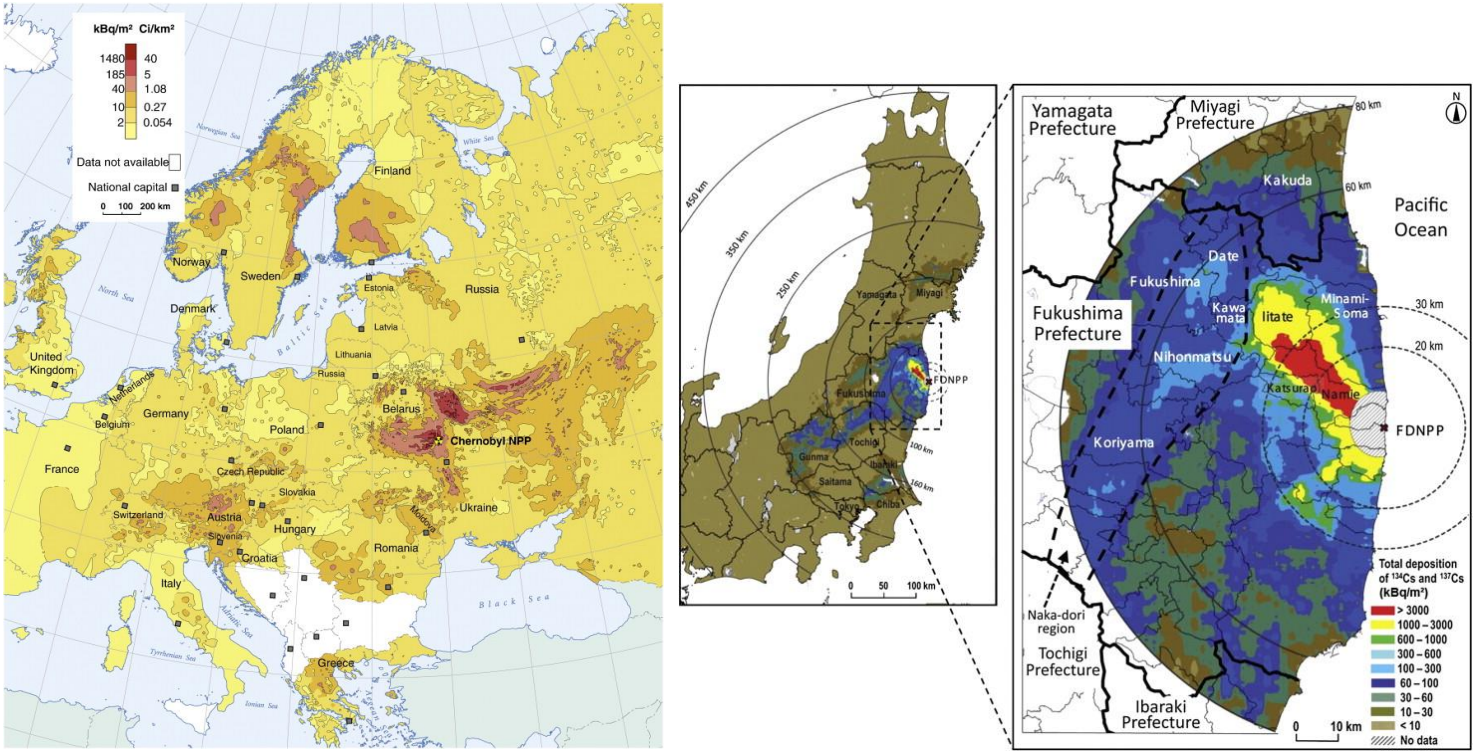

Figure 1.1. Estimated total deposition of radiocaesium after the nuclear power plant accidents (left) in Chornobyl; and (right) Fukushima (Steinhauser et al., 2014).

1.1. Rationale for quantifying radiocaesium soil-to-plant transfer on a global scale

As more countries worldwide show interest in nuclear energy, it is becoming increasingly important to be prepared for the potential environmental consequences of nuclear accidents. This includes developing robust strategies to manage impacts on the terrestrial environment. A major concern is the risk of radiocaesium entering the food chain following such accidents. To address this risk, scientists have developed models to estimate the transfer of radiocaesium from soil to plants, and these models will be required to make predictions under diverse environmental conditions, including tropical and arid climates.

However, it has never been tested whether these models can be extrapolated across diverse soils found on global scale. Radiocaesium soil-to-plant transfer models were calibrated on data from regions affected by the Chornobyl and Fukushima accidents. These models are based on regional datasets with soils originating from similar geographical and climatic zones (temperate) and thus are likely to have similar soil characteristics, such as mineralogy. It is likely that these data do not sufficiently cover the contrasting global soil conditions.

Failure to resolve this research problem will have substantial consequences. If the existing radiocaesium soil-to-plant transfer models used in emergency response tools cannot be adjusted for global application, they will not be effective in nuclear accidents in underexplored regions, such as in tropical and arid climates. This limitation may lead to underestimating the radiocaesium soil-to-plant transfer risks, exposing populations to greater health risks than anticipated. Conversely, overestimating the transfer risks may result in inefficient and unnecessary decisions on countermeasures in the early stages of a nuclear accident.

This research aims to quantify the radiocaesium bioavailability in the terrestrial environment based on plant and soil characteristics on a global scale. It contributes to improving impact assessments for food safety and optimizing remediation strategies of agricultural areas affected by nuclear accidents. In this introductory chapter, we discuss the radiocaesium soil-to-plant transfer models developed for impact assessments, followed by the processes that influence the fate of radiocaesium in the soil-plant system. We then highlight the role of clay minerals in soils on the fate of radiocaesium, as well as the importance of soil weathering affecting the soil mineral composition.

1.2. Radiocaesium soil-to-plant transfer models for impact assessments

Radionuclides released into the atmosphere can be deposited on plants and soil, and rain efficiently washes out radionuclides, increasing soil contamination (Delvaux et al., 2001; Steinhauser et al., 2014 and references therein). During the first two years after a nuclear accident, direct deposition of radionuclides on plant leaves is a more significant route of human exposure than root uptake (Figure 1.2). Pasture eaten by livestock also becomes an important pathway as radionuclides transfer to meat and milk. Exposure to radiocaesium, particularly ^{137}Cs, poses health risks. External exposure can increase the risk of cancer due to the high-energy gamma radiation emitted by ^{137}Cs. Internal exposure through ingestion or inhalation allows radiocaesium to accumulate in soft tissues, particularly in muscles (Davis, 1961). Impact assessment tools based on reference values and transport models estimate radiation doses in humans and environmental contamination. These impact assessments are crucial for optimizing radiation protection measures and guiding decision-making processes (Sweeck et al., 2020).

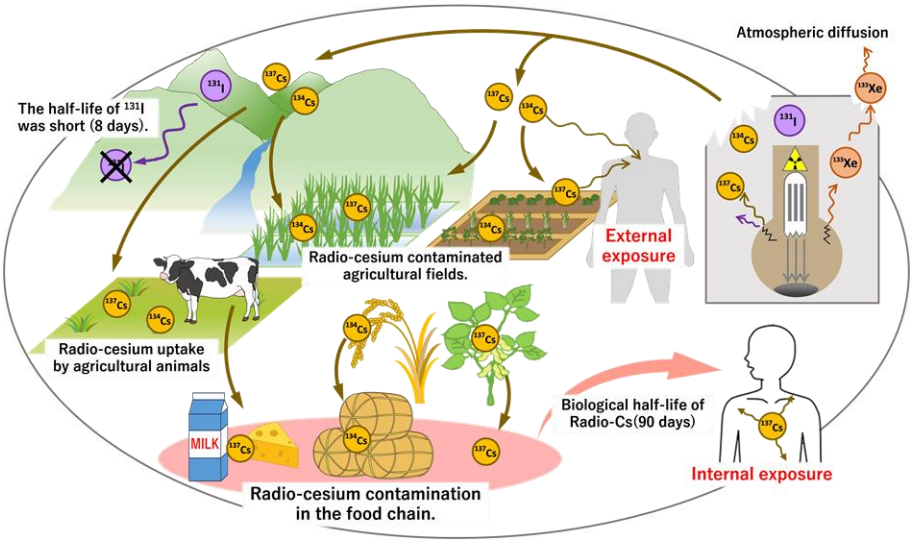

Figure 1.2. Pathways of radiocaesium entering the food chain and human exposure after the Fukushima accident (figure taken from Rai and Kawabata, 2020).

This thesis focuses on the transport of radiocaesium from soil to plants via their root systems. The contribution of food intake to the annual radiation dose in the general population has been intensively studied. The IAEA provides screening values indicating that 79% of the ^{137}Cs dose may come from the ingestion of contaminated food, the remainder being mainly the external radiation from the deposition (IAEA, 2001). The impact of the CR (defined in Section 1.3.1) on the dose in a contaminated zone is logically proportional to the CR. For example, at the typical critical deposition level of 1480 kBq ^{137}Cs m^{-2} of soil (i.e., the criterion after the Chornobyl accident to relocate the general population (Kirchmann and Van der Stricht, 2001), Figure 1.1), an average annual dose of 0.14 mSv per year is obtained in the general population, still below the accepted annual dose of 1 mSv per year (based on a food limit for ^{134}Cs and ^{137}Cs of 600 Bq kg^{-1}, Euratom Treaty, Article 31). This dose estimate assumed 260 kg soil m^{-2} (20 cm soil depth and 1300 kg m^{-3} soil density), a CR of 0.01 kg kg^{-1} for a given food crop (Kirchmann and Van der Stricht, 2001), a food consumption of 0.5 kg per person per day, and a dose conversion factor of $1.3 \cdot 10^{-8}$ Sv Bq^{-1} (ICRP, 2012). However, CR values vary several orders of magnitude (IAEA, 2009) with values 4–7 times higher in peat lands than other soil types for the same plant species (Sanchez et al., 1999). At a realistic worst-case CR of 1 kg kg^{-1}, the annual dose amounts to 13 mSv per year with the other assumptions as above, i.e., well above the accepted annual dose to the general population. All this illustrates that predicting locally applicable CR values is key for proper risk assessment of contaminated environments.

Numerous empirical and mechanistic models have been developed to estimate radiocaesium uptake by plants from soil (e.g., Table 1.1). These models are often preferred over the use of reference values reported by the IAEA (e.g., FAO/IAEA, 2010) for estimating soil-to-plant transfer of radiocaesium (Almahayni et al., 2019). Among these, the semi-mechanistic model developed by Absalom et al. (2001) and its variants (Tarsitano et al., 2011) have been compared with the steady state model used in the Food Chain and Dose Module for Terrestrial Pathways (FDMT; Müller et al., 1999), which is implemented in decision support systems such as ARGOS and Real-time Online Decision Support System for nuclear emergency management (RODOS; Ehrhardt, 1997). The Absalom model has proven more effective at identifying vulnerable agricultural areas after a nuclear accident (Brown et al., 2020). As such, this project will use the Absalom model as the reference

(Figure 1.3). Although semi-mechanistic models may not capture all relevant soil-plant system mechanisms because of the compromise between the availability of input variables and scientifically based processes, they represent a major improvement over the reference CR values, as demonstrated through comparisons with experimental data (Strebl et al., 2007). However, the Absalom model, which was calibrated primarily for European regions, had to be adjusted to accurately predict radiocaesium transfer in Japanese soils affected by the Fukushima accident (Uematsu et al., 2016) which highlights the need to account for regional differences (e.g., climate, soil properties, crop types, and land management practices).

Table 1.1. Empirical and semi-mechanistic models to predict radiocaesium soil-to-plant transfer. Categories of plants on which the models were fitted and soil model input variables are given.

type of model	*model reference*	*plant categories*	*soil variables*
empirical linear regression	Binh et al. (2003)	rice; leafy vegetables; non-leafy vegetables; leguminous vegetables	soil organic matter content; soil pH measured in water; exchangeable K content; exchangeable Ca and Mg content
	Sanzharova et al. (2002)	cereals; leafy vegetables	clay content; soil organic matter content; soil pH measured in 0.01 mol L^{-1} $CaCl_2$; cation exchange capacity; exchangeable K content; exchangeable Ca and Mg content
	Nguyen (2006)	rice; leafy vegetables	soil-radiocaesium contact time; soil organic matter content; soil pH measured in water; cation exchange capacity
semi-mechanistic	Absalom et al. (1999)	grass	soil-radiocaesium contact time; clay content; exchangeable K content
	Absalom et al. (2001)	grass	soil-radiocaesium contact time; clay content; soil organic matter content; soil pH measured in 0.01 mol L^{-1} $CaCl_2$; exchangeable K content; NH_4 in soil solution
	Keum et al. (2007)	rice	soil-radiocaesium contact time; clay content; soil organic matter content; soil pH measured in 0.01 mol L^{-1} $CaCl_2$; exchangeable K content
	Krstić et al. (2007)	grass	clay content; soil organic matter content; soil pH measured in 0.01 mol L^{-1} $CaCl_2$; exchangeable K content
	Tarsitano et al. (2011)	grass; cereals	soil-radiocaesium contact time; clay content; soil organic matter content; exchangeable K content; NH_4 in soil solution
	Uematsu (2017); Uematsu et al. (2015)	grass; rice	soil-radiocaesium contact time; clay content; soil organic matter content; Loss-On-Ignition content; soil pH measured in 0.01 mol L^{-1} $CaCl_2$; cation exchange capacity; exchangeable K content

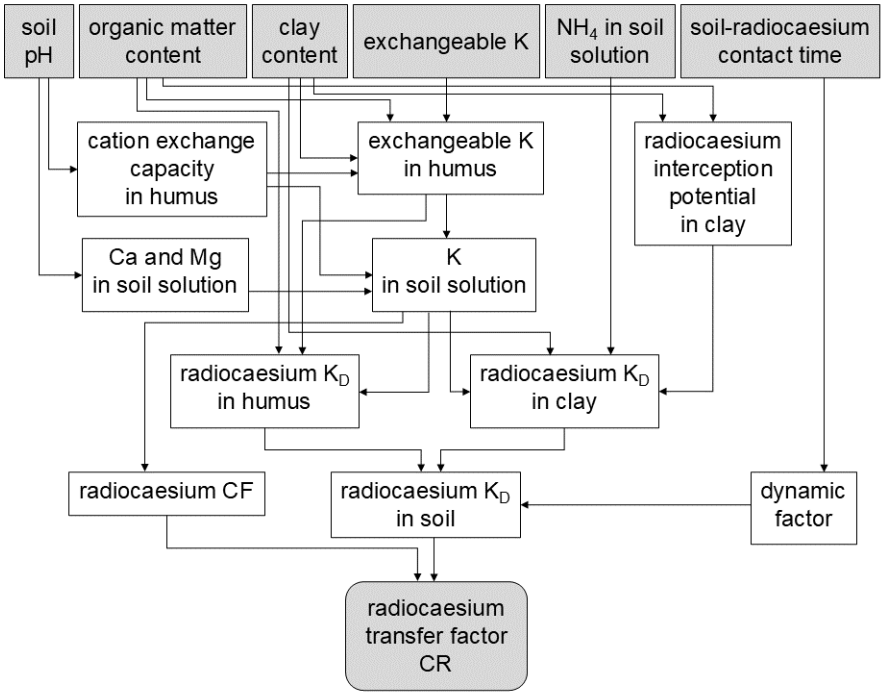

Figure 1.3. The semi-mechanistic radiocaesium soil-to-plant transfer model (or Absalom model) (adapted from Tarsitano et al., 2011). Model equations and parameter values are tabulated in Appendix I.

1.3. Radiocaesium transfer in the soil-plant system

Radiocaesium can transfer into environmental compartments, such as soil and biota.

1.3.1. Radiocaesium transfer from soil to plant

The bioavailable radiocaesium is the radiocaesium "which is freely available to cross an organism's cellular membrane from the medium the organism inhabits at a given time" (Semple et al., 2004), and thus enters the plant. The transfer of radiocaesium is empirically quantified as a ratio of radiocaesium concentration in the plant to that in the soil (CR) in units of kg kg^{-1} on dry weight (DW) basis:

$$\mathrm{CR} = \frac{\text{radiocaesium concentration in plant material (Bq kg}^{-1}\text{ DW)}}{\text{radiocaesium concentration in soil (Bq kg}^{-1}\text{ DW)}} \qquad (1.1)$$

CR values are typically determined by measuring concentrations in the edible plant part and in the total, i.e., bulk, soil, where plant roots extract nutrients, to

depths of 20 cm for crops and 10 cm for grass (IUR, 1982). Most CR values are well below 1 kg kg^{-1}, typically 0.01 kg kg^{-1} and suggest strong binding of radiocaesium to soil particles or minimal radiocaesium accumulation. The CR values sometimes exceed 1 kg kg^{-1} and suggest bioaccumulation of radiocaesium (IAEA, 2006). The CRs depend on the soil and plant characteristics, plant growth conditions, and the time that radiocaesium has been in contact with soil. The International Union of Radioecologists (IUR) and IAEA have compiled measured CR for various soil and plant combinations. However, there is a large variability among CR that cannot be explained by the soil texture class, and plant type and compartment (Almahayni et al., 2019; Delvaux et al., 2001). For example, reported CR values (IAEA, 2009) for leafy vegetables grown on loamy soil ranged between 0.0003–0.7 kg kg^{-1}, over three orders of magnitude.

The process of radiocaesium transfer from soil to plants involves the compartments: soil, soil solution, and plant. The CR can be expressed as a combination of radiocaesium uptake by plants from the solution and the distribution of radiocaesium between the soil and soil solution which can be considered as two reactions in series (Smolders et al., 1997):

$$\underbrace{\text{radiocaesium}_{\text{soil}} \underset{K_D}{\leftrightarrow} \text{radiocaesium}_{\text{soil solution}} \underset{CF}{\rightarrow} \text{radiocaesium}_{\text{plant}}}_{CR}$$

and

$$CR = \frac{\dfrac{\text{radiocaesium concentration in plant material (Bq kg}^{-1}\text{ DW)}}{\text{radiocaesium concentration in soil solution (Bq L}^{-1}\text{)}}}{\dfrac{\text{radiocaesium concentration in soil (Bq kg}^{-1}\text{ DW)}}{\text{radiocaesium concentration in soil solution (Bq L}^{-1}\text{)}}} \qquad (1.2)$$

$$CR = \frac{CF}{K_D} \qquad (1.3)$$

where the concentration factor (CF) is the ratio of radiocaesium concentrations in the plant material to that in the soil solution, in units of L kg^{-1}, and the solid-liquid distribution (K_D) is the ratio of radiocaesium concentrations in the soil (Bq kg^{-1}) to that in the soil solution (Bq L^{-1}), in units of L kg^{-1}.

1.3.2. Radiocaesium transfer from soil solution to plant

The uptake of radiocaesium by plants depends on its concentration in the soil solution (Figure 1.4), which is directly accessible to plant roots, as well as on the concentration of competing cations. Caesium dissolved in soil solution (Cs^+) behaves similarly to potassium ions (K^+), a macronutrient, and are both

taken up by the same root uptake mechanisms. This competition between Cs^+ and K^+ for uptake by plants is a key process in determining the amount of radiocaesium plants take up. Of all plant-related processes, the concentration of K^+ in the solution has the most important effect on Cs^+ uptake in plants (Zhu and Smolders, 2000). At higher K^+ concentrations (>1 mmol L^{-1}), plants are able to distinguish more effectively between K^+ and Cs^+ (Zhu and Smolders, 2000), resulting in minimal Cs^+ uptake. Note that even at these high K^+ concentrations, small amounts of Cs^+ are still taken up by plants. If K^+ concentrations decrease (<0.3 mmol L^{-1}), plant uptake systems have difficulty distinguishing between K^+ and Cs^+ (Zhu and Smolders, 2000) due to nutrient stress, leading to a more than proportional increase in Cs^+ uptake.

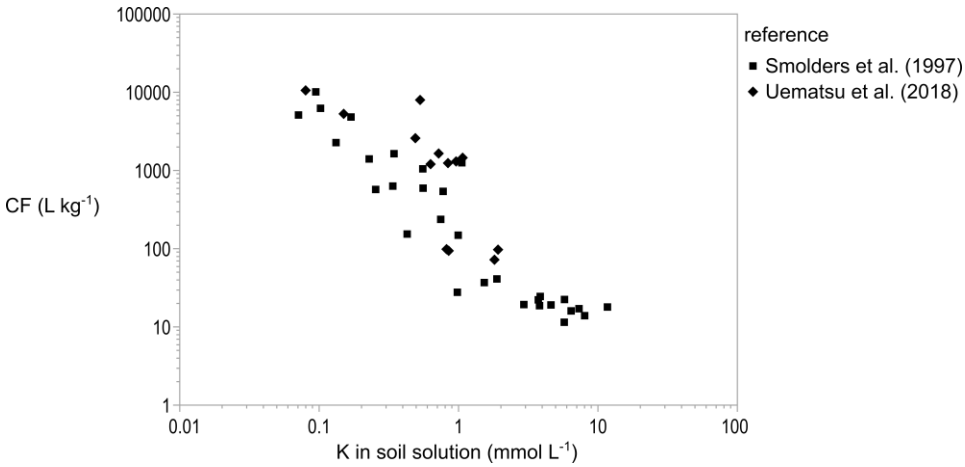

Figure 1.4. The K concentration in soil solution affects the radiocaesium uptake in grass (log-log scale) from 30 Belgian soils (Smolders et al., 1997) and 13 Japanese soils (Uematsu et al., 2018).

1.3.3. Radiocaesium transfer from soil solution to soil

The availability of radiocaesium in soil depends on its adsorption onto soil components and competition with other cations for adsorption (Figure 1.5). Caesium is selectively, i.e., preferentially, adsorbed on weathered edges, called Frayed Edge Sites (FES), of clay minerals, such as illite, constituting <1% of their total cation exchange capacity (Brouwer et al., 1983). Caesium can also bind to a lesser extent on the Regular Exchange Sites (RES) of clay minerals with limited selectivity. Only weakly hydrated monovalent cations, such as K^+ and ammonium (NH_4^+), compete effectively with Cs^+ for selective

adsorption on FES, while all cations, including K^+, calcium (Ca^{2+}) and magnesium (Mg^{2+}), compete with Cs^+ for adsorption on the RES.

In environmental conditions, radiocaesium concentrations in soil are generally very low, i.e. trace concentrations. For example, measurements of soil solution from Chornobyl detected concentrations of 1,000 Bq ^{137}Cs L^{-1}, which corresponds to $2 \cdot 10^{-12}$ mol L^{-1} (Strebl et al., 2007). In soils containing FES, about 80% of the radiocaesium is adsorbed onto FES (IAEA, 2009), meaning the majority of radiocaesium is effectively bound within the soil matrix.

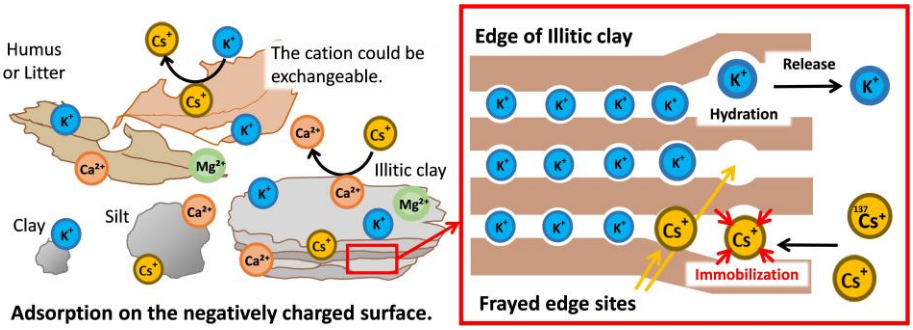

Figure 1.5. Fate of radiocaesium in the soil (left) competing with cations for adsorption on soil components; and (right) selective adsorption of the weathered edges of micaceous minerals (figure taken from Rai and Kawabata, 2020).

The adsorption of radiocaesium in soil can be evaluated by cation exchange reactions at multiple adsorption sites, each with its own cation selectivity and capacity (Cremers et al., 1988). The monovalent exchange reactions of Cs^+ and K^+ at the FES and RES can be represented as:

$$\mathrm{FES-K+Cs^+}_{(aq)} \rightleftarrows \mathrm{FES-Cs+K^+}_{(aq)} \tag{1.4}$$

$$\mathrm{RES-K+Cs^+}_{(aq)} \rightleftarrows \mathrm{RES-Cs+K^+}_{(aq)} \tag{1.5}$$

The selectivity coefficients (K_c) of Cs^+ compared to K^+ for these sites are expressed as:

$$K_C^{FES}(Cs^{trace}|K) = \frac{Z_{Cs}^{FES} \cdot [K^+]}{Z_K^{FES} \cdot [Cs^+]} = \frac{K_D^{FES}(Cs) \cdot [K^+]}{Z_K^{FES} \cdot [FES]} \tag{1.6}$$

$$K_C^{RES}(Cs|K) = \frac{Z_{Cs}^{RES} \cdot [K^+]}{Z_K^{RES} \cdot [Cs^+]} = \frac{K_D^{RES}(Cs) \cdot [K^+]}{Z_K^{RES} \cdot [CEC]} \approx 1 \tag{1.7}$$

where $K_c^{FES}(Cs^{trace}|K)$ is the selectivity coefficient of Cs at trace concentrations compared to K in the FES, $K_c^{RES}(Cs|K)$ is the selectivity coefficient of Cs

compared to K in the RES, Z_i^{FES} and Z_i^{RES} are the proportions of cation i in the FES and RES, respectively, $[K^+]$ and $[Cs^+]$ are the concentrations of K^+ and Cs^+ in the soil solution (mmol L^{-1}), respectively, $K_D^{FES}(Cs)$ and $K_D^{RES}(Cs)$ are the solid-liquid distribution coefficients of Cs in the FES and RES (L kg^{-1}), respectively, [FES] is the FES adsorption capacity (mmol kg^{-1}), and [CEC] is the total cation exchange capacity (mmol kg^{-1}).

The total K_D of radiocaesium in soil (L kg^{-1}), assuming K^+ is the main competing cation, can be calculated as the sum of adsorption on FES and RES:

$$\begin{aligned} K_D(Cs) &= K_D^{FES}(Cs) + K_D^{RES}(Cs) \\ &= \frac{K_C^{FES}(Cs^{trace}|K) \cdot Z_K^{FES} \cdot [FES]}{[K^+]} + \frac{Z_K^{RES} \cdot [CEC]}{[K^+]} \end{aligned} \tag{1.8}$$

The Radiocaesium Interception Potential (RIP) test is used to measure the adsorption of radiocaesium to the FES in soil and clay samples (Cremers et al., 1988). This laboratory test involves saturating the RES with Ca^{2+} to block them from Cs^+ (K_D^{RES} becomes 0) and saturating the FES with K^+ (Z_K^{FES} becomes 1) to allow Cs^+ exchange (Wauters et al., 1996a). Trace concentrations of radiocaesium are then added to the sample under these standard cation conditions and the ratio of adsorbed radiocaesium to the remaining radiocaesium in solution multiplied by the K^+ concentration gives the RIP (mmol kg^{-1}):

$$RIP = K_C^{FES}(Cs^{trace}|K) \cdot [FES] = K_D^{FES}(Cs) \cdot [K^+] \tag{1.9}$$

The RIP test combines the Cs^+ specific site selectivity that reflects the intensity with which Cs^+ is exchanged with K^+ at the FES, and the site capacity that reflects the quantity of Cs^+ that can be adsorbed at the FES (Delvaux et al., 2001). However, NH_4^+ competes more effectively than K^+ for selective adsorption onto FES (Wauters et al., 1996b), so in soils with limited nitrification, the concentration of NH_4^+ should also be considered. The total K_D of radiocaesium in soil, accounting for NH_4^+ competition, becomes (IAEA, 2009):

$$\begin{aligned} K_D(Cs) &= K_D^{FES}(Cs) + K_D^{RES}(Cs) \\ &= \frac{RIP}{[K^+] + K_C^{FES}(NH_4|K) \cdot [NH_4{}^+]} + \frac{\text{exch K} + \text{exch NH}_4}{[K^+] + [NH_4{}^+]} \end{aligned} \tag{1.10}$$

where $K_c^{FES}(NH_4|K)$ is the selectivity coefficient of NH_4 compared to K in the FES (value is about 5), $[NH_4^+]$ is the concentration of NH_4^+ in the soil solution

(mmol L^{-1}), and exch K and exch NH_4 are the exchangeable K^+ and NH_4^+ in the soil (mmol kg^{-1}).

1.3.4. Radiocaesium adsorption on Frayed Edge Sites of clay minerals

Radiocaesium in soil primarily adsorbs in the wedge-shaped zone at the edges of certain clay minerals (Sawhney, 1972). Clay minerals have a layered structure and weathering processes form FES in mica minerals at the mineral edges (Figure 1.6). Expanding clay minerals, such as vermiculite and smectite can also form FES by collapse of the expanded layers due to wetting-drying cycles and increasing K content in soils (Maes et al., 1985; Vandenhove et al., 2003). Mixed-layered minerals, which are common in soils, with mica, smectite and vermiculite can also form FES (e.g., Joussein et al., 2004).

However, the capacity of FES for Cs^+ adsorption does not directly correlate with the micaceous clay content, suggesting variability in the structure, selectivity, and capacity of FES depending on the degree of weathering and particle size of the clay minerals (Wauters et al., 1994). The non-linear sorption kinetics of Cs^+ reflects the heterogeneity of adsorption sites with varying structures, adsorption site capacity and selectivity for Cs^+ (Brouwer et al., 1983; Maes et al., 1985). Although theoretically, different types of radiocaesium adsorption sites are defined in literature (e.g., Bradbury and Baeyens, 2000; Brouwer et al., 1983), they cannot be reliably distinguished by current characterization methods. Instead, it is likely that FES represent a continuum of sites with varying, but generally high selectivity for Cs^+ (Bruneel, 2021).

Ongoing research continues to investigate the mechanisms of radiocaesium sorption in FES (e.g., Uno et al., 2024). Caesium has a higher affinity for FES compared to K^+ due to its lower hydration energy, which facilitates the dehydration of Cs^+ and its entry into the clay mineral interlayers. Over time, Cs^+ can become fixed in these layers, i.e., by aging. Initially, the exchange of Cs^+ and K^+ within FES is a reversible process (Brouwer et al., 1983), but over longer periods, the process becomes effectively irreversible due to slow diffusion into collapsed interlayers (Sawhney, 1972). This aging effect varies depending on soil mineralogy, as shown by the smaller effect of wetting-drying cycles on radiocaesium fixation in Japanese soils dominated by allophane (Uematsu, 2017) compared to the large effect in smectite (Maes et al., 1985). In Chornobyl, agricultural soils rapidly fixed radiocaesium (Krouglov et al., 1997), while in organic-rich, cooler environments, radiocaesium remained more bioavailable in peat soils because of the low RIP, thus a lack of clay

minerals with FES, and low K status (Sanchez et al., 1999). The effect of aging was also found in soils from Fukushima soils (Tagami et al., 2018).

The radiocaesium adsorption in soils depends on the clay mineralogy. The RIP in soils is influenced not only by clay content but also by the geological origin of the soil (Uematsu et al., 2015; Waegeneers et al., 1999), which in turn determines the soil mineralogy. The RIP varies greatly between subgroup of clay minerals (Table 1.2). However, within clay mineral species groups (e.g., montmorillonite), the variability can be larger than three orders of magnitude. This difference may be due to purity of clays, particle size and weathering of clay minerals.

Table 1.2. Radiocaesium interception potential values for various clay minerals.

layer type	*subgroup*	*octahedral layer*	*species*	*chemical formula*[a]	*RIP (mmol kg^{-1})*	*reference of RIP value*
1:1	kaolin	di	kaolinite	$[Si_4]^{IV}[Al_4]^{VI}O_{10}(OH)_8$	6.0–310	Nakao et al. (2008); Ogasawara et al. (2013)
		di	halloysite	$[Si_4]^{IV}[Al_4]^{VI}O_{10}(OH)_8 \cdot 4H_2O$	130–250	Ogasawara et al. (2013)
2:1	smectite	tri	hectorite	$[Si_8]^{IV}[Mg_{6-x}Li^{+}{}_{x}]^{VI}O_{20}(OH)_4R^{2+}{}_{\frac{x}{2}} \cdot nH_2O$	13	Ogasawara et al. (2013)
		di	montmorillonite	$[Si_8]^{IV}[Al_{4-x}Mg_x]^{VI}O_{20}(OH)_4R^{2+}{}_{\frac{x}{2}} \cdot nH_2O$	2.0–2,300	Nakao et al. (2008); Ogasawara et al. (2013); Vandenhove et al. (2005); Chapter 3
		di	beidellite	$[Si_{8-x}Al_x]^{IV}[Al_4]^{VI}O_{20}(OH)_4R^{2+}{}_{\frac{x}{2}} \cdot nH_2O$	3,400	Ogasawara et al. (2013)
	vermiculite	tri	trioctahedral vermiculite	$[Si_6Al_2]^{IV}[Mg_6]^{VI}O_{20}(OH)_4K_xR^{2+}{}_{\frac{(2-x)}{2}} \cdot nH_2O$[b]	520–2,800	Eguchi et al. (2015); Chapter 3
	mica	tri	phlogopite	$[Si_6Al_2]^{IV}[Mg_6]^{VI}O_{20}(OH)_4K_2$	2,400	Eguchi et al. (2015)

layer type	*subgroup*	*octahedral layer*	*species*	*chemical formula*[a]	*RIP (mmol kg^{-1})*	*reference of RIP value*
		tri	biotite	$[Si_{6-x}Al_{2-x}]^{IV}\left[(Al, Fe^{3+})_y(Mg, Fe^{2+})_{6+x2-3y2}\right]^{VI}O_{20}(OH, F)_4K_2$ where x <1 and y <2	1,000–2,400	Eguchi et al. (2015); Chapter 3
		di	muscovite	$[Si_6Al_2]^{IV}[Al_4]^{VI}O_{20}(OH)_4K_2$	300–740	De Preter (1990); Eguchi et al. (2015)
		di	illite	$[Si_7Al_1]^{IV}[Al_{3.5}R^{2+}{}_{0.5}]^{VI}O_{20}(OH)_4K_{1.5}$	2,900–16,000	de Koning et al. (2007); Wauters et al. (1996b, 1994); Chapter 3

[a] ideal chemical structure formulas are given. Layer silicates are divided into tetrahedral (IV) and octahedral (VI) layers.
[b] theoretical formula for trioctahedral vermiculite derived from phlogopite.

1.4. Soil clay mineralogy

From previous studies it is clear that the soil clay mineralogy affects the fate of radiocaesium in soils.

1.4.1. Clay definition

In general, the term *clay* is inconsistently used and this causes confusion (Guggenheim et al., 1995). Clay can have three meanings (Zeelmaekers, 2011):

- Mineralogical meaning: *clay* refers to layered silicates (or phyllosilicates) and has usually a crystal size smaller than 2 µm. However, it is well-known that minerals such as illite, kaolinite, and chlorite can have larger sizes.
- Particle size meaning: *clay* refers to all particles with an equivalent spherical diameter smaller than 2 µm. In general, the fraction smaller than 2 µm of soils is dominated by layered silicates because minerals such as quartz are unstable in that size range.
- Sedimentary meaning: *clay* refers to sedimentary deposits, such as Boom clay, that consist of large portions of clay-sized particles, mostly of layered silicates, but also varying portions of other minerals, such as quartz, feldspars, etc.

In addition, particle size boundaries to define *clay* differ between disciplines. Soil scientists and mineralogists agree on 2 µm, while colloid chemists say 1 µm and sedimentologists say 4 µm (Guggenheim et al., 1995). However, a single value for crystal size threshold is arbitrary when describing non-spherical shapes (Zeelmaekers, 2011), as clay minerals vary in shape (platelets, rods, etc.) and are rarely spherical. The nomenclature committees of the Association Internationale pour l'Etude des Argiles (AIPEA) and the Clay Minerals Society (CMS) define *clay* as follows “The term *clay* refers to a naturally occurring material composed primarily of fine-grained minerals, which is generally plastic at appropriate water contents and will harden when dried or fired. Although clay usually contains phyllosilicates, it may contain other materials that impart plasticity and harden when dried or fired. Associated phases in clay may include materials that do not impart plasticity and organic matter.” and define *clay mineral* as “The term *clay mineral* refers to phyllosilicate minerals and to minerals which impart plasticity to clay and

which harden upon drying or firing." These definitions relate to the properties of plasticity and hardening upon drying or firing and are decoupled from particle size thresholds (Guggenheim et al., 1995). In this thesis, *clay minerals* refers to layered silicates, *clay content* and *clay fraction* refer to the <2 µm particles and *clay* refers to deposits rich in clay minerals.

1.4.2. Clay mineral alteration in soil

The clay mineral structure (1:1, 2:1 or 2:1:1 type structure; di- or trioctahedral) and location of charge within the layers (tetra- or octahedral) influence its stability and the formation of FES. Consequently, soils with different clay mineral compositions will exhibit varying capacities for radiocaesium adsorption, which has direct implications for radiocaesium bioavailability in the environment.

Micas, common in soils from temperate regions, undergo weathering through two primary mechanisms: layer weathering and edge weathering (Figure 1.6) accompanied by a reduction of layer charge (Essington, 2015; Fanning et al., 1989). Layer weathering causes some of the interlayers to expand, while others remain closed so that the mixed-layered mica-vermiculite or -smectite are formed. This process is common in smaller clay-sized particles. Edge (or frayed-edge) weathering causes interlayers to open up at the edges and fractures of mica, which is most common in larger (e.g., silt- and sand-sized) particles. Allophane, common in volcanic soils, can transform into hydrated kaolin clay mineral (e.g., halloysite) mixed with expanding minerals (e.g., smectite) (Delvaux et al., 1990). As weathering progresses, both the expanding clay content and layer charge decrease. The weathering pathways have in common that expanding zones are formed at the edges of clay minerals and that cations that are weakly hydrated and monovalent (e.g., K^+) can open or close the interlayer of clay minerals.

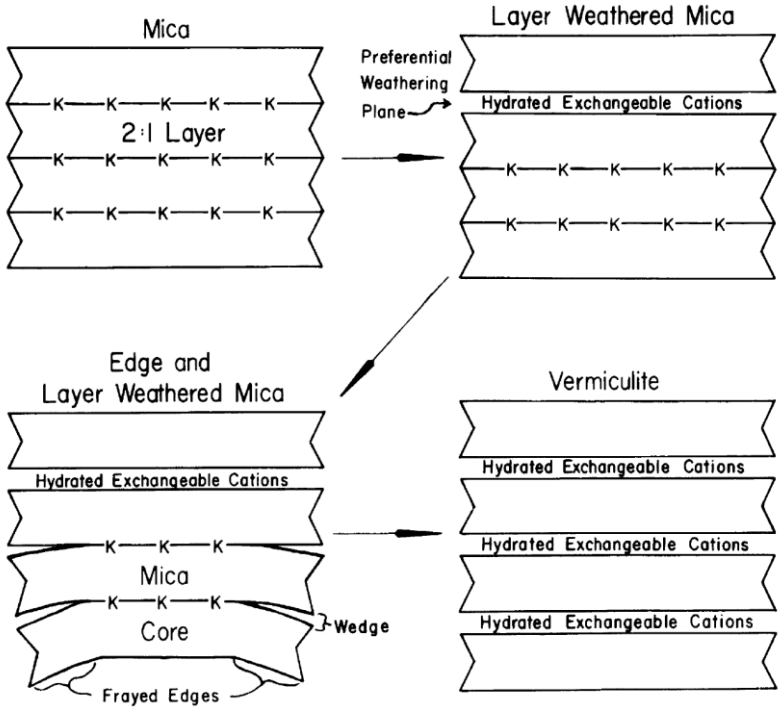

Figure 1.6. Layer-weathering and edge-weathering of micas by exchanging interlayer K with hydrated exchangeable cations, such as Ca^{2+}, K^{+}, Mg^{2+}, and sodium (Na^{+}). Note that mica minerals would normally be much wider in relation to thickness than the zone represented in the diagram (figure taken from Fanning et al., 1989).

Clay mineral formation in soils is strongly influenced by the interaction between climate and the parent material (Langmuir, 1997). In arid climates, with low precipitation and poor leaching, alkaline conditions promote the formation of clay minerals such as smectite, especially in soils derived from iron (Fe), calcium (Ca), and magnesium (Mg) rich igneous rocks such as basalt. Conversely, in more humid regions with high precipitation and better drainage, leaching increases, resulting in lower pH and lower concentrations of cations and silica. Under these conditions, minerals like kaolinite and gibbsite, which are stable in acidic environments, dominate soils formed from K and aluminum (Al) rich rocks like granite. As weathering progresses, trioctahedral micas, such as biotite transform into vermiculite, and dioctahedral micas, such as muscovite form illite which occur mainly in temperate climates. In extreme weathering environments, such as tropical regions with high rainfall and intense leaching, even kaolinite degrades,

leading to the formation of highly leached, gibbsite-rich soils. Thus, the degree of weathering and the types of minerals formed are largely determined by the balance between the intensity of leaching and the mineral composition of the parent material (Table 1.3).

The weathering sequence of Jackson et al. (1948) outlines the relationship between the intensity of weathering and the mineral composition of the clay-sized fraction of a soil (Table 1.3) (Essington, 2015). Minerals are assigned index numbers, with lower values corresponding to minerals that weather easily and are common in younger soils. Conversely, higher numbers are assigned to minerals that resist weathering and are typically found in more leached, i.e., older, soils. Note that *older* in this context does not necessarily refer to the actual age of the soil, but rather to its degree of leaching. Soils exposed to more moisture and weathering processes are considered older than those with limited moisture, regardless of their chronological age. The clay fraction in most soils consists of three to five dominant minerals. A weighted average of the index numbers for these minerals is used to determine the weathering stage of the soil (Equation 4.1). However, it is important to note that these mineral weathering indices are indicative of trends rather than strict rules. For example, feldspars and quartz can still be found in poorly weathered soils, while quartz may accumulate in highly weathered Podzols. Muscovite, which weathers very slowly, can accumulate in highly weathered soils, while halloysite can be associated with moderate weathering stages (Delvaux et al., 1989). Exceptions like these highlight the complexity and variability of soil weathering processes.

Table 1.3. Jackson weathering indices of soil clay-sized minerals and soil weathering stages (adapted from Essington, 2015; Jackson, 1964; Jackson et al., 1948; Jackson and Sherman, 1953; Sposito, 2008).

characteristics of soil chemical and physical conditions	*characteristics of soil properties*	*characteristics of minerals in the soil clay fraction*	*examples of minerals in the soil clay fraction*	*mineral weathering index*
early stage (young soils)				
Low water and humus content, very limited leaching;	Minimally weathered soils: arid or very cold regions, waterlogging, recent deposition	Soluble evaporites	gypsum; halite; sulfides; soluble salts	1
Reducing environments, cold environments;		Sparingly soluble carbonates and phosphates	calcite; dolomite; apatite	2
Limited amount of time for weathering		Primary silicates with high base cation content	olivine; amphiboles; pyroxenes	3
		Primary phyllosilicates with high Fe(II) and Mg content (trioctahedral)	biotite; glauconite; mafic chlorite	4
		Tectosilicates with isomorphic substitution	feldspars (albite and K-feldspars)	5
		Tectosilicates without isomorphic substitution	quartz	6

characteristics of soil chemical and physical conditions	*characteristics of soil properties*	*characteristics of minerals in the soil clay fraction*	*examples of minerals in the soil clay fraction*	*mineral weathering index*
intermediate stage				
Retention of Na, K, Ca, Mg, Fe(II), and silica; moderate leaching, alkalinity	Soils in temperate regions: forest or grass cover, well-developed A and B horizons, accumulation of humus and clay minerals	Primary phyllosilicates with low Fe(II) and Mg content and their initial alteration products	muscovite; illite	7
Parent material rich in Ca, Mg, and Fe(II), but not Fe(II) oxides		Mica alteration products with high Fe(III) and Mg	vermiculite; mixed-layered 2:1 layer silicates	8
Silicates easily weathered		Low Fe(III) and Mg and Al hydroxy-interlayered phyllosilicates (pedogenic chlorite)	smectites; hydroxy-interlayered vermiculite; hydroxy-interlayered smectite; Al-chlorite	9
advanced stage (old soils)				
Removal of Na, K, Ca, Mg, Fe(II), and silica	Soils under forest cover with high temperature and precipitation: accumulation of Fe(III) and Al oxides, absence of alkaline earth metals	Base cation-poor 1:1 phyllosilicates	kaolinite; halloysite	10
Intensive leaching by fresh water		Al-bearing accessory minerals	gibbsite	11
Oxidation of Fe(II)		Fe(III)-bearing accessory minerals	iron oxides (goethite; hematite)	12
Low pH and humus content		Remaining minerals	titanium oxides (anatase; rutile; ilmenite); zircon; corundum	13

1.4.3. Clay mineralogy affects radiocaesium in soil

The influence of clay mineralogy on radiocaesium adsorption has been demonstrated in various studies. For instance, a comparison of RIPs between 51 Japanese (Fukushima) soils and 88 Belgian soils revealed a difference in the relationship between RIP and clay content (Uematsu et al., 2015). The slope of the correlation between RIP and clay content was over three times lower in Fukushima soils than in Belgian soils (Figure 1.7a). This suggests a lower capacity of Fukushima soils to adsorb radiocaesium per unit of clay, despite similar FES properties in both European and Japanese soils. Even within the Fukushima region, Andosols (soils with volcanic origins) showed a smaller slope in the RIP-clay correlation compared to non-Andosol soils (Figure 1.7b), indicating that regional differences in clay mineralogy impact radiocaesium sorption. Additionally, the same study found a strong correlation between RIP in isolated clay fractions and total potassium content in nine soils, which serves as a proxy for micaceous clay content and thus for FES content (Figure 1.8). This suggests that radiocaesium adsorption capacity is closely linked to the micaceous clay minerals in the soil.

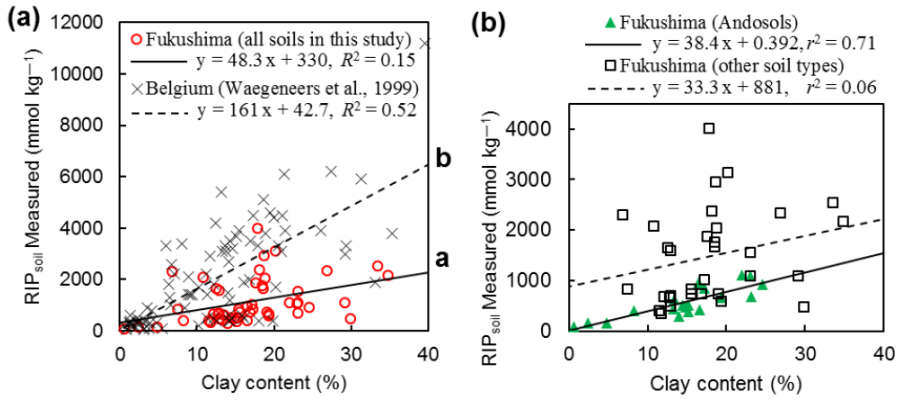

Figure 1.7. The relationship between RIP in soil and soil clay content for (a) Fukushima soils (Uematsu et al., 2015; *N* = 51) and reported for Belgian soils (Waegeneers et al., 1999; *N* = 88) and for (b) soils with andic properties (Al_o + 0.5 Fe_o ≥ 20 g kg^{-1}; *N* = 19) and other types of mineral soils (Al_o + 0.5 Fe_o < 20 g kg^{-1}; *N* = 32) separately. Linear regression lines (solid and broken lines) and corresponding equations for each of the soil groups are shown. Different letters next to the regression lines in (a) show the significant difference (p <0.001) between the slopes of the lines. Al_o and Fe_o = acid oxalate extractable Al and Fe (taken from Uematsu et al., 2015).

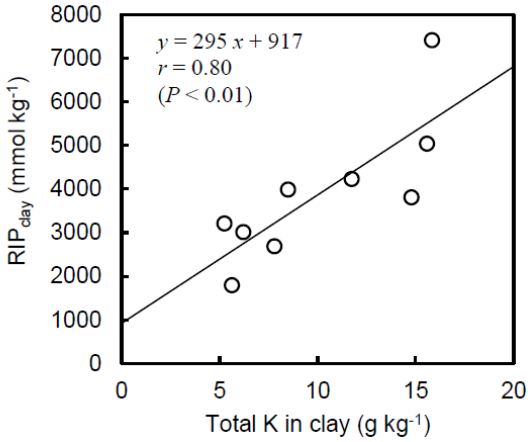

Figure 1.8. Correlation between RIPclay and total K content in clay (*N* = 9). The solid line indicates the linear regression line (taken from Uematsu et al., 2015).

Next to the FES capacity, the K buffering capacity in soil also plays an important role in radiocaesium adsorption, which is influenced by soil mineralogy. The K buffering capacity refers to the ability of the soil to maintain stable levels of K in soil solution, even when it is depleted through plant uptake or leaching, by releasing K from the exchange sites of the soil or minerals (Beckett, 1964; Fanning et al., 1989; Sparks and Huang, 1985). This capacity depends on both the total cation exchange capacity (CEC) of the soil and the amount of available K. Soils with higher CEC (>50 $cmol_c$ kg^{-1}), such as Vertisols with swelling clays, can hold more K, while soils with lower CEC (<8 $cmol_c$ kg^{-1}), such as highly weathered Ferralsols, have limited capacity for K retention (Essington, 2015). Exchangeable K in soils typically ranges from 0.2 to 0.7 $cmol_c$ kg^{-1}, depending on soil pH (Essington, 2015), and occupies <1% to 35% of the CEC (Vandebroek et al., 2012). The exchangeable potassium content, which reflects plant-available potassium, has been negatively correlated with the concentration ratio (CR), explaining up to 20% of CR variation (Nisbet et al., 1999). Both FES and K buffering capacity, which vary extensively among soils, highlight the need for more data in CR models, especially in areas where nuclear energy developments are planned. Against this background, current work was undertaken.

1.5. Research objectives and strategy

This introduction clarified that radiocaesium contamination of agricultural land is one of the most important risks of nuclear accidents. The knowledge generated after the Chornobyl and Fukushima affected areas highlighted that the RIP of soil, combined with the K status of soils, is key in determining the risk of transfer to the food chain. Organic (peat) soils have been proposed as the most vulnerable because of the low RIP (lack of clay minerals) and low K status. However, soil chemical research also revealed that the RIP in soil is not only determined by its clay content but also by its clay mineralogy. This knowledge of the role of clay mineralogy is not yet embedded in the bioavailability models, likely because the models had been calibrated to soils from regions with similar clay mineralogy.

Against this background, this research was set up with the main objectives of exploring and understanding the soil properties affecting radiocaesium bioavailability on a *global* scale. The central hypothesis was that radiocaesium sorption is affected by soil clay mineralogy and that information on clay mineralogy can be linked with other globally available soil information to make predictions at a global scale.

The specific research objectives are

- to identify gaps in the radiocaesium soil-to-plant transfer databases compiled after nuclear accidents;
- to explore the feasibility of developing global radiocaesium transfer models with the available data;
- to gain a deeper understanding of radiocaesium bioavailability in a wide variety of soils, particularly those outside of Europe;
- to evaluate the applicability of existing semi-mechanistic models of radiocaesium transfer for a wide variety of soils; and
- to investigate how these models can be adjusted to predict radiocaesium transfer in contrasting soils.

This research project was set up as a first attempt to apply the knowledge to the fate of radiocaesium in soil-plant systems beyond the specific regions for which it had been established and as a first attempt to quantify the bioavailability of radiocaesium in soils of various mineralogies found on a global scale. For this research, a systematic review of the available literature

and new experiments were set up to obtain information on the transfer of radiocaesium from soil to plants on a global scale. This information was then used to develop new data-driven models and adjust existing models to predict radiocaesium transfer at the global scale. A soil-chemical and mineralogical approach was used to study the bioavailability of radiocaesium in soils with different mineralogies.

This research project did not consider the slow release of radiocaesium due to the weathering of fallout fuel particles. It also did not address the foliar interception process, which is important in the first days and weeks after an accident.

1.6. Manuscript outline

This manuscript is structured as follows:

Chapter 2 focuses on developing a comprehensive radiocaesium soil-to-plant transfer database. Statistical analyses were performed to assess the variability in radiocaesium transfer data, and new data-driven models were developed. In addition, the chapter discusses how data-driven models and available soil information can be used to create a global radiocaesium transfer map.

Chapter 3 examines the influence of clay minerals on the bioavailability of radiocaesium. Greenhouse experiments were conducted with mixtures of different clays with sand, spiked with ^{137}Cs and grown with grass. The chapter describes how clay minerals were quantified and their role in influencing radiocaesium soil-to-plant transfer.

Chapter 4 examines the bioavailability of ^{137}Cs in a range of natural soils from various parent materials and weathering stages, including soils from tropical climates. Greenhouse experiments were used to assess the effect of K fertilization on ^{137}Cs soil-to-plant transfer. The chapter discusses the relationship between soil mineralogy and radiocaesium uptake by plants. It evaluates the applicability of existing semi-mechanistic models of radiocaesium transfer for a wide variety of soils.

Chapter 5 explores the selective adsorption of ^{137}Cs in the clay and silt fractions of 24 contrasting soils. This chapter focuses on isolating these fractions, characterizing their mineralogy, and measuring their selective adsorption properties (i.e., RIP) while evaluating the assumptions of existing semi-mechanistic models of radiocaesium transfer.

Chapter 6 integrates the insights from Chapters 2 to 5 and proposes adjustments to existing semi-mechanistic models of radiocaesium transfer. It also discusses the feasibility of modeling and mapping radiocaesium soil-to-plant transfer on a global scale, addressing the uncertainties in the process and outlining future scientific prospects.

Chapter 2
A database for predicting radiocaesium soil-to-plant transfer on a global scale

Abstract

Data-driven models can significantly enhance global predictions of radiocaesium transfer from soil to plants. However, a publicly accessible and harmonized database is lacking. Here, a systematic screening of radiocaesium soil-to-plant transfer factors (CR, i.e., concentration ratios) was made, data were selected based on the experimental design, data relevance, and traceability, and a harmonized database was constructed. The comprehensive CR database included 8,837 records of CR from 142 different studies. The CR values ranged from 0.000028 to 380 kg kg^{-1}, with the highest CR observed in soils originating from tropical climates and organic soils, and the lowest in those from temperate climates. However, the number of records from tropical (N = 404) and arid climates (N = 47) was limited. Univariate and multivariate analyses indicated that the CR value was most affected by the specific study in which the data were obtained, followed by soil properties and followed by species-based plant categories. Subsets of data were made that differed by the number of variables present and combinations of those variables. This showed that semi-mechanistic models had more predictive power than machine learning models on the small data sets (N <200). In contrast, machine learning models were superior to other models on larger datasets. A global radiocaesium transfer map was created using the machine learning model and available soil information at a global scale and identified that the most vulnerable areas are those with highly weathered soils and organic soils. However, the map was based on a limited dataset (N = 513), and essential information, such as soil exchangeable potassium (K) and mineralogy, was absent. Developing a harmonized database is crucial for data-driven models, such as machine learning techniques, that can be used to create radiocaesium transfer maps.

2.1. Introduction

The global expansion of nuclear power plants calls for a revision of radiological impact assessments so that remedial strategies are ready in case of a nuclear accident. Release of radioactive caesium (or radiocaesium) is a concern because it has a long half-life (2 years for ^{134}Cs and 30 years for ^{137}Cs) and because it is similar to potassium (K), so it can be taken up by plants entering the food chain. The transfer of radiocaesium from soil to plants is quantified using a concentration ratio (CR, or transfer factor) (Equation 1.1).

The CR mainly depends on soil and plant properties and on the time after the contamination, i.e., soil-radiocaesium contact time. Many data and models have been published on the fate of radiocaesium in the terrestrial environment, especially after the Chornobyl and Fukushima accidents (e.g., reviewed by Almahayni et al., 2019; IAEA, 2020, 2009, 2006; IUR, 1992; Li et al., 2024; Nisbet et al., 1999). The IAEA recommends radiological impact assessments based on these research findings (IAEA, 2021b, 2020, 2009). The CR values were compiled into categories for various crop types and soils with different mineral and organic matter content so that estimates based on geometric means could be made. However, it is well established that there is a large variability of the CR within these soil-plant categories (Almahayni et al., 2019), and using these fixed values for impact assessments might not be adequate. For example, CRs typically vary over six orders of magnitude, and within the soil and plant categories, there is still at least three orders of magnitude variation, such as leafy vegetables grown on loamy soils (CR = 0.0003–0.7 kg kg^{-1}, IAEA, 2009). The mechanistic models that have been developed to predict CRs typically use soil clay content, exchangeable K, NH_4 in solution, organic matter content and pH as soil variables (Absalom et al., 2001; Almahayni et al., 2019). These models had been constructed based on the concept that the CR is explained by soil solution ^{137}Cs and K concentrations as the measure of bioavailable ^{137}Cs (Absalom et al., 1999; Smolders et al., 1997). The predictive power of these models is fairly strong (Chapter 4). However, it is clear that considerable variation remains unexplained (Chapter 4) and that the calibration and validation have been mainly limited to the soil-plant conditions found in the areas affected by Chornobyl and Fukushima accidents.

New data-driven modeling approaches, such as machine learning, can enable CR predictions on a larger, i.e., a global scale. The power lies in the algorithm

improving its performance as the number of data increases. However, a comprehensive database on radiocaesium CRs and information on the variables affecting radiocaesium transfer from soil to plant is not openly accessible. For example, the IUR database (IUR, 1992) is available on demand but lacks essential information such as exchangeable K content in soil. The IAEA reports often include summarized values for soil and plant types, but the underlying data are not available for modeling (IAEA, 2020, 2009). Additionally, national databases, such as those of the Ministry of Agriculture, Forestry and Fisheries (MAFF) of Japan, are reported in Japanese (e.g., MAFF, 2017, 2015, 2014) making them challenging to access and use for international researchers.

This study aims to improve global predictions of radiocaesium transfer in the terrestrial environment and enhance impact assessments for food safety by building a comprehensive database. Data were collected from multiple sources, screened for quality and harmonized, and a database was constructed. The number of soil, plant, climate, and other variables associated with each CR record logically varied among studies. With these data, statistical multivariate analyses were performed, and different models were compared to evaluate their predictive power. On a subset of the data for which all variables were available to use the semi-mechanistic (or process-based) model, a comparison was made between the semi-mechanistic models (Absalom et al., 2001; Tarsitano et al., 2011) and data-driven models, either log-linear multiple regression or random forest modeling. On a wider and more comprehensive dataset, data-driven models were used with a global soil map to construct a global radiocaesium transfer map.

2.2. Materials and methods

2.2.1. Data collection

A total number of 8,837 CR data, derived from 142 different references were collated. Data were systematically screened and selected based on selection criteria. The data collection and selection procedure is summarized in Figure 2.1. The data sources included pot experimental data, field data from the Fukushima prefecture, IAEA technical reports, and articles obtained by systematically searching in Web of Science and Scopus.

Data from pot experiments (Gilis and Sweeck, 2019; Sanchez et al., 1999; Smolders et al., 1997; Uematsu et al., 2018; Chapter 3 and 4) with similar setup were included in the database because of data reliability and high-quality due to the standardized conditions in which the experiments were performed.

Data from the field collected by the National Agriculture and Food Research Organization (NARO) and the Ministry of Agriculture, Forestry and Fisheries (MAFF) of Japan between 2012–2017, involving crops like buckwheat, soybean, and brown rice were included.

Most data here originated from IAEA technical reports (IAEA, 2021b, 2020, 2009, 2006), carefully selected by experts. However, these CR data had been listed with descriptive statistics per plant-soil categories without original data. Therefore, that dataset was reconstructed by revisiting the source documents. In total, 272 references had been cited in the IAEA reports, of which 164 were accessible online (most non-accessible were references in Russian and Japanese), of which 124 met all the selection criteria (Table II.2).

Data from articles searched in the Web of Science and Scopus were obtained by a search string of keywords. A search string of keywords was created including four concepts: *caesium* as the element of interest, *soil* as substrate, *plant* as receiving organism, and *transfer* as a process (Table II.3). The search string was validated using the references from the IAEA reports, which are relevant to this study. Of 102 IAEA report references in the Web of Science database, 96 were obtained using that string. The article indexing databases on the Web of Science and Scopus platforms (Table II.4) were simultaneously searched on 19/12/2022 at 15:00 (CEST) using the search string. After deduplication with EndNote™ (version 20.4.1) software, fewer references remained. We selected a subset of 100 references using a random number generator. The subset was screened using Rayyan software (Ouzzani et al.,

2016). Relevant references were selected first based on the titles and abstracts and then on the full articles using the selection criteria (Table II.2) if they were accessible online. Only 10 out of 100 references from the random subset remained.

Data were extracted from the references in the case of tables by copying them and in the case of graphs by reconstructing them with an online extraction tool (such as https://plotdigitizer.com/app).

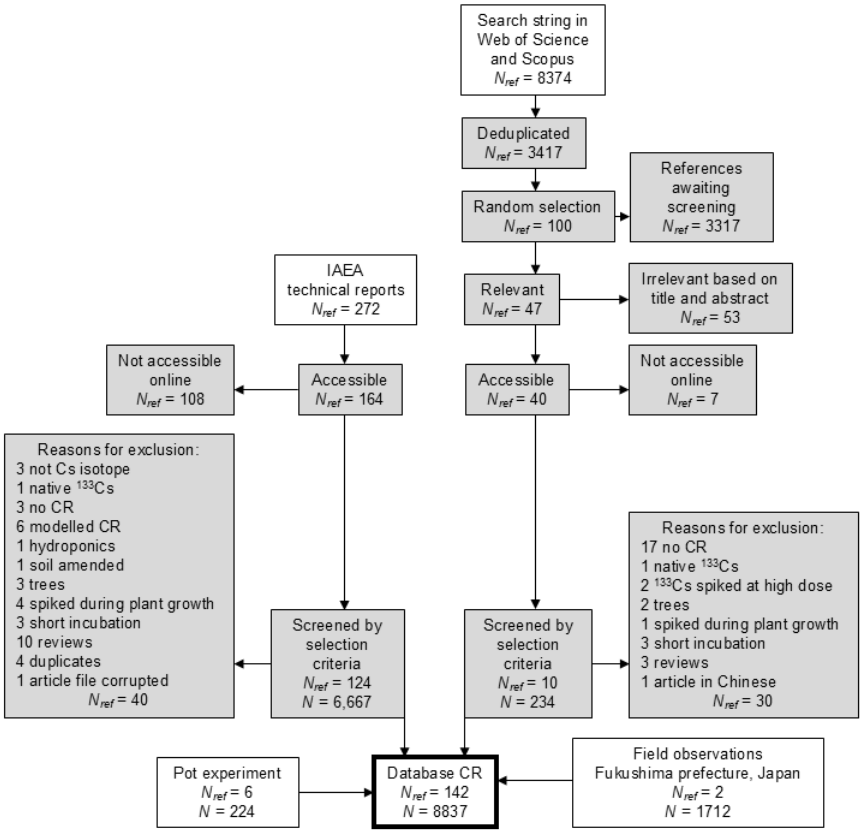

Figure 2.1. Schema of data collection and selection process for the CR database. Detailed information on the selection criteria is listed in Supplementary Information (Table II.2). N_{ref} = number of references; N = number of records. Gray boxes are data selection steps.

2.2.2. Selection criteria

Selection criteria were used to systematically filter information during the screening process, details are given in the Supplementary Information (Table II.2) and are briefly summarized here. Data were *rejected* if:

- radiocaesium in or on the plant mainly originated from foliar interception of fallout, as this database referred to root uptake of radiocaesium from soil, or
- plants were grown in hydroponics, agar, or other substrates not representative of agricultural soils, or
- the contact time between radiocaesium and soil was less than 2 months at the time of plant collection to ensure that a pseudo-equilibrium had formed, as shorter times may reflect surface contamination rather than true soil-to-plant transfer (IAEA, 2006), or
- the CR was based on stable Cs added to soil unless the dose was less than 0.001 µmol kg^{-1} substrate, or
- the soil was amended with minerals (e.g., zeolite, bentonites), or
- the nutrients in the soil were experimentally depleted prior of the plant growth, or
- the plants were trees or non-terrestrial (marine) plants, or
- background information on the CR calculation method was absent, or
- the CR was based on modeled or inferred rather than measured radiocaesium concentrations in the soil and plant, or
- the CR was reported in a reference citing other references (e.g., reviews), or
- the CR was non-paired (derived CR), i.e., radiocaesium concentrations in the plant was measured from a different substrate than where the plant grew, or
- radiocaesium concentrations were not corrected for radioactive decay.

2.2.3. Database structure

Detailed background information behind each CR was collected to refine the data into more site-specific subsets based on soil, plant, climate and experimental variables. This collation followed recommendations from reports (IAEA, 2021; IUR, 1982; FAO/IAEA, 2010).

The collected data were managed using a relational database system using SQL Server (version 16.0 Microsoft, 2022), which enabled efficient queries, updates and scalability. The data were organized into nine separate tables with clear relationships and constraints to ensure data integrity and optimal query performance. This schema design supports future scalability, allowing for the addition of new data or expansion of existing datasets without compromising performance.

The attributes (or columns) for each CR included categorical and numerical information on the reference, experimental setup, measurement quality, sampling, isotope type and concentrations, plant properties, and soil properties relevant to CRs (Table II.1). In total, 100 attributes were documented, each corresponding to a single CR, these attributes are further denoted as *variables*. The variables can be classified into soil variables (e.g., soil pH, clay content), plant variables (e.g., species, plant part) or miscellaneous (e.g., plant growth method, CR calculation method). Each CR record (or row) in the database was supplemented with as much information as possible from the original references. Unique sample codes and reference information were assigned to each record for traceability. Detailed descriptions of the input variables are provided in the Supplementary Information (Table II.1). These variables were used in models that influence the transfer of radiocaesium.

2.2.4. Data harmonization

Data from different references were harmonized to ensure compatibility and comparability. This process included:

- Converting units (e.g., Ci to Bq, g to mol, mL to L).
- Converting plant material fresh weights to dry weights using default values (FAO/IAEA, 2010).
- Converting aggregated radiocaesium CR (CR_{agg}), expressed in m^2 soil per kg dry weight (DW) plant units, to *CR* expressed in kg DW soil per kg DW plant units by using the *soil depth* and *soil density* given in the reference or using an assumed 10 cm soil layer depth for grass and 20 cm for other plants (IAEA, 2009) and soil bulk density of 1300 kg per m^3 (common for loamy soils (USDA, 2001)) as follows:

$$\mathrm{CR}\left(\frac{\frac{\mathrm{Bq}}{\mathrm{kg\ DW\ plant}}}{\frac{\mathrm{Bq}}{\mathrm{kg\ DW\ soil}}}\right) = \mathrm{CR_{agg}}\left(\frac{\frac{\mathrm{Bq}}{\mathrm{kg\ DW\ plant}}}{\frac{\mathrm{Bq}}{\mathrm{m^2\ soil}}}\right) \cdot \frac{\mathrm{soil\ depth\ (cm)}}{100} \cdot \mathrm{soil\ density}\left(\frac{\mathrm{kg}}{\mathrm{m^3}}\right) \tag{2.1}$$

The variable original CR expression method is a dummy indicating whether the CR was originally given as CR or whether it was converted as given above with given or assumed soil density.

- Converting soil humus content, soil organic matter, or loss on ignition to soil organic carbon by using a conversion factor of 0.58 (Pribyl, 2010).
- Converting exchangeable cations reported in terms of cation oxides such as mg K_2O per 100 g or mg CaO per 100 g to $cmol_c$ per kg.
- Soil pH values measured in 0.01 mol L^{-1} $CaCl_2$ or 1 mol L^{-1} KCl solution were used as equivalent numbers (with preference to soil pH in 0.01 mol L^{-1} $CaCl_2$) while pH measured in water (pH_{water}) was converted to *soil pH* with the calibrated line derived from (Ahern et al., 1995):

$$\mathrm{Soil\ pH} = 0.999 \cdot \mathrm{pH_{water}} - 0.877 \tag{2.2}$$

- Converting soil classification according to Soil Taxonomy (Soil Survey Staff, 1999) and national soil classification systems (e.g., the Russian soil classification system) to the reference soil groups of WRB (IUSS Working Group WRB FAO, 2022).
- If only minimum and maximum values were given and these data related to the same plant species on similar soils, the mean of the minimum and maximum was used. Average values were only entered into the database if these data related to the same plant species grown on similar soils.
- Missing information on the climate zone where the soil was sampled (climate zone of soil) was entered into the database based on the soil sampling location.
- Missing information on the contact time of fallout radiocaesium with substrate and time of plant harvest was entered in the database based on the most recent large-scale nuclear deposition event relative to the date of the study. Studies on radiocaesium deposition

of fallout barely reported contact time. Therefore, three reference dates of events were chosen when major radiocaesium deposition occurred. On 05/08/1963, the Partial Test Ban Treaty was signed, greatly reducing nuclear weapons testing. This date was selected for fallout from nuclear weapons testing because radiocaesium deposition occurred over decades, peaked in the 1960s, and thus could not be traced to a single date. More recent events later overshadowed radiocaesium deposition of fallout from nuclear weapons testing. On 26/04/1986, the Chornobyl nuclear power plant accident occurred, leading to the deposition of radiocaesium around the world. On 11/03/2011, the Fukushima accident caused radiocaesium deposition in east Asia.

- If information on the experiment date was missing, an average of 90 days between sowing and harvesting was assumed and entered into the database. This is a rough estimate because the growing period depends on the plant species and growing conditions. If only the year of harvest was given but not the exact date, it was assumed that harvesting took place on July 1 of the year if harvesting took place one year after radiocaesium contamination in the substrate.

2.2.5. Data analysis: models, regressions and machine learning

Statistical analyses were performed using R or JMP® Pro software (Version 17.0.0 SAS Institute Inc., Cary, NC, 1989–2023). Univariate analyses were conducted to examine the individual relationships between single variables and the CR. Geometric means (GM) and their standard errors (SE) were calculated for CR data grouped by climate zone of soil, plant category (e.g., cereals, rice, grass, leafy vegetables), soil category (clay, loam, sand, organic, coral sand), and dominant clay mineral. Significant differences in CR within categories were tested using Dunn's non-parametric comparison for all pairs, at a 5% significance level (p <0.05). Variables were ^{10}log-transformed if skewness was >1 (except pH). Single linear regressions were applied to evaluate numeric variables' effects on ^{10}log-transformed CR, while categorical variables were analyzed using one-way analysis of variance (ANOVA). Multivariate analyses were performed to account for interdependencies among variables. The combined effects of multiple variables were assessed using standard least squares multiple regression.

The performance of semi-mechanistic models (Equations I.6-I.17 from Absalom et al., 2001; Equations I.18-I.28 and I.29-I.35 from Tarsitano et al.,

2011) were compared to data-driven statistical and machine learning models using the same set of variables: plant category, soil clay content (g 100 g^{-1}), soil organic matter content (g 100 g^{-1}), soil pH, exchangeable K content ($cmol_c$ kg^{-1}), ammonium concentration in soil solution (mmol L^{-1}), and radiocaesium contact time with soil (days). A subset of data was selected for which all these variables were known (*N* = 199). Semi-mechanistic models were available for a single plant (i.e., grass), so modeled CR needed to be converted for other plants, whereas this was not necessary for data-driven models that considered plant category as a variable. Plant conversion factors for plant species (Beresford & Willey, 2019) were grouped into plant categories, and their geometric means were calculated (Table II.5), because too few CRs were reported at the plant species level. These conversion factors (f_{plant}) were then used to convert CR modeled for grass ($CR_{model\ for\ grass}$) to other plant categories (CR_{plant}):

$$\mathrm{CR}_{\mathrm{plant}} = \mathrm{CR}_{\mathrm{model\ for\ grass}} \cdot \mathrm{f}_{\mathrm{plant}} \tag{2.3}$$

A more comprehensive data analysis was performed with the data-driven models. A subset of data was selected for which minimally the CRs were based on radiocaesium concentrations and the following variables were available: plant categories, soil clay content, and exchangeable K content (*N* = 836). The statistical data-driven models were mixed-effects regressions, including fixed and random effects using Restricted Maximum Likelihood (REML) to fit the linear mixed-effects model. Dummy variables were used for plant categories with grass as the reference level. For model comparison, marginal R^2, representing the variance explained solely by the fixed effects, and conditional R^2, representing the variance explained by both the fixed and random effects (not shown), were calculated (Nakagawa and Schielzeth, 2013). The machine learning data-driven models were created using random forest regression algorithms. The model was created using the R package “randomForest” (Liaw and Wiener, 2002) with R Statistical Software version 4.4.1 (R Core Team, 2024). The dataset was split into a 70% training set and a 30% validation set because it was considered a good balance between sufficient data for model training and an independent dataset for validating model performance. A total of 500 trees were used and model variables were selected based on variance importance plots. The models were set up to predict ^{10}log-transformed CRs without transforming the variables. For this exercise, models were simplistic with no missing data, i.e., based on a limited

number of records and no cross-validation. R^2, marginal R^2 in the case of mixed-effects models, and root mean square error (RMSE) values were calculated to compare model performances.

2.2.6. Global map

A global map was created using the random forest model for grass. Soil information from SoilGrids™ (Poggio et al., 2021) (250 m resolution) was used, providing global maps of soil variables: clay content (g kg^{-1}), silt content (g kg^{-1}), sand content (g kg^{-1}), cation exchange capacity ($mmol_c$ kg^{-1}), and pH (measured in water). Soil variables given for soil depth intervals of 0–5 cm and 5–15 cm were combined (Hengl et al., 2017) to obtain soil variables of the 0–10 cm interval for grass, with pH (Equation 2.2) and units converted accordingly. The soil organic carbon content was not included because the model would be based on only 196 records. The map was created using Python software version 3.12.4 (van Rossum, 1995) to extract soil information from SoilGrids and calculate CRs (33,000 m resolution). The map was finalized in QGIS (QGIS Development Team, 2024) using the EPSG 4326 WGS 84 projection.

2.3. Results

2.3.1. Radiocaesium soil-to-plant transfer database and variables explaining the CR

The database created contained 8,837 records with information from 142 references. The CR values ranged 7 orders of magnitude, i.e., from 0.000028 kg kg^{-1} to 380 kg kg^{-1} (Figure II.1). A large variability among CR values remained even after splitting into categories of climate zone of soil, plant, soil, and dominant clay minerals (5–7 orders of magnitude differences in CRs within separate categories with *N* >100).

The univariate analysis showed the most important variables that explained the ^{10}log-transformed CR values (Table 2.1). The reference of the records, i.e., the study in which data were obtained, explained most of the CR. This may imply that methodological effects, despite efforts to harmonize data, and experimental design effects, such as soil-radiocaesium contact time and plant growth methods, introduce considerable variability in CR values in addition to the logical soil- and plant-related effects. The ammonium (NH_4) concentration in soil solutions and radiocaesium interception potential (RIP) in soils, both related to radiocaesium adsorption processes in soils, had significant and logical effects on CRs, but data were limited (*N* <500). Soil particle size category (including the category organic soil), exchangeable K content and soil clay content also affects the CR, again logically related to radiocaesium adsorption. Soil classification and climates of which soils originated had larger effects than plant category, suggesting a larger effect of the soil properties than those of plants in controlling the CR. The original CR expression method, either as CR (kg kg^{-1}) or CR_{agg} (m^2 kg^{-1}), also played a significant role, suggesting that the standard conversion method, i.e., assuming a given homogeneous root zone, was not sufficiently correct.

CRs from different climates, grouped as tropical, arid, temperate or continental, showed significant differences (Figure 2.2). The CRs measured in soils from tropical climates (grouped Af, Am, etc.) were significantly higher (p <0.05, Dunn's test) than those from other climate groups (Figure II.2). While the CRs in temperate climates (grouped Cfa, Cfb, etc.) were significantly lower. Most CRs from temperate climates were measured on Japanese soils (*N* = 3,356 out of 4,490), which were significantly lower compared to CRs measured on soils from other locations (Figure II.5). The CRs grouped by plant category showed no significant differences except rice that had significantly

lower CR (Figure 2.3). The CRs measured in organic and coral sandy soils were significantly higher than in other soil categories, while clay and loamy soils had the lowest CR (Figure 2.4). The CRs measured in soils dominated by allophane/imogolite and kaolinite were significantly larger compared to illite (Figure 2.5). However, limited data were available on soil mineralogy (*N* = 378 out of 8,837).

The highest CRs (>50 kg kg^{-1}) were measured in coral soils from the Marshall Islands (Robison et al., 2006), in sandy soils from the south-west coast of Norway (Selnaes and Strandt, 1992), and in peat soils from Northern Ireland (McGee et al., 1992). The sandy and peat soils were CR_{agg} (m^2 kg^{-1}) that were converted to CR (kg kg^{-1}) using Equation 2.1 with assumed soil density (1,300 kg m^{-3}) which was likely too low for sandy soils and too high for peat soils. Indeed, the CR_{agg} values measured in peat soils (0.038–1.3 m^2 kg^{-1}, GM = 0.20 m^2 kg^{-1}, *N* = 35, McGee et al., 1992) were the largest compared to all CR_{agg} values in this database (0.000010–1.3 m^2 kg^{-1}, GM = 0.0018 m^2 kg^{-1}, *N* = 861), so the method by which CRs were obtained and the assumptions by which data were harmonized affected the data analyses. The CRs calculated from radiocaesium deposition data (CR_{agg}, *N* = 1,061) were significantly higher than CRs based on measured radiocaesium in soil data (CR, *N* = 7,717). In addition, the plant growth methods under which CRs were obtained significantly affected the CR values, with a ranking of field monitoring < field experiment < lysimeter experiment < pot experiment (Figure II.3). The CRs from reconstituted substrates did not significantly differ from those in lysimeter and pot experiments. However, the CRs were not corrected for time (i.e., related to the duration of the experiment), which likely differed for each plant growth method as clearly shown in Figure II.4, i.e., the time and plant growth method effects might be confounded (see below: multivariate analysis).

Table 2.1. Single variable effect sizes on ^{10}log-transformed CRs ranked by R^2. n.s. = not significant (p >0.05). N = number of records. Note that N differs largely among variables because these variables were often not present for different records.

variable class	*variable*	*N*	R^2
miscellaneous	reference (i.e., source document)	8,837	0.63
soil	soil solution NH_4	128	0.45
soil	soil classification (WRB)	1,711	0.36
soil	radiocaesium interception potential	420	0.33
soil	climate zone of soil	7,533	0.32
plant	plant category (based on plant species)	8,837	0.29
soil	soil category (particle size class, organic soil, coral sand)	4,813	0.24
soil	mineralogy	378	0.15
miscellaneous	original CR expression method	8,778	0.12
soil	exchangeable K content	5,148	0.11
miscellaneous	land use where soil was sampled	2,435	0.07
soil	cation exchange capacity	4,075	0.06
miscellaneous	plant growth method	8,837	0.05
soil	clay content	3,827	0.03
soil	soil organic carbon content	3,238	0.02
soil	sand content	3,595	0.01
miscellaneous	soil-radiocaesium contact time	6,544	0.01
soil	silt content	3,489	<0.01
soil	soil pH	4,415	n.s.

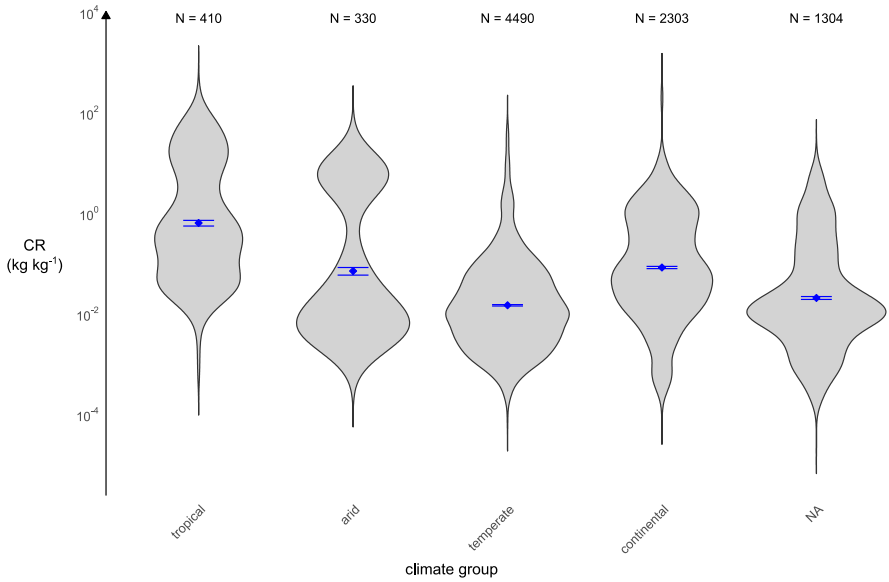

Figure 2.2. Violin plots of CRs on log-scale categorized by soils sampled in these climates show a significantly higher CR in tropical climates than in temperate and continental climates, with a large difference in the number of records. Diamonds show geometric means, and error bars are their standard errors. NA = data not available.

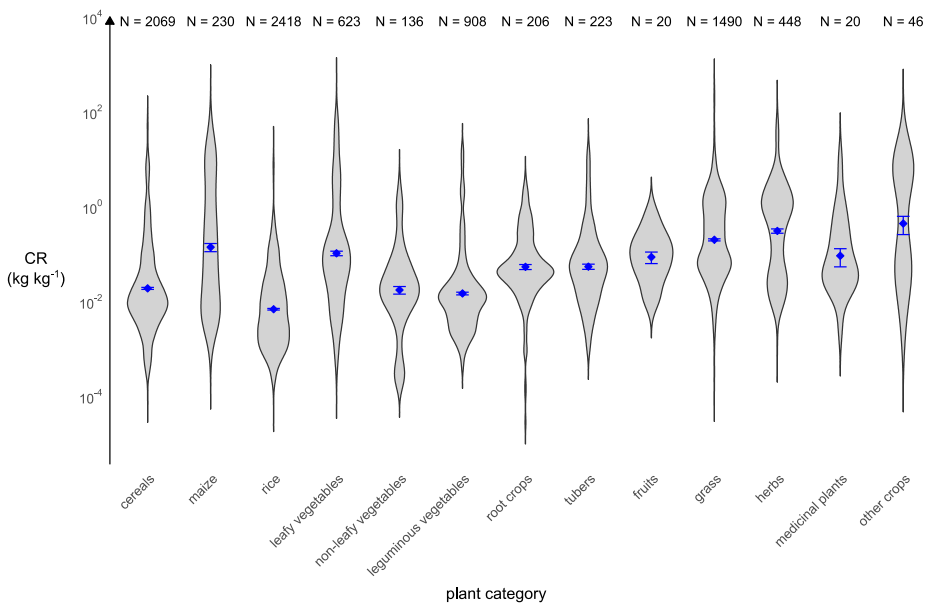

Figure 2.3. Violin plots of CRs on log-scale categorized by plant category. Diamonds show geometric means, and error bars are their standard errors.

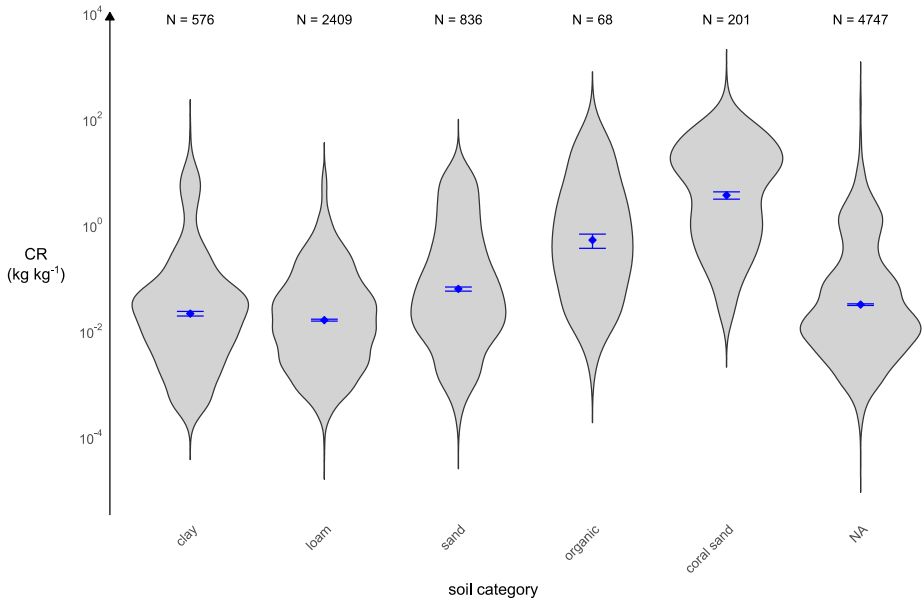

Figure 2.4. Violin plots of CRs on log-scale categorized by soil (texture) category show a significantly higher CR for organic and coral sandy soils (coral sands are dominated by carbonates and not silicate clay, e.g., island and atoll soils). Diamonds show geometric means, and error bars are their standard errors. NA = data not available.

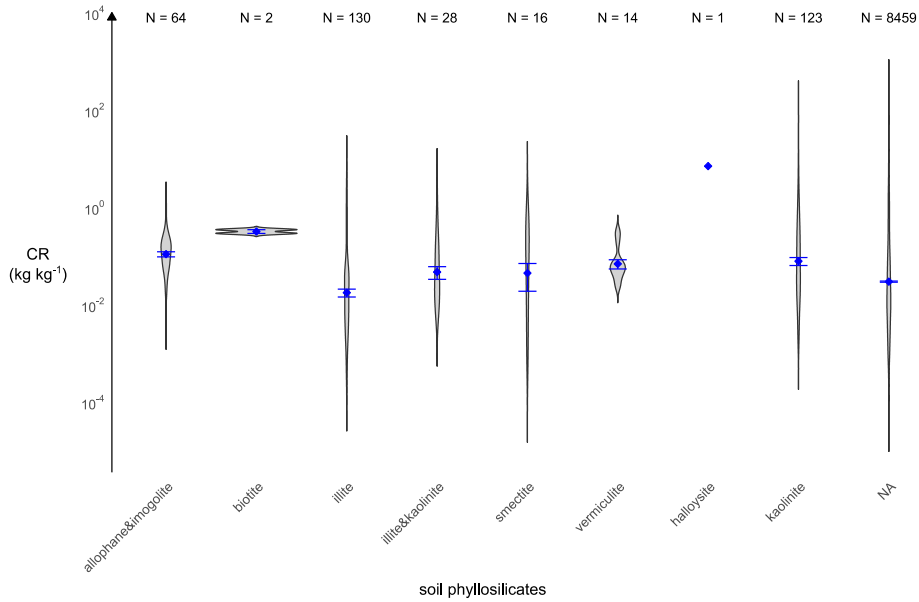

Figure 2.5. Violin plots of CRs on log-scale categorized by dominant phyllosilicate in soil show a significantly lower CR for illite compared to allophane/imogolite and kaolinite, with limited data on mineralogy. Diamonds show geometric means (except for halloysite, arithmetic mean), and error bars are their standard errors. NA = data not available.

2.3.2. Radiocaesium soil-to-plant transfer predictions

In the first step, a standard least squares regression model was constructed using the REML method. The reference (or source document, N_{ref} = 142 values) was used as a random factor. Indeed, a high multicollinearity (variance inflation factor >5) was found between reference (linked to the experiment) and time, as experiments from the same setup were typically conducted during the same time period (Figure II.6). All significant variables (including soil pH) that were identified with univariate analyses (Table 2.1) were entered as fixed categorical or continuous variables. However, silt and sand content were removed and the same was true by removing the variable soil category (clay, loam, sand, organic soil, coral sand) as these are variables logically covarying with clay content and organic matter content. The number of variables differed (Table 2.1), and hence, a final model with all these variables yielded a model that was based on a small number of observations (N = 46) that had all these variables. Hence, a compromise was made by manually entering or removing variables to obtain at least about 25% of the data, i.e., N

>2,000. The variable original CR expression method was not entered as it had only one expression in several climate classes.

The result of that first analysis (Table 2.2) yielded a model that explained 66% of the variation (*N* = 2,075) and showed that variables affecting the ^{10}log CR ranked soil pH > plant category > climate zone of soil > contact time > exchangeable K content > soil cation exchange capacity > soil organic carbon content. Soil pH remarkably ranked first here whereas univariate analyses showed no significant effects of pH. Hence, soil pH is likely a proxy for different other factors affecting radiocaesium bioavailability, e.g., more weathered soils, often devoid of clay minerals that adsorb radiocaesium and richer in oxides, typically have lower pH. Again, this soil variable was more important than the plant category. The climate zone of the soil is significant, likely due to the leverage effect of the outliers described above (tropical soils, such as coral sands). The effect of the plant growth methods (pot trials, field monitoring, Figure II.3) was non-significant whereas the effect of contact time was significant, corroborating the speculation above. Most strikingly, the clay content was not significant.

Table 2.2*.* Comparison of the variable effect sizes on ^{10}log-transformed CRs in a multiple mixed regression model using reference (the source document) as random effect. The adjusted R^2, i.e., adjusting for the number of variables in the model, the slope of the effect (positive or negative relation), and the log-transformation of *p*-values (logworth) are given. Larger values of the logworth indicate higher statistical significance in explaining the CR. n.s. = not significant (*p* >0.05).

N	R^2_{adj}	*variable*	*slope*	*logworth*	*p-value*
2,075	0.66	soil pH	-	13	<0.0001
		plant category (based on plant species)		12	<0.0001
		climate zone of soil		8.8	<0.0001
		^{10}log(soil-radiocaesium contact time)	-	5.0	<0.0001
		^{10}log(exchangeable K content)	-	3.6	0.0003
		^{10}log(cation exchange capacity)	-	1.9	0.012
		^{10}log(soil organic carbon content)	+	1.6	0.027
		plant growth method			n.s.
		clay content			n.s.

In a second step, different models were compared (Table 2.3). For a small subset of data (*N* = 199) for which all soil variables were available to use semi-mechanistic models of Absalom2001, Absalom2011, and Tarsitano2011, it is clear that these models performed better than the random forest model, while the mixed-effects (reference as random effect and other variables as fixed effects) performed best. However, if more soil variables were used than those required by the semi-mechanistic models, the random forest model outperformed the semi-mechanistic model (R^2 = 0.86, RMSE = 0.45, *N* = 531). Note that the random forest and mixed-effects models were calibrated on a dataset with poor coverage, specifically from tropical (*N* = 16), arid (*N* = 2), and continental (*N* = 7) regions. It included a very different number of data per plant category: grass (*N* = 137), leafy vegetables (*N* = 25), non-leafy vegetables (*N* = 3), rice (*N* = 306), root crops (*N* = 40), and tubers (*N* = 2). The performance of the models was highly dependent on the number of data, for instance, models with soil organic carbon content were poor because data on organic carbon was limited (*N* = 214).

The radiocaesium transfer map (Figure 2.6) was made with a random forest model based on variables available in soil maps and calibrated to records from around the world (Table 2.3). Less variability in CR was explained by a model calibrated for Europe due to a limited number of records from this region. The random forest model for Japan, with almost all data from Fukushima, explained more variability and was more precise (i.e., lower RMSE) than the model for Europe because the data on which the model was calibrated came from a small region with similar climates and less soil heterogeneity.

Soil data used from SoilGrids to create the global radiocaesium soil-to-plant transfer map were compared to measured data (Figure II.7). Data were extracted from SoilGrids maps by using coordinates from soil samples reported in previous studies (Gilis and Sweeck, 2019; Chapter 4). These studies reported wet chemistry data from the soil samples. Overall, soil variables were poorly predicted, specially the cation exchange capacity where the SoilGrids maps underestimated measured values by more than a factor 6. For some records, there was no data available in SoilGrids.

The global radiocaesium soil-to-plant transfer map showed that the highest radiocaesium transfer risk for grass was in tropical climates and cold regions with organic soils (Figure 2.6).

Table 2.3. Comparison of semi-mechanistic and data-driven models with data-driven either log-linear multiple regression or random forest (p <0.05) to predict the ^{10}log-transformed CR. The best performing models within each group are given in bold. Data shows that semi-mechanistic models work well if limited data is available, but data-driven models work best when more data is available. The reference level for dummy variables for plant category was grass in regression equations. Standard errors of estimates in brackets and the normal distribution of random intercepts are given in equations.

region	*model*	*N*	*R^2*	*RMSE*
comparison of semi-mechanistic and data-driven models[a]				
global	Absalom2001 (Equations I.6-I.17) based on plant category, clay, orgC, pH, exchK, solutionNH_4, time.	199	0.50	0.79
global	Absalom2011 (Equations I.18-I.28) based on plant category, clay, orgC, pH, exchK, solutionNH_4, time.	199	0.47	0.76
global	Tarsitano2011 (Equations I.29-I.35) based on plant category, clay, orgC, exchK, solutionNH_4, time.	199	0.42	0.79
global	$^{10}\mathrm{log}(\mathrm{CR}) = 0.73(\pm 0.68) - 0.0013(\pm 0.0035) \cdot \mathrm{clay} + 0.29(\pm 0.12) \cdot {}^{10}\mathrm{log}(\mathrm{orgC}) - 0.31(\pm 0.05) \cdot \mathrm{pH} - 1.1(\pm 0.1) \cdot {}^{10}\mathrm{log}(\mathrm{exchK}) + 0.064(\pm 0.025) \cdot \mathrm{solutionNH_4} - 0.25(\pm 0.30) \cdot {}^{10}\mathrm{log}(\mathrm{time}) - 0.48(\pm 0.33)\mathrm{plant_{leafy\ vegetables}} + 0.27(\pm 0.26)\mathrm{plant_{rice}} + 0.18(\pm 0.32)\mathrm{plant_{root\ crops}} + N(0{,}0.086)$	199	**0.59**[b]	**0.59**
global	Random forest based on plant category, clay, orgC, pH, exchK, solutionNH_4, time.	199	0.44	0.77
comparison of data-driven model performances[a]				
global	$^{10}\mathrm{log}(\mathrm{CR}) = 4.2(\pm 0.4) - 0.024(\pm 0.004) \cdot \mathrm{clay} - 0.024(\pm 0.004) \cdot \mathrm{silt} - 0.021(\pm 0.003) \cdot \mathrm{sand} - 0.27(\pm 0.03) \cdot \mathrm{pH} - 0.94(\pm 0.08) \cdot {}^{10}\mathrm{log}(\mathrm{exchK}) - 1.1(\pm 0.1) \cdot {}^{10}\mathrm{log}(\mathrm{time}) + 0.71(\pm 0.18)\mathrm{plant_{leafy\ vegetables}} + 1.4(\pm 0.3)\mathrm{plant_{non-leafy\ vegetables}} - 0.026(\pm 0.171)\mathrm{plant_{rice}} + 1.1(\pm 0.2)\mathrm{plant_{root\ crops}} + 0.86(\pm 0.34)\mathrm{plant_{tubers}} + N(0{,}0.19)$	531	0.67[b]	0.49
global	Random forest based on plant category, clay, silt, sand, pH, exchK, time.	531	**0.86**	**0.45**
comparison of models for global radiocaesium transfer map[a]				
global	Random forest based on plant category, clay, silt, sand, pH, CEC, time.	513	**0.73**	**0.57**
Europe	Random forest based on plant category, clay, silt, sand, pH, CEC, time.	136	0.54	0.66
Japan	Random forest based on plant category, clay, silt, sand, pH, CEC, time.	339	0.60	0.51

[a] clay = clay content, silt = silt content, sand = sand content, orgC = soil organic carbon content, pH = soil pH, CEC = cation exchange capacity, exchK = exchangeable potassium content, time = soil-radiocaesium contact time; [b] marginal R^2.

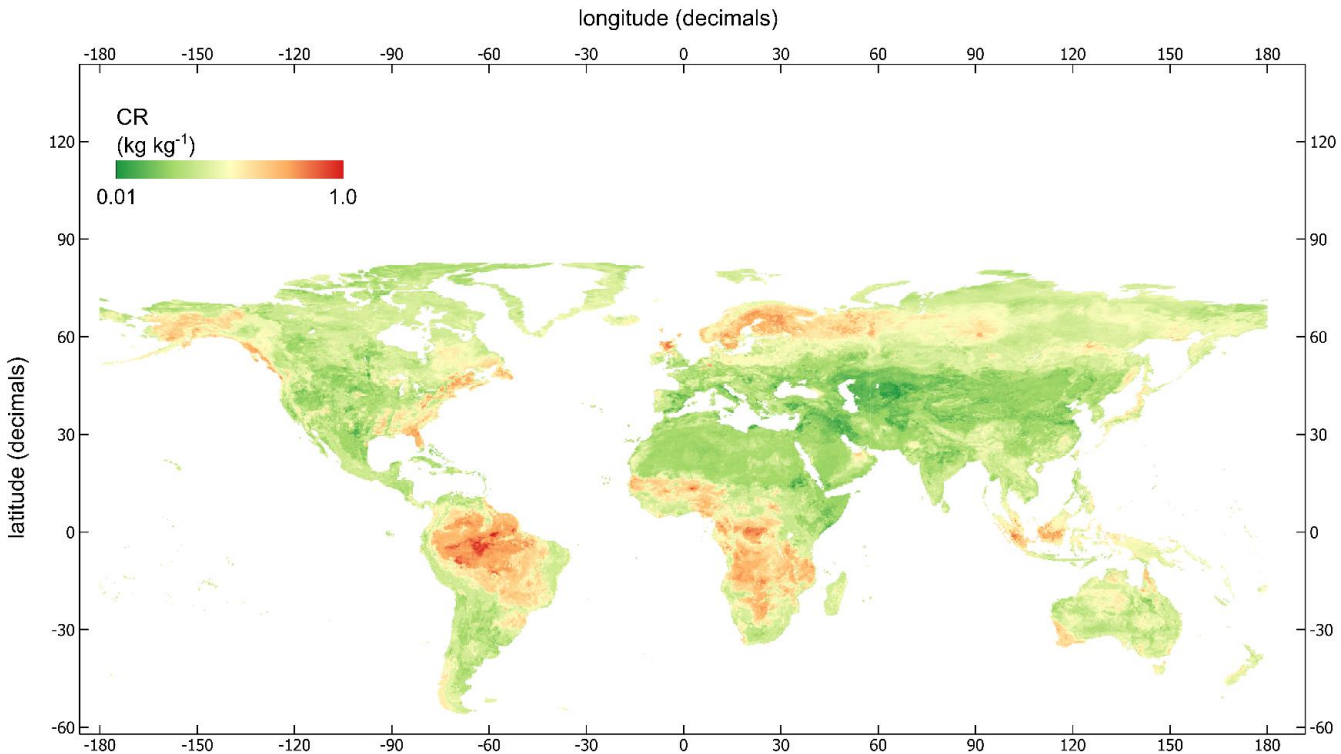

Figure 2.6. Global radiocaesium soil-to-plant transfer map showing larger risks in regions with organic soils and tropical climate. CRs were calculated for grass after radiocaesium was in contact with soil for 90 days. The map is a EPSG 4326 WGS 84 projection.

2.4. Discussion

Harmonizing radiocaesium soil-to-plant transfer data is challenging due to substantial variability introduced by methodological and design factors, which can confound more logical soil- and plant-related effects. In each radiocaesium transfer study, different objectives and experimental setups (e.g., field vs. pot experiments) yield differences in measured units, compartments studied, available information, etc. Assumptions made during harmonization to standardize datasets may inadvertently introduce additional errors. Nevertheless, accounting for this variability allows underlying effects of soil and plant characteristics to be revealed (Table 2.1 vs. Table 2.2). Furthermore, extracting and filtering relevant data from these studies is prone to errors and time-consuming. With many studies still to be reviewed (*N* >3,000), ongoing efforts to gather and standardize data are important for improving the reliability of radiocaesium transfer prediction models.

A rather sensitive assumption is required to convert the area-based CR (m^2 per kg), i.e., aggregated CR to the mass-based CR where soil depth and bulk density data are often missing. For example, peat soils, high in organic matter, typically have bulk densities much lower than the assumed 1,300 kg per m^3, whereas highly weathered soils, dominated by iron oxides, often exceed this density. Such conversions can substantially overestimate CR values for organic soils or underestimate them for highly weathered soils.

In this study, the database covers a wide range of CR values of more than seven orders of magnitude (Figure II.1). Most of these data are primarily post-accidental and biased towards temperate regions, such as Europe and Japan (Figure II.5). There is a data gap for underexplored regions such as tropical and arid climates, where radiocaesium bioavailability can be markedly different due to environmental conditions (Figure 2.2). Radioecological studies in these regions have historically been deprioritized due to lower radiocaesium deposition rates, yet the variability in CRs in these areas can be substantial. High CR values are often observed in tropical regions, particularly coral sandy soils common on islands and atolls (Figure 2.4), with limited capacity to adsorb radiocaesium. Only limited information is available on soil mineralogy (Figure 2.5), even though it is crucial in determining the extent of radiocaesium adsorption in soils.

Grouping plants into categories generalizes the effect of plant type on the CR. In this database, the significance of differences in CRs among plant categories

is limited (Figure 2.3). While investigating plant species effects on CR would be valuable, this information is currently lacking. The semi-mechanistic model requires plant categories as input variables, so we derived conversion factors (Beresford and Willey, 2019) and compared them with previously reported factors (Table II.5) but they do not agree. It is questionable whether plant conversion factors representing average values at the category and species level capture variability in the CR. However, these plant effects should be taken into account. Plant categories significantly affected CRs (Tables Table **2.1** and Table **2.2**). So plant type has an important effect on CRs, but so do other variables. This highlights the importance of comparing plants grown under similar conditions on the same substrate (Beresford and Willey, 2019; Frissel et al., 2002), particularly regarding nutrient (K) availability to clarify the effect of plant type on radiocaesium uptake.

There are notable differences in CRs between plant growth methods, with pot trials yielding higher CRs than field trials (Figure II.3). This difference was previously attributed to factors such as more K depletion in limited-volume pots, resulting in less K:Cs competition for plant uptake and to the limited soil-radiocaesium contact time after spiking (Frissel et al., 1990; IAEA, 2006). However, when corrected for random variation of the study (or reference), for time and other soil and plant variables, the plant growth method is of no importance (Table 2.2), as previously disputed (Gerzabek et al., 1998; Horak and Gerzabek, 1989; Strebl et al., 2007).

The mixed multivariate regression model indicates that soil pH is the most important soil variable explaining CRs (Table 2.2), but not in explaining CRs as a single variable (Table 2.1). This difference highlights how multivariate models can capture interactions between variables and account for indirect effects that univariate analyses may overlook. Some studies report a negative effect of soil pH on radiocaesium plant uptake (e.g., Ogura et al., 2014), while others report no effect (e.g., Keum et al., 2007; Van Bergeijk et al., 1992). It is possible that this statistical effect of pH is not a causal effect (Wauters et al., 1994), but that soil pH may be a proxy for other properties that have a logical (mechanisms known) effect on CR, e.g., pH correlates positively with RIP and is explained by the parent material and its weathering products (Waegeneers et al., 1999).

A striking outcome of the mixed multivariate regression model is the lack of an effect of soil clay content on CRs after correcting for other factors. On the one hand, this might be related to the correction for cation exchange capacity

and organic carbon content which are covarying with clay content. On the other hand, it is still striking as it contrasts the paradigm in many models and studies proposing clay content as the most important soil variable explaining radiocaesium bioavailability (e.g., Skarlou et al., 1996, Squire and Middleton 1966). However, this striking observation also corroborates comparative studies showing no effect of clay content on radiocaesium bioavailability (Keum et al., 2007; Smolders et al., 1997; Chapter 4 and 5). This failure is due to the various types of clay minerals and Cs^+ adsorption sites on those clay minerals that are not differentiated by particle size (Sandalls and Bennett, 1992; Chapter 4 and 5).

The performance of radiocaesium soil-to-plant transfer models depends largely on the dataset size (Table 2.3). Semi-mechanistic models (Absalom et al., 2001; Tarsitano et al., 2011), although not calibrated to this dataset, performed reasonably well with small dataset sizes (N <200). However, a mixed-effects regression model calibrated to the small dataset performed better. For larger datasets (N >500), the random forest regression model yielded the best performance. Random forest models generally benefit from more data, with a rule of thumb suggesting a dataset size of approximately 200 times the number of variables (Van Der Ploeg et al., 2014), i.e., for 7 variables N = 1,400. This allows random forest models to reduce overfitting and capture complex interactions, leading to better generalization across diverse conditions.

A random forest model for global scale is used to create a radiocaesium transfer map for grass, using soil variables from SoilGrids with 250 m by 250 m data resolution. The density of soil data in SoilGrids seems sufficient for a global assessment, but has limitations at local scales. For example, in Europe and northern America, SoilGrids includes about 4 soil profiles per 10 km^2, whereas large regions in Asia, such as India, have less than 1 profile per 10 km^2 (Poggio et al., 2021). Despite lacking data on key variables such as soil K content and mineralogy, SoilGrids reflects global trends in soil properties, identifying different regions: soil particle size classes identify loess regions (e.g., north-west Europe, Ukraine); soil organic carbon identifies regions of Histosols (e.g., Scotland, Siberia); low soil pH identifies regions of young volcanic soils (Andosols) and highly weathered soils (e.g., Acrisols and Ferralsols); cation exchange capacity identifies large regions of weathered clays (e.g., central Brazil) and swelling clays (e.g., Vertisols) (Poggio et al., 2021).

The radiocaesium transfer model predicts higher transfer rates in cold regions with organic soils (e.g., northern Eurasia) and tropical regions with highly weathered soils (e.g., Brazil, central Africa, and southeast Asia). Peat soils with high organic matter contents (Sanchez et al., 1999; Valcke and Cremers, 1994) and highly weathered tropical soils usually have little to no clay minerals that bind radiocaesium selectively, and thus high CRs. In regions such as central Africa and Brazil, soils have developed from old Precambrian continental shields and subjected to intense weathering conditions in these tropical climates (Van Wambeke, 1992). Although India also has soils derived from old shields, the distinct wet and dry seasons promote the formation of Vertisols with smectite clay minerals characterized by a high CEC. These clay minerals can form radiocaesium selective adsorption sites that lower the CR. We suggest to collect more harmonized data in underexplored regions, include information on soil K content and mineralogy, and critically validate the map with CR observations to make the radiocaesium transfer map suitable for impact assessments.

2.5. Conclusion

The construction of a database for modeling radiocaesium transfer from soil to plants reveals data gaps, such as limited records from tropical and arid climates, limited information on the soil K content and mineralogy, and limited records suitable for modeling. Global radiocaesium transfer models benefit from larger datasets and the inclusion of a wide range of variables, with data-driven approaches, such as random forest models, showing good performance. While data-driven models perform best with large datasets, semi-mechanistic models remain reliable with smaller datasets. This study demonstrates that models dependent on database quality can be effectively used to create radiocaesium transfer risk maps, which are valuable tools for decision-makers to discover potential high radiocaesium transfer risks across different regions and to form preliminary assessments. This study also suggests that, at a global scale, soil clay content is probably not an important variable affecting the radiocaesium transfer but rather that soil mineralogy (soil weathering) and soil exchangeable K are more important.

Chapter 3
Quantitative clay mineralogy predicts radiocaesium bioavailability to ryegrass grown on clay-sand mixtures

Vanheukelom, M., Sweeck, L., Van Hees, M., Weyns, N., Van Orshoven, J., Smolders, E., 2023. Quantitative clay mineralogy predicts radiocesium bioavailability to ryegrass grown on reconstituted soils. Sci. Total Environ. 873, 162372. https://doi.org/10.1016/J.SCITOTENV.2023.162372

Abstract

Current radiocaesium (^{137}Cs) models to evaluate the risk of ^{137}Cs transfer from soil to plants are based on the clay and exchangeable potassium (K) contents in soil. These models disregard the mineralogy of the clay fraction and are likely not capable of accurately predicting the ^{137}Cs transfer factor (CR) in soils of contrasting parent rocks and weathering stages. The objectives of this study were to test that hypothesis and to identify whether quantitative information on mineralogy can improve the predictions. A pot cultivation experiment was set up with clay-sand mixtures in single and double clay doses that were fertilized, spiked with ^{137}Cs and grown with ryegrass for 30 days. Four clays (only of type 2:1 phyllosilicates: illite, biotite, smectite and vermiculite) along with six deposits from clay-rich geological units (mix of type 1:1, 2:1, 2:1:1 phyllosilicates) were compared. The CR generally decreased with increasing clay dose for each of these ten different clay groups, however, the CR varied two orders of magnitude across clay groups and doses. The CR was highest for clays with little ^{137}Cs specific sites such as smectite and where the exchangeable K content was low compared to the other clays. The CR was well predicted from the soil solution ^{137}Cs and K concentrations (R^2 = 0.72 for log transformed CR), corroborating earlier findings in natural soils. The CR (log transformed) was statistically unrelated to total phyllosilicate content or 1:1 and 2:1:1 type phyllosilicate content while it significantly decreased with increasing 2:1 phyllosilicate content (R^2 = 0.32). A multiple regression model with four different X-ray diffraction (XRD) based phyllosilicate groups yielded strongest predictive power (R^2 = 0.79). We conclude that XRD quantification is valuable for describing ^{137}Cs bioavailability in plant substrates. These findings now await confirmation for natural soils.

3.1. Introduction

After nuclear incidents, radiocaesium (e.g.,^{137}Cs) can be released into the environment. Radiocaesium deposited on agricultural land can enter the food chain, which poses a risk to human health (IAEA, 2009). To manage this risk, decision-makers need models to predict the extent of transfer of ^{137}Cs from soil to plants. Plant roots absorb the ^{137}Cs from the soil solution and its concentration depends on the total amount deposited and on the sorption to soil particles. It is generally known that the adsorption of ^{137}Cs cations at trace concentrations is controlled by the sorption on the highly selective Frayed Edge Sites (FES) of phyllosilicates (Sawhney, 1972). The FES constitute the wedge-shaped zones between closed and open interlayers of weathered mica-like minerals where the ^{137}Cs cations are very selectively sorbed.

The FES content of phyllosilicates varies largely, ranging between high for weathered micas such as illite to none for kaolinite, unweathered micas and smectites (Durrant et al., 2018; Missana et al., 2014). Not all minerals have these FES to the same extent, so the selective adsorption of ^{137}Cs cations in soils is determined by the type and content of minerals. The mineralogy of the soil is governed by the parent material and the weathering process and, hence, it is predictable that ^{137}Cs bioavailability is also affected by the soil weathering stage and its content of phyllosilicates.

The bioavailability of ^{137}Cs not only depends on the FES content but also on the prevailing concentration of competing ions of which potassium (K^+) and ammonium (NH_4^+) cations are most relevant. The bioavailability of ^{137}Cs is a complex function of the K concentration in solution. On the one hand, K and ^{137}Cs cations compete for non-selective adsorption on soil particles; on the other hand, K and ^{137}Cs cations compete for uptake through plant roots (Shaw and Bell, 1991). Of particular interest is the latter where the concentration of K controls how much ^{137}Cs can be transferred from solution to the plant. At K concentrations in soil solution of the order of less than 1 mmol L^{-1}, the plant uptake of ^{137}Cs from solution sharply increases with decreasing K concentrations (Smolders et al., 1997). If the K concentration is higher, the ^{137}Cs uptake from solution is almost unaffected by the K concentration.

The bioavailability of ^{137}Cs, generally defined as the ability of ^{137}Cs to move from the soil to the plant compartment in the environment (Desmet et al., 1991; Semple et al., 2004), is expressed by the ^{137}Cs soil-to-plant transfer factor (CR), which is the ratio of the ^{137}Cs concentration in the plant material to that

in the soil (IAEA, 2009). The retention of ^{137}Cs on the FES in the soil can be quantified as the Radiocesium Interception Potential (RIP) (Cremers et al., 1988). The RIP is defined as the product of the selectivity coefficient of Cs^+ to K^+ (i.e., intensity) and the FES capacity of the soil particles (i.e., quantity) assuming that K^+ is the only cation which saturates the FES. The RIP of a soil can be determined experimentally by the method proposed by Wauters et al. (1996c; 1996a; 1996b) and the solid-liquid distribution coefficient K_D of ^{137}Cs is the RIP divided by the concentration of the competing cations in solution. In the plant compartment, the uptake of ^{137}Cs is controlled by the soil solution ^{137}Cs and K concentrations.

Taken together, it follows that the CR depends on the RIP of the soil and the soil solution K concentration; both these variables depend in turn on the clay content, the mineralogy, and the exchangeable K content. The ^{137}Cs CR has been experimentally determined for many soil and plant type combinations (IAEA, 2009). Models created based on the concepts described above predict the CR based on the clay size particle content and the exchangeable K content, thereby assuming one mean value for the RIP per unit clay (Absalom et al., 2001, 1999; Tarsitano et al., 2011).

Current ^{137}Cs transfer models fail to predict the CR for a set of distinct soil types (Almahayni et al., 2019; Uematsu et al., 2016). A possible explanation is that the clay mineralogy is ignored and the RIP per unit of clay content in the soil may differ largely among soils at widely varying weathering stages. Only for soils formed from similar parent material or similar weathering stage as the soils used to develop the CR models (e.g., Sanchez et al., 1999; Smolders et al., 1997), the model predictions agree with the observations. Hence, it is expected that prediction of CR fails when soils with more contrasting parent materials and weathering stages are included. In Chapter 2, we concluded that soil pH, although statistically significant, was likely a proxy for mineralogical properties affecting CR. It is known that quantitative mineralogy can improve the clay to RIP conversion (Maes et al., 1999a) and, hence, improve the CR prediction.

Against this background, this study was set up to identify whether quantitative mineralogy can improve the ^{137}Cs CR prediction compared to predictions of existing CR models for ^{137}Cs (Absalom et al., 2001, 1999; Tarsitano et al., 2011). As a first step, a greenhouse study was set up with clay-sand mixtures, i.e., clay-sand mixtures in single and double clay doses that were fertilized, spiked with ^{137}Cs and grown with ryegrass for 30 days. We selected clays with

contrasting properties and measured the RIP and CR of ^{137}Cs in these model soils. We quantified the mineralogy of the clays using X-ray diffraction (XRD). Finally, we compared the experimentally observed ^{137}Cs CR with the CR predicted either from exchangeable K and clay content or from a model that included XRD data.

3.2. Materials and methods

The experimental design is a pot experiment with a full factorial combination of ten different clays or clay deposits, each dosed at two levels in sand with three replicates.

3.2.1. Clay selection

Ten clays from subsurface geological units were collected (Table 3.1). Four commercially available mineral clays containing predominately 2:1 phyllosilicates were chosen: illite, biotite, smectite (bentonite) and vermiculite. Six clays were collected from deposits exploited by the ceramic industry consisting of various minerals: Boom clay, Campine clay, Ieper clay, Red-firing river clay, Red loam, and Westerwald clay. Both categories are noted here as *clay*.

3.2.2. Clay composition and characterization

Mineralogy

Subsamples were taken from the deposit clays to account for possible heterogeneities in composition among the multiple containers in which they were delivered. Only one subsample of the mineral clays was taken for analysis. The subsamples were oven-dried (60°C). They were crushed by pestle and mortar until all material passed through a 0.5 mm sieve. Each sample was prepared following the internal standard method for powder XRD (Środoń et al., 2001), with the addition of 10 wt% zincite (ZnO) of known weight (± 0.001 g) for quantification purposes. The clay and ZnO were milled (McCrone Micronizing Mill) together with about 4 mL of ethanol for 5 min to obtain a homogenous mixture. The mixture was placed under a fume hood until dry. The mixture was passed through a 0.355 mm sieve to obtain a fine powder. Next, the powder was inserted in a side-loading holder by gently tapping the holder on a flat surface to distribute the powder evenly throughout the holder cavity. The XRD measurements were carried out with a diffractometer (PW1830, Philips) in a Bragg-Brentano arrangement and 173 mm goniometer radius. The diffractometer was equipped with Cu-K_α radiation, a graphite crystal monochromator and a gas proportional detector. The powders were scanned at 45 kV and 30 mA and ranging over 5–65 °2θ with 0.02 °2θ step size and 2 s counting time. The minerals in the powder were identified and quantified using QUANTA (© Chevron ETC). The software uses the Mineral Intensity Factors method (Moore and Reynolds, 1997) where the sum of identified mineral phases is fitted to the recorded XRD pattern. The

mineral identification procedure described by Moore and Reynolds (1997) was followed. The estimated quantities expressed as weight percentages (wt%) were normalized. The precision of the method was previously reported by Środoń et al. (2001) and the uncertainty was estimated to be 2–3% per mineral phase.

Selective and non-selective adsorption capacity

The radiocaesium interception potential (RIP) and cation exchange capacity (CEC) were determined separately for the clays and sand for comparison with the clay-sand mixtures. The weight of air-dried samples was corrected for moisture content by oven-drying (105°C) subsamples.

The RIP was determined based on the procedure described by Wauters et al. (1996b). The air-dry clays and sand were prepared in triplicate and brought into contact with a solution of 100 mmol L^{-1} $CaCl_2$ and 0.5 mmol L^{-1} KCl. The solid-liquid ratio (S:L) was 0.5 g clay or 2.0 g sand to 160 mL solution. The clays, a reference clay (illite du Puy, France) and sand were weighted in dry dialysis bags (VISKING®, MWCO 12–14 kDa) and filled with 10 mL of the Ca-K solution. The dialysis bags were transferred into bottles filled with 150 mL outer Ca-K solution for pre-equilibration and shaken end-over-end for 24 h. The outer solution was renewed and shaken again for 24 h. Finally, the outer solution was labelled with carrier-free ^{137}CsCl to obtain an activity of 200 kBq L^{-1}. After 24 h of shaking, the outer solution was sampled and analyzed. The initial and remaining ^{137}Cs concentrations in solution were measured using a NaI(Tl) gamma counter (1480 WIZARD 3”, PerkinElmer). For every batch of four triplicates, at least four blanks were measured to correct for background counts. The adsorbed ^{137}Cs on the solid phase was calculated as the difference in solution ^{137}Cs between starting time and 24 h contact with the solid phase. The ^{137}Cs K_D is calculated as the ratio of adsorbed ^{137}Cs (kBq kg^{-1} soil) to that in solution (kBq L^{-1}) and the RIP (mmol kg^{-1}) is calculated as the ratio of K_D, with the 0.5 mmol L^{-1} K in solution. The RIP of the clay (RIP_{clay}) and sand (RIP_{sand}) were summed proportionally as they occur in the substrate (*RIP calculated*). A blank sample was also prepared following the same procedure but without clay or sand to determine the adsorption of ^{137}Cs on the membrane and in the bottle. The RIP of the blank was <0.1 mmol kg^{-1}.

The CEC was determined following the cobalthexamine method (Ciesielski and Sterckeman, 1997) with adjusted S:L depending on the CEC. The oven-dry (105°C) clays and sand, prepared in duplicate, were brought into contact with 16.6 mmol L^{-1} $Co(NH_3)_6Cl_3$ and placed in an end-over-end shaker for 1 h.

After centrifugation, the supernatant was filtered at 0.45 µm (Acrodisc®). The initial and remaining Co concentrations in solution were measured using an inductively coupled plasma mass spectrometer (7700 Series ICP-MS, Agilent Technologies). For the entire batch of duplicates, two blanks were measured twice to verify the quality of the measurement. The CEC was calculated as the difference of the Co equivalent charge concentration in solution per solid weight between samples before and after 1 h contact with the solid phase.

The CEC of the clay-sand mixtures (*CEC mixture*) was determined before they were spiked (Section 3.2.3). The RIP of the clay-sand mixtures after plant growth (*RIP mixture*) was determined by the method described above with 1 g of mixture.

3.2.3. Pot experiment

Preparing clay-sand mixtures

Quartz sand was obtained from a building supply store (river sand, unwashed). The plant substrate was a mixture of clays were mixed with sand. In these mixtures, however, clay particles were not fixed in a structure because these artificial substrates lacked aggregating agents such as organic matter and metal oxides, hence clay flocculation was required to limit the risk of clay migration during watering of plants. The illite, biotite, smectite and vermiculite were bathed in a solution with ionic strength well above 0.1 mol to enhance flocculation. The four clays were first ground and passed through a 1 mm sieve. The clays were bathed in a 0.4 mol L^{-1} $CaCl_2$, 0.1 mol L^{-1} $MgCl_2$ and 0.025 mol L^{-1} KCl solution with a S:L of 1 kg to 5 L. After 24 h, the clays were washed with deionized water and air-dried. The six deposit clays were left untreated because sufficient aggregating agents were present.

A single and double dose of clay was mixed with sand to study the effect of the dose of clay on ^{137}Cs transfer. The clay doses were 5 wt% or 10 wt% for the mineral clays and 10 wt% or 20 wt% for the clay deposits. The doses of the clay deposits were chosen larger because about half of the clay consisted of minerals that were not phyllosilicates (Table 3.1), e.g., quartz, feldspars.

The clay-sand mixtures were fertilized and spiked with ^{137}Cs. A nutrient solution was composed, based on the hydroponic solution by Hoagland and Arnon (1950), so that it contained the elements necessary for a plant and growth would not be hampered by deficiencies. Importantly, the K concentration (2.84 mmol L^{-1}) was chosen high enough to prevent the K content from masking the role of mineralogy. The N:P:K-ratio was adjusted

according to Steiner (1961). The nutrient solution contained 1.83 mmol L^{-1} $Ca(NO_3)_2$, 1.19 mmol L^{-1} $MgSO_4$, 1.14 mmol L^{-1} KCl, 0.52 mmol L^{-1} K_2HPO_4, 0.44 mmol L^{-1} KH_2PO_4, 0.20 mmol L^{-1} KNO_3, 0.10 mmol L^{-1} $NH_4H_2PO_4$, $4.63 \cdot 10^{-3}$ mmol L^{-1} H_3BO_3, $1.64 \cdot 10^{-3}$ mmol L^{-1} $FeSO_4$, $9.15 \cdot 10^{-4}$ mmol L^{-1} $MnCl_2$, $8.06 \cdot 10^{-4}$ mmol L^{-1} EDTA-Na_2, $7.65 \cdot 10^{-5}$ mmol L^{-1} $ZnSO_4$, $5.56 \cdot 10^{-5}$ mmol L^{-1} H_2MoO_4, $3.20 \cdot 10^{-5}$ mmol L^{-1} $CuSO_4$. Carrier-free ^{137}CsCl was added to the nutrient solution to obtain a concentration of about 450 kBq kg^{-1} clay-sand mixture. The ^{137}Cs spiked nutrient solution was added to the clay-sand mixture until field capacity was reached, determined by the saturated paste method (USDA, 1954). The mixture was equilibrated for three weeks prior to seeding and incubation was made at room temperature in buckets covered with a lid to prevent excessive drying, but not airtight so that conditions remained aerobic. The mixture was stirred every 2–3 days and deionized water was added to correct for weight loss.

Plant growth

Grass was sown on the ^{137}Cs spiked clay-sand mixtures after separation of the pore water and one week of equilibration at field capacity (next subsection). About 3.8 kg of each mixture was divided over three pots of 1 L volume. The bulk density of the mixtures varied greatly, so the pots were filled according to equal volume (D'Souza et al., 1980). Per pot, 0.65 g seeds of ryegrass (*Lolium perenne* L.) were spread on the surface and at least one centimeter from the rim so that all plant roots were evenly in contact with the mixture. The seeds were buried under 60 g of mixture. The pots were covered with a tissue to reduce drying of the top layer which was removed after the grass had germinated.

The cultivation experiment was carried out in a growing chamber with a day/night cycle of 14/10 h at 24/18°C. The position of the pots was randomized. The pots were watered with deionized water every 2–3 days based on weight loss. The germinated grass in the Boom clay (BC) and Campine clay (CC) pots did not grow further, so watering was stopped after 18 days. Grass shoots were harvested for each of the replicate pots after 30 days. The above-ground plant material was cut off about 10 mm above surface to prevent ^{137}Cs contamination from the mixture. The fresh weight of the shoots was recorded. After harvesting, the remaining grass residues were removed from the mixture. The mixture in replicate pots was put in the same bucket and air-dried.

Substrate analyses

Subsamples of the clay-sand mixtures were taken for measurements before and after plant growth. These subsamples were taken from the mixtures in buckets before plant growth and from the replicate pots combined after the pot experiment. All analyses were done in triplicate samples. The total ^{137}Cs concentration in clay-sand mixture was determined on the subsamples taken from the mixtures in buckets prior to plant growth. The ^{137}Cs activity was recorded with a gamma counter (1480 WIZARD 3", PerkinElmer). The pH was measured in 0.01 mol L^{-1} $CaCl_2$ at a S:L of 1 kg mixture to 2.5 L solution and shaken for 2 h before recording (PC 5000 L, pHenomenal®). The exchangeable K, Ca, Mg and ^{137}Cs concentrations were determined by ammonium acetate extraction at pH 7. The mixtures were brought into contact with 1 mol L^{-1} ammonium acetate at a S:L of 1 kg to 18 L and placed in an end-over-end shaker for 24 h. Afterwards, the supernatant was filtered at 0.45 µm. The K, Ca and Mg concentrations were measured with microwave plasma atomic emission spectroscopy (4200 MP-AES, Agilent Technologies). The ^{137}Cs activity was recorded with the gamma counter. The pore water in the mixtures was separated by centrifugation at 21–23 days after spiking and incubation. The mixtures at field capacity were transferred to centrifuge cups with a perforated plate covered with a 2.5 µm filter (Whatman®) and reservoir to collect the liquid. After centrifugation, the recovered pore water was filtered at 0.45 µm and K, Ca, Mg and ^{137}Cs concentrations were measured.

The pore water concentrations of K, Ca, Mg and ^{137}Cs in the mixtures were measured after plant growth and air-dry storage by equilibrating the mixture again for three weeks at field capacity and separating the pore water as described previously.

Plant analyses

The grass shoot dry weight was recorded after drying in the oven (70 °C) for one week. The shoots were calcinated (550°C) overnight. The ash was dissolved in 2 mL of 12 mol L^{-1} HCl, calcinated again and dissolved in diluted 0.1 mol L^{-1} HCl. The ^{137}Cs concentration in solution was recorded. The K, Ca and Mg concentrations were measured after filtering the solution at 0.45 µm.

The transfer factor (CR) was calculated as the ratio of ^{137}Cs concentration in the grass shoots to that in the clay-sand mixture. The concentration factor (CF), a measure of ^{137}Cs plant uptake, was calculated as the ratio of ^{137}Cs concentration in the grass shoots to that in the pore water.

3.2.4. Statistical analyses

The statistical analyses were performed using the JMP® Pro software (Version 16. SAS Institute Inc., Cary, NC, 1989–2022). All calculated and measured variables (except pH) were log-transformed prior to performing regression analyses. The arithmetic mean and standard deviation were calculated of the replicate samples. The CR and CF were calculated based on data of non-corresponding replicates. Therefore, standard deviations of the CR and CF were calculated based on the error of the nominator and the error of the denominator because the sampling was unpaired and no covariance was assumed. The variability of the data was expressed as the coefficient of variation (CV), i.e., the standard deviation divided by the mean. The Tukey-Kramer HSD test was performed with the significance level at 0.05 to verify the effect of clay type and dose, considered together as a treatment, on the CR replicates. Pearson correlation coefficients were calculated on the log-transformed variables (except pH) (Table III.4). Standard least squares regression and backward stepwise regression were used for two and more selected explanatory variables, respectively, to obtain relationships describing the CR.

3.3. Results and discussion

3.3.1. Selected properties of the mineral clays and deposit clays

The mineral clays and deposit clays had varying adsorption properties (Table 3.1). The CEC_{clay} varied by a factor 50 and the RIP_{clay} by a factor 22. The mineral clays had the most contrasting CEC and RIP values, while the deposit clays had values in between. All clays and deposit clays contained fractions of non-phyllosilicate minerals that were unlikely to adsorb ^{137}Cs. Thus, the presence of these non-phyllosilicates diluted the weight-based RIP. Quartz, for example, is chemically inert and is negligible with respect to cation adsorption (Bellenger and Staunton, 2008). The RIP of the samples converted to RIP_{phyll}, by dividing the value measured on the whole sample by the fraction of phyllosilicates, varied up to a factor 30 (details not shown in Table 3.1). This correction allowed to compare the properties of the clays with data from literature, which were usually determined on the clay fraction or pure clays.

Table 3.1. Selected properties of the studied mineral clays and deposit clays. The mineral composition, cation exchange capacity (CEC_{clay}) and radiocaesium interception potential (RIP_{clay}). Mineral phases belonging to the same phyllosilicate structure group are summed up as *2:1* for micas and other 2:1 type phyllosilicates, *1:1* for kaolin and *2:1:1* for chloritic minerals. A more detailed mineral composition of the samples (Table III.1) and $RIP_{calculated}$ (Table III.2) are given as supplementary material. Data is ordered by decreasing RIP_{clay} value. The standard deviations are given in brackets (n = 2 or 3, see below). The limit of detection is 0.1 g 100 g^{-1}.

			mineral content								
			2:1	1:1	2:1:1	quartz	other	CEC_{clay}[c]		RIP_{clay}[d]	
clay	code	origin	g 100 g^{-1}					$cmol_c$ kg^{-1}		mmol kg^{-1}	
illite[a]	ILL	Auvergne (France)	67.0	1.0	1.0	21.0	10.0	22.6	(0.2)	8400	(1460)
Ieper Group clay	IC	Rumbeke (Belgium)	55.1	6.3	2.9	22.5	13.2	30.8	(0.5)	5710	(170)
Boom Formation	BC	Rumst (Belgium)	45.3	10	2.0	28.8	13.5	19.2	(0.9)	5570	(100)
Red loam	RL	Veldwezelt (Belgium)	22.8	3.0	2.0	53.0	19.2	9.8	(0.5)	3480	(150)
Red-firing river clay	RFC	Hedikhuizen (The Netherlands)	25.4	3.7	2.7	58.5	9.7	9.3	(0.2)	3380	(200)
Campine Group clay	CC	Beerse (Belgium)	28.4	6.9	3.3	52.1	9.3	7.4	(0.1)	2560	(170)
biotite[b]	BIO	Bancroft (Canada)	97.3	<0.1	<0.1	<0.1	2.7	2.9	(<0.1)	2430	(40)
Westerwald clay	WC	Boden (Germany)	15.6	18.0	<0.1	64.2	2.3	3.2	(0.1)	900	(15)
vermiculite[b]	VER	(Russia)[e]	86.0	<0.1	9.0	<0.1	5.0	106.5	(0.9)	523	(47)
smectite[a]	BEN	Wyoming (USA)	92.6	<0.1	<0.1	3.0	4.4	71.7	(1.8)	385	(39)

[a] dioctahedral 2:1 phyllosilicate; [b] trioctahedral 2:1 phyllosilicate; [c] n = 2; [d] n = 3; [e] (Thiry, 1997; Thiry et al., 1996)

The non-expanding phyllosilicates illite (ILL) and biotite (BIO) had a larger RIP and smaller CEC while the expanding phyllosilicates smectite (BEN) and vermiculite (VER) had a smaller RIP and larger CEC. The largest RIP value was measured for ILL, which indicated that the ILL clay had the most selective ^{137}Cs adsorption sites (i.e., FES) of all the clays in this study. This was no surprise as it was known that illite strongly binds ^{137}Cs (Sawhney, 1972). After correction for mineral dilution, the RIP_{phyll} value (12,170 mmol kg^{-1} phyllosilicates) agreed well with the RIP of pure illite (~ 10,000–16,000 mmol kg^{-1}; de Koning et al., 2007; Wauters et al., 1996c). The CEC was not markedly large compared to the other clays and the value agreed well with the CEC of illite (~ 10–40 $cmol_c$ kg^{-1}; Grim, 1968). The RIP of BIO was larger than previously reported (~ 1,000 mmol kg^{-1}; Eguchi et al., 2015), and the CEC was very small compared to previously reported values (~ 35 $cmol_c$ kg^{-1}; Fanning et al., 1989). The BIO clay came from a rock, so it had not yet been exposed to weathering. The smallest RIP values and yet the largest CEC values were obtained for BEN and VER. The RIP of BEN was larger than previously reported values (~ 18–36 mmol kg^{-1}; Ogasawara et al., 2013), and the CEC was in the same value range (~ 76 $cmol_c$ kg^{-1}; Thiry, 1997). The K_D of VER was previously determined in various Ca-K scenarios for purified 100–200 µm isolated platelets (~ 2,500–4,000 L kg^{-1} for equivalent K fractions of <0.01–0.16; Thiry et al., 1996), and the CEC was in the same range (~ 144 $cmol_c$ kg^{-1}; Thiry, 1997). Both smectitic and vermiculitic clays had expanded interlayers that were also accessible to monovalent as well as divalent cations with larger hydrated radius. This interlayer surface added up to the total adsorption capacity, resulting in a large CEC compared to the other clays in this study. However, expanded clays did not bind ^{137}Cs selectively to the same extent, resulting in a small RIP. We assumed that the sand used in the pot experiment was chemically inert. The sand had a CEC smaller than 0.2 $cmol_c$ kg^{-1} (and standard deviation <0.1 $cmol_c$ kg^{-1} for n = 2) and a RIP of 11 mmol kg^{-1} (and standard deviation <1 mmol kg^{-1} for n = 3). The RIP_{sand} was a factor 35 lower than the lowest measured RIP_{clay} (BEN). However, in a 5% clay-sand mixture, the RIP_{sand} could have contributed up to 35% of the total RIP so it was defensible to include the RIP_{sand} to determine the RIP calculated.

The RIP measured on the clay-sand mixtures after plant growth agreed well with the RIP calculated by adding up the RIPs of the clay fraction and sand fraction (Table 3.1; Table III.2) (N = 20, R^2 = 0.88***, RMSE = 0.21), with a tendency of higher RIP after plant growth than before (Figure 3.1).

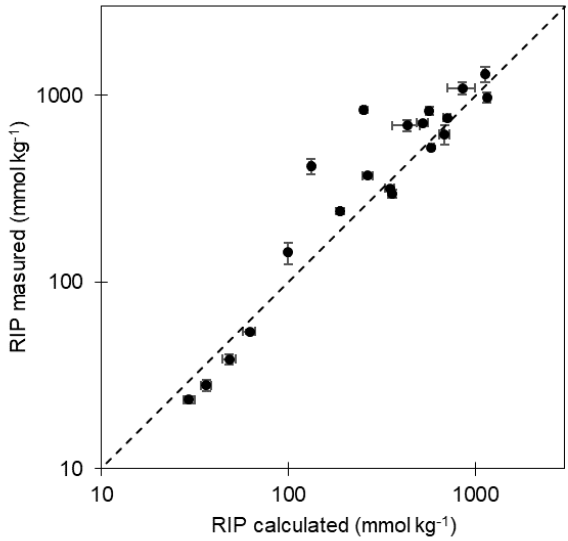

Figure 3.1. The radiocaesium interception potential (RIP) (mmol kg^{-1}) (y-axis) measured on the clay-sand mixture ($RIP_{mixture}$) after plant growth and (x-axis) calculated as the sum of its components RIP_{clay} and RIP_{sand} measured on the pure samples before mixing and plant growth. The dashed line shows the 1:1 line. Error bars show the standard deviations (*n* = 3).

The agreement of the RIP measured on the separate clays and the mixtures showed that the RIP of the clays could be approximated by calculating RIP per unit of clay. However, the RIP of some clays changed during plant growth. For the BIO mixtures, the RIP measured after plant growth was about a factor 3 larger than the RIP calculated before plant growth (Figure 3.1). This increase in RIP during plant growth (e.g., BIO, ILL) was presumably due to the combination of wetting-drying cycles and plant nutrient uptake, with the latter causing K^+ depletion in the rhizosphere. This induced cation leaching, oxidation of structural Fe^{2+} and consequent opening of the interlayers of phyllosilicates (Scott and Amonette, 1988). This interlayer opening created FES resulting in a higher RIP (Maes et al., 1999b). Biotite has a trioctahedral structure that alters more readily than dioctahedral structures such as muscovite or illite (Bassett, 1960). For the substrates with expanding phyllosilicates (e.g., VER, BEN), the alternating factors could have led to the collapse of the interlayers, creating FES and resulting in a larger RIP. However, the RIP values before and after plant growth generally differed only marginally.

3.3.2. Clay type and content controlling the ^{137}Cs bioavailability

The dry matter yields of grass varied within a factor 2 between the different clay-sand mixtures (Table 3.2), except for the BIO10 and VER10 mixtures. The Ca + Mg concentration in pore water (Table III.2) for both BIO10 and VER10 was above 100 mmol L^{-1} during plant growth, indicating that salinity affected growth. Moreover, the grass failed to grow on the BC and CC mixtures, so no data were obtained (Table 3.2; Table III.3). The pH for BC and CC mixtures was below 3.5 (Table III.2), indicating that the pyrite in the mixtures oxidized during plant growth (Craen et al., 2008). Pyrite was also present in IC, but unlike on the BC and CC, the grass did grow on the IC mixtures. The carbonate minerals present in IC may have buffered the pH to above 6.5 (Table III.2).

Table 3.2. Selected properties of the substrate and grass shoots *before* and *after* 30 days of plant growth. The radiocaesium interception potential ($RIP_{mixture}$) was measured on the clay-sand mixture after plant growth. Data are arithmetic means of replicate measurements (n = 3) and ordered by decreasing ^{137}Cs transfer factor (CR). The standard deviations of CR are given in brackets (n = 3). The minimum, maximum and mean values are given at the bottom of the table. If no data have been obtained, "-" is noted.

	mixture clay	$RIP_{mixture}$		K in pore water *before*		K in pore water *after*		shoot yield	shoot K		CR^f	
code	g 100 g^{-1}	mmol kg^{-1}		mmol L^{-1}		mmol L^{-1}		g	g kg^{-1}		kg kg^{-1}	
WC	10	144	(19)	1.45	(0.02)	0.05	(<0.01)	0.72	14.3	(0.8)	2.19[a]	(0.04)
WC	20	240	(8)	1.28	(0.02)	0.19	(0.01)	0.72	17.1	(1.0)	0.941[b]	(0.039)
RFC	10	319	(<1)	0.12	(<0.01)	0.03	(<0.01)	0.57	11.6	(0.4)	0.641[c]	(0.035)
BEN	5	23.4	(1.1)	5.02	(0.06)	2.15	(0.04)	0.85	21.3	(0.7)	0.625[c]	(0.038)
BEN	10	38.7	(2.4)	6.99	(0.13)	5.22	(0.11)	0.72	30.7	(0.6)	0.371[d]	(0.020)
RL	10	299	(15)	0.08	(<0.01)	0.04	(<0.01)	0.57	8.7	(0.7)	0.369[d]	(0.032)
BIO	10	837	(33)	16.09	(0.59)	13.05	(0.74)	0.36	31.2	(2.2)	0.351[d]	(0.038)
VER	5	28.0	(2.0)	1.44	(0.06)	1.23	(0.03)	0.60	25.5	(2.0)	0.333[d,e]	(0.014)
BIO	5	420	(40)	9.47	(0.18)	3.64	(0.04)	0.70	24.8	(2.3)	0.294[d,e]	(0.029)
RFC	20	620	(73)	0.07	(<0.01)	0.03	(<0.01)	0.76	13.7	(0.6)	0.268[e]	(0.007)
VER	10	54.4	(1.2)	3.65	(0.09)	2.26	(0.04)	0.34	30.1	(2.1)	0.183[f]	(0.013)
RL	20	761	(14)	0.06	(<0.01)	0.04	(0.01)	0.65	11.8	(0.9)	0.168[f]	(0.010)
ILL	5	689	(48)	6.58	(0.11)	2.94	(0.02)	0.74	25.6	(1.4)	0.0524[g]	(0.0015)
ILL	10	1100	(80)	9.14	(0.12)	5.68	(0.10)	0.71	26.4	(1.0)	0.0435[g]	(0.0025)
IC	10	528	(12)	6.11	(0.17)	4.28	(0.10)	0.72	19.4	(2.1)	0.0324[h]	(0.0034)
IC	20	975	(61)	6.58	(0.12)	5.42	(0.31)	0.86	20.2	(3.0)	0.0151[i]	(0.0034)

code	mixture clay	$RIP_{mixture}$		K in pore water *before*		K in pore water *after*		shoot yield	shoot K	CR^f
	g 100 g^{-1}	mmol kg^{-1}		mmol L^{-1}		mmol L^{-1}		g	g kg^{-1}	kg kg^{-1}
BC	10	830	(41)	5.90	(0.17)	-	-	-	-	-
BC	20	1310	(120)	6.24	(0.15)	-	-	-	-	-
CC	10	372	(13)	0.67	(0.06)	-	-	-	-	-
CC	20	715	(17)	0.28	(0.02)	-	-	-	-	-
min		23		0.06		0.03		0.34	8.7	0.0151
max		1310		16.09		13.05		0.86	31.2	2.19
median		474		4.34		2.20		0.72	20.8	0.313

[f] italicized superscript letter refers to Tukey-Kramer HSD connecting letters of log CR that are no different at p <0.05.

The substrate properties influenced the ^{137}Cs bioavailability. The ^{137}Cs CR varied widely from 0.02 kg kg^{-1} to 2.19 kg kg^{-1} (Table 3.2). The CR values were reproducible with limited variability among replicates (CV <10%, except for BIO10 (11%) and IC20 (22%)). The CR decreased with increasing clay content for each of the clay types (except for BIO), however the CR was not exactly halved by doubling the clay content. The K depletions in the pore water during plant growth were more pronounced at lower (5–10 wt%) than at higher (10–20 wt%) clay doses, explaining why the CR were not exactly halved by doubling the dose of clay. As expected, the RIP and exchangeable K content doubled when the clay content was doubled.

We aimed to keep the K concentration in the pore water above 1 mmol L^{-1} to minimize the effect of K on ^{137}Cs bioavailability and focus on the role of the mineralogy. Unfortunately, the pore water K was over a factor 10 below 1 mmol L^{-1} for some mixtures (RFC and RL, Table 3.2). After plant growth, the K concentration of the WC mixtures was also reduced to below 1 mmol L^{-1}. The exchangeable K content of the VER substrates was smaller than expected (Table III.2). The concentrated ammonium acetate method used to obtain the exchangeable K content may have collapsed the interlayers (de Koning and Comans, 2004) preventing the K exchange with NH_4 cations. Therefore, the exchangeable K content measured after application of the cobalt hexamine method instead of the ammonium acetate method was used for further analyses of VER substrates (data not shown).

3.3.3. The ^{137}Cs bioavailability explained by pore water composition

The plant uptake of ^{137}Cs from pore water, expressed by the ^{137}Cs CF, was clearly affected by the K concentration in the pore water (Figure 3.2). In a previous study on Belgian soils (Figure 5 in Smolders et al., 1997), the CF increased exponentially as the K concentration in the soil solution decreased below 1 mmol L^{-1}. The CF remained nearly the same at K concentrations above 1 mmol L^{-1} in soil solution (open symbols, Figure 3.2). The CF in this experiment ranged in the same order of magnitude and was similarly related to K in solution (Figure 3.2).

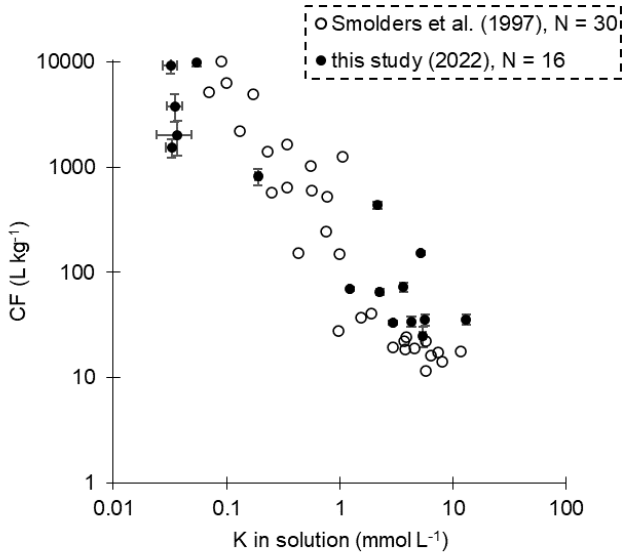

Figure 3.2. Graph showing how the K concentration in solution affected the ^{137}Cs plant uptake. The plant shoot to soil solution ^{137}Cs concentration ratio, that is the concentration factor (CF, L kg^{-1}), increased when the K concentration in solution (mmol L^{-1}) for pore water conditions after plant growth decreased below 1 mmol L^{-1}. Error bars show the standard deviations (*n* = 3).

3.3.4. Relating ^{137}Cs CR to clay mineralogy and substrate properties

The factors involved in ^{137}Cs transfer were statistically related to the properties of the substrate. No relation was found between the ^{137}Cs CR values and the fraction of phyllosilicates ((a) in Figure 3.3). However, CR was weakly and negatively related to the type of 2:1 phyllosilicates (Table 3.3). The CR was unrelated to the 1:1 phyllosilicates in clay-sand mixtures in which they were detected (*N* = 8, n.s.). The same was true for phyllosilicates of type 2:1:1 (*N* = 8, n.s.). The CR was weakly and negatively related to the RIP ((b) in Figure 3.3 and Table 3.3). However, the mixtures with expanding clays BEN and VER had a distinct RIP while the CR did not differ much from the other mixtures. The relation improved if the expanding clays were omitted from the analysis (*N* = 12, R^2 = 0.65**). As demonstrated before (Figure 3.2), K played an important role for the fate of ^{137}Cs in the soil-plant system ((c) in Figure 3.3). The CR could be explained by the K concentration in pore water (Table 3.2) after plant growth and the $RIP_{mixture}$ ((d) in Figure 3.3). The RIP to pore water K ratio is the ^{137}Cs K_D based on a simplified formula (Wauters et al., 1996a)

assuming that the concentrations of NH_4 and Na in pore water are low enough to be neglected.

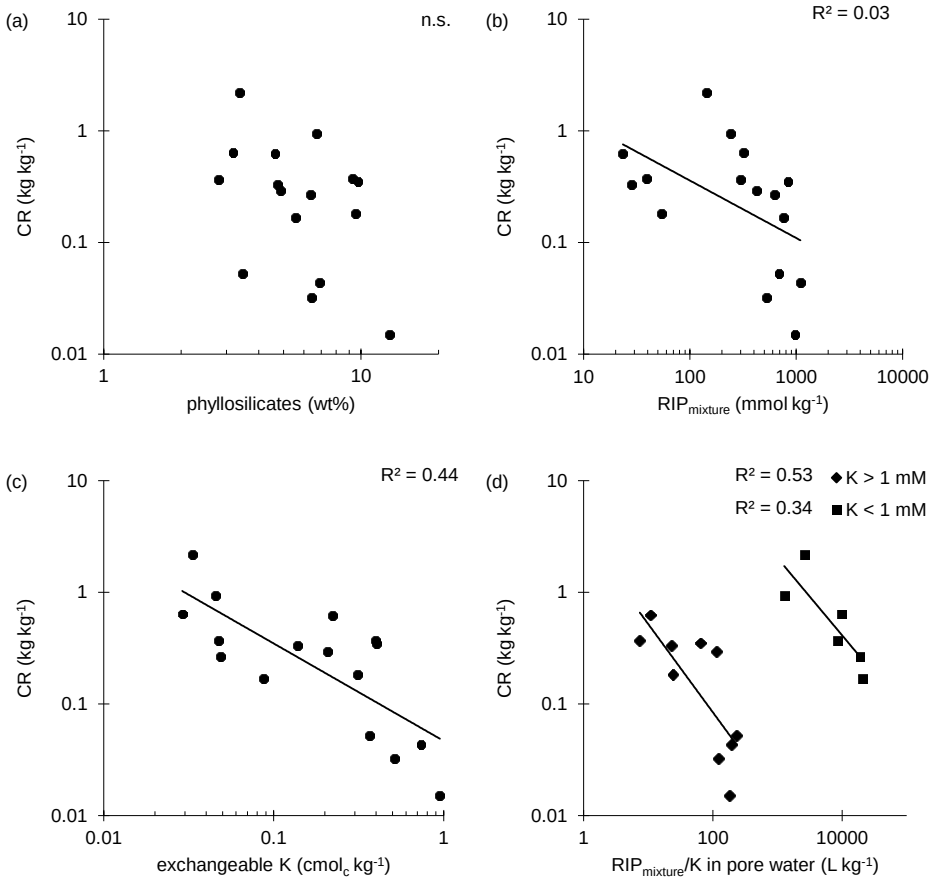

Figure 3.3. The ^{137}Cs CR (*N* = 16) predicted by (a) the fraction of phyllosilicates in the clay-sand mixtures (b) the RIP of the clay-sand mixtures measured after plant growth (c) the exchangeable K content (d) the ratio of the RIP of the clay-sand mixtures to the K concentration in pore water after plant growth. The points on the graph are mean CR values (*n* = 3).

The effect of the K concentration in the pore water on the fate of ^{137}Cs can be observed graphically as a shift of the CR value to a higher level when the K concentration in the pore water is below a certain threshold level for mixtures with similar RIP-K ratios ((d) Figure 3.3).

Table 3.3. Statistical models relating the transfer factors (CR in kg kg^{-1}) to the clay mineralogy and substrate properties (*N* = 16). Models are sorted by increasing R^2 and decreasing Root Mean Square Error. Parameter uncertainties are standard error in brackets. $RIP_{mixture}$ is expressed in mmol kg^{-1}, %2:1 is the total 2:1 phyllosilicate content in g 100 g^{-1}, %di2:1 is the dioctahedral 2:1 phyllosilicate content of illite or smectite (subscript) in g 100 g^{-1}, %tri2:1 is the trioctahedral 2:1 phyllosilicate content in g 100 g^{-1}, %1:1 is the total 1:1 phyllosilicate content in g 100 g^{-1}, K is the K concentration in pore water after growth in mmol L^{-1} and ex K is the exchangeable K content in $cmol_c$ kg^{-1}.

model equation	*R2*	*RMSE*
$\log_{10}\mathrm{CR} = (0.58 \pm 0.57) - (0.51 \pm 0.23)\log_{10}\mathrm{RIP_{mixture}}$	0.26*	0.51
$\log_{10}\mathrm{CR} = (0.26 \pm 0.38) - (1.35 \pm 0.52)\log_{10}\%2{:}1$	0.32*	0.49
$\log_{10}\mathrm{CR} = (0.61 \pm 0.46) - (0.54 \pm 0.19)\log_{10}\mathrm{RIP_{mixture}} - (0.31 \pm 0.11)\log_{10}\mathrm{K}$	0.54**	0.42
$\log_{10}\mathrm{CR} = -(1.34 \pm 0.19) - (0.80 \pm 0.19)\log_{10}\mathrm{ex\ K}$	0.56***	0.39
$\log_{10}\mathrm{CR} = -(2.86 \pm 0.57) - (0.54 \pm 0.16)\log_{10}\%\mathrm{di2{:}1_{ill}} - (1.11 \pm 0.30)\log_{10}\%\mathrm{di2{:}1_{sme}} - (1.22 \pm 0.32)\log_{10}\%\mathrm{tri2{:}1}$	0.59*	0.41
$\log_{10}\mathrm{CR} = -(0.22 \pm 0.37) - (0.45 \pm 0.14)\log_{10}\mathrm{RIP_{mixture}} - (0.76 \pm 0.14)\log_{10}\mathrm{ex\ K}$	0.76***	0.30
$\log_{10}\mathrm{CR} = -(2.59 \pm 0.44) - (0.90 \pm 0.16)\log_{10}\%\mathrm{di2{:}1_{ill}} - (1.14 \pm 0.23)\log_{10}\%\mathrm{di2{:}1_{sme}} - (1.21 \pm 0.24)\log_{10}\%\mathrm{tri2{:}1} + (0.52 \pm 0.16)\log_{10}\%1{:}1$	0.79**	0.31

The ^{137}Cs CR could be predicted based on the mechanisms of K competition and the ^{137}Cs selective adsorption. The CR could be predicted in a multiple linear regression with the $RIP_{mixture}$ and the K concentration in the pore water (Table 3.3), which logically followed from the important roles of sorption and ion competition effects as showed in the analysis of soil solution based CR prediction (Figure 3.2 and Figure 3.3d). The CR prediction improved if instead of the pore water K, the exchangeable K content was considered (Table 3.3), which reflected the K buffering capacity.

The RIP is a soil property that is not reflected in general purpose soil maps while the mineralogy may be inferred from soil classification. Hence, the mineralogy was put forward as an estimator for FES and K buffering capacity with a view to upgrade soil maps with FES and K buffering capacity derived from available soil information for each mapping unit. Logically, the ^{137}Cs selective adsorption could not be described by the total phyllosilicate content and the CR was not significantly affected by total clay content (Figure 3.3a). The 2:1 phyllosilicate content correlated negatively to the CR, but the correlation was poor (Table 3.3). More detailed information of the 2:1 clay

types (Table III.1) better explained the CR and the best model was reached with $R^2 = 0.79$ when four different clay mineral fractions were used (Table 3.3). In that best model, the parameter values for each of the three different 2:1 clay fractions (log transformed) were similar and not different from 1, so there was a proportional decrease in CR when these fractions increased. Most strikingly, there was a statistically positive effect of 1:1 phyllosilicates on the CR. This was unexpected, as 1:1 clays, devoid of FES, were expected to have no effect on the CR (see univariate analysis). Possibly this relation was statistical rather than causal, due to a lower content of 2:1 phyllosilicates, which have FES and typically lower CRs.

To assess if mineralogical information could improve CR predictions, we first tested this statistically (Table 3.3) and then compared these findings with existing semi-mechanistic CR models for natural soils. These models were calibrated with particle-size clay content rather than detailed mineralogy variables. A CR model for grass on mineral soils (Absalom et al., 1999) had time (58 days since contact with ^{137}Cs), exchangeable K content and total phyllosilicate content as model variables (Equations I.1-I.5). That CR model performed only slightly better ($R^2 = 0.60$***, RMSE = 0.38, details not shown) compared to the exchangeable K content regression model (Table 3.3). Substituting 2:1 phyllosilicate content for total phyllosilicate in the Absalom model did not improve its performance ($R^2 = 0.51$**, RMSE = 0.42). The other models made for organic soils (Equations I.6-I.17 from Absalom et al., 2001; Equations I.29-I.35 from Tarsitano et al., 2011) all performed worse and largely underestimated ^{137}Cs transfer, presumably because these were calibrated on soils with a high content of organic matter. We suggest future verification of mineralogical data in CR models using natural soils, which would require changing the model structure and recalibrating parameters to improve CR predictions.

3.4. Conclusion

Our pot cultivation experiment showed that both the amount and type of phyllosilicates in a substrate have an important role on the ^{137}Cs bioavailability, with a logical effect of the type of mineral clays (illite, biotite, smectite or vermiculite) that affect the bioavailability. The CR cannot be predicted with a regression model based on the exchangeable K level and 2:1 type phyllosilicates. However, differentiating the 2:1 type clays explained the CR in statistical terms but it is likely that this advanced XRD is unfeasible for

routine analysis of soils, let be that it can be combined with existing soil map information for geospatial assessments. The existing models predicted the CR little or no better than a simple regression model of only the exchangeable K content. Further research on natural soils across different parent rocks and weathering stages is required to reveal to what extent XRD based soil mineralogy can predict ^{137}Cs bioavailability.

Chapter 4
Highly weathered mineral soils have highest transfer risk of radiocaesium contamination after a nuclear accident: a global soil-plant study

Vanheukelom, M., Sweeck, L., Almahayni, T., De Bruyn, M., Steegmans, P., Fondu, L., Van Gompel, A., Van Hees, M., Wannijn, J., Smolders, E., 2024. Highly weathered mineral soils have highest transfer risk of radiocaesium contamination after a nuclear accident: A global soil-plant study. Sci. Total Environ. 173583.
https://doi.org/https://doi.org/10.1016/j.scitotenv.2024.173583

Abstract

Accidental release of radiocaesium (^{137}Cs) from nuclear power plants may result in long-term contamination of environmental and food production systems. Assessment of food chain contamination with ^{137}Cs relies on ^{137}Cs soil-to-plant transfer data and models mainly available for regions affected by the Chornobyl and Fukushima accidents. Similar data and models are lacking for other regions. Such information is needed given the global expansion of nuclear energy. We collected 38 soils worldwide of contrasting parent materials and weathering stages. The soils were spiked with ^{137}Cs and sown with ryegrass in greenhouse conditions. The ^{137}Cs grass-soil concentration ratio varied four orders of magnitude among soils. It was highest in Ferralsols due to the low ^{137}Cs interception potential of kaolinite clay and the low exchangeable potassium in these soils. Our results demonstrate, for the first time, the high plant uptake of ^{137}Cs in highly weathered tropical soils. The most recent ^{137}Cs transfer model, mainly calibrated to temperate soils dominated by weathered micas, poorly predicts the underlying processes in highly weathered tropical soils. Nevertheless, the model still reasonably predicts ^{137}Cs bioavailability across all soils (R^2 = 0.8 on a log-log scale), despite the poor predictions of intermediate variables contributing to the ^{137}Cs transfer processes. This leads to offsetting errors in the final predictions of the ^{137}Cs bioavailability, i.e., it overestimates the sorption of ^{137}Cs but it underestimates the K deficiency, the latter counteracting the former trend.

4.1. Introduction

Caesium-137 (^{137}Cs) is one of the most critical radionuclides released after nuclear accidents because of its long half-live (30 years) and its similarity to potassium (K), which makes it easy to enter the human food chain. Decision-makers rely on ^{137}Cs soil-to-plant transfer data and models to predict the concentrations of ^{137}Cs entering the food chain. Although models were developed after the Chornobyl and Fukushima accidents to predict ^{137}Cs transfer to plants for European and Japanese soils, there is a need for transfer models applicable to other (e.g., tropical) regions, as the use of nuclear power increases worldwide.

The transfer of ^{137}Cs, expressed as the concentration ratio (CR) of ^{137}Cs in plants to that in soil, shows substantial variation. The IAEA compiled ^{137}Cs CR values for grass, ranging from 10^{-4} to 10 kg kg^{-1} (IAEA, 2021b, 2020, 2009), with no clear explanation based on soil texture (e.g., sand, loam, clay) (Almahayni et al., 2019). After the Chornobyl accident, the highest soil-to-plant transfer of ^{137}Cs was observed in peatlands because peat soils are devoid of clay minerals, which selectively retain ^{137}Cs. Greenhouse studies confirmed exceptionally large CR values, often >1 kg kg^{-1}, for plants grown in peat (Sanchez et al., 1999). Further research revealed that ^{137}Cs uptake in plants is controlled by the ratio of ^{137}Cs and K in soil solution (Smolders et al., 1997). Both elements use the same uptake systems in plant roots (Zhu and Smolders, 2000). Predicting soil ^{137}Cs transfer to plants requires considering Cs^+:K^+ competition at the soil-root interface and ^{137}Cs adsorption to soil particles. The retention of ^{137}Cs in soil takes place on the Cs^+ selective binding sites called Frayed Edge Sites (FES), quantified using Radiocaesium Interception Potential (RIP), which combines the selectivity coefficient of Cs^+ relative to K^+ (i.e., intensity) and the FES capacity of the soil (i.e., quantity) (Cremers et al., 1988).

The lack of ^{137}Cs soil-to-plant transfer models calibrated for regions outside Europe and Japan remains a concern. Existing models (Absalom et al., 2001, 1999; Tarsitano et al., 2011) do not account for the effect of soil mineralogy on the ^{137}Cs transfer to plants. Furthermore, model parameters are lacking for highly weathered soils prevalent in tropical regions. A recent pot trial showed nearly two orders of magnitude variation in ^{137}Cs CR among synthetic soils prepared by mixing sand with different clay minerals (Chapter 3) and showed that next to exchangeable K and clay content, the type of minerals matters for

^{137}Cs bioavailability. Global diversity in soil mineralogy challenges assumptions of these models, particularly regarding the 2:1 phyllosilicates with high FES amounts found at intermediate weathering stages, whereas they are smaller in very young (e.g., volcanic) soils and almost absent in highly weathered stages dominated by 1:1 phyllosilicates (Joussein et al., 2004).

This study aimed to measure the CR values of ^{137}Cs in soils with diverse mineralogies at varying stages of development and to validate the extent to which existing models can realistically predict ^{137}Cs transfer from these soils. Two soil sequences were sampled representing different weathering stages affecting soil mineralogy. In addition, 26 other soils with contrasting soil properties, covering Andosols and Ferralsols, were included in the collection. A greenhouse experiment was set up with these soils. A subset of the soils was fertilized without and with K to investigate its effect on ^{137}Cs CR reduction. The soils were characterized, spiked with ^{137}Cs and grown with grass.

4.2. Materials and methods

4.2.1. Soil collection

Topsoils (0–20 cm) came from 6 locations of a sequence in Kenya, 6 locations of a sequence in Philippines and 26 locations (no sequence) worldwide (Figure IV.1; Table IV.1). The soils were classified according to the World Reference Base for Soil Resource (IUSS Working Group WRB FAO, 2022) or derived from the 250 m gridded world map SoilGrids™ (https://soilgrids.org) based on the geo-referenced location. The soils covered nine Köppen-Geiger climate subgroups (Beck et al., 2018) and fourteen reference WRB soil groups.

4.2.2. Soil characterization

Subsamples of air-dried soil, sieved at 2 mm, were used for characterization. All air-dry soil weights were corrected for moisture content (105 °C). Particle size distribution was determined by laser diffraction. Subsamples of 5 g were taken using a sample splitter and put in deionized water. Carbonates were removed using 3 mol L^{-1} HCl, and organic matter was removed using 3 mol L^{-1} H_2O_2 in doses until the reaction ceased. Before measurement, the particles were ultrasonically dispersed. For Ferralsol samples, iron (hydr)oxides were removed using 10 mL of 0.56 mol L^{-1} oxalic acid. One Ferralsol was re-measured to compare the effect of iron removal and ultrasonic dispersion (Table IV.5). Particles were measured by laser diffraction (LS 13 320,

Beckman Coulter). For a selection of samples (*N* = 28), the particle size distribution was also determined by the pipet method (ISO 11277, 1998) without iron removal. All fractional weights were corrected for losses and normalized to percentages. As the particle size distributions yielded different results depending on the method, the highest clay content was used for modeling unless stated otherwise. The total carbon and organic carbon (C) contents were determined by dry combustion. Organic C samples were acidified with 3 mol L^{-1} HCl and dried (50 °C). Carbon release was measured upon combustion (900 °C) (EA 1108, Carlo Erba). Inorganic C was calculated as the difference in %C between total C and organic C.

Soil mineralogy was determined on bulk powder samples with added standard by X-ray diffraction (XRD) (Środoń et al., 2001; Zeelmaekers, 2011). Oven-dried (60 °C) soils were crushed by pestle and mortar until all material passed through a 0.5 mm sieve. Soil (90 wt%) and zincite standard (10 wt%) were analytically weighted and wet-milled (McCrone Micronizing Mill) in ethanol for 7 min to obtain a homogenous mixture. Mixtures were placed under a fume hood until dry. The powder was passed through a 0.355 mm sieve. The powder was inserted in a side-loading holder. Measurements were carried out with two diffractometers in Bragg-Brentano arrangements with Cu-K_α radiation: with 173 mm goniometer radius, a graphite crystal monochromator, a gas proportional detector scanning at 45 kV and 30 mA, ranging over 5–65 °2θ with 0.02 °2θ step size and 2 s counting time (PW1830, Philips), or with 250 mm radius, a variable divergence slit, two solar slits, a position sensitive detector (LynxEye, Bruker) scanning at 40 kV and 40 mA over 3–75 °2θ at 0.01 °2θ in 0.2 s (D8 Advance, Bruker). The minerals in the powder were identified and quantified using two methods belonging to the respective diffractometers. Quanta software (© Chevron ETC) used the Mineral Intensity Factors method (Moore and Reynolds, 1997), where the sum of single reflections of the mineral phases was fitted to the recorded XRD pattern. Profex software (version 5.2.0) (Doebelin and Kleeberg, 2015) used the Rietveld method, where the whole pattern simulated by calibrated crystallographic parameters is fitted to the recorded pattern. Seven samples were measured and processed independently using two setups for comparison (Table IV.2), but patterns of the former diffractometer and method were used for data analysis. The soil weathering index (WI) was calculated (Table IV.2):

$$\mathrm{WI} = \sum_{i=1}^{12} \%m \cdot i \qquad (4.1)$$

where *%m* represents the percentage of each mineral phase in the bulk soil, and *i* represents the index (*i*) of weatherability of the corresponding mineral (Jackson et al., 1948; Jackson and Sherman, 1953). The weathering index of minerals ranges from 1 to 12, with 1 indicating the youngest mineral (e.g., gypsum) and 12 the most stable mineral (e.g., anatase).

The cation exchange capacity (CEC) was determined using cobalt hexamine (Ciesielski and Sterckeman, 1997). Samples of air-dry soil with 16.6 mmol L^{-1} $Co(NH_3)_6Cl_3$ were shaken end-over-end (1 h). After centrifugation (15 min), the supernatant was filtered at 0.45 µm (Acrodisc®). The cation concentrations were measured (7700 Series ICP-MS, Agilent Technologies; 4200 MP-AES, Agilent Technologies). The CEC was calculated as the difference between the initial and final Co equivalent charge concentration in solution per soil weight.

The RIP of the soils was determined by exchanging $^{137}Cs^{+}$ with K^{+} on the selective adsorption sites while blocking non-selective sites with Ca^{2+} (Wauters et al., 1996b). Samples of 1 g air-dry soil in dialysis membrane bags (VISKING®, MWCO 12–14 kDa; Spectra/Por®, MWCO 6–8 kDa) with 10 mL of 0.5 mmol L^{-1} K and 100 mmol L^{-1} Ca solution were placed in pots containing 150 mL K-Ca solution, and shaken end-over-end (24 h). The outer K-Ca solution was renewed and shaken (24 h). Next, the outer solution was renewed with 200 kBq mL^{-1} ^{137}Cs with K-Ca solution and shaken (24 h). The ^{137}Cs concentration in the initial and final outer solution was measured with a gamma counter (1480 WIZARD 3”, Perkin Elmer). The RIP was calculated by multiplying the measured ^{137}Cs solid-liquid distribution with 0.5 mmol L^{-1} K in solution.

4.2.3. Pot experiment

The experiment included two sets of soil batches taken worldwide (experiment A, *N* = 26) and from sequences (experiment B, performed after experiment A, *N* = 12). Air-dried soils were sieved at 4 mm, and about 3 kg soil was transferred to buckets before fertilization and spiking (Figure IV.3). Carrier-free $^{137}CsCl$ was added at a rate of 400 kBq kg^{-1}. All soils were NP-fertilized. Three soils with low K buffering capacity (a sandy, a volcanic, and a weathered tropical soil with CEC <5 $cmol_c$ kg^{-1} of which <2% occupied by K) in experiment A and the sequences in experiment B were subjected to two K fertilizer treatments: without (no K, *N* = 38) and with (+K, *N* = 15) fertilizer. Fertilizer,

including NH_4NO_3, $NaH_2PO_4 \cdot H_2O$ and $MgSO_4 \cdot 7H_2O$, was added at rates of 50 mg N-NO_3 kg^{-1}, 50 mg N-NH_4 kg^{-1}, 13 mg P kg^{-1}, 16 mg S kg^{-1}, and 12 mg Mg kg^{-1}. In the case of Ferralsols, where extremely high phosphorus sorption on iron-containing (oxyhydr)oxides is typical (De Bauw et al., 2021), 5 g of granules containing 46% $Ca(H_2PO_4)_2 \cdot H_2O$ were added per pot to reach a final P dose of 57 mg P kg^{-1} (with 6 mg K kg^{-1} as impurity). Additional KCl was added to the 15 soils with the +K treatment at a rate of 150 mg K kg^{-1}. The fertilizer as stock solution together with the ^{137}Cs in deionized water were added to the soil to obtain 50% of the moisture content of a fully saturated soil, the latter was determined by the saturated paste method (USDA, 1954). The soils were incubated in covered buckets at room temperature for 14 days, during which deionized water was added to correct for weight loss, and soils were mixed with spatulas every 2–3 days. Soil moisture content was increased to 55% (Cavinti to 75%; Luisana to 85%) using deionized water for at least 7 days for solution separation.

Soil solution was separated by centrifugation. The moist soils were placed in an in-house made two-compartment cup, which featured a 2.5 µm filter (Whatman®) placed on a porous plate, separating the soil from the solution. After centrifugation (30 min, 4,000 *g*), the solution collected in the lower compartment was filtered at 0.45 µm. The separation process took about 20 days to ensure that a sufficient volume of solution was obtained from each of the soils (Figure IV.3). Soils were mixed and deionized water was added. The ^{137}Cs concentration in soil solution was determined with a NaI(Tl) scintillation gamma counter (measuring time 10–50 min, average counting efficiency ~16%;1480 WIZARD 3", Perkin Elmer). Samples with too low ^{137}Cs concentrations (i.e., below the detection limit of the NaI(Tl) counter) were measured using a high purity germanium gamma detector (16–24 h, efficiency ~10–40%; SEGe, Canberra). The K, Na, Ca and Mg concentrations were measured using ICP-MS. The NH_4 concentration was measured colorimetrically (SA 40, Skalar).

Before potting the soil, subsamples were taken to analyze the soil pH, total ^{137}Cs content, and exchangeable cations. The soil pH was determined in diluted $CaCl_2$ suspension (Schofield and Taylor, 1955). Samples of 5 g air-dry soil in 12.5 mL of 0.01 mol L^{-1} $CaCl_2$ were shaken end-over-end (2 h) and pH measured (PC 5000 L, pHenomenal®). The total soil ^{137}Cs concentration was determined by measuring air-dry soil samples with a gamma counter. Exchangeable cations in soil were determined using ammonium acetate.

Samples of 1 g air-dry soil in 18 mL of 1 mol L^{-1} NH_4CH_3COO were shaken end-over-end (24 h). After centrifugation (15 min, 1,300 *g*), the supernatant was filtered at 0.45 µm. The ^{137}Cs concentration in supernatant was determined with a gamma counter. The K, Na, Ca and Mg concentrations were measured using MP-AES. Only in experiment A (*N* = 29) the exchangeable NH_4 was determined following the same procedure, but instead 1 mol L^{-1} KCl was used. The NH_4 concentration in the supernatant was measured colorimetrically. In experiment B (*N* = 24), samples of the sequence soils were taken after plant growth to measure exchangeable ^{137}Cs, K, Na, Ca and Mg.

After the 42–45 days pre-incubation period, soils were divided over three 1 L pots, which were filled to an equal volume. Per pot, 0.65 g seeds of grass (*Lolium perenne* L.) were sown by spreading seeds on the surface, at least 1 cm from the rim and buried under about 60 g soil. The pots were covered until germination to prevent excessive drying of the soil. Cultivation was carried out in a growing chamber with a day/night rhythm of 14/10 h at 24/18 °C. The pots were watered (~50% moisture content) with deionized water every 2–3 days based on weight loss and pot positions were randomized. Grass shoots were harvested after 30 days. The above-ground plant material was cut off 1 cm above the surface to prevent ^{137}Cs contamination from the soil. The fresh weight of the plant material was recorded. The dry weight was recorded after drying the plant material in the oven (65 °C) for 6 days. The shoots were calcinated (550 °C), ash was dissolved in 2 mL of 12 mol L^{-1} HCl, calcinated again and dissolved in diluted 0.1 mol L^{-1} HCl. The ^{137}Cs concentrations were analyzed with a NaI(Tl) or Ge detector. The K, Na, Ca and Mg concentrations were measured with ICP-MS or MP-AES.

4.2.4. Statistical analyses

JMP® Pro software (Version 17.0.0 SAS Institute Inc., Cary, NC, 1989–2023) was used. Standard deviations of the CR and CF values were derived using error propagation formula because soil, solution and plant samples were not paired. Variables with skewness >0.5 were log-transformed unless stated otherwise. Significant differences in dry-weight grass yields among experiments A and B were tested using a non-parametric Wilcoxon Rank-Sum at a 5% significance level. Significant differences between replicate ^{137}Cs CR values among soils were tested using a Tukey-Kramer HSD test at a 5% significance level for equal sample sizes. Significant differences in dry-weight grass yields and ^{137}Cs CR values among texture/organic C/pH groups or WRB soil class groups were tested using a non-parametric comparison for all pairs

Dunn's test at a 5% significance level. Pearson correlation coefficients were calculated on the log-transformed means (n = 3), except for pH, which is inherently on a log-scale (Table IV.8; Table IV.9). Multiple linear regression was used, taking into account interaction-effects (p <0.05), to obtain relations describing CR with selected explanatory variables.

4.3. Results

4.3.1. Soil properties

The soils differed in their physico-chemical properties and the stage of weathering (Table 4.1; Table IV.2). Soils had various properties with clay contents ranging between 2.8% and 83%, soil pH ranging over 3.0–7.8, soil organic C contents (%SOC) ranging over 0.23–14% and CEC ranging over 1.9–91 $cmol_c$ kg^{-1}. The Kenyan soil sequence developed from volcanic ash showed a gradient in weathering index ranging over 3.7–7.9 from young, organic soils on the mountain to more weathered clayey soils in the valley with components such as kaolinite (6–24%), but also 2:1 phyllosilicates (6–16%) increasing in concentration. The Philippine sequence with weathering indices ranging over 4.6–9.2 was dominated by kaolinite (15–68%), which became more abundant as weathering increased. In parallel, soil originating from volcanic ashes in Miyakonojo (Japan) was at an early stage of development (Shoji and Takahashi, 2002) and contained mainly allophane and feldspar. It also included some muscovite (7%), which was not derived from volcanic ash, but from mica-bearing aeolian deposits from Chinese deserts (Nakao et al., 2021). Soils from sedimentary parent material in Europe, such as loess deposits, were moderately developed which contained 2:1 phyllosilicates (up to 50%) and some kaolinite (<20%). Soils from volcanic plateaus in Behenjy (Madagascar) and Luisiana (Philippines) were highly weathered and contained mainly kaolinite (>30%).

The yields of clay content were compared among different particle size distribution methods. For one Ferralsol, iron removal and ultrasonic dispersion treatments before laser diffraction measurement were compared (Table IV.5). The clay content ranged from 30% to 44%, depending on the dispersion treatment, indicating the slight sensitivity of the procedural difference in this method. However, a much higher clay content of 83% was found following the standard pipet method without iron removal (ISO 11277) on the same soil (Table IV.5). Clay yield differences after the pipet and laser diffraction methods were also found for other soils. In the following sections, the highest clay content determined for each soil was used, usually the pipet method, because it best matched the total phyllosilicate content after XRD (Figure IV.7b).

The muscovite and 2:1 phyllosilicate content explained 52% of the variability in soil RIP (R^2 = 0.52, root mean square error (RMSE) = 0.43, N = 38). Soil

RIP was low in the youngest, volcanic soil (Andosols), but increased up to 50-fold in the more developed soils (Kastanozem/Chernozem/Phaeozem), and decreased again up to 440-fold in the weathered tropical soil (Ferralsols) (Table IV.3). Furthermore, the geometric mean (GM) of the RIP per unit clay was generally low in the Andosols and Ferralsols (<1,000 mmol kg^{-1} clay) compared to the moderately weathered soils (25,600 mmol kg^{-1} clay) (Table 4.1; Figure IV.4). It was previously found that the mineralogy and the weathering stage of the soil partially controlled the RIP of soils from the same parent material (Joussein et al., 2004). In this study, with soils from diverse parent materials, the variation in soil RIP can largely be explained by mineralogy and weathering stage.

A similar trend emerged for the CEC: this was low for the Andosol despite the high clay content and organic matter (Table 4.1), the CECs of the more developed soils were higher, except the sandy soils, and the CEC of the Ferralsols was low despite the high clay contents.

However, the method for determining weathering stages based on soil bulk mineralogy must be critically reviewed. For example, the weathering index for Lixisols and Acrisols was around 6, lower than expected. On the one hand, this may be due to the method used to determine the index: it was applied to minerals in the bulk soil rather than only clay-sized minerals, as originally intended (Jackson, 1964; Jackson et al., 1948; Jackson and Sherman, 1953). Soils with high sand fractions may, therefore, have unexpectedly low weathering indices, which may misrepresent their true stage of weathering. On the other hand, soil classification does not always reflect the mineralogical composition of the soil because it is based primarily based on soil-forming processes that determine soil horizon development rather than mineralogy. While extreme reference (WRB) soil groups such as Andosols and Ferralsols generally reflect the mineralogical composition, intermediate weathering stages based on soil classification may not always match those based on mineralogical indicators.

Table 4.1. Summary of selected characteristics of the soils. More details are in the Supplementary information (Table IV.3).

soil classes[a]	*N*[b]	clay[c]			SOC[d]			CEC[e]			RIP per unit clay[f]			weathering index		
WRB		%			%			$cmol_c\ kg^{-1}$ soil			mmol kg^{-1} clay			–		
		min	max	**GM**	min	max	**GM**	min	max	**GM**	min	max	**GM**	min	max	**GM**
Andosol	2	23	34	**28**	5.6	14	**8.7**	5.1	6.2	**5.6**	502	1,080	**738**	2.5	3.7	**3.0**
Kastanozem/Chernozem/Phaeozem	3	18	24	**21**	1.0	1.4	**1.2**	13	33	**21**	17,500	29,400	**21,900**	4.8	5.8	**5.2**
Fluvisol	3	10	14	**12**	0.87	1.0	**0.94**	17	91	**50**	21,600	32,300	**25,600**	5.4	5.6	**5.5**
Gleysol	2	22	32	**26**	1.3	1.8	**1.5**	5.4	32	**13**	2,340	6,300	**3,840**	5.2	6.1	**5.6**
Luvisol/Lixisol	3	6.0	27	**13**	0.45	1.3	**0.88**	2.9	20	**9.4**	12,900	27,900	**19,200**	5.5	6.0	**5.7**
Nitisol	2	42	46	**44**	5.3	8.4	**6.7**	46	50	**48**	3,980	10,900	**6,580**	5.1	6.6	**5.8**
Anthrosol	2	2.8	6.0	**4.1**	2.3	2.9	**2.6**	1.9	9.2	**4.2**	3,000	18,000	**7,340**	5.9	6.0	**5.9**
Cambisol	10	5.7	49	**27**	0.23	2.3	**1.3**	8.4	34	**21**	1,700	20,200	**6,000**	4.6	7.6	**6.1**
Vertisol	3	32	39	**35**	1.2	2.0	**1.6**	19	26	**22**	3,680	14,900	**6,380**	6.0	7.1	**6.6**
Acrisol	5	14	62	**29**	0.56	3.7	**1.9**	9.9	84	**34**	209	15,300	**3,970**	6.1	9.2	**6.9**
Ferralsol	3	42	83	**61**	0.54	2.9	**1.4**	2.3	8.3	**5.2**	32.5	5,670	**316**	7.9	9.3	**8.7**

[a] soils by World Reference Base classes ranked according to increasing soil weathering stage; [b] number of soils per group; [c] clay content data of highest clay yield; [d] soil organic carbon; [e] cation exchange capacity; [f] radiocaesium interception potential per unit clay of highest clay yield

4.3.2. Pot experiment

The shoot yield averaged 0.73 g dry weight per pot among all soils and treatments (Table IV.7). Yield ranged from 0.044 g to 2.9 g and was significantly higher (p <0.05) in experiment B (1.5 ± 0.6 g, mean ± standard deviation) compared to experiment A (0.56 ± 0.36 g), likely because seeds used for A were 3 years older than those for B. Dry matter yields were unaffected (p >0.05) by WRB soil class groups or single soil properties. No significant correlations were found between yield and ^{137}Cs CR (Table IV.8). The ^{137}Cs CR ranged over 4 orders of magnitude between 0.0047 and 47 kg kg^{-1} (Figure 4.1; Figure IV.4; Table IV.7). The exchangeable K content in soils before plant growth within a soil class group varied up to 29-fold (Ferralsols, no K) (Figure IV.4; Table IV.6). The ^{137}Cs CR was significantly (p <0.05) affected by the soil and treatment, as the log CR values of the replicates differed for 20 out of 53 treated soils (Table IV.7). However, neither the soil classification based on clay, sand and organic matter contents (IAEA, 2009) nor the WRB soil class grouping explained the log CR values (p >0.05).

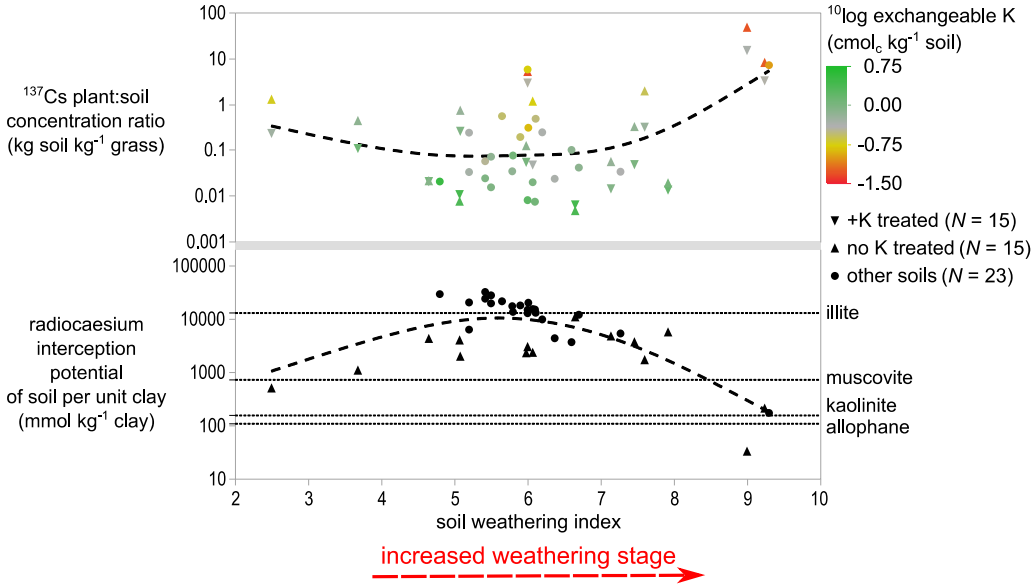

Figure 4.1. Top: grass-soil ^{137}Cs concentrations ratios (log scale) in relation to calculated weathering index based on mineralogy. Data are combined from soils with (+K, *N* = 15) and without K (no K, *N* = 15) fertilizer treatment, in addition to those (*N* = 23) where K treatment was not assessed. Points on the graph are arithmetic mean CR values (*n* = 3) and are colored depending on exchangeable K content in soils (note log scale). Bottom: RIP of soil per unit clay (highest clay content) as soil weathering increases. The dotted lines are RIP of allophane (111 mmol kg^{-1}), illite (10,000–16,000 mmol kg^{-1}; de Koning et al., 2007; Wauters et al., 1996c), muscovite (740 mmol kg^{-1}; De Preter, 1990) and kaolinite (6–310 mmol kg^{-1}; Nakao et al., 2008; Ogasawara et al., 2013). The dashed lines are cubic spline regression curves (λ = 3, standardized) (Top: R^2 = 0.36, sum of squares error (SSE) = 32; Bottom: R^2 = 0.69, SSE = 7.9).

4.3.3. K addition lowered ^{137}Cs transfer

Adding K (150 mg kg^{-1} equivalent to 0.38 $cmol_c$ kg^{-1}) reduced the CR values up to 24-fold (Gleysol) (Figure IV.6). However, the effect of K addition varied depending on the soil properties and the initial K concentration in the soil. Despite the reduction of ^{137}Cs transfer to grass by adding K, CR is still high (>0.1 kg kg^{-1}) for the young, volcanic soil (Andosol), the sandy soil (Anthrosol), and the weathered tropical soil (Ferralsol) with low initial exchangeable K content (<0.5 $cmol_c$ kg^{-1}) and low K solid-liquid distribution coefficient (K_D <5 L kg^{-1}). Adding K was not effective in soils (Nitisols) with a high initial exchangeable K content (>2.0 $cmol_c$ kg^{-1}).

4.3.4. Single soil properties explained ^{137}Cs transfer

Soil properties such as organic C, clay content (highest clay content obtained by various methods) (Figure 4.2a) or phyllosilicate content (Figure IV.7a) did not explain CR by single regression (p >0.05). However, clay content determined exclusively by the laser diffraction method explained 25% of the CR, yet laser diffraction clay content underestimated the phyllosilicate content determined by XRD (Figure IV.7b). The variability of CR was slightly influenced by soil pH (Figure 4.2b) and, to a larger extent, by the NH_4 concentration in solution (R^2 = 0.58, not shown). The RIP explained 68% (Figure 4.2c), and exchangeable K content before plant growth explained 68% (Figure 4.2d) of the CR. CR was better explained by the exchangeable K content after (R^2 = 0.81, RMSE = 0.41, N = 24) than before (R^2 = 0.74, RMSE = 0.48, N = 24) plant growth (data after plant growth Table IV.7). This is likely because exchangeable K measured after plant growth better reflects in situ soil conditions during plant uptake. However, exchangeable K after growth was only available for N = 24 out of 53.

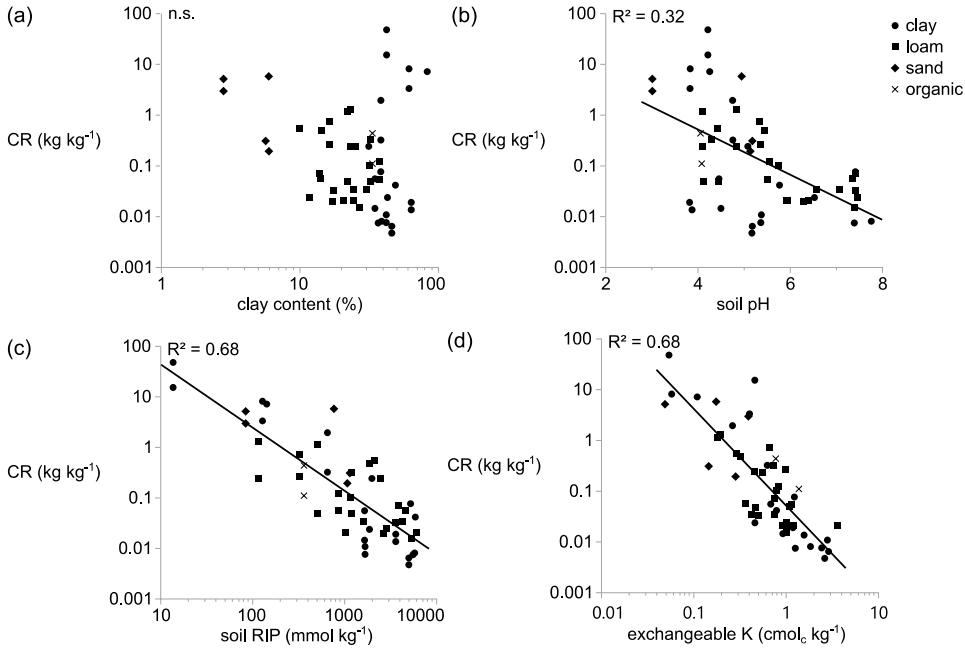

Figure 4.2. Soil properties explaining the grass-soil ^{137}Cs concentration ratio CR (N = 53), which are (a) clay content (highest clay yield), (b) soil pH, (c) radiocaesium interception potential, and (d) exchangeable K content before plant growth. Points on the graphs are mean values (n = 3) which are marked according to the classification based on the clay, sand and organic matter contents (IAEA, 2009): clay (clay ≥ 35%, circle), loam (18% < clay < 35%, square), sand (sand ≥ 65% and clay < 18%, diamond), and organic (organic matter ≥ 20%, cross).

4.3.5. Soil solution ^{137}Cs and K explain ^{137}Cs uptake by plants

The ^{137}Cs transfer from soil to grass is largely controlled by ^{137}Cs concentration in soil solution and $^{137}Cs^{+}$:K^{+} competition for plant uptake. Hence, the ^{137}Cs plant-solution concentration ratios (i.e., CF values) were well predicted by single linear regression with the K in solution (R^2 = 0.69***, RMSE = 0.39) (Figure 4.3).

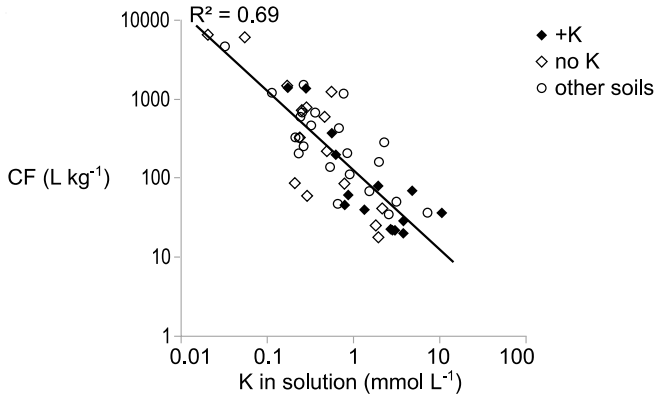

Figure 4.3. The grass-soil solution ^{137}Cs concentration factor (CF) as a function of the solution K concentration (*N* = 53). Symbols indicate the K treatment. Points on the graphs are mean values (*n* = 3) and soil solutions are sampled before grass growth.

4.3.6. ^{137}Cs soil-plant transfer predicted by existing models

The ^{137}Cs soil-to-plant transfer models of Absalom et al. (2001; 1999) and Tarsitano et al. (2011) were tested on the data in this study. The Absalom 2001 (Equations I.6-I.17) and Tarsitano 2011 (Equations I.29-I.35) models performed well (Table 4.2) for soils of various weathering stages (Figure 4.4). The highest clay content values were used as model variables for consistency and because predictions were better (except for Absalom 1999 with Equations I.1-I.5, R_{adj}^2 = 0.28, RMSE = 0.84, mean observed over predicted ratio (O/P) = 16,000). The largest underestimation of CR (mean O/P = 5–11) by the Absalom 2001 and Tarsitano 2011 models was for low RIP values (<1,000 mmol kg^{-1}). This underestimation increased (mean O/P = 7–12) if laser diffraction clay contents were used. Although it predicted the CR satisfactorily, the Tarsitano 2011 model incorrectly predicted K concentration in soil solution (Figure IV.8a) and ^{137}Cs K_D in low RIP soils (Figure IV.8b). This suggests compensatory effects of both variables.

A regression model with the same soil property input variables performed better than the Absalom 2001 and Tarsitano 2011 models (Table 4.2). The prediction was further improved when RIP was included in the regression. The best regression model, using a stepwise mixed selection of variables (p <0.05), was based on clay content, RIP, exchangeable K and NH_4 in soil solution.

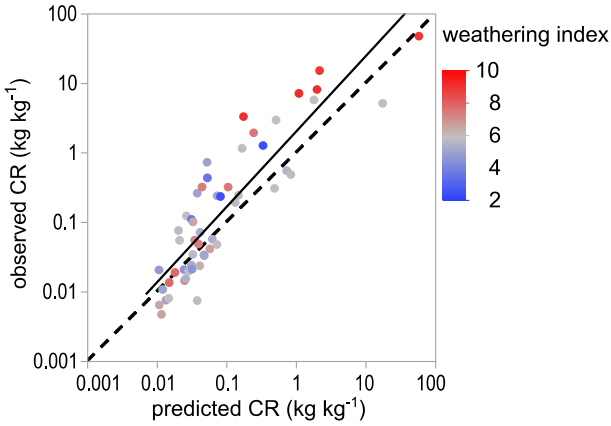

Figure 4.4. Predictions of ^{137}Cs grass-soil concentration ratio with the Tarsitano 2011 model compared with observed CR values (N = 53). Points on the graph are mean CR values (n = 3). They are colored according to a calculated weathering index based on mineralogy, with the youngest (Andosols) equal to 2.5 (blue) and the oldest (Ferralsols) equal to 9.3 (red). The full line is the regression line, and the broken line is the 1:1 line.

Table 4.2. Comparison of predicted ^{137}Cs grass-soil concentration ratios with the observed values (*N* = 53), all predictions were evaluated for log transformed CR values. Standard errors of estimates are given in brackets.

Model and soil variables in predictions	R_{adj}^2 [g]	RMSE[h]	mean O/P[i]
Absalom 1999 (Equations I.1-I.5) with %clay, K_{exch}	n.s.	0.96	98,000
Absalom 2001 (Equations I.6-I.17) with %clay, %SOC, pH, K_{exch}, $NH_{4,solution}$	0.77***	0.47	6.7
Tarsitano 2011 (Equations I.29-I.35) with %clay, %SOC, K_{exch}, $NH_{4,solution}$	**0.78*** **	**0.46**	**2.9**
$\log_{10} \mathrm{CR} = -0.88(0.37) + 0.091(0.245) \log_{10} \%\mathrm{clay} + 0.37(0.18) \log_{10} \%\mathrm{SOC} - 1.4(0.2) \log_{10} \mathrm{K_{exch}} + 0.51(0.08) \log_{10} \mathrm{NH_{4,solution}} - 1.0(0.4)[\log_{10} \%\mathrm{clay} - 1.4] \cdot [\log_{10} \mathrm{K_{exch}} + 0.22]$	0.83***	0.41	1.5
$\log_{10} \mathrm{CR} = 1.2(0.3) - 0.78\,(0.11)\log_{10} \mathrm{RIP} - 1.2\,(0.2)\log_{10} \mathrm{K_{exch}}$	0.84***	0.40	1.5
$\log_{10} \mathrm{CR} = 1.1(0.3) - 0.62(0.10) \log_{10} \mathrm{RIP} - 0.94(0.15) \log_{10} \mathrm{K_{exch}} + 0.29(0.07) \log_{10} \mathrm{NH_{4,solution}}$	0.88***	0.34	1.3
$\log_{10} \mathrm{CR} = 0.98(0.44) + 0.016(0.186) \log_{10} \%\mathrm{clay} - 0.58(0.01) \log_{10} \mathrm{RIP} - 0.89(0.16) \log_{10} \mathrm{K_{exch}} + 0.34(0.07) \log_{10} \mathrm{NH_{4,solution}} - 0.49(0.22)[\log_{10} \%\mathrm{clay} - 1.4] \cdot [\log_{10} \mathrm{RIP} - 3.0]$	0.89***	0.33	1.3

[g] adjusted correlation coefficient and significance (**p* <0.05; ***p* <0.01; ****p* <0.001; not significant (n.s.) for *p* >0.05); [h] root mean square error; [i] mean observed over predicted ratio

4.4. Discussion

The contrasting parent materials and weathering stages of soils in this study affect mineralogy and, hence, RIP. The RIP/%clay are of the same order of magnitude for each soil class as previously reported in Vandebroek et al., (2012) (Figure IV.2), except the Kenyan Ferralsol with 2:1 phyllosilicates (Table IV.2). Moreover, RIP/%clay values correspond well to the range of RIPs of pure clay minerals that dominate in soils at certain weathering stages (Figure 4.1), such as illite in younger and kaolinite in weathered soils.

The interpretation of data on a clay unit basis in relation to mineralogy critically depends on the clay isolation method that is, unfortunately, not standardized and rather operationally defined. Here, the clay content of a Ferralsol ranged from 9.7% to 83% (Table IV.3) for different dispersion and measuring techniques. Moreover, using the same measurement technique, the clay content of that Ferralsol varied from 30% to 44% for different dispersion treatments (Table IV.5). The standard WRB book of soil classification has no standardized protocol for the pre-treatments aimed at complete dispersion of the primary particles (e.g., removal of iron as cementing material) and states that all such pre-treatments are considered optional. These operational differences mainly affect the extremes of the weathering sequences, which are young volcanic (Churchman and Tate, 1987) and weathered tropical soils (Bartoli et al., 1991), because of strong soil particle aggregation.

The ^{137}Cs CR ranges over four orders of magnitude between 0.0047 and 47 kg kg^{-1} (Figure 1). Overall, the CR values per soil class in this study are similar to those previously reported (IAEA, 2021; IAEA, 2020). However, the highest CR value obtained for one of the Ferralsols in this study is over 430-fold higher than the recently reported GM of CR for grass in tropical environments (0.11 kg kg^{-1}, N = 16) (IAEA, 2021). That CR is even higher than for Histosols (44 kg kg^{-1}; Sanchez et al., 1999), which were considered the soils with highest ^{137}Cs transfer risk after the Chornobyl accident. In contrast, there is also a Ferralsol for which the CR is similar to those of soils from temperate climates (0.013 kg kg^{-1}) in which 2:1 phyllosilicates (>10%) have been observed (Table IV.2; Table IV.7). Within a reference WRB soil group, the variability in CR value was up to 3,500-fold (Figure IV.4). It is questionable whether grouping CR values by soil texture or class (i.e., IAEA, 2021; IAEA, 2020; IAEA, 2009) provides a reliable estimate for ^{137}Cs bioavailability.

The CR values ordered by weathering stages reveal a decreasing and subsequently increasing trend in ^{137}Cs grass-soil transfer with the degree of weathering (Figure 4.1). The trend of the RIP/%clay logically mirrors that trend, which is expected because ^{137}Cs adsorption selectivity changes due to soil weathering (Chorover et al., 1999; Joussein et al., 2004). Young volcanic soils have a high CR (>1 kg kg^{-1}) due to limited weathering, so 2:1 phyllosilicates in these soils have few frayed edges, and consequently, selective adsorption of ^{137}Cs is limited. In contrast, more developed soils have low CRs (0.01 kg kg^{-1}) because weathering leads to the formation of frayed edges on certain 2:1 phyllosilicates (e.g., illite). Weathered tropical soils have the highest CRs (>10 kg kg^{-1}) due to the dominance of 1:1 phyllosilicates with limited ^{137}Cs selective adsorption.

The role of weathering is also clear within the soil sequences, with comparable parent material (Figure IV.5). In the sequence from Kenya, the proportion of 2:1 phyllosilicates increased with weathering (RIP/%clay increases, i.e., first stage of weathering). In the sequence from the Philippines, weathering increased the proportion of kaolinite (RIP/%clay decreases, i.e., second stage of weathering).

In parallel, as phyllosilicate structures change during weathering, accompanied by a decrease of structural charge and release of K from mineral layers, the K buffering capacity of the soil changes, i.e., more K is available in soil solution and more K exchange sites are created. This is reflected in the K distribution between the soil solution and exchange sites (Figure IV.6). Although no clear trend of change in K distribution with weathering was found for the soils in this study, these changes in K buffering capacity, along with RIP, likely contribute to the variation in CR values (Figure 4.1).

Overall, the Tarsitano 2011 model can predict the ^{137}Cs grass transfer for soils of contrasting parent materials and weathering stages (Figure 4.4; Table 4.2), despite the poor predictions of underlying processes, i.e., the K_D values of ^{137}Cs or the soil solution K concentrations (Figure IV.8). This is likely due to the model not being calibrated for these diverse soils. We expected that the ^{137}Cs transfer models made for soils from temperate regions would not work for soils from tropical regions. This suggests that the underlying processes have counteracting effects yielding good predictions of the CR. The Absalom 2001 and Tarsitano 2011 models disregard the effect of mineralogy on ^{137}Cs transfer to plants; they effectively assume a constant RIP value per unit clay, which is reasonable for temperate regions where 2:1 phyllosilicates dominate

the clay fraction (Figure 4.1; Table IV.2). However, this assumption was unrealistic when predicting ^{137}Cs transfer from the volcanic and highly weathered tropical soils, as the RIP/%clay in such soils was considerably lower than in the temperate soils (due to the absence of 2:1 phyllosilicates), resulting in underestimating ^{137}Cs transfer (Figure 4.4). These models should be improved, given that linear models, which were fitted to the soils of this study, outperform them (Table 4.2).

Even though these semi-mechanistic models predicted the observed CRs better than expected, the uncertainty of prediction remained high for all models (RMSE >0.45 ^{10}log(kg kg^{-1}); see section 6.3.3). Previous studies on temperate undisturbed soils suggest that the bioavailability of radiocaesium may be more than a factor of 20 higher in field conditions than sieved soils in pot experiments (Fernagut and Merckx, 1997; see section 6.3.2). This underestimation of could be much greater in highly weathered tropical soils, highlighting the need for further research.

4.5. Conclusion

Even with a limited soil collection, this study highlights the potential for high soil-to-plant transfer of ^{137}Cs in highly weathered soils and the limited benefit of K fertilization as a countermeasure in such soils. Therefore, it is important to be able to predict ^{137}Cs transfer from these soils realistically to support risk assessment and remediation of contaminated sites on a global scale. Existing transfer models, such as the model of Tarsitano 2011, can predict short-term ^{137}Cs soil-to-grass transfer for soils from contrasting parent materials and weathering stages, likely due to the predominant role of exchangeable K content of the soil. Hence, for risk assessment, it appears critical to have regional-specific information on exchangeable K, and this may be problematic to obtain for tropical weathered soils, as shown recently (Albinet et al., 2022). It is also clear that global mapping of ^{137}Cs risk needs more consensus on clay isolation methods, especially for highly weathered tropical soils.

Chapter 5
The clay mineralogy rather than the clay content determines radiocaesium adsorption in soils

Abstract

In the case of nuclear incidents, radioactive caesium (^{137}Cs) contaminates soils and enters the food chain by plant uptake. After the Chornobyl and Fukushima accidents, models were developed to predict the bioavailability of ^{137}Cs in soils. The premise of these models is that ^{137}Cs sorption in soils is controlled by their clay content (0–2 µm), i.e., that ^{137}Cs sorbs mainly to minerals in the clay fraction and that the mineralogy has relatively small effects. This study tested this premise with 24 soil samples collected globally. The ^{137}Cs adsorption was measured as the Radiocaesium Interception Potential (RIP), for all bulk soil samples and in their corresponding clay (0–2 µm) and silt (2–50 µm) fractions, along with XRD-based analysis mineralogy of the fractions. The RIP in soil varied by factor 438 among soils and was *unrelated* to its clay content (p >0.05). The RIP in the clay fraction was lowest for young volcanic soils (370 mmol kg^{-1} clay) with allophane and mica and for highly weathered tropical soils dominated by kaolinite (100 mmol kg^{-1} clay). In contrast, the RIP of the clay fraction was almost two orders of magnitude higher for intermediate-weathered temperate soils dominated by illite (19 000 mmol kg^{-1} clay). The RIP of the soil was significantly related to the illite content of the soil (R^2 = 0.50, p <0.001). The comparison of the RIP in intact soil samples with corresponding values on its fractions showed that, on average among all soils, 76% of the RIP originated in the clay fraction. However, for three soils, over 50% and up to 67% of the soil RIP was in the silt fraction for soils with high silt content. Most strikingly, the soil RIP was overestimated by a factor 2 by the sum of RIPs in the clay and silt fractions, showing that isolation of clay by dispersion releases K from the interlayers and opens selective ^{137}Cs sorption sites not accessible in intact soil samples in the short term. It is concluded that soil mineralogy has a paramount effect on the RIP of soils and that the clay fraction of soils is only a proxy for the RIP. The validity of existing ^{137}Cs bioavailability models require recalibration for its use on a global scale.

5.1. Introduction

Global interest in nuclear energy requires environmental impact analyses that rely on models predicting the transfer of radiocaesium from soil to plants. There are concerns about radiocaesium (^{137}Cs) due to the long half-life (30 years) and biochemical similarity to potassium (K), a major plant nutrient, which allows it to transfer from soil into the food chain. Following nuclear incidents, such as Chornobyl and Fukushima, models were developed to predict ^{137}Cs soil-to-plant transfer in affected regions (Absalom et al., 2001, 1999; Tarsitano et al., 2011; Uematsu et al., 2016). These models account for ^{137}Cs adsorption in soil and the effects of competing ions, mainly K, that control its absorption and translocation to the edible fraction of the crop. Radiocaesium, in trace concentrations, is selectively adsorbed into wedge-shaped edges of micaceous clay minerals in soils formed by weathering (Fanning et al., 1989; Sawhney, 1972), called frayed edge sites (FES). The radiocaesium interception potential (RIP), reflecting selectivity for $^{137}Cs^{+}$ and the capacity of adsorption sites, can be easily quantified by laboratory tests (Cremers et al., 1988; Wauters et al., 1996c). The RIP in soil depends on both the content of FES-bearing clay minerals and the amount of FES within these minerals, which varies with clay mineral type and weathering stage (Maes et al., 1999b, 1999a). Thus, the bioavailability of ^{137}Cs in soils is influenced by soil mineralogy, which depends on the parent material and the weathering stage.

However, the above-mentioned soil-to-plant transfer models typically assume a uniform mineral composition, which does not accurately reflect the diversity in soil mineralogy on a global scale. These models assume that the RIP in the soil is related to the clay content, and the RIP in the soil is derived by multiplying soil clay content, i.e., 0–2 µm fraction, with the RIP of the clay fraction in soil (RIP_{clay}). In so doing, the models implicitly assume that (1) clay minerals with FES, commonly found in the clay fraction, are absent in other soil texture fractions, such as silt or sand, and (2) variations in the mineral composition of the clay fraction itself do not significantly affect the overall RIP of the soil. Despite these simplifications, these models have shown a high predictive power, even across soils from contrasting locations, weathering stages, and soil mineralogy (Chapter 4). However, a proper fit of the ^{137}Cs bioavailability data does not imply that the model assumptions are valid because compensating mechanisms, e.g., incorrect estimates of available K, occur, as recently discussed (Chapter 4). In a recent study where different

clay minerals were mixed with sand (artificial soils), it was shown that the RIP and ^{137}Cs transfer to grass varied over two orders of magnitude at equal clay content (Chapter 3). A follow-up study with natural soil samples collected globally showed that the soil RIP divided by its clay content (RIP/clay) varied three orders of magnitude (Chapter 4). Lowest RIP/clay ratios were found in soils dominated by young clays, such as allophane and mica (740 mmol kg^{-1} clay), and in soils with highly weathered clays, such as kaolinite (320 mmol kg^{-1} clay). The largest ratios were found in soils of temperate regions in which illite dominates (26,000 mmol kg^{-1} clay). In that study, the RIP and soil mineralogy were determined only on the bulk soils, but the mineralogy and RIP of the clay and silt fractions were not determined.

This study aims to verify or falsify the main premise of radiocaesium soil-to-plant transfer models, i.e., that soil RIP is primarily controlled by its clay content and that the RIP of the clay fraction is fairly constant. Specifically, we measured RIPs in soils and in their corresponding isolated texture fraction (0–2 µm and 2–50 µm) and measured mineralogy by X-ray diffraction (XRD) in both fractions. We selected soils of two weathering sequences from Kenya (N = 8), the Philippines (N = 6), and soils of various parent materials and weathering stages sampled around the world (N = 10). The 0–2 µm and 2–50 µm fractions were isolated using ultrasonic disaggregation and Na^+-resin without removing any cementing soil constituents such as organic matter or iron minerals, reflecting their condition in the intact soil.

5.2. Materials and methods

5.2.1. Soil collection

Soil sequences sampled in Kenya (*N* = 8) and the Philippines (*N* = 6) represented soils at various weathering stages. In addition, soils were sampled at multiple locations worldwide (*N* = 10), representing soils from various parent materials. The geology of the parent materials was derived from a global map (onegeology.org). Soils from Japan (Miyakonojo) were derived from volcanic rocks from non-alkali pyroclastic flows and (Ogata; Yoshiki) from sedimentary rocks of the Late Pleistocene-Holocene. Soils from the Philippines were derived from felsic volcanic rocks of the Quaternary period. Soil from Spain (Isla Mayor) was derived from alluvial deposits of the Holocene epoch. Soils from Austria (Gross Enzersdorf) and United States (Sidney) were derived from Cenozoic sedimentary rocks, and in Italy (Aliminusa) this deposit was turbidite. Soils from Kenya (Mount Elgon) were derived from Cenozoic volcanic rocks and (Endebess; Kitale) from Neoproterozoic metamorphic rocks, including andesite and dacite. Soil from China (Changchun) was derived from Paleozoic felsic plutonic rocks. Soil from Madagascar (Behenjy) was derived from Neoarchean plutonic and metamorphic rocks. The intact soil samples, noted as bulk soils, were characterized in a previous ^{137}Cs pot experiment with grass (Chapter 4), except for two soils from Kenya (Mount Elgon 3 and Kitale 3), which were characterized following the same procedures.

5.2.2. Clay and silt isolation from soil

The texture fractions were isolated from soils by mechanical disaggregation and dispersion using a sodium cation resin (Na^+-resin) (Rouiller et al., 1972). This method was preferred over the widely used standardized pipet method with removal or organic matter or other cementing materials (ISO11277, 1998) as it is assumed to be a less biased method and appropriate for andic (Delvaux et al., 1989) and ferralitic (Bartoli et al., 1991) soils.

Air-dried bulk soils were milled and sieved (2 mm). Air-dried bulk soil weights were corrected for moisture (60 °C). Deionized water (solid : liquid of 1 g soil : 20 mL water) was added to the soils and shaken end-over-end (16 h). Sand fractions were separated by wet sieving (50 µm, certified DIN ISO 3310-1, VWR®) and were repeatedly ultrasonically treated (15 min at 90 J min^{-1}, Misonix Sonicator® XL2020) until the sand grains were clear. The <50 µm fractions were flocculated by adding drops of saturated $CaCl_2$ so that the

excess water could be removed by siphoning. The Na^+-resin (>500 µm, Amberlite® IR-120 (H), Supelco®) was added to <50 µm fractions (1 g soil : 10 mL resin) and were shaken end-over-end (16 h). The resin was removed by wet sieving (500 µm superimposing 50 µm) and washed with deionized water until the filtrate was clear. The <50 µm fractions in deionized water (500 mL) in graduated cylinders were placed in a water bath (20.0 ± 0.5 °C). The <50 µm was plunged, and the 0–2 µm fraction (clay fraction hereafter) in the suspension was siphoned off 20 cm below the surface using an upward pointed tube connected to a pump after 15 h 28 min 18 sec. Plunging and siphoning were repeated (3–5 times) until the suspension was clear. The remaining 2–50 µm fraction (silt fraction hereafter) was recovered. All fractions were dried in the oven (60 °C, 48 h). Fractions were cooled to room temperature in a desiccator and weighted analytically (accuracy 0.0001 g, OHAUS Adventurer™ AR2140).

The particle size distributions were compared between the Na^+-resin method and the pipet method using reference soils from proficiency tests (Table V.1). The clay contents for three of the four soils matched very well for both methods, but for one soil (from a temperate region), the resin method identified twice as much clay as the pipet method.

5.2.3. X-ray diffraction (XRD)

The mineralogy of clay and silt fractions was analyzed by XRD. The mineralogy of bulk soils was quantified, and the soil weathering index was calculated (Equation 4.1), which was previously reported (Chapter 4, Table V.2). The clay and silt fractions were prepared as oriented slides to enhance the basal reflections (Moore and Reynolds, 1997) in air-dried Ca-form and solvated ethylene glycol form. The fractions in deionized water (5 mL) were ultrasonically disaggregated (1 min at 420 J min^{-1}, Sonics Vibra-cell™ VCX-130) and put in dialysis membrane bags (6–8 kDa, Spectra/Por®). These were immersed in 1 mol L^{-1} $CaCl_2$ solution (250 mL, 16 h). Excess electrolytes were removed by replacing the outer solution with deionized water and shaking until the conductivity of the outer solution matched that of deionized water. The fractions were recovered from the dialysis bags and dried in the oven (60 °C, 16 h).

Subsamples of clay and silt fractions were taken to make smear slides on glass plates for XRD measurement. Dried fractions were deposited on a glass plate (10 mg cm^{-2}), and two drops of deionized water were added to form a paste that was smeared until a uniform, thick film with a smooth surface was

obtained. The Ca-saturated smear slides were air-dried and measured by XRD. The smear slides were placed in a desiccator filled with ethylene glycol and in the oven (60 °C, 16 h). The smear slides solvated with ethylene glycol were measured by XRD. The XRD device (Bruker D8 Advance) in reflection geometry with Cu-K_α radiation with Ni-K_β filter had a 435 mm goniometer radius, rotating sample holder (15 rpm), divergence slit (0.25°), fixed anti-scatter slits (5.69 mm), soller slits (2.5°), detector slit (11.55 mm), a multistrip detector (Bruker Lynxeye) scanning at 40 kV and 30 mA, ranging over 2–47 °2θ with 0.015 °2θ step size and 0.5 s counting time.

Mineralogies of clay fractions were quantified, and silt fractions were identified by Sybilla software (© Chevron ETC) that used the multispecimen method by fitting the model on the XRD record in air-dried Ca-form and in ethylene glycol solvated states (Zeelmaekers, 2011). A constant function removed the background, patterns were shifted to match kaolinite mineral peaks, and the step size was increased (0.05 °2θ) to facilitate calculations, which was acceptable given the wide clay peaks. The results of quantified phases were accepted if the model fit in the ethylene glycol state matched the model in the air-dry state, and the average of quantified phases in two states was taken (Table 5.2; Table V.4).

5.2.4. Radiocaesium Interception Potential (RIP)

The RIP of clay and silt fractions was analyzed by exchanging ^{137}Cs with K-cations at selective adsorption sites and blocking non-selective sites with Ca-cations (Wauters et al. 1996b). The RIP of bulk soils were previously reported (Chapter 4, Table V.3 in this study). Subsamples of clay and silt fractions (0.2–0.4 g) were put in dialysis membrane bags (6–8 kDa, Spectra/Por®). A solution of 0.5 mmol K L^{-1} and 100 mmol Ca L^{-1} was added to membrane bags (10 mL) and in pots (150 mL). Membrane bags were immersed in the pots and shaken end-over-end (24 h). The outer K-Ca solution (150 mL) was renewed and shaken (24 h). Next, the outer solution was renewed with carrier-free 200 kBq ^{137}Cs mL^{-1} with K-Ca solution and shaken (24 h). The ^{137}Cs concentration in the initial and final outer solution was measured with a gamma counter (Perkin Elmer 1480 WIZARD 3”). The RIP was calculated by multiplying the measured ^{137}Cs solid-liquid distribution coefficient by 0.5 mmol K L^{-1} in solution.

5.2.5. Statistical analyses

JMP® Pro software (Version 17.0.0 SAS Institute Inc., Cary, NC, 1989–2024) was used. Pearson correlation coefficients were calculated with a pairwise

method on the means (n = 1 or n = 3) or log-transformed means if skewness was closer to 0 after transformation (Table V.5). Linear regression was used (p <0.05) to obtain relations describing RIP with selected explanatory variables.

5.3. Results

5.3.1. Properties of bulk soil and fractions

The grouping of the 24 soil samples by weathering stages showed that the youngest soils had the highest carbon contents (5.2 g 100 g^{-1}) and the most weathered soils had finer textures (32 g 100 g^{-1}), while soils in the intermediate stage of weathering had the highest pH and CEC (5.9 and 23 $cmol_c$ kg^{-1}) (Table 5.1).

Table 5.1. Properties of bulk soils as weathering index (WI, Equation 4.1) increased (detailed in Table V.2 and Table V.3). Soils were grouped as young (WI = 2.5–4.7), intermediate (WI = 4.7–7.0), or weathered (WI = 7.0–9.2) based on X-ray diffraction mineralogy measured on bulk soil. The number of soils per group (*N*), minimum (min), maximum (max), and geometric mean (GM) for each group are given.

soil group	*N*	weathering index			<2 µm			50–2000 µm			organic C			pH			CEC			RIP_{soil}		
					g 100 g^{-1}												$cmol_c$ kg^{-1}			mmol kg^{-1}		
		min	max	**GM**	min	max	**GM**	min	max	**GM**	min	max	**GM**	min	max	**GM**	min	max	**GM**	min	max	**GM**
young	3	2.5	4.6	**3.5**	20	31	**26**	9	38	**22**	1.8	14	**5.2**	4.1	5.9	**4.9**	5.1	24	**9.2**	120	1,000	**350**
intermediate	13	4.8	6.9	**5.6**	8	65	**33**	3	73	**19**	0.8	8.4	**1.9**	4.1	7.8	**5.9**	5.4	50	**23**	330	6,100	**2,400**
weathered	7	7.1	9.2	**8.0**	25	68	**43**	20	68	**32**	0.6	2.9	**1.7**	3.8	4.8	**4.3**	2.3	28	**11**	14	3,600	**570**

5.3.2. Mineralogy of the soil fractions

Not all mineral phases could be quantified (Figure V.3 to Figure V.26), so the mineralogy of the fractions was only indicative. The Sybilla software library only included mineral phases of illite, expanding vermiculite or smectite, kaolinite, and chlorite phyllosilicates, and mixed-layered combinations of these. Other phases, such as allophane, mica, and feldspars, could not be quantified, so mineralogies of the clay fractions were proportions of a limited selection of the aforementioned phyllosilicates (Table 5.2; Table V.4).

It was assumed that the soil sequences were derived from the same parent material, i.e., with similar mineral composition, so similar mineral phases were identified within the sequence. The sequence of soils from Kenya had enrichment of kaolinite and illite in the clay fraction with increasing weathering (Figure V.1). The youngest soil at the highest sampling point on the mountain (Mount Elgon 1) did not have clear peaks of phyllosilicates that could be distinguished from the background noise in the XRD pattern (Figure V.4). However, the right-tailed broad peak around 4.4–4.5 Å of hkl reflections indicated the presence of disordered 1:1 phyllosilicates, such as kaolinite and halloysite. Wider humps around 3.52 Å and 2.50 Å confirmed the presence of allophane, previously determined by oxalic acid extraction (3 g allophane 100 g^{-1} bulk soil, Chapter 4). In more weathered soils on the mountain slope (Figure V.18), the kaolinite peak was clear around 7.20–7.50 Å. This broad peak indicated a mixed-layer mineral phase with kaolinite. A small peak around 10.1 Å indicated illite mineral phases. In a moist valley soil (Endebess, Figure V.20), a broad peak at 15.3 Å that shifted to 16.3 Å after ethylene glycol treatment indicated swelling phyllosilicates, which was to be expected in a Vertisol (Table V.3). In the most weathered upland soils (Kitale 2 and 3, Figure V.23 and Figure V.24). the kaolinite and illite peaks were largest (Figure V.1).

The sequence of soils from the Philippines showed enrichment of kaolinite in the clay fractions with increasing weathering (Figure V.2). In the youngest soil (Pagsanjan 1, Figure V.5), a peak at 14.8 Å shifted to 16.6 Å by ethylene glycol indicating the presence of expanding phyllosilicates. In one soil (Pagsanjan 5, Figure V.22), a small peak at 11.3 Å suggested the presence of illite, but it was barely detectable in the XRD pattern after ethylene glycol treatment. The most weathered soil of the sequence (Cavinti, Figure V.26) showed the largest kaolinite peaks at 7.28 Å and 3.59 Å.

The variability in mineralogy between young and highly weathered soils was even more pronounced in the other soils that differed in parent material and

weathering stage. The youngest soil from Miyakonojo (Japan), derived from volcanic ash, contained allophane characterized by wide humps around 3.50 Å and 2.50 Å in the clay fraction (Figure V.3) and what was previously confirmed by oxalic acid extraction (11 g allophane 100 g^{-1} bulk soil, Chapter 4). But otherwise, no clear peaks of phyllosilicates could be identified in the volcanic soil. Soils in the intermediate stage of weathering, such as Rots (France) (Figure V.12) and Isla Mayor (Spain) (Figure V.15) had mainly peaks of illite at 10 Å, 5 Å, and 3.33 Å. In the same group of soils with intermediate weathering stage, expanding phyllosilicates with shifting peaks after ethylene glycol treatment were very clear in Ogata (Japan) with 15.3 Å peak shifting to 16.7 Å (Figure V.10) and in Changchun (China) with 14.3 Å peak shifting to 17.5 Å (Figure V.13). These soils with intermediate stage of weathering also contained, to a lesser extent, kaolinite with peaks at 7.1–7.2 Å. In some soils, such as Yoshiki, Japan, mica was identified in the silt fraction by peaks around 10 Å, 5 Å, and 2.55 Å (Figure V.27). The weathered soil from Behenjy (Madagascar) had peaks of kaolinite at 7.16 Å, 4.37 Å, and 3.57 Å (Figure V.25).

Table 5.2. Mineralogy of the clay fraction and RIPs of the clay and silt fractions of soils grouped with increasing weathering index (detailed in Table V.4). I = illite; S = expanding phyllosilicate; C = chlorite; K = kaolinite. Note: Mineral phases quantified are limited to illite, vermiculite, smectite, kaolinite, chlorite, and their mixed layers; other phases (e.g., allophane, mica, feldspars) were not included in the analysis.

		mineralogy clay fraction				RIP	
location	weathering index	I	S	C	K	<2 µm	2–50 µm
city, country		g 100 g^{-1}				mmol kg^{-1}	
young							
Miyakonojo, Japan	2.5	<0.5	<0.5	<0.5	<0.5	370	230
Mount Elgon, Kenya (1)	3.7	56	16	<0.5	28	1,200	1,100
Pagsanjan, Philippines (1)	4.6	<0.5	35	<0.5	65	2,100	420
intermediate							
Sidney, United States	4.8	60	33	<0.5	7	14,000	2,900
Mount Elgon, Kenya (2)	5.1	56	15	<0.5	29	3,900	2,800
Pagsanjan, Philippines (2)	5.1	<0.5	42	<0.5	58	1,200	500
Gross Enzersdorf, Austria	5.2	65	31	1	3	16,000	1,500
Ogata, Japan	5.2	1	66	<0.5	33	6,500	3,800
Mount Elgon, Kenya (3)	5.4	48	18	<0.5	34	5,300	2,100
Rots, France	5.5	68	23	<0.5	9	16,000	790
Changchun, China	5.8	57	27	<0.5	16	11,000	2,300
Pagsanjan, Philippines (3)	6.0	<0.5	31	<0.5	69	2,300	1,200
Isla Mayor, Spain	6.0	67	18	6	9	14,000	2,400
Yoshiki, Japan	6.0	34	14	<0.5	52	7,500	5,600
Kitale, Kenya (1)	6.1	31	10	<0.5	59	3,800	440
Mount Elgon, Kenya (4)	6.6	50	18	<0.5	32	7,100	4,000
Aliminusa, Italy	6.7	46	26	<0.5	28	19,000	1,500
weathered							
Endebess, Kenya	7.1	47	20	<0.5	33	5,800	720
Pagsanjan, Philippines (4)	7.5	<0.5	36	<0.5	64	4,900	2,000
Pagsanjan, Philippines (5)	7.6	13	18	<0.5	69	12,000	1,200
Kitale, Kenya (2)	7.9	36	10	<0.5	54	6,700	3,700
Kitale, Kenya (3)	7.9	23	6	<0.5	71	4,900	3,000
Behenjy, Madagascar	9.0	<0.5	<0.5	53	47	100	68
Cavinti, Philippines	9.2	<0.5	12	<0.5	88	1,400	34

5.3.3. ^{137}Cs adsorption in bulk soil and fractions

The RIP of bulk soils was lowest in the youngest (350 mmol kg^{-1}) and most weathered soils (570 mmol kg^{-1}). Soil RIP was not correlated to the texture, organic C, or CEC (Table V.5) but was positively correlated with pH (r = 0.66, p <0.001), possibly because pH acts as a proxy for other factors influencing RIP, as pH has no direct effect on ^{137}Cs sorption in soils (Wauters et al., 1994). Lower pH often characterizes highly weathered soils with fewer FES-bearing clay minerals. Notably, RIP measured in bulk soils was *not* explained by the clay content (p >0.05) (Figure 5.1).

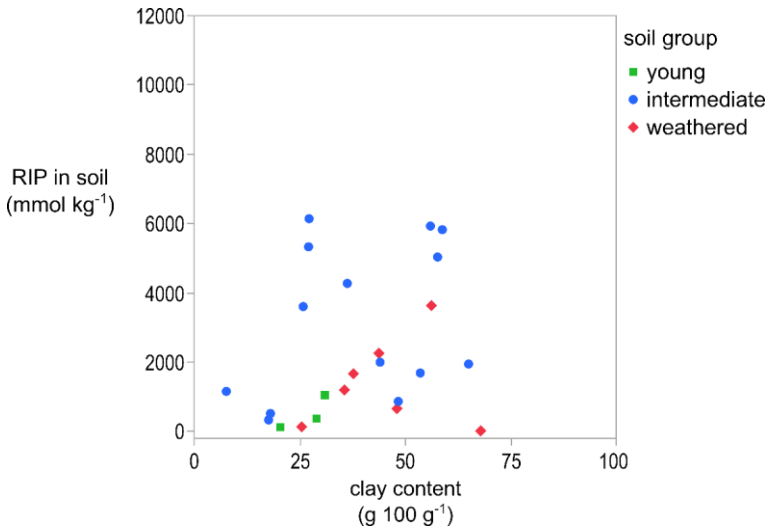

Figure 5.1. The RIP in bulk soil is not linearly related to its clay content of the soil (p >0.05).

The RIP was larger in the clay than in the silt fraction for all soils (Table 5.2). The RIP in the clay fraction varied with soil weathering stages (Figure 5.2). The youngest soils had a RIP corresponding to that measured in mica (300–740 mmol kg^{-1}; De Preter, 1990; Eguchi et al., 2015). Intermediate-weathered soils had a highly variable RIP, and soils dominated by illite had a RIP similar to that measured in pure illite (12,600–16,000 mmol kg^{-1}; de Koning et al., 2007; Wauters et al., 1994). Weathered soils had a low RIP when illite was absent, corresponding to the RIP measured in kaolinite (6–310 mmol kg^{-1}; Nakao et al., 2008; Ogasawara et al., 2013).

The RIP in the clay fraction can be explained by its mineralogy and, overall, the RIP in the clay fraction was positively correlated with its illite content (R^2 = 0.43, p <0.001, Figure 5.3). Young soils had a low RIP (<3,000 mmol kg^{-1}) in

the clay fraction with low illite content (<0.5 g 100 g^{-1}), except for a soil from Mount Elgon (Kenya 1, illite >50 g 100 g^{-1}), but the illite content was likely overestimated by XRD quantification by not taking into account other mineral phases, such as quartz, hematite, and allophane. Intermediate-weathered soils, dominated by illite (>30 g 100 g^{-1}), had the highest RIP (up to 19,000 mmol kg^{-1}). Except for Mount Elgon (Kenya 2), which, despite its high illite content (>50 g 100 g^{-1}), had a low RIP for reasons explained above. Other intermediate-weathered soils, dominated by expanding phyllosilicates (i.e., high-charge smectite and regular smectite >30 g 100 g^{-1}), had lower RIPs (<10,000 mmol kg^{-1}). More weathered soils, dominated by kaolinite (up to 88 g 100 g^{-1}), had low RIP (<10,000 mmol kg^{-1}). However, a weathered soil from the Philippines sequence (Pagsanjan 5) with over factor 5 higher RIP (12,000 mmol kg^{-1}) compared with other soils from that sequence (geometric mean (GM) = 2100 mmol kg^{-1}, N = 5) had illite (13 g 100 g^{-1}) while it was not detectable in other soils. The lowest RIP (100 mmol kg^{-1}) in the clay fraction was measured in a highly weathered soil from Behenjy (Madagascar) in which illite or expanding phyllosilicates were not detectable (<0.5 g 100 g^{-1}).

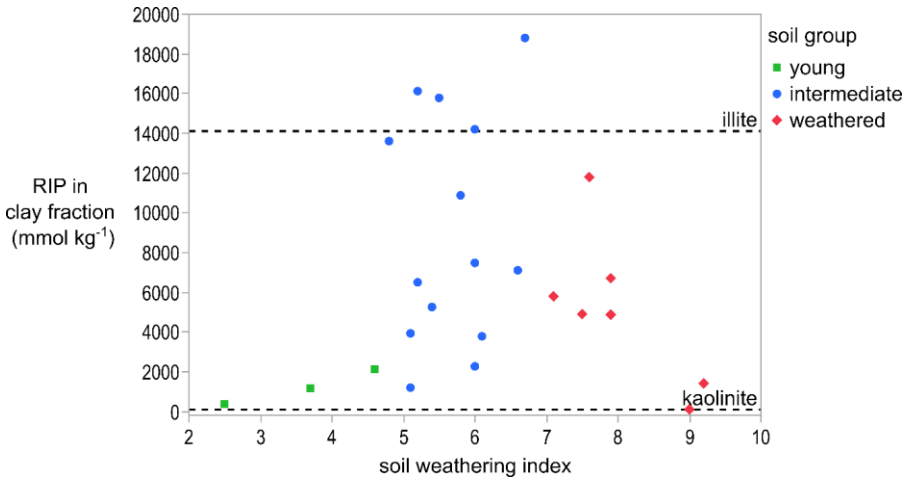

Figure 5.2. RIPs in the clay fractions of soils as a function of soil weathering. The dashed lines are RIP of illite (GM = 14,100 mmol kg^{-1}; de Koning et al., 2007; Wauters et al., 1994) and kaolinite (GM = 77 mmol kg^{-1}; Nakao et al., 2008; Ogasawara et al., 2013). The data suggest an upward trend between young and intermediate weathering followed by a decrease in highly weathered soils.

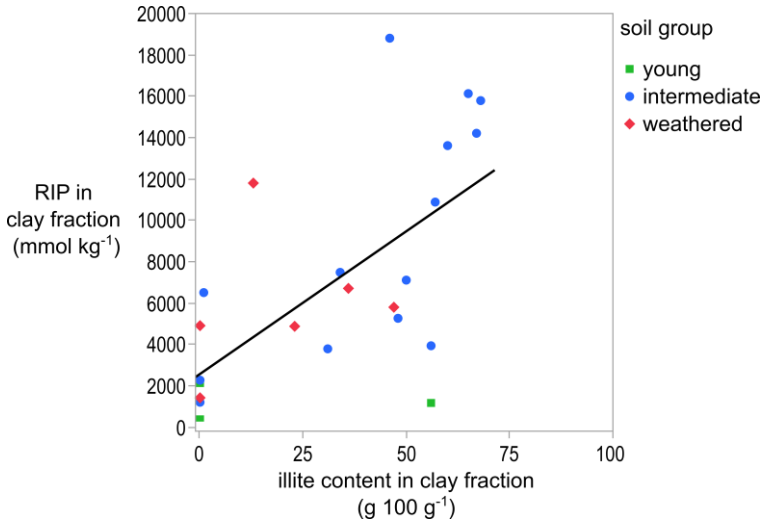

Figure 5.3. The RIP in the clay fraction increases with increasing illite content in the clay fraction (R^2 = 0.43, p <0.001). The solid line is the regression line.

As stated before, the bulk soil RIP is *unrelated* to the clay content in the soil (Figure 5.1) and the clay fraction RIP is related to the illite content in the clay fraction (Figure 5.3). Altogether, the bulk soil RIP is significantly related to the illite content in soil, i.e., the fraction illite in the clay fraction multiplied with the clay content (R^2 = 0.50, p <0.001). Note that the illite content might be overestimated in some soils, as not all mineral phases in the clay fraction could be fully quantified.

For three soils, however, over 50% and up to 67% of the soil RIP was found in the silt fraction. The XRD detected weathered mica and other phyllosilicates in the silt fraction but these were not quantified (Figure V.27). The fraction of theoretical RIPs located in the silt fractions rises with the silt content, i.e., mass fraction of 2–50 µm soil particles (R^2 = 0.18, p <0.05; Figure 5.4).

The RIP in the bulk soil was calculated from the RIP measured in the clay and the silt fractions, weighted by their respective mass fractions. This theoretical, i.e., calculated, RIP was then compared to the independently measured RIP in the bulk soil (R^2 = 0.69, p <0.001, Figure 5.5). However, this theoretical RIP overestimated the measured RIP by a factor of 2.0 on average and up to 9.1 for the soil from Pagsanjan (Philippines 5), suggesting that soil fractionation opens FES not accessible in the bulk soil (see discussion). The fraction of the theoretical RIP found in the clay fraction was logically high, averaging 76%.

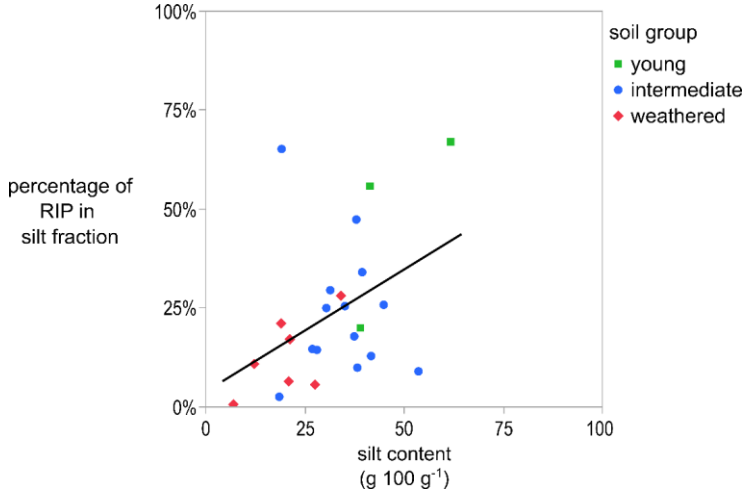

Figure 5.4. The percentage of soil RIP present in the silt fraction increases with increasing silt content of the soil (R^2 = 0.18, p <0.05). The solid line is the regression line.

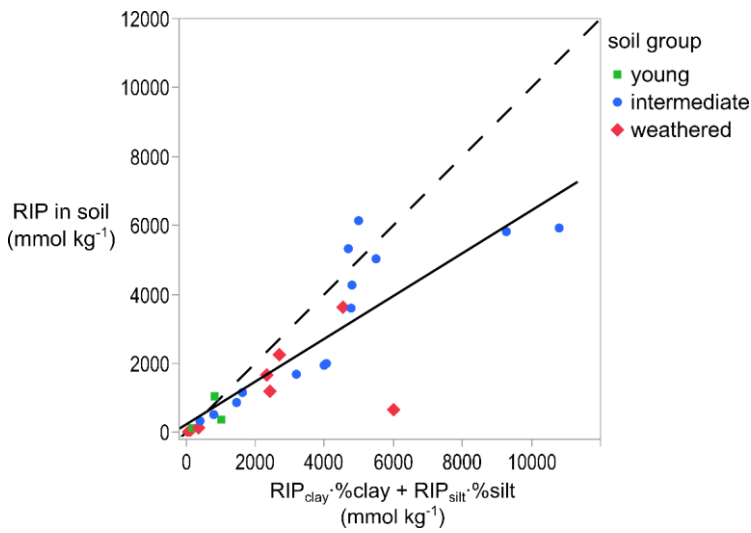

Figure 5.5. Comparison of RIPs measured in bulk soils with the theoretical RIP calculated from the RIP in the clay and silt fractions multiplied with their corresponding mass fractions in soil (R^2 = 0.69, p <0.001). The solid line is the regression line and the dashed line is the 1:1 line, illustrating, on average, a lower RIP based in the bulk soil than in the size fractions from that soil.

5.4. Discussion

The Absalom model (Absalom et al., 2001; Tarsitano et al., 2011), which predicts radiocaesium bioavailability and is used for impact assessments (i.e., Brown et al., 2020), relies on the assumption that ^{137}Cs sorption in soils is controlled by their clay content (0–2 µm). This implies that ^{137}Cs sorbs mainly to minerals in the clay fraction and that the mineralogy has relatively small effects. This assumption may be acceptable in regions with similar mineralogy, but on a global scale, this premise is incorrect, as shown unequivocally in this study. First of all, the clay content does not control the RIP in bulk soil (Figure 5.1) and, secondly, the mineralogy of that fraction has large effects on the RIP (Figure 5.3). This study confirms (Chapter 4) that ^{137}Cs sorption in the soil is influenced by the mineralogy, which is determined by the parent material and the weathering stage. Soils with intermediate weathering stages, where illite dominates, show the highest RIP (>10,000 mmol kg^{-1}) in the clay fraction due to selective adsorption sites characteristic of illite. In contrast, the lowest RIP (<500 mmol kg^{-1}) is observed in the clay fraction of young soils, where selective adsorption sites in mica have not yet formed, and in highly weathered soils, where phyllosilicates with selective adsorption sites have disappeared (Figure 5.2; Table 5.2). Soils dominated by illite show the highest RIP in the clay fraction, as illite contributes mainly to the RIP (Figure 5.3). Compared to illite, other phyllosilicates, such as expanding phyllosilicates and kaolinite, contribute minimally to the RIP.

On average, 24% of the RIP in soils is found in the silt fraction. However, the contribution of the silt fraction to the total RIP increases as the silt content of the soil increases, suggesting that the silt fraction plays a notable role in ^{137}Cs retention in soils with higher silt content. The XRD patterns in this study show phyllosilicates are mainly present in the clay fraction. However, weathered mica and kaolinite peaks are also observed in the silt fraction, questioning the reliability of the clay cut-off for phyllosilicates. A previous study on Japanese soils (Uematsu et al., 2015) found that RIP in the clay fraction, multiplied by the clay content (RIP_{clay} %clay), underestimated the RIP in the bulk soil samples (RIP_{soil}) by a factor 2 (up to factor 5). This discrepancy was most notable in soils with lower clay content, such as Cambisols and Gleysols, and was attributed to ^{137}Cs-sorbing minerals in larger soil fractions. Alternatively, not all clay particles were recovered from the soils given that a subsample was taken of the clay fraction with a pipet (20 mL subsample of 500 mL clay+silt suspension). Another study on Japanese soils (Nakao et al., 2015), in which

the clay fraction was isolated by siphoning (the entire suspension), found that RIP_{clay} %clay did not match RIP_{soil}. For soils where RIP_{clay} %clay underestimated RIP_{soil}, it was suggested that mica in larger fractions, derived from aeolian deposits from Chinese deserts, is a major contributor to the RIP. Conversely, for soils where the RIP_{clay} %clay overestimated RIP_{soil}, it was suggested that selective adsorption sites in the isolated clay fraction were made accessible or reactive, which would not be exposed in the bulk soil due to interactions with organic matter.

This study examined the clay and silt fractions to quantify mineralogy and ^{137}Cs adsorption. The Na^{+}-resin may have attracted K from the clay mineral interlayers causing more FES to form. In addition, we mechanically broke up soil aggregates to release phyllosilicate particles and did not chemically remove organic matter or other soil cementing materials to represent soil conditions. The sum of the ^{137}Cs adsorption in both fractions overestimates RIP_{soil} by a factor of 2.0, likely related to creating and opening up FES not accessible in bulk soils, even when relying on the more gentle resin method for soil fractionation. This non-additivity of reactions in both fractions shows the limitation of soil fractionation to study the soil chemical reactions in the bulk soils. In parallel, non-additive behavior has also been observed for other heavy metals adsorbing to soil components like metal oxides and organic matter due to interactions between organic matter and oxide on the metal cation adsorption (Christl and Kretzschmar, 2001; Vermeer et al., 1999).

In the long term, the accessibility of radiocaesium to selective adsorption sites in soil aggregates and its migration into deeper mineral structures may contribute to the effect of aging, with the radiocaesium solid-liquid distribution (and RIP) in soil increasing over time. Such suggests, but does not prove, that the theoretical RIP observed after soil fractionation may still be the correct one in the long term. Previous research concluded that adsorption increases in expanding phyllosilicates such as montmorillonite (Maes et al., 1985; Degryse et al., 2004), biotite (Chapter 3), and in soils containing these phyllosilicates (Roig et al., 2007; Uematsu, 2017) after inducing collapses of mineral open edges on which radiocaesium is selectively adsorbed (McKinley et al., 2004). In addition, radiocaesium would migrate into deeper mineral structures over time, as observed in illite (Fuller et al., 2015) common in European soils and in weathered biotite (Mukai et al., 2016) common in Fukushima soils. Soil aggregates and soil structure may also contribute to the increasing adsorption

of radiocaesium over time, highlighting the need to understand the fate of radiocaesium in soils under field conditions over longer time frames.

This study falsified the assumptions of the Absalom model and its variants to predict the adsorption of radiocaesium in soils, they are clearly not valid on a global scale. However, it was shown that these models could still predict the *bioavailability* of radiocaesium with reasonable accuracy even in soils not initially included in the calibration of these models, e.g., in highly weathered soils, due to counteracting effects. That is because, on the one hand, they overestimate RIPs in weathered soils, but on the other hand, they underestimate K availability in the same soils (Chapter 4). Hence, despite incorrect assumptions, these models are still useful after recalibration using site-specific soil properties when available, until new and better models are developed. These new models may be based on soil mineralogy, but it is already clear from soil maps that information on soil mineralogy is not available globally; hence, proxies for this will be needed for implementing better models in global soil information systems.

5.5. Conclusion

This study reveals that ^{137}Cs sorption in soils is not controlled by the clay content (0–2 µm) but rather by the mineralogy, which is influenced by parent material and weathering stages. Among phyllosilicates, illite contributes most to the ^{137}Cs sorption occurring mainly in the smallest (<2 µm) soil fractions. However, this was not true for soils with weathered mica in the larger (2–50 µm) soil fractions. The ^{137}Cs sorption in soil fractions overestimated that in bulk soil by a factor of 2, probably due to the breaking up of soil structure and aggregates, thus artificially increasing the accessibility of adsorption sites for radiocaesium in the short term. This calls for caution when extrapolating the fate of radiocaesium in isolated fractions from laboratory studies to structured soils under field conditions.

Chapter 6
Advancing global radiocaesium soil-to-plant transfer predictions: Feasibility, modeling, mapping, and future challenges

This research aimed to explore and understand the soil properties affecting radiocaesium bioavailability on a global scale. The impetus for this research was a lack of data and knowledge on radiocaesium sorption in soils with properties beyond the ones that were most studied before in the areas affected by the Chornobyl and Fukushima nuclear accidents. The central hypothesis was that radiocaesium sorption is affected by the clay mineralogy in soils, and that information on clay mineralogy can be linked with other globally available soil information to make predictions at a global scale.

The first objective was to identify gaps in the radiocaesium soil-to-plant transfer databases compiled after nuclear accidents. Our approach started by collecting existing information on radiocaesium soil-plant concentration ratios (CR) from the literature, creating a comprehensive and harmonized database with 8,837 entries. That database revealed the extreme variability in CRs, the CR ranged over seven orders of magnitude. A key outcome of that database was the lack of data from tropical and arid climates (Chapter 2).

The next objective was to explore the feasibility of developing global radiocaesium transfer models. A subset of the database was used to create global-scale models for a radiocaesium transfer map (Chapter 2). However, the map was not reliable because of limited data coverage, especially in tropical and arid regions, missing data on soil K content and mineralogy, and no validation with CR observations.

To deepen understanding of radiocaesium bioavailability in diverse soils, including those outside Europe, pot experiments were conducted in clay-sand mixtures and natural soils. These experiments confirmed that clay mineralogy is key in affecting the CR. The highest transfer was observed in soils without illite-type clay minerals, such as volcanic, sandy, peat and highly weathered soils, while the lowest transfer occurred in soils rich in illite-type clay minerals (Chapters 3 and 4).

An additional objective was to evaluate the applicability of existing semi-mechanistic models, like the Absalom model and its variants, which were originally calibrated to temperate soils. Rather unexpectedly, these models could predict the CRs even for soil types that fall outside their calibration

range, such as highly weathered tropical soils (Chapters 3 and 4). This was attributed to a dominant effect of the exchangeable K content of the soil on the CR. Despite this, it is recommended adjusting these models because their underlying assumptions do not allow the models to represent radiocaesium adsorption in diverse soils on a global scale (Chapter 5).

Overall, this research has demonstrated that clay mineralogy in soils is an important factor explaining radiocaesium bioavailability in soils covering the spectrum of all weathering stages (Chapters 3, 4, and 5). A recurrent observation is that the RIP of the soil exhibits a bell-shaped pattern to the soil weathering stages, being lowest at low or high weathering stages and peaking at intermittent weathering stages where weathered micas dominate the clay mineralogy (Figure 6.1). The reverse trend is logically found for the CR (Figure 6.1).

The final objective is to investigate how these models can be adjusted to predict radiocaesium transfer in contrasting soils. In this concluding chapter, we apply the insights from this research to incorporate soil mineralogy into the radiocaesium soil-to-plant transfer models, thereby enhancing their applicability on a global scale. In cases where soil mineralogy data are unavailable, we will try identifying effective proxies in global soil maps. We also extend the discussion on limitations of the available data in global soil maps, such as the soil available K and mineralogy, and how these limitations affect the creation of reliable radiocaesium transfer models and risk maps. These limitations and our suggestions provide a foundation for future research.

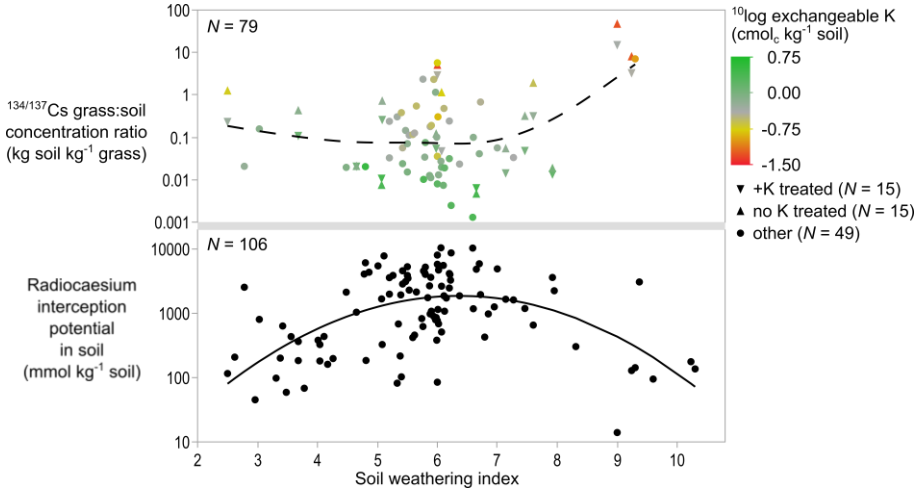

Figure 6.1. The soil weathering stage affecting (top) CRs from (*N* = 53) Chapter 4 was supplemented by data from (*N* = 7) Uematsu et al. (2018) and (*N* = 19) Gilis and Sweeck (2019); and (bottom) soil RIPs from (*N* = 38) Chapter 4 was supplemented by data from (*N* = 10) Uematsu et al. (2018), (*N* = 19) Gilis and Sweeck (2019), and (*N* = 39) Steegmans et al. (2023). The dashed line is cubic spline regression curves (λ = 2.5, standardized; R^2 = 0.29, sum of squares error = 49). The solid line is a quadratic curve fitted on the data ($\log_{10}(\mathrm{RIP}) = 3.3 - 0.091 \cdot (\mathrm{WI} - 6.4)^2$, R^2 = 0.33, RMSE = 0.52). Points on the graph are arithmetic mean values (*n* = 3) and are colored depending on exchangeable K content in soils (log scale).

6.1. Feasibility of predicting radiocaesium adsorption in soils on a global scale

The equation for radiocaesium adsorption in soil predicted in the Absalom models (Absalom et al., 2001; Tarsitano et al., 2011) must be adjusted to be applied globally. A straightforward approach would be to *measure* radiocaesium adsorption in soil (i.e., RIP), as proposed in Fukushima, Japan (Uematsu, 2017), and use these measurements as input variables for the model. However, this involves adding radiocaesium to soil samples, which is costly, requires permits, and generates radioactive waste. These measurements would only be relevant for radiocaesium research, while information on soil mineralogy could be used instead.

This work aims to improve the Absalom model's predictions of radiocaesium adsorption in contrasting soils. We work here in two steps (Table 6.1). The first step is to validate the application of the RIP theory, originally developed for soils from temperate climates, to a wider range of soils. The semi-mechanistic models (Absalom et al., 2001; Tarsitano et al., 2011) are based on the principle that the CR is explained by radiocaesium and K concentrations in soil solution, which reflects the bioavailable radiocaesium (Absalom et al., 1999; Smolders et al., 1997). In turn, the radiocaesium concentration in the soil solution is derived from the radiocaesium solid-liquid distribution and RIP theory, which has been established for soils from regions affected by the Chornobyl (Cremers et al., 1988; Wauters et al., 1996a) and Fukushima (Uematsu, 2017) accidents. In the first step, we will therefore test to what extent soil solution radiocaesium concentrations can be predicted with the RIP theory for soils collected globally.

The second step was to refine the Absalom model's predictions of RIPs. The Absalom RIP model is based solely on the soil clay and organic matter contents. The Absalom RIP model using default variables and structure was compared with RIPs based on additional soil properties, including soil mineralogy. In anticipation of global soil mineralogy maps, the model was compared to RIPs based on soil classification as a substitute for soil mineralogy, which is available in global soil maps.

In this concluding section, data from the previous chapters are collated and complemented with data from literature and additional experiments to investigate how incorporating soil mineralogy and proxies improves model predictions of radiocaesium adsorption in contrasting soils.

6.1.1. Materials and methods

Data of soil solution radiocaesium concentrations and of RIPs were collated from this research (Chapter 4) and complemented with data from Gilis and Sweeck (2019); Sanchez et al. (1999); Smolders et al. (1997); Uematsu et al. (2015); Uematsu et al. (2018); Vandebroek et al. (2012) and a soil sequence dataset from Steegmans et al. (2023) created for this project (Table 6.1). Soil data from Gilis and Sweeck (2019); Steegmans et al. (2023); and Uematsu et al. (2018) on soil mineralogy, soil clay content, soil organic carbon, and cation exchange capacity were obtained using the previously described methods (Chapter 4) and are listed in Supplementary Information (Table VI.1; Table VI.2; Table VI.3). Statistical analyses, non-linear curve fittings, and multiple regression analysis were performed using JMP® Pro software (Version 17.0.0 SAS Institute Inc., Cary, NC, 1989–2024).

Table 6.1. Soil variables and the number of observations (*N*) that were used in each step.

Soil variables	*Reference*	*Soil origin*	*N*
step 1: predict radiocaesium in soil solution with the RIP theory			
$^{134 \text{ or } 137}Cs$, K, and NH_4 in soil solution; exchangeable K; **RIP**	Chapter 4	Worldwide	53
	Smolders et al. (1997)	Belgium	30
	Uematsu et al. (2018)	Japan	22
step 2: predict RIP			
RIP; **soil classification**; clay content; soil organic carbon; soil pH	Chapter 4	Worldwide	38
	Smolders et al. (1997)	Belgium	30
	Sanchez et al. (1999)	United Kingdom	23
	Vandebroek et al. (2012)	Worldwide	87
	Uematsu et al. (2015)	Japan	25
	Uematsu et al. (2018)	Japan	22
	Gilis and Sweeck (2019)	Belgium	6
		Norway	2
		Spain	6
		United Kingdom	6
	Steegmans et al. (2023)[a]	Chile[a]	5[a]
		France[a]	7[a]
		Guatemala[a]	11[a]
		Kenya[a]	2[a]
		Spain[a]	6[a]
		Vietnam[a]	8[a]
RIP; **soil mineralogy**; soil organic carbon; soil pH; cation exchange capacity	Chapter 4	Worldwide	38
	Uematsu et al. (2018)	Japan	10
	Gilis and Sweeck (2019)	Belgium	6
		Norway	2
		Spain	5
		United Kingdom	6
	Steegmans et al. (2023)[a]	Chile[a]	5[a]
		France[a]	7[a]
		Guatemala[a]	11[a]
		Kenya[a]	2[a]
		Spain[a]	6[a]
		Vietnam[a]	8[a]

[a] soil sequences

6.1.2. Results and discussion

In the first step, the soil solution radiocaesium concentration was predicted from the radiocaesium solid-liquid distribution ratio K_D (IAEA, 2009) and a dynamic factor to account for aging of radiocaesium in soil (Equation I.2):

$$^{134\text{ or }137}\mathrm{Cs}_{\text{soil solution}} = \frac{^{134\text{ or }137}\mathrm{Cs}_{\text{soil}}}{^{134\text{ or }137}\mathrm{Cs}\mathrm{K_D}^{total}} \cdot \text{dynamic factor}$$

$$= \frac{^{134\text{ or }137}\mathrm{Cs}_{\text{soil}}}{^{134\text{ or }137}\mathrm{Cs}\mathrm{K_D}^{FES} + {}^{134\text{ or }137}\mathrm{Cs}\mathrm{K_D}^{RES}} \cdot \text{dynamic factor}$$

$$^{134\text{ or }137}\mathrm{Cs}_{\text{soil solution}} = \frac{^{134\text{ or }137}\mathrm{Cs}_{\text{soil}}}{\frac{\mathrm{RIP}}{\mathrm{K}_{\text{soil solution}} + 5.3 \cdot \mathrm{NH}_{4\text{soil solution}}} + \frac{\text{exchangeable K} \cdot 10}{\mathrm{K}_{\text{soil solution}} + \mathrm{NH}_{4\text{soil solution}}}} \cdot (0.814 \cdot \mathrm{e}^{-0.0019 \cdot \text{contact time}} + (1 - 0.814) \cdot \mathrm{e}^{-0.00019 \cdot \text{contact time}}) \quad (6.1)$$

where $^{134\text{ or }137}\mathrm{Cs}_{\text{soil solution}}$ is the ^{134}Cs or ^{137}Cs in soil solution (kBq L^{-1}), $^{134\text{ or }137}\mathrm{Cs}_{\text{soil}}$ is the total ^{134}Cs or ^{137}Cs in soil (kBq kg^{-1}), RIP is the radiocaesium interception potential in soil (mmol kg^{-1}), $K_{\text{soil solution}}$ is the K concentration in soil solution (mmol L^{-1}), 5.3 is the NH_4-to-K trace selectivity coefficient, $NH_{4\text{ soil solution}}$ is the NH_4 concentration in soil solution (mmol L^{-1}), exchangeable K is the exchangeable K content in soil ($cmol_c$ kg^{-1}), and contact time is the soil-radiocaesium contact time during incubation (days).

The soil solution radiocaesium concentration was explained for 89% by Equation 6.1 (Figure 6.2). This implies that RIP theory explains the fate of radiocaesium in soils of contrasting mineralogies, including volcanic soils sampled in temperate climates and highly weathered soils sampled in tropical climates. However, the slope is 0.78 instead of 1, i.e., the radiocaesium concentration in soil solution is overestimated with no difference in that overestimation among soils from contrasting climates. This is not explained and is puzzling.

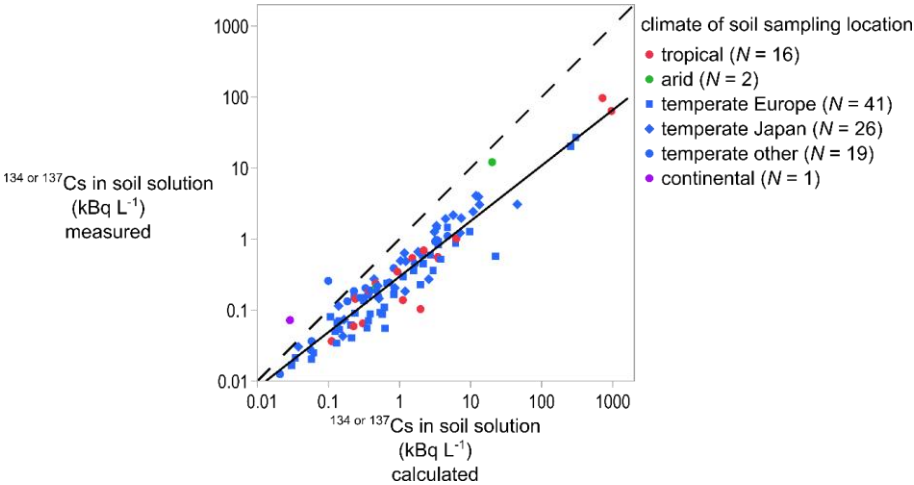

Figure 6.2. ^{134}Cs or ^{137}Cs in soil solution that is available to plants that is measured in agreement with the calculation based on RIP theory (Equation 6.1) and corrected for aging (R^2 = 0.89, p <0.001, RMSE = 0.24, N = 105). The solid line is the regression line and the dashed line is the 1:1 line.

In the second step, the soil RIP was predicted from the Absalom 2001 model (Equations I.16-I.17 from Absalom et al., 2001) and its variants Absalom 2011 (Equations I.27-I.28 from Tarsitano et al., 2011) and Tarsitano 2011 (Equations I.34-I.35 from Tarsitano et al., 2011):

$$\mathrm{RIP} = \mathrm{clay} \cdot 10^{a_9 - a_8 \cdot \frac{\mathrm{SOM}}{\mathrm{clay}}} \tag{6.2}$$

where RIP is the radiocaesium interception potential in soil (mol kg^{-1}), clay is the soil clay content (g 100 g^{-1}), SOM is the soil organic matter content (g 100 g^{-1}), a_9 is a constant value of 1.74 ± 0.17 for Absalom 2001 or 1.55 ± 0.07 for Absalom 2011 or 1.65 ± 0.06 for Tarsitano 2011 (^{10}log(mol kg^{-1})), and a_8 is a constant value of 0.043 ± 0.017 for Absalom 2001 or 0.027 ± 0.004 for Absalom 2011 or 0.077 ± 0.013 for Tarsitano 2011 (^{10}log(mol kg^{-1})) (Table I.4).

In this model, the first term *clay* states that the RIP is proportional to the content of clay in the soil. The second term represents the RIP in the clay fraction equal to a constant value, assuming that the clay minerals in the fraction have a fixed amount of FES, and a correction for organic-rich soils that have less clay minerals with FES. In Chapter 5, both assumptions were rejected for soils of contrasting parent material and stage of weathering.

A multivariate model was created to predict soil RIP based on soil properties including mineralogy determined for 106 soil samples (Table 6.1). Various combinations of variables were tested (data not shown), and the weathering index calculated from bulk mineralogy, combined with a quadratic function (cf. Figure 6.1), added value to the model. However, applying the weathering index to bulk soil derived from various parent materials rather than minerals from the clay fraction, as originally intended, may misrepresent true weathering stages for some soils.

The ^{10}log-transformed soil RIP was best predicted by a multivariate model with the soil weathering index, mica, 2:1, 1:1 and 2:1:1 clay mineral contents in soil, soil organic carbon, soil pH, and cation exchange capacity (R^2 = 0.67, p <0.001, RMSE = 0.37, N = 106):

$$\begin{aligned}\log_{10}(\mathrm{RIP}) = &\left((1.8 \pm 0.4) - (0.053 \pm 0.012) \cdot \left(\mathrm{WI} - (6.9 \pm 0.6)\right)^2\right) \\ &+(0.0063 \pm 0.0070) \cdot \mathrm{mica} + (0.019 \pm 0.005) \cdot \mathrm{2{:}1clay} \\ &-(0.0013 \pm 0.0060) \cdot \mathrm{1{:}1clay} \\ &+(0.26 \pm 0.29) \cdot \left(\frac{\mathrm{SOC}}{\mathrm{mica} + \mathrm{2{:}1clay} + \mathrm{1{:}1clay} + \mathrm{2{:}1{:}1clay}}\right)^{(0.29 \pm 0.15)} \\ &+(0.0022 \pm 0.0027) \cdot \mathrm{CEC} + (0.19 \pm 0.04) \cdot \mathrm{pH}\end{aligned} \tag{6.3}$$

where RIP is the radiocaesium interception potential in soil (mmol kg^{-1}), WI is the soil weathering index, mica is the soil mica content (g 100 g^{-1}), 2:1clay is the soil 2:1 clay mineral content (g 100 g^{-1}), 1:1clay is the soil 1:1 clay mineral content (g 100 g^{-1}), 2:1:1clay is the soil 2:1:1 clay mineral content (g 100 g^{-1}), SOC is the soil organic carbon content (g 100 g^{-1}), CEC is the cation exchange capacity (cmol$_c$ kg^{-1}), and pH is the soil pH. Standard errors of estimates are given in brackets.

Another multivariate model was created to predict soil RIP based on soil properties and soil classification as a proxy for mineralogy. A combination was tested with soil clay content, soil organic carbon, soil pH, cation exchange capacity, and reference WRB soil groups (IUSS Working Group WRB FAO, 2022). The soil pH was related to soil organic carbon content (R^2 = 0.18, N = 281) and cation exchange capacity (R^2 = 0.19, N = 279), so these were left out of the model.

The ^{10}log-transformed soil RIP was finally fitted to a multivariate model with the reference soil groups, soil clay content, and soil pH (R^2 = 0.69, p <0.001, RMSE = 0.42, N = 284, Table 6.2).

Table 6.2. The ^{10}log-transformed soil RIP multivariate model estimates and standard error for each reference soil group (WRB) and variable and the number of observations (*N*) are given. The variable effect sizes on ^{10}log-transformed RIPs are compared by the log-transformation of *p*-values (logworth). Larger values of the logworth indicate higher statistical significance in explaining the RIP. See Eqs. (6.2 and (6.3 for meanings of abbreviations.

variable	*N*	*estimate*	*standard error*	*logworth*	*p-value*
intercept		1.1	0.2		<0.0001
^{10}log(clay)	284	0.74	0.09	15	<0.0001
reference soil groups	284			13	<0.0001
Acrisol	8	-0.16	0.15		0.29
Alisol	1	0.17	0.41		0.67
Andosol	38	-0.42	0.08		<0.0001
Arenosol	1	0.21	0.42		0.61
Anthrosol	6	0.11	0.18		0.53
Chernozem	7	0.23	0.16		0.16
Calcisol	6	0.11	0.18		0.54
Cambisol	54	0.019	0.075		0.80
Fluvisol	13	0.24	0.12		0.05
Ferralsol	15	-0.83	0.13		<0.0001
Gleysol	37	0.12	0.09		0.16
Histosol	16	-0.62	0.13		<0.0001
Kastanozem	2	0.48	0.29		0.10
Leptosol	1	-0.46	0.41		0.26
Luvisol	29	0.29	0.09		0.0016
Lixisol	2	0.19	0.29		0.52
Nitisol	11	-0.11	0.14		0.42
Phaeozem	2	0.28	0.29		0.34
Podzol	16	-0.16	0.14		0.26
Regosol	8	0.23	0.15		0.13
Vertisol[b]	11	0	N.A.		N.A.
pH	284	0.19	0.03	11	<0.0001

[b] reference level

Both clay content and soil pH significantly influenced soil RIP. Clay content alone explains only 28% of the variability in soil RIP (R^2 = 0.28, *N* = 298), as the type of clay mineral is also important. Clay mineralogy is unknown at a large scale in soil maps, in contrast with soil classification. To some extent, soil classification is associated with soil weathering stage and, hence, soil mineralogy. However, soil classification criteria, partially rely on properties, such as the clay fraction CEC that should be <16 $cmol_c$ kg^{-1} for Ferrasols, making soil classification not a truly independent proxy for mineralogy.

On the one hand, combining clay content with soil classification explains a substantial portion of soil RIP, as certain reference (WRB) soil groups can be distinguished with expected low RIP. For example, volcanic soils (Andosols), peat soils (Histosols), and highly weathered soils (Ferralsols), typically have lower RIP relative to Vertisols (reference in multivariate model), which are dominated by swelling clays. As shown in Table 6.2, model estimates predict RIPs to be 6.8 times lower (1/6.8 = $10^{-0.83}$) in Ferralsols and 1.4 times lower in Acrisols relative to Vertisols, all at equal soil pH and clay content.

On the other hand, for less extreme soil groups, soil classification has no significant effect. For Cambisols, for instance, the standard error is about four times larger than the estimate itself, suggesting that this reference soil group explains less variability in soil RIP than other groups. Cambisols have a relatively undeveloped soil structure, so the link with soil mineralogy and RIP is logically less obvious.

As observed in previous Chapters 2, 4 and 5, soil RIP correlated positively to soil pH (R^2 = 0.39, *N* = 281). Soil pH was also associated with other soil properties, such as SOC and CEC. Rather than a direct mechanism by which pH affects Cs adsorption, these variables likely are linked with soil mineralogy. Highly weathered soils, often low in Cs-adsorbing clay minerals, typically have low pH. Organic-rich soils have higher soil organic carbon, resulting in fewer clay minerals. Soils with higher CEC (after correcting for organic content) tend to contain swelling clays, which can form Cs-adsorbing sites. These general trends may apply to a wide range of contrasting soils, while for more comparable soils, the effects of these variables may be less obvious.

On the same dataset (*N* = 106), the soil RIP was explained for 5% by Equation 6.2, for 67% by Equation 6.3 (including soil mineralogy), and for 56% by the model of Table 6.2 (excluding soil mineralogy, but using the WRB classification as a proxy) (Figure 6.3). The soil variables without soil mineralogy or soil classification explained 52% (not shown).

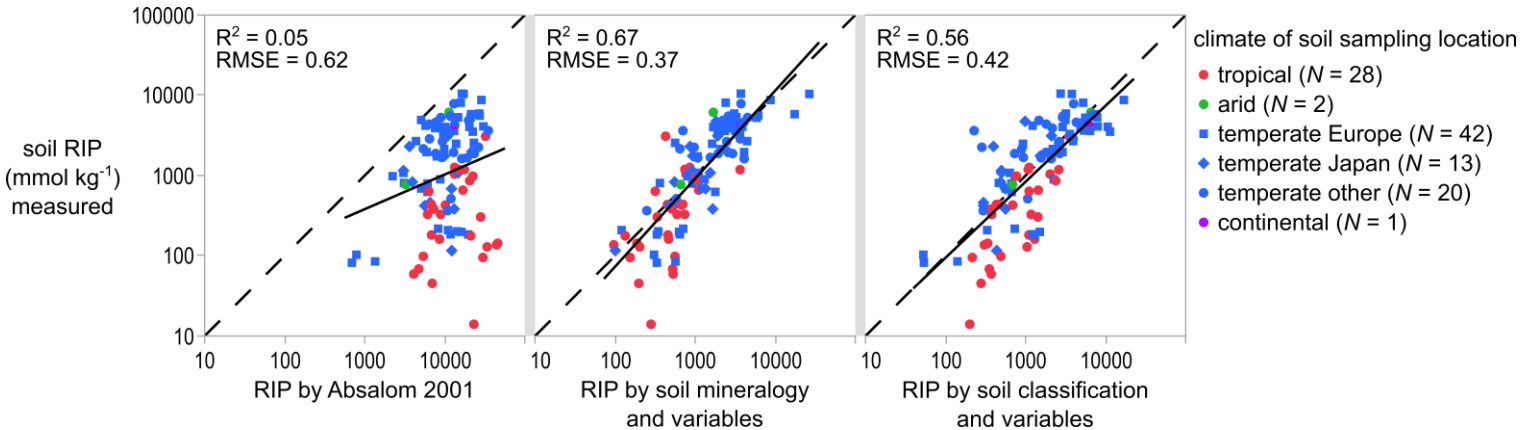

Figure 6.3. Comparison between the measured RIP in soils (N = 106) and (left) RIP based on clay and SOM (Absalom 2001 model, Eq. (6.2); (center) RIP based on soil WI, mica, 2:1, 1:1, 2:1:1 clay mineral contents, SOC, CEC and pH (fitted on N = 106, Eq. (6.3); and (right) RIP based on soil classification (WRB), clay, and pH (fitted on N = 284, Table 6.2). The solid lines are the regression lines, and the dashed lines are the 1:1 lines.

With this limited dataset, it is hence demonstrated that soil mineralogy information can greatly improve the predictions of radiocaesium adsorption in contrasting soils. Soil mineralogy maps exist for regions, such as Scotland (Butler et al., 2018), and on a global scale (Ito and Wagai, 2017), but the latter are not based on measured mineralogy data, but derived from soil classification. Because of a lack of reliable soil mineralogy datasets, it can be proposed to explore proxies for soil mineralogy, e.g., soil classification. However, the multivariate model based on the larger dataset (N = 284, Table 6.2) offered limited added value when applied to the smaller dataset (N = 106), explaining 56% of the ^{10}log-transformed soil RIP compared to 52% explained by soil variables alone. Further insights into soil mineralogy might be gained by including parent material information from geologic maps (e.g., https://portal.onegeology.org), an approach worth exploring in the future.

6.2. Modeling and mapping radiocaesium transfer risks on a global scale

Once the radiocaesium soil-to-plant transfer model is fit for purpose, it can be adjusted to predict transfer for different plant species and used, combined with soil and plant maps, to create radiocaesium soil-to-plant transfer maps (Figure 6.4). A similar exercise was conducted earlier (Chapter 2), but information on plant species was lacking, and the model did not account for soil exchangeable K content or mineralogy. Here, we further explore how radiocaesium transfer models can be adjusted for global scale purposes and applied in decision support systems.

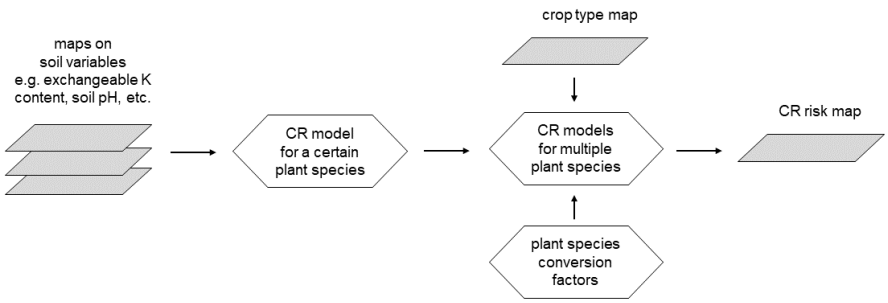

Figure 6.4. Creation of radiocaesium soil-to-plant transfer (CR) maps based on soil and plant variable maps, a conversion for plant species, and a radiocaesium soil-to-plant transfer model.

The uptake of radiocaesium by plants is closely linked to their K requirements: plants with a higher K demand likely take up more radiocaesium, especially in soils with low K levels (Zhu and Smolders, 2000). This has previously been linked to plant phylogeny, as plants within the same evolutionary group tend to share fundamental characteristics, including similar radiocaesium uptake rates (Willey, 2010). Plant species data collected on similar substrates (Beresford and Willey, 2019) provide the best available method for predicting CR at the plant species level, as it allows CR values to be estimated for species where CR data are lacking (Frissel et al., 2002). However, these plant conversion factors exist primarily for perennial crops and have yet to be validated, particularly for more exotic annual crops. For example, cassava, a root crop with a growth period of 6–18 months, typically grows in less fertilized and watered conditions, whereas banana requires substantial K fertilization to produce fruit throughout the year.

Data on available soil K is one of the most critical variables influencing radiocaesium uptake from soils (Smolders et al., 1997). However, to our knowledge, a global map of soil exchangeable K does not yet exist. There are regional maps, such as for Europe (LUCAS database; Orgiazzi et al., 2018) and Africa (AfSP database; Leenaars et al., 2014), where K is measured using the 1 mol L^{-1} ammonium acetate method at pH 7 or corrected for when measured according to Mehlich 3 (Hengl et al., 2015). In contrast to these soil databases, there are also initiatives using soil spectrometry data. For example, in the United States, exchangeable K has been successfully predicted using mid-infrared spectrometry data from the NSSC-KSSL database, comprising 40,000 samples (Albinet et al., 2022). Such spectrometry-based approaches could significantly reduce the cost and labor of wet chemistry measurements.

However, mapping radiocaesium transfer on a global scale also presents several challenges: missing data in underexposed areas, such as tropical and arid regions, could cause global CR models to largely under(- or over)estimate radiocaesium transfer in these areas; CR models simplify plant-soil interactions, which may not apply to all soil-plant combinations; the lack of global maps of variables, such as available K in soil and mineralogy, that directly influence radiocaesium bioavailability make global CR models unreliable; the reliance on proxies, such as soil classification, to estimate mineralogy make global CR models even more unreliable. Validation of CR models for different regions and plants is therefore critical.

Once the radiocaesium soil-to-plant transfer models and maps are sufficiently reliable (see Section 6.3), they can be integrated into decision support systems for both pre- and post-nuclear emergencies (Figure 6.5). Before any release of radiocaesium into the environment, these maps could help identify vulnerable areas where radiocaesium transfer risks are higher so that appropriate countermeasure strategies can be prepared. After radiocaesium release, these maps can inform decision-makers on where to collect soil samples. Based on the measured radiocaesium levels, planting restrictions and food safety measures can be implemented, and countermeasure strategies can be created. Ideally, these measured values would be used to update the radiocaesium soil-to-plant transfer database linked to the model and map. An example of such a decision support system is the Decision Support System for Nuclear Emergencies Affecting Food and Agriculture (DSS4NAFA; Lee Zhi Yi and Dercon, 2019), which facilitates the selection of sampling locations, data collection, analysis, visualization, and risk communication and can be linked with the Optimizing Remediation Efforts Affecting Food and Agriculture (OREFA; Abrams et al., 2023) tool, which helps to optimize countermeasure strategies.

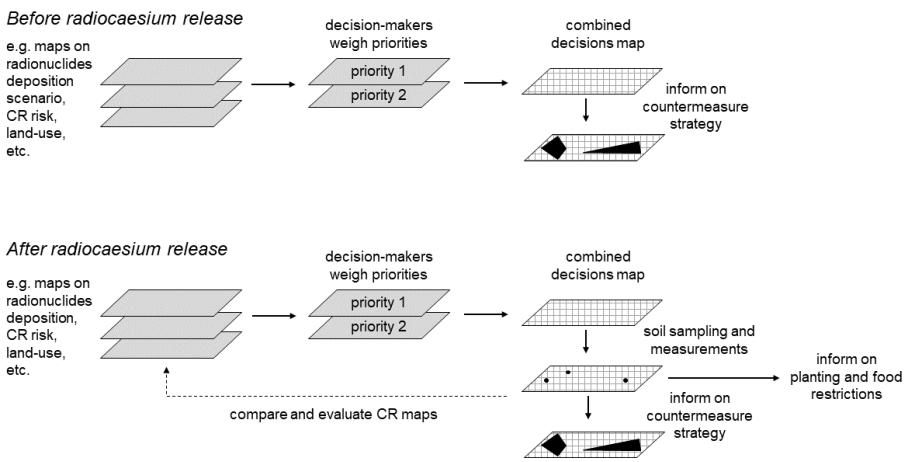

Figure 6.5. Integration of the radiocaesium soil-to-plant transfer (CR) map into a decision-support system before and after accidental release of radiocaesium into the environment.

6.3. Remaining limitations and suggestions for future studies

This project was unable to produce a ready-to-use global radiocaesium soil-to-plant transfer map due to considerably large uncertainties related to both the models and the soil input variables derived from global datasets.

6.3.1. Expanding data coverage for model calibration

The model for the map (Chapter 2) was calibrated using a CR dataset (in total *N* = 513) with limited coverage. The CRs were mainly derived from field observations and experiments with soils from temperate climates (*N* = 488), the majority of which were from Fukushima (*N* = 279 out of 488). Consequently, the model was biased towards soils from temperate regions. Limited CR data were available for tropical (*N* = 16) and arid (*N* = 2) regions, mainly from pot experiments conducted as part of this project. These regions are historically underrepresented due to lower research prioritization.

6.3.2. Refining models to reflect field conditions

In this project, CRs were obtained from pot experiments and were compared with the CR predicted by semi-mechanistic models (Chapter 4). The Absalom 2001 model itself was initially based on pot experimental data (Absalom et al., 2001) and later that model was refined with field observations (Tarsitano et al., 2011). Further investigation is needed to determine whether models should be adapted to reflect undisturbed soil-plant conditions. Although the plant growth method (e.g., pot trials, lysimeter experiments, field observations) does not significantly affect the CR once corrected for the soil-radiocaesium contact time (Chapter 2), the method of growing plants in soils to obtain CRs still requires careful consideration. Pot experiments involve soil manipulation, such as soil sieving and mixing in of radiocaesium, which enhances radiocaesium adsorption and renders it less available. Indeed, comparative studies on radiocaesium CRs in sieved and corresponding undisturbed soils showed that the CRs were factors 2–26 lower in the pots with sieved soils than in undisturbed soils, the range depending on the soil sample (Table 6.3; Fernagut and Merckx, 1997).

Table 6.3. CR data from undisturbed and disturbed soils from Belgium showing the effect of soil manipulation involved in experiments with disturbed soils (adapted from Fernagut and Merckx, 1997).

soil sampling location in Belgium	clay content	CR in undisturbed soil	CR in disturbed soil	ratio undisturbed/disturbed
	g 100 g^{-1}	m^2 kg^{-1}		
Meldert	51	27	1.0	26
Warzee	23	5.7	0.2	26
Wilsele	10	7.1	0.4	16
Zwijnaarde	3	34.5	3.1	11
Maizeret	17	9.1	3.8	2.4

In field conditions, radiocaesium is deposited on undisturbed soils, where soil structure and aggregation can prevent adsorption. Clay minerals are cemented in soil aggregates, so their Cs^+ adsorption sites are not available to bind Cs^+ which makes the radiocaesium bioavailability higher than expected (Chapter 5). To our knowledge, the effect of soil structure on radiocaesium bioavailability in the field in soils of various mineralogies has not yet been studied, and certainly not for soils from understudied tropical climates. Its role in the short-term and long-term radiocaesium bioavailability with respect to the aging of radiocaesium in soil (Krouglov et al., 1997) and the vertical distribution (Jagercikova et al., 2015) would be interesting. Furthermore, the effect of nutrient balances, such as K depletion, needs special attention in radiocaesium bioavailability experiments in soils of various mineralogies. With nutrient depletion of K^+, the Cs^+:K^+ competition for plant uptake will decrease, causing Cs^+ to be taken up by plants disproportionately. Studies of soils in temperate climates show that nutrient depletion occurs faster in pots than in the field, where deeper soil layers can serve as reservoirs. However, we do not know if this nutrient reservoir also applies to soil-plant systems in tropical climates. We recommend further research to reassess the representativeness of pot-derived CR for field conditions in soils of various mineralogies, particularly in understudied highly weathered tropical soils.

6.3.3. Managing model uncertainty in predictions

All models discussed and created in this project, whether semi-mechanistic, regression-based, or machine learning models, have considerable uncertainties. Most models have a RMSE greater than 0.50 ^{10}log(kg kg^{-1}) in predicting ^{10}log-transformed CR values, implying large deviations between the

model-predicted CR and the observed CR. The RMSE represents the prediction errors, assuming that these errors follow a normal distribution. The 95% confidence interval of the predicted CR is within ± 1.96 times the RMSE (degrees of freedom is >100). For instance, the random forest model used for the radiocaesium transfer map (Chapter 2) has an RMSE of 0.57 for ^{10}log-transformed CR. This implies that, for a predicted CR value of CR = 0.01 kg kg^{-1} (or ^{10}log(CR) = -2 ^{10}log(kg kg^{-1})), we expect that about 95% of the ^{10}log(CR) predictions will fall within the interval [-3.1 ^{10}log(kg kg^{-1}), -0.88 ^{10}log(kg kg^{-1})] or for CR [0.00076 kg kg^{-1}, 0.13 kg kg^{-1}]. Thus, the range of possible CR values, spans over two orders of magnitude, reflecting a large uncertainty in the random forest model predictions. Even the best random forest model had a RMSE of 0.45, which corresponds to a range of more than an order of magnitude in the confidence interval of CR.

6.3.4. Addressing uncertainties in soil variable data

In addition to model uncertainties, the soil variables derived from digital soil maps, such as SoilGrids, also contribute to uncertainties in the predicted radiocaesium transfer risk. While, to our knowledge, SoilGrids is the best available global soil map, it has limitations. SoilGrids provides transparency by publishing the uncertainties for all soil variables, except soil classification (WRB), in global maps. Various aspects cause these uncertainties: limited point observations, missing reliable proxies, and modeling choices (more information on https://www.isric.org/explore/soilgrids/faq-soilgrids). SoilGrids is not meant for use at the local scale because national data providers often have access to more detailed point datasets (Poggio et al., 2021). For example, SoilGrids does not have soil profile data for the Fukushima prefecture, whereas the National Agriculture and Food Research Organization of Japan has a detailed soil map of Japan (http://soil-inventory.dc.affrc.go.jp). Regions that have a low density of soil profile observations, such as central Asia, coastal areas, and deserts, have higher uncertainties. Researchers from Croatia and Rajasthan in India addressed this by organizing a soil sampling and measuring campaign. They noted that particle sizes were incorrectly predicted because the SoilGrids database included only one or zero profiles in those areas, so the clay content was underestimated in Croatia (N = 686, Radočaj et al., 2023) and overestimated in desert areas in Rajasthan (N = 24, Dandabathula et al., 2022). SoilGrids uses soil proxies, such as parent material, that influence soil formation to make the best possible predictions of soil variables. However, information on these proxies is often missing.

Furthermore, the makers of SoilGrids claim their random forest model is also a cause of uncertainty and that other models can give more accurate results at the expense of heavier calculations. Other researchers suggest making soil maps following a bottom-up approach by combining smaller maps generated from models specifically calibrated to the local environment rather than the quicker top-down approach (e.g., SoilGrids) (Bohn and Miller, 2024). However, we argue that a model can only be as good or reliable as the dataset on which the model is based, and for the interest of this project, the focus should be on the methods for soil particle size analysis (i.e., soil texture).

6.3.5. Accounting for particle size distribution methods

During the experimental research for this project, it became clear that no consistency exists for particle size determinations of soils and that, depending on the method, the clay content of a single soil can vary by a factor of 8 (Chapter 4). The problem with global soil maps is that data obtained by various particle size definitions and methods are combined. The World Soil Information Service (WoSIS) Soil Profile database on which SoilGrids is based, lists information on soil sample sieving (1 or 2 mm sieve); the upper limit for the silt fraction (e.g., the threshold of the international system is 20 µm, of USDA is 50 µm, and ISO/FAO standard is 63 µm); chemical treatments to break up aggregates (hydrogen peroxide, etc.); dispersion treatment (hexametaphosphate, etc.); and the instrument to sample the clay fraction (pipet, hydrometer, analyzer, field hand estimate) (Ribeiro et al., 2018). These chemical and dispersion steps are the most critical steps. Often, clay minerals are trapped in larger soil aggregates. Breaking up these aggregates and making a stable suspension of soil particles when measured is a challenge and explains why clay content is underestimated in many cases, while silt is overestimated. However, in a snapshot of the WoSIS database in 2019 (Batjes et al., 2020) out of the soil profiles >140,000 with clay, silt, and sand information, only 0.18% of soil profiles did not chemically treat the soil, and 0.05% did not disperse to obtain clay content; however, for >95% of data; no chemical treatment or dispersion methods were reported. While it is a positive development that the soil profile database lists the methods of particle size distribution, it is unfortunate that the methods were poorly reported so that underestimates of clay contents due to incomplete dispersion cannot be corrected.

6.3.6. Establishing acceptable uncertainty levels in radiocaesium transfer risks

We conclude with one *certainty*: that there is much *uncertainty* in radiocaesium soil-to-plant transfer predictions on a global scale. The RMSE of $^{10}\log(CR)$ values drops from 0.57 to 0.45 by adopting machine learning models depending on the available information and number of records (Chapter 2) and within a comparative study of pot trials, the RMSE is still not lower than 0.33 (Chapter 4). These RMSE are equivalent to a width of the CR 95% confidence intervals of factors 13 (= $10^{1.96 \cdot 0.57}$) to still 4.4 (= $10^{1.96 \cdot 0.33}$). Risk assessments often aim to minimize uncertainty, but the question becomes how much uncertainty in radiation dose predictions is acceptable for decision-making and protective measures. Radiation protection guidelines typically adhere to principles like As Low As Reasonably Achievable (ALARA). In practice, the degree of uncertainty that is acceptable given the constraints (listed above, among others) often leads to the use of models with reasonable uncertainty ranges that can guide precautionary measures. There are ethical aspects to this level of acceptance of uncertainty: how should we balance the uncertainty of radiocaesium transfer models with societal needs for nuclear energy, agriculture in contaminated areas, or land use in post-accident scenarios? In the aftermath of the Chornobyl accident, when the transfer of radioactive caesium in Cumbria, United Kingdom, was underestimated, the debate arose around tolerance of uncertainties from which it was decided that the debate should be opened up to the rest of society and that scientists have a duty to be transparent about these uncertainties (Wynne, 1992).

6.3.7. Future studies

The ultimate goal of this research is to provide decision-makers with estimates of radiocaesium transfer risk from soil to crops on a global scale. In the absence of soil mineralogy maps, further work is needed to find reliable proxies to predict radiocaesium adsorption in soils at a global scale. Future studies on digital soil mapping should prioritize improving the harmonization of soil particle size data. More research is needed on the influence of soil structure and mineralogy on radiocaesium bioavailability in field conditions, particularly in tropical regions, where little is known about the long-term behavior of radiocaesium. Such research would offer valuable insights into radiocaesium aging, its vertical distribution, and its long-term bioavailability in diverse soils.

Bibliography

Abrams, F., Sweeck, L., Camps, J., Van Orshoven, J., 2023. Reducing the impact of decontamination efforts on downstream ecosystems in large-scale nuclear emergencies affecting food and agriculture. International Atomic Energy Agency (IAEA).

Absalom, J.P., Young, S.D., Crout, N.M.J., Nisbet, A.F., Woodman, R.F.M., Smolders, E., Gillett, A.G., 1999. Predicting soil to plant transfer of radiocesium using soil characteristics. Environ. Sci. Technol. 33, 1218–1223. https://doi.org/10.1021/es9808853

Absalom, J.P., Young, S.D., Crout, N.M.J., Sanchez, A., Wright, S.M., Smolders, E., Nisbet, A.F., Gillett, A.G., 2001. Predicting the transfer of radiocaesium from organic soils to plants using soil characteristics. J. Environ. Radioact. 52, 31–43. https://doi.org/10.1016/S0265-931X(00)00098-9

Agriculture, J.F.D. of N.T. in F. and, 2010. Handbook of Parameter Values for the Prediction of Radionuclide Transfer in Terrestrial and Freshwater Environments. IAEA, International Atomic Energy Agency (IAEA).

Ahern, C.R., Baker, D.E., Aitken, R.L., 1995. Models for relating pH measurements in water and calcium chloride for a wide range of pH, soil types and depths. Plant Soil 171, 47–52. https://doi.org/https://doi.org/10.1007/BF00009563

Albinet, F., Peng, Y., Eguchi, T., Smolders, E., Dercon, G., 2022. Prediction of exchangeable potassium in soil through mid-infrared spectroscopy and deep learning: From prediction to explainability. Artif. Intell. Agric. 6, 230–241. https://doi.org/10.1016/j.aiia.2022.10.001

Almahayni, T., Beresford, N.A., Crout, N.M.J., Sweeck, L., 2019. Fit-for-purpose modelling of radiocaesium soil-to-plant transfer for nuclear emergencies: a review. J. Environ. Radioact. 201, 58–66. https://doi.org/10.1016/j.jenvrad.2019.01.006

Aurelio, M.A., Peña, R.E., 2010. Geology of the Philippines, 2nd ed. Mines and Geosciences Bureau, Quezon City.

Ballatore, T.J., Olaka, L., 2015. Atlas of Mount Elgon.

Bartoli, F., Burtin, G., Herbillon, A.J., 1991. Disaggregation and clay dispersion of Oxisols: Na resin, a recommended methodology. Geoderma 49, 301–317. https://doi.org/10.1016/0016-7061(91)90082-5

Bassett, W.A., 1960. Role of hydroxyl orientation in mica alteration. GSA Bull. 71, 449–456. https://doi.org/10.1130/0016-7606(1960)71[449:ROHOIM]2.0.CO;2

Batjes, N.H., Ribeiro, E., Van Oostrum, A., 2020. Standardised soil profile data to support global mapping and modelling (WoSIS snapshot 2019). Earth Syst. Sci. Data 12, 299–320. https://doi.org/10.5194/essd-12-299-2020

Beck, H.E., Zimmermann, N.E., McVicar, T.R., Vergopolan, N., Berg, A., Wood, E.F., 2018. Present and future köppen-geiger climate

classification maps at 1-km resolution. Sci. Data 5, 1–12. https://doi.org/10.1038/sdata.2018.214

Beckett, P.H.T., 1964. Studies on Soil Potassium Ii. the 'Immediate' Q/I Relations of Labile Potassium in the Soil. Eur. J. Soil Sci. 15, 9–23. https://doi.org/10.1111/j.1365-2389.1964.tb00240.x

Bellenger, J.P., Staunton, S., 2008. Adsorption and desorption of 85Sr and 137Cs on reference minerals, with and without inorganic and organic surface coatings. J. Environ. Radioact. 99, 831–840. https://doi.org/10.1016/j.jenvrad.2007.10.010

Beresford, N.A., Fesenko, S., Konoplev, A., Skuterud, L., Smith, J.T., Voigt, G., 2016. Thirty years after the Chernobyl accident: What lessons have we learnt? J. Environ. Radioact. 157, 77–89. https://doi.org/10.1016/j.jenvrad.2016.02.003

Beresford, N.A., Willey, N., 2019. Moving radiation protection on from the limitations of empirical concentration ratios. J. Environ. Radioact. 208–209, 106020. https://doi.org/10.1016/j.jenvrad.2019.106020

Binh, N.T., Y, T., Sieu, L.N., Ngo, N.T., Phuc, N. Van, Huong, M.T., Quang, N.H., Nhan, D.D., 2003. The transfer of radionuclides in the terrestrial environments Recent research results in monsoon tropical condition of Vietnam.

Bohn, M.P., Miller, B.A., 2024. Locally enhanced digital soil mapping in support of a bottom-up approach is more accurate than conventional soil mapping and top-down digital soil mapping. Geoderma 442, 116781. https://doi.org/10.1016/j.geoderma.2024.116781

Bradbury, M.H., Baeyens, B., 2000. A generalised sorption model for the concentration dependent uptake of caesium by argillaceous rocks. J. Contam. Hydrol. 42, 141–163. https://doi.org/10.1016/S0169-7722(99)00094-7

Brindley, G.W., Brown, G., 1980. Crystal structures of clay minerals and their X-ray identification, Monograph (Mineralogical Society (Great Britain)) ; no. 5. Mineralogical Society, London. https://doi.org/https://doi.org/10.1180/mono-5

Brouwer, E., Baeyens, B., Maes, A., Cremers, A., 1983. Cesium and rubidium ion equilibria in illite clay. J. Phys. Chem. 87, 1213–1219. https://doi.org/10.1021/j100230a024

Brown, J.E., Beresford, N.A., Hosseini, A., Barnett, C.L., 2020. Applying process-based models to the Borssele scenario. Radioprotection 55, S109–S117. https://doi.org/10.1051/radiopro/2020020

Bruneel, Y., 2021. Sorption of Radionuclides on Glauconite from the Neogene.

Buekers, J., 2007. Fixation of cadmium , copper , nickel and zinc in soil : kinetics , mechanisms and its effect on metal bioavailability.

Buekers, J., Van Laer, L., Amery, F., Van Buggenhout, S., Maes, A., Smolders, E., 2007. Role of soil constituents in fixation of soluble Zn, Cu, Ni and Cd added to soils. Eur. J. Soil Sci. 58, 1514–1524.

https://doi.org/10.1111/j.1365-2389.2007.00958.x

Butler, B.M., O'Rourke, S.M., Hillier, S., 2018. Using rule-based regression models to predict and interpret soil properties from X-ray powder diffraction data. Geoderma 329, 43–53. https://doi.org/10.1016/j.geoderma.2018.04.005

Carating, R.B., Galanta, R.G., Bacatio, C.D., 2014. The Soils of the Philippines, 1st ed. Springer Dordrecht. https://doi.org/10.1007/978-94-017-8682-9

Chorover, J., DiChiaro, M.J., Chadwick, O.A., 1999. Structural Charge and Cesium Retention in a Chronosequence of Tephritic Soils. Soil Sci. Soc. Am. J. 63, 169–177. https://doi.org/10.2136/sssaj1999.03615995006300010024x

Christl, I., Kretzschmar, R., 2001. Interaction of copper and fulvic acid at the hematite-water interface. Geochim. Cosmochim. Acta 65, 3435–3442. https://doi.org/10.1016/S0016-7037(01)00695-0

Churchman, G.J., Tate, K.R., 1987. Stability of aggregates of different size grades in allophanic soils from volcanic ash in New Zealand. J. Soil Sci. 38, 19–27. https://doi.org/10.1111/j.1365-2389.1987.tb02119.x

Ciesielski, H., Sterckeman, T., 1997. Determination of cation exchange capacity and exchangeable cations in soils by means of cobalt hexamine trichloride. Effects of experimental conditions. Agronomie 17, 1–7. https://doi.org/10.1051/agro:19970101

Cremers, A., Elsen, A., Preter, P. De, Maes, A., 1988. Quantitative analysis of radiocaesium retention in soils. Nature 335, 247–249. https://doi.org/10.1038/335247a0

D'Souza, T.J., Fagniart, E., Kirchmann, R., 1980. Effects of clay mineral type and organic matter on the uptake of radiocesium by pasture plants.

Dandabathula, G., Salunkhe, S.S., Bera, A.K., Ghosh, K., Hari, R., Biradar, P., Chirala, K.R., Gaur, M.K., 2022. Validation of SoilGrids 2.0 in an Arid Region of India using In Situ Measurements. Eur. J. Environ. Earth Sci. 3, 49–58. https://doi.org/10.24018/ejgeo.2022.3.6.356

Davis, J.J., 1961. Cesium and Its Relationship to Potassium in Ecology, in: Schultz, V., Klement, A.W. (Eds.), Radioecology. Reinhold Publishing Corporation; The American Institute of Biological Sciences Washington, D.C., New York, p. 746.

De Bauw, P., Shimamura, E., Rakotoson, T., Andriamananjara, A., Verbeeck, M., Merckx, R., Smolders, E., 2021. Farm yard manure application mitigates aluminium toxicity and phosphorus deficiency for different upland rice genotypes. J. Agron. Crop Sci. 207, 148–162. https://doi.org/10.1111/jac.12436

de Koning, A., Comans, R.N.J., 2004. Reversibility of radiocaesium sorption on illite. Geochim. Cosmochim. Acta 68, 2815–2823. https://doi.org/10.1016/j.gca.2003.12.025

de Koning, A., Konoplev, A. V., Comans, R.N.J., 2007. Measuring the specific

caesium sorption capacity of soils, sediments and clay minerals. Appl. Geochemistry 22, 219–229. https://doi.org/10.1016/j.apgeochem.2006.07.013

De Preter, P., 1990. Radiocesium retention in the aquatic, terrestrial and urban environment: a quantitative and unifying analysis. Diss. Agric. s. n. Leuven : s.n.,.

Delvaux, B., Herbillon, A.J., Vielvoye, L., 1989. Characterization of a weathering sequence of soils derived from volcanic ash in Cameroon. Taxonomic, mineralogical and agronomic implications. Geoderma 45, 375–388. https://doi.org/10.1016/0016-7061(89)90017-7

Delvaux, B., Herbillon, A.J., Vielvoye, L., Mestdagh, M.M., 1990. Surface properties and clay mineralogy of hydrated halloysitic soil clays. II: Evidence for the presence of halloysite/smectite (H/Sm) mixed-layer clays. Clay Miner. 25, 141–160. https://doi.org/10.1180/claymin.1990.025.2.02

Delvaux, B., Kruyts, N., Maes, E., Smolders, E., 2001. Fate of Radiocesium in Soil and Rhizosphere, in: Trace Elements in the Rhizosphere. pp. 61–91. https://doi.org/10.1201/9781420039993.ch4

Dengra i Grau, F.X. [VerfasserIn], 2020. Evaluation of the radiocaesium behaviour in Japanese soils influenced by clay mineralogy, potassium application and zeolite amendments : agricultural countermeasures for nuclear emergency 82, LI Seiten, Illustrationen, Diagramme.

Desmet, G.M., Van Loon, L.R., Howard, B.J., 1991. Chemical speciation and bioavailability of elements in the environment and their relevance to radioecology. Sci. Total Environ. 100, 105–124. https://doi.org/10.1016/0048-9697(91)90375-O

Doebelin, N., Kleeberg, R., 2015. Profex: a graphical user interface for the Rietveld refinement program BGMN. J. Appl. Crystallogr. 48, 1573–1580. https://doi.org/10.1107/S1600576715014685

Durrant, C.B., Begg, J.D., Kersting, A.B., Zavarin, M., 2018. Cesium sorption reversibility and kinetics on illite, montmorillonite, and kaolinite. Sci. Total Environ. 610–611, 511–520. https://doi.org/10.1016/j.scitotenv.2017.08.122

Eguchi, T., Ohta, T., Ishikawa, T., Matsunami, H., Takahashi, Y., Kubo, K., Yamaguchi, N., Kihou, N., Shinano, T., 2015. Influence of the nonexchangeable potassium of mica on radiocesium uptake by paddy rice. J. Environ. Radioact. 147, 33–42. https://doi.org/10.1016/j.jenvrad.2015.05.002

Ehrhardt, J., 1997. The RODOS System: Decision Support for Off-Site Emergency Management in Europe. Radiat. Prot. Dosimetry 73, 35–40. https://doi.org/10.1093/oxfordjournals.rpd.a032160

Essington, M.E., 2015. Soil and Water Chemistry An Integrative Approach, 2nd ed. CRC Press, Boca Raton. https://doi.org/10.1201/b18385

Fanning, D.S., Keramidas, V.Z., El-Desoky, M.A., 1989. Micas, in: Dixon, J.B., Weed, S.B. (Eds.), Minerals in Soil Environments, SSSA Book Series.

Soil Science Society of America, Madison, Wisconsin, USA, pp. 551–634. https://doi.org/10.2136/sssabookser1.2ed.c12

Fernagut, B., Merckx, R., 1997. De beschikbaarheid van radiocesium in graslandbodems .

Frissel, M.J., Deb, D.L., Fathony, M., Lin, Y.M., Mollah, A.S., Ngo, N.T., Othman, I., Robison, W.L., Skarlou-Alexiou, V., Topcuoğlu, S., Twining, J.R., Uchida, S., Wasserman, M.A., 2002. Generic values for soil-to-plant transfer factors of radiocesium. J. Environ. Radioact. 58, 113–128. https://doi.org/10.1016/S0265-931X(01)00061-3

Frissel, M.J., Noordijk, H., Bergeijk, K.E. van, 1990. The impact of extreme environmental conditions, as occurring in natural ecosystems, on the soil-to-plant transfer of radionuclides. Elsevier Applied Science, United Kingdom.

Gerzabek, M.H., Strebl, F., Temmel, B., 1998. Plant uptake of radionuclides in lysimeter experiments. Environ. Pollut. 99, 93–103. https://doi.org/10.1016/S0269-7491(97)00167-X

Gilis, B., Sweeck, L., 2019. Bodem-plant transfer van radioactief cesium-137 Transfer naar spinazie en radijzen. Thomas More.

Grim, R.E., 1968. Clay mineralogy, 2nd ed. McGraw-Hill, New York.

Guggenheim, Stephen, Martin, R.T., Alietti, A., Drits, V.A., Formoso, M.L.L., Galán, E., Köster, H.M., Morgan, D.J., Paquet, H., Watanabe, T., Bain, D.C., Ferrell, R.E., Bish, D.L., Fanning, D.S., Guggenheim, S., Kodama, H., Wicks, F.J., 1995. Definition of clay and clay mineral: Joint report of the AIPEA nomenclature and CMS nomenclature committees. Clays Clay Miner. 43, 255–256. https://doi.org/10.1346/CCMN.1995.0430213

Hengl, T., De Jesus, J.M., Heuvelink, G.B.M., Gonzalez, M.R., Kilibarda, M., Blagotić, A., Shangguan, W., Wright, M.N., Geng, X., Bauer-Marschallinger, B., Guevara, M.A., Vargas, R., MacMillan, R.A., Batjes, N.H., Leenaars, J.G.B., Ribeiro, E., Wheeler, I., Mantel, S., Kempen, B., 2017. SoilGrids250m: Global gridded soil information based on machine learning, PLoS ONE. https://doi.org/10.1371/journal.pone.0169748

Hengl, T., Heuvelink, G.B.M., Kempen, B., Leenaars, J.G.B., Walsh, M.G., Shepherd, K.D., Sila, A., MacMillan, R.A., De Jesus, J.M., Tamene, L., Tondoh, J.E., 2015. Mapping soil properties of Africa at 250 m resolution: Random forests significantly improve current predictions. PLoS One 10, 1–26. https://doi.org/10.1371/journal.pone.0125814

Hoagland, D.R., Arnon, D.I., 1950. The water-culture method for growing plants without soil. Circ. Calif. Agric. Exp. Stn. 347, 32.

Horak, O., Gerzabek, M.H., 1989. Österreichisches Forschungszentrum 4515.

IAEA, 2024. Nuclear Cogeneration for Climate Change Mitigation and Sustainable Development Goals, TECDOC Series. INTERNATIONAL ATOMIC ENERGY AGENCY, Vienna.

IAEA, 2021a. The Potential Role of Nuclear Energy in National Climate

Change Mitigation Strategies, TECDOC Series. INTERNATIONAL ATOMIC ENERGY AGENCY, Vienna.

IAEA, 2021b. Soil–Plant Transfer of Radionuclides in Non-temperate Environments, TECDOC Series. INTERNATIONAL ATOMIC ENERGY AGENCY, Vienna.

IAEA, 2020. Environmental Transfer of Radionuclides in Japan following the Accident at the Fukushima Daiichi Nuclear Power Plant, TECDOC Series. INTERNATIONAL ATOMIC ENERGY AGENCY, Vienna.

IAEA, 2009. Quantification of Radionuclide Transfer in Terrestrial and Freshwater Environments for Radiological Assessments, TECDOC Series. INTERNATIONAL ATOMIC ENERGY AGENCY, Vienna.

IAEA, 2006. Classification of Soil Systems on the Basis of Transfer Factors of Radionuclides from Soil to Reference Plants, TECDOC Series. INTERNATIONAL ATOMIC ENERGY AGENCY, Vienna. https://doi.org/10.1051/radiopro/2002097

IAEA, 2001. Generic Models for Use in Assessing the Impact of Discharges of Radioactive Substances to the Environment, Safety Report Series. Vienna, Austria.

ICRP, 2012. ICRP publication 119: Compendium of dose coefficients based on ICRP publication 60, Annals of the ICRP. https://doi.org/10.1016/j.icrp.2013.05.003

IEA, 2022. Nuclear Power and Secure Energy Transitions. Nucl. Power Secur. Energy Transitions. https://doi.org/10.1787/aca1d7ee-en

ISO, 1998. Soil quality —Determination of particle size distribution in mineral soil material— Method by sieving and sedimentation, 1st ed. Geneva, CH.

Ito, A., Wagai, R., 2017. Global distribution of clay-size minerals on land surface for biogeochemical and climatological studies. Sci. Data 4, 1–11. https://doi.org/10.1038/sdata.2017.103

IUR, 1992. VIIIth report of the working group soil-to-plant transfer factors. Balen, Belgium.

IUR, 1982. Report IUR Working Group Soil-to-Plant Transfer. Part I. Wageningen.

IUSS Working Group WRB FAO, 2022. World Reference Base for Soil Resources. International soil classification system for naming soils and creating legends for soil maps., 4th ed, International Union of Soil Sciences (IUSS)21. Vienna.

Jackson, M.L., 1975. Soil Chemical Analysis-Advanced Course, second. ed, Soil Chemical Analysis-Advanced Course. Published by the author, Winsconsin.

Jackson, M.L., 1964. Chemical composition of soils, in: Bear, F.E. (Ed.), Chemistry of the Soil. Reinhold Publishing Corporation, New York, pp. 71–141.

Jackson, M.L., Sherman, G.D., 1953. Chemical Weathering of Minerals in

Soils. Adv. Agron. 5, 219–318. https://doi.org/10.1016/S0065-2113(08)60231-X

Jackson, M.L., Tyler, S.A., Willis, A.L., Bourbeau, G.A., Pennington, R.P., 1948. Weathering sequence of clay-size minerals in soils and sediments. I: Fundamental generalizations. J. Phys. Colloid Chem. 52, 1237–1260. https://doi.org/10.1021/j150463a015

Jagercikova, M., Cornu, S., Le Bas, C., Evrard, O., 2015. Vertical distributions of 137Cs in soils: a meta-analysis. J. Soils Sediments 15, 81–95. https://doi.org/10.1007/s11368-014-0982-5

Joussein, E., Kruyts, N., Righi, D., Petit, S., Delvaux, B., 2004. Specific Retention of Radiocesium in Volcanic Ash Soils Devoid of Micaceous Clay Minerals. Soil Sci. Soc. Am. J. 68, 313–319. https://doi.org/10.2136/sssaj2004.3130

Keum, D.K., Lee, H., Kang, H.S., Jun, I., Choi, Y.H., Lee, C.W., 2007. Predicting the transfer of 137Cs to rice plants by a dynamic compartment model with a consideration of the soil properties. J. Environ. Radioact. 92, 1–15. https://doi.org/10.1016/j.jenvrad.2006.08.007

Kirchmann, R., Van der Stricht, E., 2001. Radioecology : radioactivity and ecosystems. Liège : Fortemps.

Krouglov, S. V., Filipas, A.S., Alexakhin, R.M., Arkhipov, N.P., 1997. Long-term study on the transfer of 137Cs and 90Sr from Chernobyl-contaminated soils to grain crops. J. Environ. Radioact. 34, 267–286. https://doi.org/10.1016/0265-931X(96)00043-4

Krstić, D., Stevanović, N., Milivojević, J., Nikezić, D., 2007. Determination of the soil-to-grass transfer of 137Cs and its relation to several soil properties at various locations in Serbia. Isotopes Environ. Health Stud. 43, 65–73. https://doi.org/10.1080/10256010601154171

Langmuir, D., 1997. Aqueous environmental geochemistry. Prentice Hall, Upper Saddle River, N.J.

Lee Zhi Yi, A., Dercon, G., 2019. Data management and visualisation in response to large-scale nuclear emergencies affecting food and agriculture. FAO/IAEA, Vienna.

Leenaars, J., Kempen, B., van Oostrum, A., Batjes, N., 2014. Africa Soil Profiles database: Version 1.2. GlobalSoilMap 51–57. https://doi.org/10.1201/b16500-13

Li, P., Gong, Y., Tanaka, T., Thiry, Y., Huang, Q., Komatsuzaki, M., 2024. Modeling long-term transfers of radiocesium in farmland under different tillage and cover crop treatments. Sci. Total Environ. 907, 167849. https://doi.org/10.1016/j.scitotenv.2023.167849

Liaw, A., Wiener, M., 2002. Classification and Regression by randomForest. R News 2, 18–22.

Maes, A., Verheyden, D., Cremers, A., 1985. Formation of highly selective cesium-exchange sites in montmorillonites. Clays Clay Miner. 33, 251–257. https://doi.org/10.1346/ccmn.1985.0330312

Maes, E., Iserentant, A., Herbauts, J., Delvaux, B., 1999a. Influence of the nature of clay minerals on the fixation of radiocaesium traces in an acid brown earth–podzol weathering sequence. Eur. J. Soil Sci. 50, 117–125. https://doi.org/10.1046/j.1365-2389.1999.00224.x

Maes, E., Vielvoye, L., Stone, W., Delvaux, B., 1999b. Fixation of radiocaesium traces in a weathering sequence mica → vermiculite → hydroxy interlayered vermiculite. Eur. J. Soil Sci. 50, 107–115. https://doi.org/10.1046/j.1365-2389.1999.00223.x

MAFF, 2017. Annual Report of Ministry of Agriculture, Forestry and Fisheries Affiliated Radioactivity Research: H26 Report. Tokyo.

MAFF, 2015. Annual Report of Ministry of Agriculture, Forestry and Fisheries Affiliated Radioactivity Research: H25 Report. Tokyo.

MAFF, 2014. Annual Report of Ministry of Agriculture, Forestry and Fisheries Affiliated Radioactivity Research: H24 Report. Tokyo.

McGee, E.J., Colgan, P.A., Dawson, D.E., Rafferty, B., 1992. Effects of Topography on Caesium-I37 in Montane Peat Soils and Vegetation*, ANALYST.

McKeague, J.A., 1967. An evaluation of 0.1 M pyrophosphate and pyrophosphate–dithionite in comparison with oxalate as extractants of the accumulation products in Podzols and some other soils. Can. J. Soil Sci. 47, 95–99. https://doi.org/10.4141/cjss67-017

McKeague, J.A., Day, J.H., 1966. Dithionite and oxalate-extractable Fe and Al as aids in differentiating various classes of soils. Can. J. Soil Sci. 46, 13–22. https://doi.org/10.4141/cjss66-003

McKinley, J.P., Zachara, J.M., Heald, S.M., Dohnalkova, A., Newville, M.G., Sutton, S.R., 2004. Microscale Distribution of Cesium Sorbed to Biotite and Muscovite. Environ. Sci. Technol. 38, 1017–1023. https://doi.org/10.1021/es034569m

Missana, T., García-Gutiérrez, M., Benedicto, A., Ayora, C., De-Pourcq, K., 2014. Modelling of Cs sorption in natural mixed-clays and the effects of ion competition. Appl. Geochemistry 49, 95–102. https://doi.org/10.1016/j.apgeochem.2014.06.011

Moore, D.M.M., Reynolds, R.C.J., 1997. X-Ray Diffraction and the Identification and Analysis of Clay Minerals, 2nd ed. Oxford University Press.

Mukai, H., Hirose, A., Motai, S., Kikuchi, R., Tanoi, K., 2016. Cesium adsorption / desorption behavior of clay minerals considering actual contamination conditions in Fukushima. Nat. Publ. Gr. 1–7. https://doi.org/10.1038/srep21543

Müller, H., Gering, F., Hübner, S., 1999. Documentation of the Terrestrial Food Chain and Dose Module FDMT in RODOS PV4. 0. RODOS (WG3)-TN (99) 9.

Nakagawa, S., Schielzeth, H., 2013. A general and simple method for obtaining R2 from generalized linear mixed-effects models. Methods

Ecol. Evol. 4, 133–142. https://doi.org/10.1111/j.2041-210x.2012.00261.x

Nakao, A., Takeda, A., Ogasawara, S., Yanai, J., Sano, O., Ito, T., 2015. Relationships between Paddy Soil Radiocesium Interception Potentials and Physicochemical Properties in Fukushima, Japan. J. Environ. Qual. 44, 780–788. https://doi.org/10.2134/jeq2014.10.0423

Nakao, A., Thiry, Y., Funakawa, S., Kosaki, T., 2008. Characterization of the frayed edge site of micaceous minerals in soil clays influenced by different pedogenetic conditions in Japan and northern Thailand. Soil Sci. Plant Nutr. 54, 479–489. https://doi.org/10.1111/j.1747-0765.2008.00262.x

Nelson, D.W., Sommers, L.E., 1996. Total carbon, organic carbon, and organic matter. Methods Soil Anal. Part 3 Chem. Methods 961–1010. https://doi.org/10.2136/sssabookser5.3.c34

Neugschwandtner, R.W., Száková, J., Pachtrog, V., Tlustoš, P., Černý, J., Kulhánek, M., Kaul, H.P., Euteneuer, P., Moitzi, G., Wagentristl, H., 2020. Basic soil chemical properties after 15 years in a long-term tillage and crop rotation experiment. Int. Agrophysics 34, 133–140. https://doi.org/10.31545/intagr/114880

Nguyen, H.Q., 2006. “The classification of soil systems on the basis of transfer factors from soil to reference plants”, Classification of Soil Systems on the Basis of Transfer Factors from Soil to Reference Plants. Vienna. https://doi.org/IAEA-TECDOC- 1497

Nisbet, A.F.., Woodman, R.F.M.., Haylock, R.G.E.., 1999. Recommended soil-to-plant transfer factors for radiocaesium and radiostrontium for use in arable systems. National Radiological Protection Board.

Ogasawara, S., Nakao, A., Yanai, J., 2013. Radiocesium interception potential (RIP) of smectite and kaolin reference minerals containing illite (micaceous mineral) as impurity. Soil Sci. Plant Nutr. 59, 852–857. https://doi.org/10.1080/00380768.2013.862158

Ogura, S.I., Suzuki, T., Saito, M., 2014. Distribution of radioactive cesium in soil and its uptake by herbaceous plants in temperate pastures with different management after the Fukushima Dai-Ichi Nuclear Power Station accident. Soil Sci. Plant Nutr. 60, 790–800. https://doi.org/10.1080/00380768.2014.954269

Orgiazzi, A., Ballabio, C., Panagos, P., Jones, A., Fernández-Ugalde, O., 2018. LUCAS Soil, the largest expandable soil dataset for Europe: a review. Eur. J. Soil Sci. 69, 140–153. https://doi.org/10.1111/ejss.12499

Ouzzani, M., Hammady, H., Fedorowicz, Z., Elmagarmid, A., 2016. Rayyan-a web and mobile app for systematic reviews. Syst. Rev. 5, 1–10. https://doi.org/10.1186/s13643-016-0384-4

Parfitt, R.L., Kimble, J.M., 1989. Conditions for Formation of Allophane in Soils. Soil Sci. Soc. Am. J. 53, 971–977. https://doi.org/10.2136/sssaj1989.03615995005300030057x

Poggio, L., de Sousa, L.M., Batjes, N.H., Heuvelink, G.B.M., Kempen, B.,

Ribeiro, E., Rossiter, D., 2021. SoilGrids 2.0: producing soil information for the globe with quantified spatial uncertainty. SOIL 7, 217–240. https://doi.org/10.5194/soil-7-217-2021

Pribyl, D.W., 2010. A critical review of the conventional SOC to SOM conversion factor. Geoderma. https://doi.org/10.1016/j.geoderma.2010.02.003

QGIS Development Team, 2024. QGIS Geographic Information System.

R Core Team, 2024. R: A Language and Environment for Statistical Computing.

Radočaj, D., Jurišić, M., Rapčan, I., Domazetović, F., Milošević, R., Plaščak, I., 2023. An Independent Validation of SoilGrids Accuracy for Soil Texture Components in Croatia. Land 12. https://doi.org/10.3390/land12051034

Rai, H., Kawabata, M., 2020. The Dynamics of Radio-Cesium in Soils and Mechanism of Cesium Uptake Into Higher Plants : Newly Elucidated Mechanism of Cesium Uptake Into Rice Plants 11, 80–90. https://doi.org/10.3389/fpls.2020.00528

Ribeiro, E., Batjes, N.H., Van Oostrum, A.J.M., 2018. World Soil Information Service (WoSIS) – Towards the standardization and harmonization of world soil data, Procedures manual 2018, Report 2018/01. Wageningen. https://doi.org/10.17027/isric-wdcsoils.20180001

Robison, W.L., Hamilton, T.F., Conrado, C.L., Kehl, S., 2006. Uptake of caesium-137 by leafy vegetables and grains from calcareous soils. International Atomic Energy Agency (IAEA).

Roig, M., Vidal, M., Rauret, G., Rigol, A., 2007. Prediction of Radionuclide Aging in Soils from the Chernobyl and Mediterranean Areas. J. Environ. Qual. 36, 943–952. https://doi.org/10.2134/jeq2006.0402

Rouiller, J., Burtin, G., Souchier, B., 1972. LA DISPERSION DES SOLS DANS L'ANALYSE GRANULOMETRIQUE, METHODE UTILISANT LES RESINES ECHANGEUSES D'IONS.

Sanchez, A.L., Wright, S.M., Smolders, E., Naylor, C., Stevens, P.A., Kennedy, V.H., Dodd, B.A., Singleton, D.L., Barnett, C.L., 1999. High plant uptake of radiocesium from organic soils due to Cs mobility and low soil K content. Environ. Sci. Technol. 33, 2752–2757. https://doi.org/10.1021/es990058h

Sandalls, J., Bennett, L., 1992. Radiocaesium in upland herbage in Cumbria, UK: A three year field study. J. Environ. Radioact. 16, 147–165. https://doi.org/10.1016/0265-931X(92)90013-J

Sanzharova, N.I., Fesenko, S. V., Spiridonov, S., 2002. The classification of Russian soils on the basis of transfer factors of radionuclides from soil to farm crops. Radioprotection 37, C1-521-C1-526. https://doi.org/10.1051/radiopro/2002097

Saracanlao, R.J., Ryckel, H., Everaert, M., Verbeeck, M., Smolders, E., 2022. Increasing phosphorus fertilizer value of recycled iron phosphates in

strong P-fixing soils by prolonged flooding and organic matter addition. https://doi.org/https://doi.org/10.21203/rs.3.rs-2138400/v1

Sawhney, B.L., 1972. Selective Sorption and Fixation of Cations by Clay Minerals: A Review. Clays Clay Miner. 20, 93–100. https://doi.org/10.1346/CCMN.1972.0200208

Schofield, R.K., Taylor, A.W., 1955. The Measurement of Soil pH. Soil Sci. Soc. Am. J. 19, 164–167. https://doi.org/https://doi.org/10.2136/sssaj1955.03615995001900020013x

Scott, A.D., Amonette, J., 1988. Role of Iron in Mica Weathering BT - Iron in Soils and Clay Minerals, in: Stucki, J.W., Goodman, B.A., Schwertmann, U. (Eds.), . Springer Netherlands, Dordrecht, pp. 537–623. https://doi.org/10.1007/978-94-009-4007-9_16

Selnaes, T.D., Strandt, P., 1992. Comparison of the Uptake of Radiocaesium From Soil to Grass After Nuclear Weapons Tests and the Chernobyl Accident*, ANALYST.

Semple, K.T., Doick, K.J., Jones, K.C., Burauel, P., Craven, A., Harms, H., 2004. Defining bioavailability and bioaccessibility of contaminated soil and sediment is complicated. Environ. Sci. Technol. 38, 228A-231A. https://doi.org/10.1021/es040548w

Shaw, G., Bell, J.N.B., 1991. Competitive Effects of Potassium and Ammonium on Caesium Uptake Kinetics in Wheat. J. Environ. Radioact. 13, 283–296. https://doi.org/10.1016/0265-931X(91)90002-W

Shoji, S., Takahashi, T., 2002. Environmental and agricultural significance of volcanic ash soils. Glob. Environ. Res. Ed. 6, 113–135.

Siderius, W., Njeru, E.B., 1976. Kenya Soil Survey - Soils of Trans Nzoia District - Site evaluation report. Nairobi.

Six, L., Pypers, P., Degryse, F., Smolders, E., Merckx, R., 2012. The performance of DGT versus conventional soil phosphorus tests in tropical soils - An isotope dilution study. Plant Soil 359, 267–279. https://doi.org/10.1007/s11104-012-1192-9

Skarlou, V., Papanicolaou, E.P., Nobeli, C., 1996. Soil to plant transfer of radioactive cesium and its relation to soil and plant properties, Geoderma. ELSEVIER.

Smolders, E., Van Den Brande, K., Merckx, R., 1997. Concentrations of 137Cs and K in soil solution plant availability of 137Cs in soils. Environ. Sci. Technol. 31, 3432–3438. https://doi.org/10.1021/es970113r

Soil Survey Staff, 1999. Soil Taxonomy: A basic system of soil classification for making and interpreting soil surveys, 2nd editio. ed, U.S. Department of Agriculture Handbook 436. Natural Resources Conservation Service, Washington DC, USA. https://doi.org/10.1007/BF01574372

Sparks, D.L., Huang, P.M., 1985. Physical chemistry of soil potassium. Potassium Agric. 201–276. https://doi.org/10.2134/1985.potassium.c9

Sposito, G., 2008. The Chemistry of Soils, 2nd ed, Science. Oxford University

Press, New York. https://doi.org/10.1126/science.ns-20.493.29

Squire, H.M., Middleton, L.J., 1966. Behaviour of cs137 in soils and pastures a long term experiment. Radiat. Bot. 6, 413–423. https://doi.org/10.1016/s0033-7560(66)80074-1

Środoń, J., Drits, V.A., McCarty, D.K., Hsieh, J.C.C., Eberl, D.D., 2001. Quantitative x-ray diffraction analysis of clay-bearing rocks from random preparations. Clays Clay Miner. 49, 514–528.

Steegmans, P., Sweeck, L., Smolders, E., 2023. Impact of soil weathering on radiocaesium uptake. KU Leuven.

Steiner, A.A., 1961. A universal method for preparing nutrient solutions of a certain desired composition. Plant Soil 15, 134–154. https://doi.org/10.1007/BF01347224

Steinhauser, G., Brandl, A., Johnson, T.E., 2014. Comparison of the Chernobyl and Fukushima nuclear accidents: A review of the environmental impacts. Sci. Total Environ. 470–471, 800–817. https://doi.org/10.1016/j.scitotenv.2013.10.029

Strebl, F., Ehlken, S., Gerzabek, M.H., Kirchner, G., 2007. Behaviour of radionuclides in soil/crop systems following contamination. Radioact. Environ. 10, 19–42. https://doi.org/10.1016/S1569-4860(06)10002-9

Sweeck, L., Camps, J., Mikailova, R., Almahayni, T., 2020. Role of modelling in monitoring soil and food during different stages of a nuclear emergency. J. Environ. Radioact. 225, 106444. https://doi.org/10.1016/j.jenvrad.2020.106444

Tagami, K., Tsukada, H., Uchida, S., Howard, B.J., 2018. Changes in the Soil to Brown Rice Concentration Ratio of Radiocaesium before and after the Fukushima Daiichi Nuclear Power Plant Accident in 2011. Environ. Sci. Technol. 52, 8339–8345. https://doi.org/10.1021/acs.est.8b01745

Tarsitano, D., Young, S.D., Crout, N.M.J., 2011. Evaluating and reducing a model of radiocaesium soil-plant uptake. J. Environ. Radioact. 102, 262–269. https://doi.org/10.1016/j.jenvrad.2010.11.017

Thiry, Y., 1997. ETUDE DU CYCLE DE RADIOCESIUM EN ECOSYSTEME FORESTIER: Distribution et fracteurs de mobilité. Université Catholique de Louvain.

Thiry, Y., Vandecasteele, C.M., Delvaux, B., 1996. Ability of specimen minerals to fix radiocaesium: effect of the chemical environment. Sck-cen, Mol Belgium.

Torrent, J., Schwertmann, U., Schulze, D.G., 1980. Iron oxide mineralogy of some soils of two river terrace sequences in Spain. Geoderma 23, 191–208. https://doi.org/10.1016/0016-7061(80)90002-6

Uematsu, S., 2017. Radiocaesium transfer to crops in the Fukushima affected environments: a soil chemical and plant physiological approach. KULeuven.

Uematsu, S., Smolders, E., Sweeck, L., Wannijn, J., Van Hees, M., Vandenhove, H., 2015. Predicting radiocaesium sorption characteristics

with soil chemical properties for Japanese soils. Sci. Total Environ. 524–525, 148–156. https://doi.org/10.1016/j.scitotenv.2015.04.028

Uematsu, S., Vandenhove, H., Sweeck, L., Van Hees, M., Smolders, E., 2018. Radiocaesium bioavailability to flooded paddy rice is related to soil solution radiocaesium and potassium concentrations. Plant Soil 428, 415–426. https://doi.org/10.1007/s11104-018-3686-6

Uematsu, S., Vandenhove, H., Sweeck, L., Van Hees, M., Wannijn, J., Smolders, E., 2016. Variability of the soil-to-plant radiocaesium transfer factor for Japanese soils predicted with soil and plant properties. J. Environ. Radioact. 153, 51–60. https://doi.org/10.1016/j.jenvrad.2015.12.012

USDA, 2001. Soil Quality Test Kit Guide. Soil Qual. Inst. 82. https://doi.org/10.1037/t15144-000

USDA, 1954. Diagnosis and improvement of saline and alkali soils, Soil Science Society of America Journal. United States Departement of Agriculture. Soil and Water Conservative Research Branch, Agricultural Research Service. https://doi.org/10.2136/sssaj1954.03615995001800030032x

Valcke, E., Cremers, A., 1994. Sorption-desorption dynamics of radiocaesium in organic matter soils.

Van Bergeijk, K.E., Noordijk, H., Lembrechts, J., Frissel, M.J., 1992. Influence of pH, soil type and soil organic matter content on soil-to-plant transfer of radiocesium and -strontium as analyzed by a nonparametric method. J. Environ. Radioact. 15, 265–276. https://doi.org/10.1016/0265-931X(92)90062-X

Van Der Ploeg, T., Austin, P.C., Steyerberg, E.W., 2014. Modern modelling techniques are data hungry: A simulation study for predicting dichotomous endpoints. BMC Med. Res. Methodol. 14, 1–13. https://doi.org/10.1186/1471-2288-14-137

van Rossum, G., 1995. Python tutorial. Amsterdam.

Van Wambeke, A., 1992. Soils of the tropics: properties and appraisal, 1st ed. McGraw-Hill, New York.

Vandebroek, L., Van Hees, M., Delvaux, B., Spaargaren, O., Thiry, Y., 2012. Relevance of Radiocaesium Interception Potential (RIP) on a worldwide scale to assess soil vulnerability to 137Cs contamination. J. Environ. Radioact. 104, 87–93. https://doi.org/10.1016/j.jenvrad.2011.09.002

Vandenhove, H., Cremers, A., Smolders, E., Van Hees, M., 2005. Effect of K and bentonite additions on Cs-transfer to ryegrass. J. Environ. Radioact. 81, 233–253. https://doi.org/10.1016/j.jenvrad.2004.01.038

Vandenhove, H., Smolders, E., Cremers, A., 2003. Potassium bentonites reduce radiocaesium availability to plants. Eur. J. Soil Sci. 54, 91–102. https://doi.org/10.1046/j.1365-2389.2003.00509.x

Vanheukelom, M., Sweeck, L., Almahayni, T., De Bruyn, M., Steegmans, P., Fondu, L., Van Gompel, A., Van Hees, M., Wannijn, J., Smolders, E.,

2024. Highly weathered mineral soils have highest transfer risk of radiocaesium contamination after a nuclear accident: A global soil-plant study. Sci. Total Environ. 173583. https://doi.org/https://doi.org/10.1016/j.scitotenv.2024.173583

Vanheukelom, M., Sweeck, L., Van Hees, M., Weyns, N., Van Orshoven, J., Smolders, E., 2023. Quantitative clay mineralogy predicts radiocesium bioavailability to ryegrass grown on reconstituted soils. Sci. Total Environ. 873, 162372. https://doi.org/10.1016/J.SCITOTENV.2023.162372

Vermeer, A.W.P., McCulloch, J.K., Van Riemsdijk, W.H., Koopal, L.K., 1999. Metal ion adsorption to complexes of humic acid and metal oxides: Deviations from the additivity rule. Environ. Sci. Technol. 33, 3892–3897. https://doi.org/10.1021/es990260k

Waegeneers, N., Smolders, E., Merckx, R., 1999. A Statistical Approach for Estimating the Radiocesium Interception Potential of Soils. J. Environ. Qual. 28, 1005–1011. https://doi.org/10.2134/jeq1999.00472425002800030034x

Wauters, J., Elsen, A., Cremers, A., 1996a. Prediction of solid/liquid distribution coefficients of radiocaesium in soils and sediments. Part three: A quantitative test of a K(D) predictive equation. Appl. Geochemistry 11, 601–603. https://doi.org/10.1016/0883-2927(96)00029-7

Wauters, J., Elsen, A., Cremers, A., Konoplev, A. V., Bulgakov, A.A., Comans, R.N.J., 1996b. Prediction of solid/liquid distribution coefficients of radiocaesium in soils and sediments. Part one: A simplified procedure for the solid phase characterisation. Appl. Geochemistry 11, 589–594. https://doi.org/10.1016/0883-2927(96)00027-3

Wauters, J., Sweeck, L., Valcke, E., Elsen, A., Cremers, A., 1994. Availability of radiocaesium in soils: a new methodology. Sci. Total Environ. 157, 239–248. https://doi.org/10.1016/0048-9697(94)90585-1

Wauters, J., Vidal, M., Elsen, A., Cremers, A., 1996c. Prediction of solid/liquid distribution coefficients of radiocaesium in soils and sediments. Part two: A new procedure for solid phase speciation of radiocaesium. Appl. Geochemistry 11, 595–599. https://doi.org/10.1016/0883-2927(96)00028-5

Willey, N.J., 2010. Phylogeny can be used to make useful predictions of soil-to-plant transfer factors for radionuclides. Radiat. Environ. Biophys. 49, 613–623. https://doi.org/10.1007/s00411-010-0320-2

Wynne, B., 1992. Uncertainty and environmental learning: Reconceiving science and policy in the preventive paradigm, in: Global Environmental Change. pp. 111–127. https://doi.org/10.1016/0959-3780(92)90017-2

Zeelmaekers, E., 2011. Computerized qualitative and quantitative clay mineralogy: introduction and application to known geological cases. K.U.Leuven. Faculteit Wetenschappen, Leuven.

Zhu, Y.-G.G., Smolders, E., 2000. Plant uptake of radiocaesium: a review of

mechanisms, regulation and application. J. Exp. Bot. 51, 1635–1645. https://doi.org/10.1093/jexbot/51.351.1635

Supplementary information

APPENDIX I

The fate of radiocaesium in the soil-plant system

APPENDIX II

A database for predicting radiocaesium soil-to-plant transfer on a global scale

APPENDIX III

Quantitative clay mineralogy predicts radiocesium bioavailability to ryegrass grown on clay-sand mixtures

APPENDIX IV

Highly weathered mineral soils have highest transfer risk of radiocaesium contamination after a nuclear accident: a global soil-plant study

APPENDIX V

The clay mineralogy rather than the clay content determines radiocaesium adsorption in soils

APPENDIX VI

Advancing global radiocaesium soil-to-plant transfer predictions: Feasibility, modeling, mapping, and future challenges

Appendix I
The fate of radiocaesium in the soil-plant system

The equations and parameter values of the Absalom 1999 (Absalom et al., 1999), Absalom 2001 (Absalom et al., 2001), Absalom 2011 and Tarsitano 2011 (Tarsitano et al., 2011) models, mentioned in all chapters, are given here.

Table I.1. Model equations of the Absalom model and its variants.

Absalom 1999

$$CR = \frac{CF}{K_{D_{labile}}} \cdot D \tag{I.1}$$

$$D = P_{fast} \cdot e^{-k_{fast} \cdot t} + (1 - P_{fast}) \cdot e^{-k_{slow} \cdot t} \tag{I.2}$$

$$\log_{10}(CF) = -a_2 \cdot \log_{10}\left(\min\left(\frac{[K^+]}{1000}, a_{lim}\right) - a_1\right) \tag{I.3}$$

$$[K^+] = b_3 \cdot \frac{exchK}{CEC_{clay} \cdot \frac{clay}{100}} + b_4 \tag{I.4}$$

$$K_{D_{labile}} = \frac{RIP}{[K^+]} = \frac{b_5 + b_6 \cdot (clay)^2}{\left(\frac{[K^+]}{1000}\right)^{n_1}} \tag{I.5}$$

Absalom 2001

$$CR = \frac{CF}{K_{D_{labile}}} \cdot D \tag{I.6}$$

$$D = P_{fast} \cdot e^{-k_{fast} \cdot K_{D_r} \cdot t} + (1 - P_{fast}) \cdot e^{-k_{slow} \cdot K_{D_r} \cdot t} \tag{I.7}$$

$$\log_{10}(CF) = -a_1 - a_2 \cdot \log_{10}\left(\frac{[K^+]}{1000}\right) \tag{I.8}$$

$$[K^+] = \frac{exchK_{humus} \cdot \sqrt{[Ca^{2+} + Mg^{2+}]}}{k_{G_{humus}} \cdot (CEC_{humus} - exchK_{humus})} \cdot 1000 \tag{I.9}$$

$$\log_{10}\left(\frac{[Ca^{2+} + Mg^{2+}]}{1000}\right) = -a_3 + a_4 \cdot pH \tag{I.10}$$

$$CEC_{humus} = a_5 + a_6 \cdot pH \tag{I.11}$$

$$exchK_{humus} = \frac{exchK}{\frac{k_{G_{clay}} \cdot CEC_{clay} \cdot \frac{clay}{100}}{k_{G_{humus}} \cdot CEC_{humus}} + \frac{SOM}{100}} \tag{I.12}$$

$$K_{D_r} = \frac{K_{D_{clay}}}{K_{D_{labile}}} \tag{I.13}$$

$$K_{D_{labile}} = K_{D_{humus}} + K_{D_{clay}} \tag{I.14}$$

$$K_{D_{humus}} = \frac{0.01 \cdot \frac{SOM}{100} \cdot exchK_{humus}}{\frac{[K^+]}{1000}} \tag{I.15}$$

$$K_{D_{clay}} = \frac{RIP}{[K^+] + a_7 \cdot [NH_4{}^+]} = \frac{RIP_{clay} \cdot \frac{clay}{100}}{\frac{[K^+]}{1000} + a_7 \cdot \frac{[NH_4{}^+]}{1000}} \tag{I.16}$$

$$\log_{10}(RIP_{clay}) = a_9 - a_8 \cdot \frac{SOM}{clay} \tag{I.17}$$

Absalom 2011

$$CR = \frac{CF}{K_{D_{labile}}} \cdot D \tag{I.18}$$

$$D = e^{-k_{fast} \cdot t} \tag{I.19}$$

$$\log_{10}(CF) = -a_1 - a_2 \cdot \log_{10}\left(\frac{[K^+]}{1000}\right) \tag{I.20}$$

$$[K^+] = \frac{exchK_{humus} \cdot \sqrt{[Ca^{2+} + Mg^{2+}]}}{k_{G_{humus}} \cdot (CEC_{humus} - exchK_{humus})} \cdot 1000 \tag{I.21}$$

$$\log_{10}\left(\frac{[Ca^{2+} + Mg^{2+}]}{1000}\right) = -a_3 + a_4 \cdot pH \tag{I.22}$$

$$CEC_{humus} = a_5 + a_6 \cdot pH \tag{I.23}$$

$$exchK_{humus} = \frac{exchK}{\frac{k_{G_{clay}} \cdot CEC_{clay} \cdot \frac{clay}{100}}{k_{G_{humus}} \cdot CEC_{humus}} + \frac{SOM}{100}} \tag{I.24}$$

$$K_{D_{labile}} = K_{D_{humus}} + K_{D_{clay}} \tag{I.25}$$

$$K_{D_{humus}} = \frac{0.01 \cdot \frac{SOM}{100} \cdot exchK_{humus}}{\frac{[K^+]}{1000}} \tag{I.26}$$

$$K_{D_{clay}} = \frac{RIP}{[K^+] + a_7 \cdot [NH_4{}^+]} = \frac{RIP_{clay} \cdot \frac{clay}{100}}{\frac{[K^+]}{1000} + a_7 \cdot \frac{[NH_4{}^+]}{1000}} \tag{I.27}$$

$$\log_{10}(RIP_{clay}) = a_9 - a_8 \cdot \frac{SOM}{clay} \tag{I.28}$$

Tarsitano 2011

$$CR = \frac{CF}{K_{D_{labile}}} \cdot D \tag{I.29}$$

$$D = e^{-k_{fast} \cdot t} \tag{I.30}$$

$$\log_{10}(CF) = -a_1 - a_2 \cdot \log_{10}\left(\frac{[K^+]}{1000}\right) \tag{I.31}$$

$$[K^+] = \frac{exchK}{\alpha \cdot \frac{SOM}{100} + \beta \cdot \frac{clay}{100} - \gamma \cdot exchK} \cdot 1000 \tag{I.32}$$

$$K_{D_{labile}} = K_{D_{min}} + K_{D_{clay}} \tag{I.33}$$

$$K_{D_{clay}} = \frac{RIP}{[K^+] + a_7 \cdot [NH_4{}^+]} = \frac{RIP_{clay} \cdot \frac{clay}{100}}{\frac{[K^+]}{1000} + a_7 \cdot \frac{[NH_4{}^+]}{1000}} \tag{I.34}$$

$$\log_{10}(RIP_{clay}) = a_9 - a_8 \cdot \frac{SOM}{clay} \tag{I.35}$$

Table I.2. Input variables of the Absalom model and its variants. (adapted from Tarsitano et al., 2011)

variable	*description*	*unit*
clay	soil clay content	$\mathrm{g\ 100\ g^{-1}}$
SOM	soil organic matter content	$\mathrm{g\ 100\ g^{-1}}$
pH	soil pH	–
exchK	exchangeable K^+ content in the soil	$\mathrm{cmol_c\ kg^{-1}}$
$[\mathrm{NH_4}^+]$	concentration of K^+ in the soil solution	$\mathrm{mmol\ L^{-1}}$
t	soil-radiocaesium contact time	days

Table I.3. Model variables of the Absalom model and its variants. (adapted from Tarsitano et al., 2011)

variable	*description*	*unit*
CR	radiocaesium concentration ratio	$\mathrm{kg\ kg^{-1}}$
CF	grass concentration factor	$\mathrm{L\ kg^{-1}}$
D	dynamic factor (0–1) describing the change in labile radiocaesium with time	–
$\mathrm{K_{D_{labile}}}$	radiocaesium solid-liquid distribution coefficient of the labile fraction describing the constant distribution between the adsorbed labile and solution radiocaesium concentrations	$\mathrm{L\ kg^{-1}}$
$\mathrm{K_{D_r}}$	proportion of the labile radiocaesium adsorbed on the clay fraction	$\mathrm{L\ kg^{-1}}$
$\mathrm{K_{D_{humus}}}$	radiocaesium solid-liquid distribution coefficient on the humus fraction	$\mathrm{L\ kg^{-1}}$
$\mathrm{K_{D_{clay}}}$	radiocaesium solid-liquid distribution coefficient on the clay fraction	$\mathrm{L\ kg^{-1}}$
$\mathrm{CEC_{humus}}$	cation exchange capacity in the humus fraction	$\mathrm{cmol_c\ kg^{-1}}$
$\mathrm{exchK_{humus}}$	exchangeable K^+ content in the humus fraction	$\mathrm{cmol_c\ kg^{-1}}$
$[\mathrm{K^+}]$	concentration of K^+ in the soil solution	$\mathrm{mmol\ L^{-1}}$
$[\mathrm{Ca^{2+}} + \mathrm{Mg^{2+}}]$	concentration of Ca^{2+} and Mg^{2+} in the soil solution	$\mathrm{mmol\ L^{-1}}$
RIP	radiocaesium interception potential of the soil	$\mathrm{mol\ kg^{-1}\ soil}$
$\mathrm{RIP_{clay}}$	radiocaesium interception potential of the clay fraction	$\mathrm{mol\ kg^{-1}\ clay}$

Table I.4. Parameter values of the Absalom model and its variants. (adapted from Tarsitano et al., 2011)

para-meter	*description*	*unit*	*value*			
			Absalom 1999	*Absalom 2001*	*Absalom 2011*	*Tarsitano 2011*
a_1	baseline log-transformed radiocaesium CF in grass when the log-transformed K concentration in the soil solution is zero which indicates the intrinsic radiocaesium uptake ratio under low or negligible K availability	$\log_{10}(\mathrm{L\ kg^{-1}})$	5.23	2.57 ± 0.10	3.10 ± 0.20	2.49 ± 0.21
a_2	rate at which the log-transformed radiocaesium CF in plants decreases in response to increasing log-transformed K concentrations in the soil solution where a higher value of a_2 suggests a stronger inverse relationship between K availability and radiocaesium uptake in plants	$\log_{10}(\mathrm{L\ kg^{-1}}) \cdot \log_{10}(\mathrm{L\ mol^{-1}})$	2.42	1.56 ± 0.32	1.80 ± 0.05	1.64 ± 0.06
a_{lim}	K^+ concentration above which CF has a constant minimum value	$\mathrm{mol\ L^{-1}}$	0.0024			

para-meter	*description*	*unit*	*value*			
			Absalom 1999	*Absalom 2001*	*Absalom 2011*	*Tarsitano 2011*
b_3	rate of change in the proportion of K occupying the inorganic CEC in response to changes in the concentration of K in the soil solution	$\mathrm{mol\ L^{-1}}$	0.0000765			
b_4	baseline proportion of K occupying the inorganic CEC in the soil, when the concentration of K in the soil solution is zero	$\mathrm{mol\ L^{-1}}$	0.0000625			
a_3	baseline log-transformed concentration of Ca^{2+} and Mg^{2+} in the soil solution when soil pH is zero which reflects the inherent availability of Ca^{2+} and Mg^{2+} in soils when the pH effect is minimal	$\log_{10}(\mathrm{mol\ L^{-1}})$		3.368	3.368	

para-meter	description	unit	value			
			Absalom 1999	Absalom 2001	Absalom 2011	Tarsitano 2011
a_4	rate at which the log-transformed concentration of Ca^{2+} and Mg^{2+} in the soil solution increases as soil pH increases where higher soil pH is associated with increased availability of Ca^{2+} and Mg^{2+} in the soil solution	–		0.16	0.16	
b_5	baseline $K_{D\ labile}$ reflecting the radiocaesium retention potential of the soil matrix when Cs^+:K^+ interactions are minimized	$\mathrm{L\ kg^{-1} \cdot mol^{n_1}\ L^{-n_1}}$	2.38			
b_6	clay-dependent coefficient reflecting how radiocaesium in increasingly retained in the soil matrix when the clay content increases	$\mathrm{L\ kg^{-1} \cdot mol^{n_1}\ L^{-n_1}}$	0.27			
n_1	exponent coefficient reflecting the sensitivity of the $K_{D\ labile}$ to variations in K concentration in the soil solution	–	0.676			

para-meter	*description*	*unit*	*value*			
			Absalom 1999	*Absalom 2001*	*Absalom 2011*	*Tarsitano 2011*
a_5	baseline CEC of the humus fraction to provide the intrinsic CEC value when the effect of proton competition on organic adsorption sites is minimal	$\mathrm{cmol_c\ kg^{-1}}$		-34.66	-34.66	
a_6	rate of increase in the CEC of the humus fraction as pH rises which reflects how the specific adsorption on organic sites (mainly carboxyl groups) increases with pH as proton competition decreases	$\mathrm{cmol_c\ kg^{-1} \cdot \log_{10}(L\ mol^{-1})}$		29.72	29.72	
a_7	empirical parameter accounting for the competitive effect of NH_4^+ on radiocaesium adsorption in the clay fraction which reflects the stronger competition of NH_4^+ over K^+ ions for selective adsorption sites in clay	–		4.167 ± 0.27	1.51 ± 0.35	1.51 ± 0.35

para-meter	*description*	*unit*	*value*			
			Absalom 1999	*Absalom 2001*	*Absalom 2011*	*Tarsitano 2011*
a_8	coefficient describing the inverse relationship between the RIP in the clay fraction and the ratio of SOM to clay content indicating how increasing organic matter relative to clay content decreases the ability of clay to specifically adsorb radiocaesium	$\log_{10}(\mathrm{mol\ kg^{-1}})$		0.043 ± 0.017	0.027 ± 0.004	0.077 ± 0.013
a_9	baseline coefficient representing the intrinsic RIP of the clay fraction when the organic matter has minimal influence	$\log_{10}(\mathrm{mol\ kg^{-1}})$		1.74 ± 0.17	1.55 ± 0.07	1.65 ± 0.06
$k_{G_{humus}}$	Gapon exchange coefficient for humus	$\mathrm{mol^{-0.5}\ L^{0.5}}$		2.32 ± 0.10	1.68 ± 0.25	
$k_{G_{clay}}$	Gapon exchange coefficient for clay	$\mathrm{mol^{-0.5}\ L^{0.5}}$		3.18 ± 0.44	4.60 ± 0.73	
CEC_{clay}	average CEC of clay across pH range 2.5–8 (*N* = 60)	$\mathrm{cmol_c\ kg^{-1}\ clay}$	50	50	50	
k_{fast}	time constant for fast radiocaesium:soil fixation	$\mathrm{d^{-1}}$	0.0019	0.0019		

para-meter	*description*	*unit*	*value*			
			Absalom 1999	*Absalom 2001*	*Absalom 2011*	*Tarsitano 2011*
k_{slow}	time constant for slow radiocaesium:soil fixation	d^{-1}	0.00019	0.00019	0.000253 ± 0.000090	0.000273 ± 0.000085
P_{fast}	proportion of soil radiocaesium undergoing fast fixation	–	0.814	0.814		
α	coefficient representing the effect of SOM on the K^+ concentration in the soil solution	$cmol_c\ kg^{-1} \cdot L\ mol^{-1}$				2451 ± 372
β	coefficient representing the effect of clay on the K^+ concentration in the soil solution	$cmol_c\ kg^{-1} \cdot L\ mol^{-1}$				4645 ± 677
γ	coefficient representing the effect of exchK on the K^+ concentration in the soil solution	$L\ mol^{-1}$				69.2 ± 46.6
$K_{D_{min}}$	minimum value of the labile radiocaesium solid-liquid distribution coefficient	$L\ kg^{-1}$				134.8 ± 30.65

Appendix II
A database for predicting radiocaesium soil-to-plant transfer on a global scale

A detailed description of the information recorded in the radiocaesium soil-to-plant transfer database is given below.

Table II.1. Description of attributes (or columns) in the database grouped per table (or relation). Options were given for a limited selection of choices.

attribute table	*attribute*	*description*	*options*
reference	title	Title of the reference.	
	year	Year of publication of the reference.	
	authors	Authors that contributed to the reference.	
	journal	Journal name in which the reference was published.	
	url	URL of the location of the web page to access the reference.	
	language	Language in which the reference was published.	
	pages	Number of pages of reference.	
	volume	Journal volume in which the reference was published.	
	remarks	Remarks on the reference (e.g., comments related to the entry of the data into the database or factors affecting the quality of the data).	
experiment_siteCondition	soil_condition	Condition of the soil in which the plant was grown: aerated silica-based soils; flooded silica-based soils; other such as coral marine-based soils (e.g., Atoll soil).	aerated; flooded; other
	land_use	Land use at the location where the soil was sampled at the moment of the study.	arable; grassland; forest; paddy; subsoil; not specified
	soil_code	Code of the substrate sample, soil, or plot assigned in the study (e.g., table number and row number in reference). If no code was given in the reference, a logical code was assigned so that the information of the record could be traced within the reference.	
	experiment_date	Date the plant material was harvested.	

attribute table	*attribute*	*description*	*options*
caesium	isotopes	Caesium isotopes that were investigated. If ^{134}Cs and ^{137}Cs were both given, the summed concentration was calculated.	133Cs; 134Cs; 137Cs; 134Cs+137Cs; not specified
soil_origin	climate	Climate zone of the location where the soil was sampled according to the Köppen Climate Classification System (Beck et al., 2018). If no climate data were given in the reference, the climate zone was determined from the coordinate data or soil origin (land or city).	tropical (Af, Am, As, Aw); arid (BSh, BSk, BWh, BWk); temperate (Cfa, Cfb, Cfc, Csa, Csb, Csc, Cwa, Cwb, Cwc); continental (Dfa, Dfb. Dfc, Dfd, Dsa, Dsb, Dsc, Dwa, Dwb, Dwc, Dwd); polar (EF, ET)
	precipitation_mm	Average annual precipitation at the sampling location, expressed in mm.	
	country	Country of the location where the soil was sampled. If the country was unknown, the location of the research institute was chosen.	
	city	City of the location where the soil was sampled. This was left empty if the city was unknown or the study was conducted across the country.	
soil_class	soil_major_group	Reference soil group according to World Reference Base (IUSS Working Group WRB FAO, 2022). If no soil classes were given in the literature, the reference soil group was determined from the coordinate data of the location where the soil was sampled or soil origin (city) using the global reference WRB soil group map (https://soilgrids.org/).	Andosol; Cambisol; Ferralsol; etc.
	soil_qualifier	Soil qualifiers for specific soil characteristics according to World Reference Base (IUSS Working Group WRB FAO, 2022). If the soil qualifier was unknown, this was left empty.	Haplic; Cambic; Calcic; etc.

attribute table	*attribute*	*description*	*options*
plant_info	plant_category	Category of plants based on plant species as defined in IAEA (2021) which in turn is based on IAEA (2009): cereals (wheat, barley, oats, sorghum, millet (grain or flour)); maize (corn); rice; leafy vegetables (cabbage, cauliflower, spinach, leek, lettuce); non-leafy vegetables (chili pepper, cucumber, eggplant, pumpkin, tomato, onions, garlic); leguminous vegetables (beans, lentil, peas); root crops (carrot, radish); tubers (potato, swedes); fruits (herbaceous plants, shrubs, woody trees, non-woody trees); grass (cultivated, pasture, leguminous fodder); herbs (tea, thyme, spices); medicinal plants (shrubs, woody trees, non-woody trees); other crops (cacao beans, coffee beans, peanuts).	cereals; maize; rice; grass; leafy vegetables; non-leafy vegetables; leguminous vegetables; root crops; tubers; fruits; herbs; medicinal plants; other crops
	plant_common_name	Common name of the plant (e.g., cabbage, carrot, grass, parsley).	
	plant_genus	Genus of the plant, or family if only family of plant was recorded (e.g., Brassica, Daucus, Lolium, Petroselinum).	not specified; mixture; Brassica; Daucus; Lolium; Petroselinum; etc.
	plant_species	Species of the plant (e.g., B. oleracea, D. carota, L. perenne, P. crispum).	not specified; mixture; oleracea; carota; perenne; crispum; etc.
quality_control	quality_control	Quality control procedures that were applied to make measurement results as reliable and reproducible as possible, such as participation in proficiency testing (interlaboratory control) and the use of reference materials for internal validation of results (intralaboratory control) (IAEA, 2021).	proficiency tests; intercomparison exercises; reference materials; none
	sampling_strategy	Sampling strategy was reported.	yes; no
	equipment_sampling	Sampling equipment was reported.	yes; no

attribute table	*attribute*	*description*	*options*
	equipment_measurement	Measurement equipment was reported.	yes; no
measurement	soilCs_BqPerKg	Total or extractable concentration of native or added caesium isotope in the substrate (e.g., soil), expressed in Bq per kg oven-dry substrate or µmol per kg oven-dry substrate. Concentration in the soil in the field referred to the upper 10 cm of soil layer for grass and 20 cm for all crops. Concentration in litter or plant basis was not considered.	
	soilCs_error_BqPerKg	Standard deviation of the caesium isotope concentration in the substrate in case of replicates.	
	soilCs_noOfObservation	Number of observations or replicates of caesium isotope in the substrate.	
	poreWaterCs_BqPerL	Concentration of caesium isotope in pore water or soil solution before or after plant harvest, expressed in Bq per L pore water or µmol per L pore water. If concentrations were given before and after harvest, the average was taken.	
	poreWaterCs_error_BqPerL	Standard deviation of the caesium isotope concentration in pore water in case of replicates.	
	poreWaterCs_noOfObservation	Number of observations or replicates of caesium isotope in pore water.	
	plantCs_BqPerKg	Concentration of caesium isotope in the plant part, expressed in Bq per kg plant material or µmol per kg plant material. If not stated otherwise, the concentration in the plant referred to the concentration in the edible part at harvest.	

attribute table	*attribute*	*description*	*options*
	plantCs__error_BqPerKg	Standard deviation of the caesium isotope concentration in plant in case of replicates.	
	plantCs_noOfObservation	Number of observations or replicates of caesium isotope in the plant.	
	plant_weightBasis	Plant material weight was measured on a fresh or oven-dry weight basis. If not stated otherwise, it was assumed that plant material was measured on a fresh weight basis.	dry; wet
	plant_washedNotWashed	Plant material was washed or not before activity measurements.	washed; not washed
	plant_biomassYield_g	Fresh or oven-dry weight of plant material, expressed in g plant material.	
	CR_m2PerKg	The ratio of concentrations (CR) of caesium isotope in the plant material, expressed in Bq per kg dried plant material, to that in the substrate (e.g., soil), expressed in Bq per m^2 substrate.	
	CR_KgPerKg	Ratio of concentrations (CR) of caesium isotope in the plant material, expressed in Bq per kg dried plant material, to that in the substrate (e.g., soil), expressed in Bq per kg oven-dry substrate layer. For grass, the activity 0–10 cm soil layer is taken, and for other crops, the 0–20 cm soil layer. Activity in deeper layers may be neglected. If only the CR based on deposition activity on soil was reported, expressed in m^2 substrate per kg plant, and no activity measurements were made on soil samples, the CR was calculated with deposition correction based on recorded or assumed soil sampling depth (10 or 20 cm) and soil density (1300 kg per m^3).	
	CR_error_KgPerKg	Standard deviation of CR in case of replicates.	

attribute table	attribute	description	options
	CR_noOf Oberserva tion	Number of observations or replicates of CR.	
	CR_dataA cquisition	CR information was extracted from the reference by copying numerical data from tables or graphs using an online data extraction tool.	CR given; conc given; CR graph; conc graph; recovery
	CR_expre ssion	CR was obtained from measured concentrations in the substrate; or calculated based on activity deposition measurements per unit of soil surface area and measured soil density, i.e., the investigator(s) corrected for soil density; or calculated based on activity deposition measurements per unit of soil surface area and assumed soil density (1300 kg per m^3), i.e., the investigator(s) did not correct for soil density.	measured; deposition and soil density corrected; deposition and not corrected
	dominant PhyllMiner al	Mineral that dominates the group of layered minerals on a weight basis. If multiple dominant minerals were present in the same content range, the mineral with the highest radiocaesium interception potential per unit clay weight was listed (e.g., illite > biotite > vermiculite > smectite > kaolinite > halloysite > allophane & imogolite).	illite; biotite; smectite; vermiculite; kaolinite; halloysite; allophane&imogolite
	quantified Mineralog y	Information on substrate mineralogy available: qualitative or mineral composition quantified in weight percentages.	qualitative; quantitative; none
	pH_salt	pH of the substrate was measured in salt solution (e.g., 0.01 mol per L $CaCl_2$ or 1 mol per L KCl)	
	pH_water	pH of the substrate was measured in water, or if the pH method was not specified.	
	OC_perce ntage	Organic carbon content of the substrate, expressed in weight percentage or g per 100 g. If humus content or soil organic matter was given, a conversion factor of 0.58 was used to convert to OC.	
	LOI_perce ntage	Organic matter content of the substrate based on Loss-On-Ignition, expressed in weight percentage or g per 100 g oven-dry substrate.	

attribute table	*attribute*	*description*	*options*
	moistureContent_percentage	Water holding capacity of the substrate, expressed in g water per 100 g oven-dry substrate.	
	EC_microSPerCm	Conductivity of the substrate, expressed in µS per cm.	
	CEC_cmolcPerKg	Cation exchange capacity of the substrate, expressed in cmol(+) cations per kg oven-dry substrate or milli-equivalents cations per 100 g oven-dry substrate. If the total CEC was not reported, the sum of the exchanged base cations (Ca, K, Mg, Na) was calculated in the case of (nearly) 100% base saturation.	
	RIP_mmolPerKg	Radiocaesium interception potential of the substrate, expressed in mmol per kg oven-dry substrate.	
	poreWater_K_mmolPerL	Potassium concentration in pore water or soil solution before or after plant harvest, expressed in mmol K per L pore water. If concentrations were given before and after harvest, the average was taken.	
	poreWater_NH4_mmolPerL	Ammonium concentration in pore water or soil solution before or after plant harvest, expressed in mmol NH_4 per L pore water. If concentrations were given before and after harvest, the average was taken.	
	poreWater_Na_mmolPerL	Sodium concentration in pore water or soil solution before or after plant harvest, expressed in mmol Na per L pore water. If concentrations were given before and after harvest, the average was taken.	

attribute table	attribute	description	options
	poreWater_CaMg_mmolPerL	Calcium and magnesium concentration in pore water or soil solution before or after plant harvest, expressed in mmol Ca+Mg per L pore water. If the concentrations were given separately, they were summed. If concentrations were given before and after harvest, the average was taken.	
	exchangeable_K_cmolcPerKg	Exchangeable potassium content in the substrate, expressed in cmol(+) K per kg oven-dry substrate or milli-equivalents K per 100 g oven-dry substrate. If contents were given before and after harvest, the average was taken.	
	exchangeable_NH4_cmolcPerKg	Exchangeable ammonium content in the substrate, expressed in cmol(+) NH_4 per kg oven-dry substrate or milli-equivalents NH_4 per 100 g oven-dry substrate. If contents were given before and after harvest, the average was taken.	
	exchangeable_Na_cmolcPerKg	Exchangeable sodium content in the substrate, expressed in cmol(+) Na per kg oven-dry substrate or milli-equivalents Na per 100 g oven-dry substrate. If contents were given before and after harvest, the average was taken.	
	exchangeable_CaMg_cmolcPerKg	Exchangeable calcium and magnesium content in the substrate, expressed in cmol(+) Ca+Mg per kg oven-dry substrate or milli-equivalents Ca+Mg per 100 g oven-dry substrate. If the contents were given separately, they were summed. If contents were given before and after harvest, the average was taken.	
	plant_K_gPerKg	Concentration of potassium in the plant part, expressed in g K per kg plant material. If not stated otherwise, the concentration in the plant referred to the concentration in the edible part at harvest.	
	plant_Na_gPerKg	Concentration of sodium in the plant part, expressed in g Na per kg plant material. If not stated otherwise, the concentration in the plant referred to the concentration in the edible part at harvest.	

attribute table	*attribute*	*description*	*options*
	plant_CaMg_gPerKg	Concentration of calcium and magnesium in the plant part, expressed in g Ca+Mg per kg plant material. If not stated otherwise, the concentration in the plant referred to the concentration in the edible part at harvest.	
	total_K_gPerKg	Total or extractable concentration of potassium in the substrate, expressed in g K per kg oven-dry substrate. If concentrations were given before and after harvest, the average was taken.	
	total_NH4_gPerKg	Total or extractable concentration of ammonium in the substrate, expressed in g NH_4 per kg oven-dry substrate. If concentrations were given before and after harvest, the average was taken.	
	total_Na_gPerKg	Total or extractable concentration of sodium in the substrate, expressed in g Na per kg oven-dry substrate. If concentrations were given before and after harvest, the average was taken.	
	total_CaMg_gPerKg	Total or extractable concentration of calcium and magnesium in the substrate, expressed in g Ca+Mg per kg oven-dry substrate. If concentrations were given before and after harvest, the average was taken.	
	total_Fe_gPerKg	Acid digestible iron concentration in the substrate, expressed in g Fe per kg oven-dry substrate.	
	total_Al_gPerKg	Acid digestible aluminium concentration in the substrate, expressed in g Al per kg oven-dry substrate.	
	oxalate_Fe_gPerKg	Oxalate extractable iron concentration in the substrate, expressed in g Fe per kg oven-dry substrate.	
	oxalate_Al_gPerKg	Oxalate extractable aluminium concentration in the substrate, expressed in g Al per kg oven-dry substrate.	
	dithionite_Fe_gPerKg	Dithionite extractable iron concentration in the substrate, expressed in g Fe per kg oven-dry substrate.	

attribute table	*attribute*	*description*	*options*
	dithionite_Al_gPerKg	Dithionite extractable aluminium concentration in the substrate, expressed in g Al per kg oven-dry substrate.	
plantGrowthIsotope_condition	plantGrowth_method	Type of experiment in which the plant grew: in the field, in a lysimeter, in a pot or other container, or in artificially reconstituted soil.	field; monitoring; lysimeter; pot/container; reconstituted
	isotope_source	Source of caesium isotope: artificial (i.e., added by the investigator), accidental (i.e., nuclear power plant accidents such as Three Miles Islands, Chornobyl, Fukushima), nuclear weapons, both artificial and accidental, other (e.g., sea spray, contaminated sludge).	spiked; fallout; fallout+spiked; other
	isotopeApplication_method	Method by which caesium isotope was applied to the substrate.	deposition; solution mixed; topsoil solution; topsoil spray; unknown
	isotopeContact_days	Time elapsed between contact of the caesium isotope with the substrate and harvest, expressed in days. If the study examined fallout isotopes from nuclear weapons but no date was reported, the date of the Partial Test Ban Treaty in 1963 was assumed. If it was not known when the plant was harvested, an average growth period of 90 days was taken between sowing and harvesting. This was a rough estimate because the growth period depended on plant type and growing conditions. When only the harvest year was given but not the exact date, it was assumed that the harvest occurred on 1 July of the year in question. This assumption was made only if the harvest occurred more than one year after caesium isotope was in contact with the substrate.	
	plantGrowth_stage	Growth stage of the plant at the moment when the plant came in contact with the substrate containing a caesium isotope.	not specified; seed; seedling; mature
	isotopeSpeciation	Speciation of cesium isotope when administered to the substrate: soluble isotope without carrier or isotope on a particulate carrier.	carrier-free; carrier; not specified

attribute table	*attribute*	*description*	*options*
	isotopeDose_BqPerKg	Caesium isotopes applied to the substrate, expressed in Bq or µmol per m^2 or per kg substrate.	
	sampling_location_code	Sampling location number was assigned to identify in the database plants grown under the same conditions, meaning if, on the same substrate, plants were planted and harvested in multiple rotations.	
	fertilizer_type	Fertilizers had not been applied to the substrate (native) or had been applied and when (before or during plant growth).	native; prior to plant growth; during plant growth; prior+during plant growth
	fertilizer_composition	Nutrients specified that were administered to the substrate in co-application and/or in different treatments.	
	irrigation_mm	Average water applied over time during plant growth, expressed in millimeters per day.	
	plant_part	Compartment or part of the plant that was analyzed.	shoot; roots; whole plant; grain; seeds; pod; bud; leaf; stem; pod; bud; head; fruit; berry; tuber; bark; nut
	CR_pool	Pool of caesium isotope studied: native (i.e., caesium isotope already present in the substrate), added (i.e., caesium isotope administered by the investigator).	native; added; both
	CR_extraction	Ratio of caesium isotope concentrations calculated based on the total or extractable caesium isotope concentration.	total; NH4CH3CO2; KCl

attribute table	*attribute*	*description*	*options*
	soilDensity_kgPerm3	Soil density expressed in kg per m^3 (= 0.001 g per cm^3).	
	soilDepth_cm	Thickness of the caesium isotope-containing layer, expressed in cm. If the sampling depth was not reported, a depth of 10 cm was assumed for grasses and 20 cm for all other plants based on the plowing depth (IAEA, 2009). If the layer was mixed by harvesting, the thickness of the layer was set higher.	
	particleSize_method	Method by which clay content was determined.	pipet; laser diffraction; hydrometer
	mechanical_dispersion	Method by which substrate particles were disaggregated and/or dispersed mechanically.	none; ultrasonic
	chemical_dispersion	Method by which substrate particles were disaggregated and/or dispersed chemically.	none; oxalic acid; NaHMP; resin; pH-adjusted NaHMP
	sand_percentage	Particle size distribution of sand (2000–50 µm), expressed in weight percentage or g per 100 g.	
	silt_percentage	Particle size distribution of silt (50–2.0 µm), expressed in weight percentage or g per 100 g.	
	clay_percentage	Particle size distribution of clay (<2.0 µm), expressed in weight percentage or g per 100 g.	

attribute table	*attribute*	*description*	*options*
	soil_category	Soil category according to the classification based on soil the percentages of clay, sand, and organic matter in Table 3.3 in IAEA (2021). For the mineral soils, three groups were created according to the sand and clay percentages referred to the mineral matter: ‘Sand group’: Sand content ≥ 65% and clay content < 18%, or particle sizes described as sandy; ‘Clay group’: Clay content ≥ 35%, or particle sizes described as clayey; ‘Loam group’: Clay content between 18% and 35%, or particle sizes described as loamy; ‘Organic group’: Organic matter content ≥ 20% OR SOC≥11.6%; 'Coral sand': Marshall Islands soils (predominance of calcium carbonate ($CaCO_3$), with some $MgCO_3$ and no silicate clay); ‘Unspecified soil group’: No characterization information	sand; loam; clay; organic; coral sand; unspecified

Table II.2. Description of selection criteria and its relation to attribute(s) or column(s) to reject data.

attributes	*description*
plant_washed NotWashed; isotopeApplic ation_method	Data on the transfer of caesium isotope other than through the root system were not included in this database, such as caesium foliar interception of caesium, i.e., direct uptake of caesium via above-ground plant parts such as leaves and stems. Studies that reported that caesium contaminated soil particles splashed onto plant parts, causing the caesium concentration in plant material to be higher than expected, were rejected.
plantGrowth_ method	Data on the transfer of caesium isotope from substrates not representative of agricultural soils, such as hydroponics and agar, were rejected.
isotopeContac t_days	If the contact time of caesium isotope with the substrate was less than two months before seeding or planting (IAEA, 2006), data were rejected. If there is only a very short contact time (a few weeks or less) between soil particles and caesium isotope during incubation or if caesium isotope is spiked during plant growth, direct uptake of caesium by the plant may have occurred, and direct uptake always dominates over indirect uptake from the soil.
isotopes; isotopeDose_ BqPerKg	If the stable isotope of caesium (^{133}Cs) was considered, but the spike concentrations, i.e. dose, were not relevant for trace concentrations of radiocaesium in the environment, i.e., more than 0.001 µmol per kg substrate, data were rejected. If native stable caesium was considered, i.e., that is naturally found in soils, the caesium was already fixed in the soil, so it behaved differently from radiocaesium recently entering the soil, i.e., spiked, data were rejected.
plantGrowth_ method; fertilizer_type; fertilizer_com position	Data on artificial substrates not representative of agricultural soils, such as studied on countermeasures where soils have been amended with minerals such as synthetic zeolites and bentonites, were rejected. If artificial soils were relevant to agricultural soils, the plant growth method was assumed to be on reconstituted soil.
fertilizer_type; fertilizer_com position	If the nutrients in substrates, such as potassium, nitrogen and phosphorus, were depleted before plant growth, so that the substrates were not representative of agricultural soil and the nutrient status of the substrate affected caesium uptake in plants, data were rejected.
plant_categor y; plant_part	Data on transfer of caesium isotope to trees and their fruits were not included in the database because of the complex internal distribution of caesium in the plant. Data on transfer of caesium isotope to non-terrestrial plants, such as marine plants, were not included in the database because they are less relevant to caesium uptake in terrestrial crops.
plantGrowth_s tage; experiment_d ate	Data on transfer of caesium isotope to juvenile plants not representative of harvest-ready plants were not included in the database because their juvenile-stage nutrient demand may differ from the nutrient demand of mature, harvest-ready plants. The nutrient demand of plants, i.e., potassium demand, influences radiocaesium uptake in the plant.

attributes	*description*
CR_m2PerKg; CR_KgPerKg	If no information was given on the method that the CR was calculated, i.e., as deposition-based (or aggregated) CR (m^2 kg^{-1}) or as weight-based CR (kg kg^{-1}), or if no information was given on caesium isotope concentrations in plant material or soil, data were rejected.
CR_expression	Data on the transfer of caesium isotope modeled or inferred from, e.g., soil properties or caesium solid-liquid distribution coefficients rather than measured in the substrate and plant, were rejected.
CR_expression	Data on the transfer of caesium isotope reported in references citing other references, such as review articles or reports, were rejected to avoid duplicate entries, to obtain as much information as possible from the original reference to insert into the database, and for data traceability.
CR_expression	If the CR was based on non-paired samples (or derived CR), i.e., caesium isotope concentrations in the plant was measured from a substrate different from the one in which the plant had actually grown, data were rejected because soil caesium isotope concentrations can vary spatially in the field, and ideally should be measured directly at the plant roots.
soilCs_BqPerKg; poreWaterCs_BqPerL; plantCs_BqPerKg; CR_m2PerKg; CR_KgPerKg; isotopeDose_BqPerKg	If activity was not corrected for radioactive decay within an experiment or study, data were rejected.

Table II.3. Keyword string used to search the Web of Science databases. The same keyword string was used for Scopus, but the syntax differed. Keywords were combined using the OR and NEAR operators, concepts were combined using the AND operator, and meeting abstracts were excluded using the NOT operator. Keywords of 200 plant species according to Latin botanical nomenclature were combined, giving 33 additional references. The symbols *, ? and $ were used for multiple options of characters. TS = topic (to search for matches in reference titles, abstracts, author keywords, and Keywords Plus®), DT = document type.

concept	*keyword string*
caesium	TS=(“13?Cs” OR “Cs-13?” OR “*c$esium” OR ((“fission” OR “radio*”) NEAR/9 “Cs”))
soil	TS=(“soil*” OR “field$” OR “pasture$” OR “farmland$” OR “grassland$” OR “peatland$” OR “plot” OR “terrestrial”)
plant	TS=("plant$” OR “crop$” OR “rice” OR “wheat$” OR “root$” OR “grass*” OR “herb*” OR “fodder” OR “leave$” OR “leaf” OR “seed$” OR “tuber$” OR “vegetable$” OR “fruit$” OR “vegetation” OR “food chain$” OR “*berr*” + Latin names of plant species
transfer	TS=(“transfer” OR “uptake” OR (“take” NEAR/6 “up”) OR “concentration ratio$” OR “bioavailab*” OR “phytoavailab*” OR “absorption” OR ((“availab*” OR “mobil*” OR “distribution” OR “accumulation”) NEAR/9 (“13?Cs” OR “Cs-13?” OR “*c$esium” OR ((“fission” OR “radio*”) NEAR/9 “Cs”))))
excluded	NOT DT=("Meeting Abstract”)

Table II.4. Details of online accessible databases for reference and citation indexing used in this study.

platform	*database*	*edition*	*timeframe coverage*
Web of Science™	Web of Science Core Collection	Science Citation Index – Expanded (SCI-EXPANDED)	1955–2022
		Social Sciences Citation Index (SSCI)	1956–2022
		Conference Proceedings Citation Index – Science (CPCI-S)	1990–2022
		Conference Proceedings Citation Index – Social Science & Humanities (CPCI-SSH)	1990–2022
		Emerging Sources Citation Index (ESCI)	2018–2022
	BIOSIS Citation Index		1992–2022
	Current Contents Connect		1998–2022
	Chinese Science Citation Database℠		1989 – 2022
	Data Citation Index	Science (DCI-S)	1900–2022
		Social Sciences & Humanities (DCI-SSH)	1900–2022
	Derwent Innovations Index		1966–2022
	KCI-Korean Journal Database		1980–2022
	MEDLINE®		1950–2022
	SciELO Citation Index		2002–2022
	Zoological Record		1864–2022
Elsevier	Scopus		1788–2022

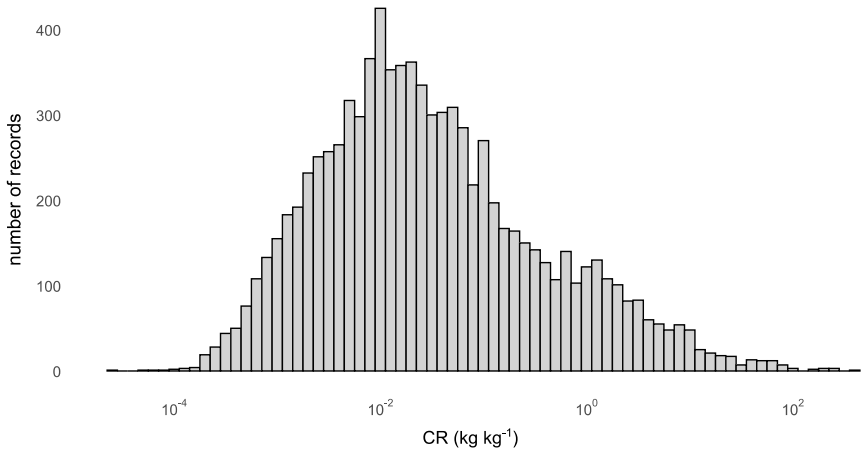

Figure II.1. Histogram of all records currently in the (*N* = 8,837) database showing the large variability of CRs (0.000028–380 kg kg^{-1}) on log-scale.

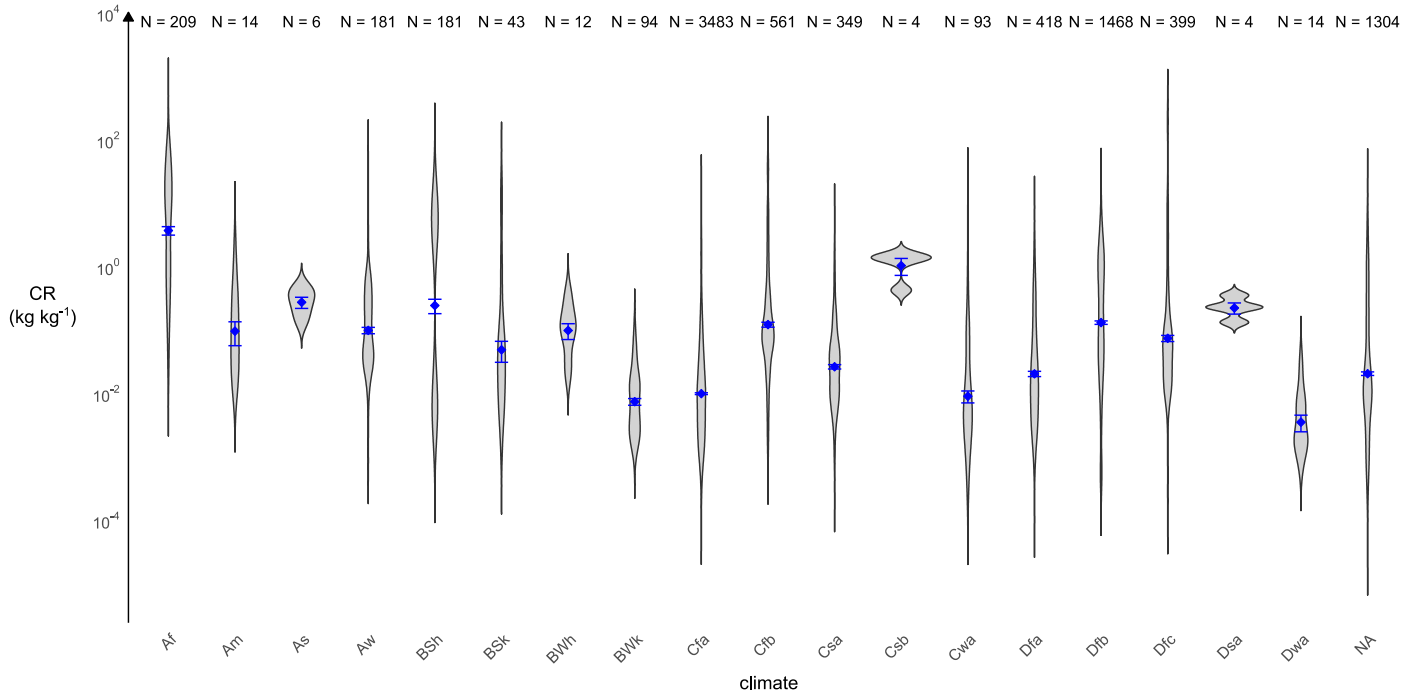

Figure II.2. Violin plots of CRs on log-scale categorized by soils sampled in tropical (Af, Am, As, Aw), arid (BSh, BSk, BWh, BWk), temperate (Cfa, Cfb, Csa, Csb, Cwa) and continental (Dfa, Dfb, Dfc, Dsa, Dwa) climates. Diamonds show geometric means, and error bars are the standard errors of the geometric means. NA = data not available.

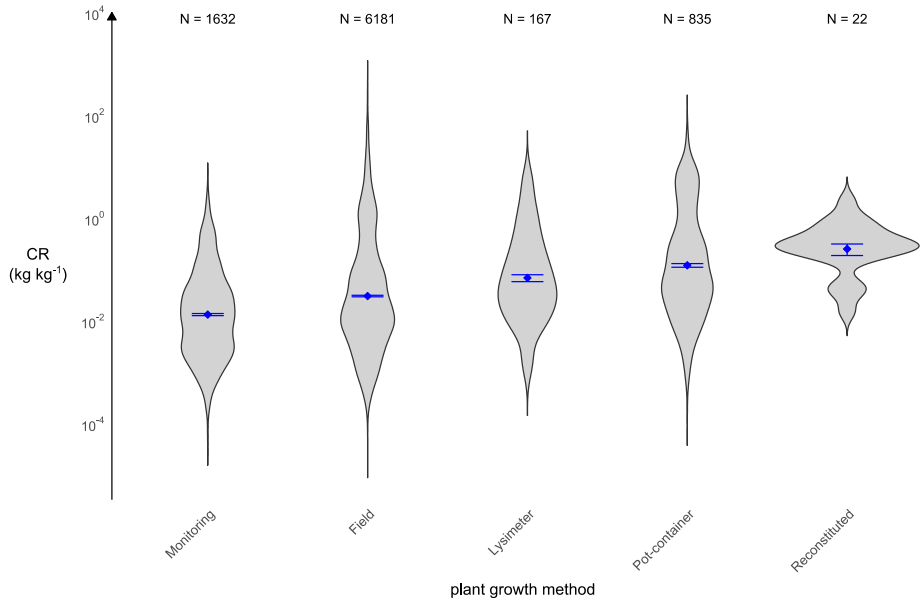

Figure II.3. Violin plots of CRs on log-scale categorized by the plant growth methods to obtain CRs, showing that CR ranks (p <0.05): monitoring < field < lysimeter < pot with natural soil < pot trial with reconstituted soil. Diamonds show geometric means, and error bars are the standard errors of the geometric means. NA = data not available.

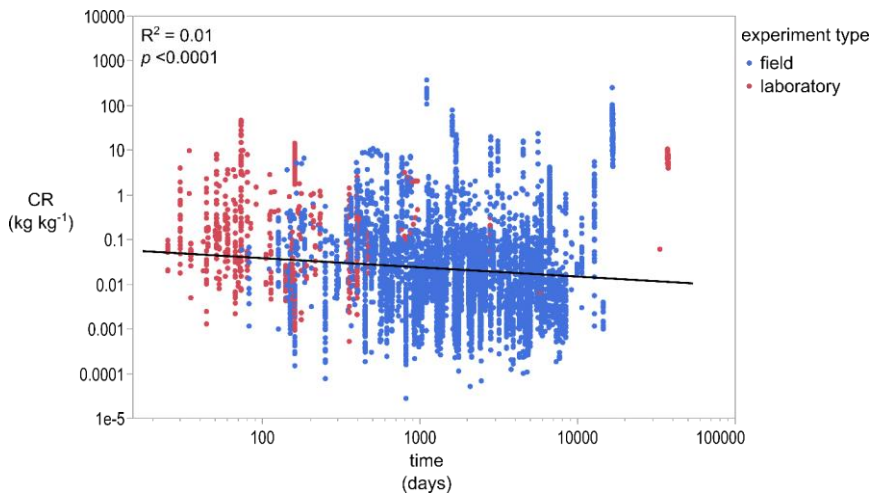

Figure II.4. CR related to soil-radiocaesium contact time showing that laboratory experiments (in red: pot/container experiments with soils and with reconstituted soils) are performed over a shorter time period compared to CRs observed in the field (in blue: monitoring, field, and lysimeter) (N = 8,837).

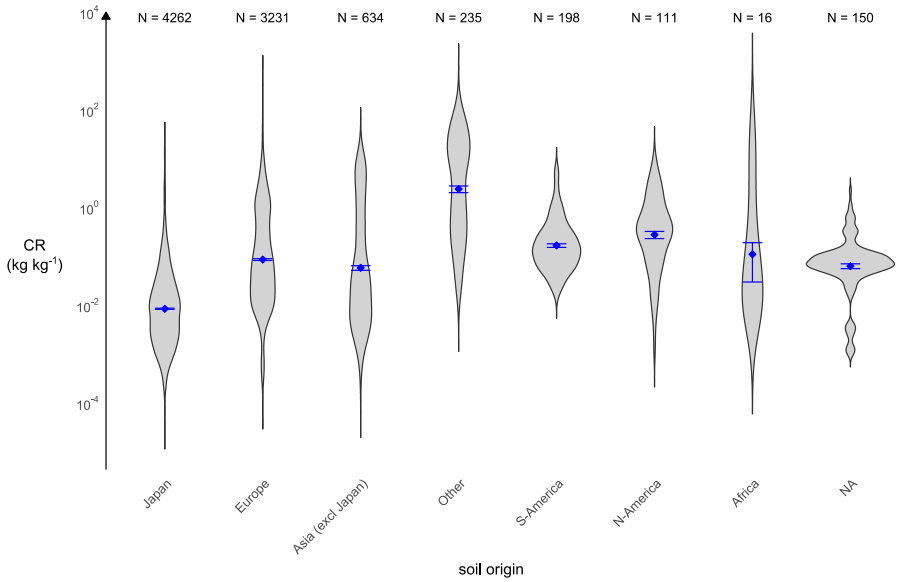

Figure II.5. Violin plots of CRs on log-scale categorized by soil origin showing that most of the data in the current database was obtained in Japan, where CRs were lower. Diamonds show geometric means, and error bars their standard errors. NA = data not available.

Table II.5. Plant conversion factors, relative to grass, calculated for each plant category by taking the geometric mean of conversion factors for plant species (Beresford and Willey, 2019) within each plant category compared to those recommended in a IAEA technical report (Frissel et al., 2002; IAEA, 2006).

	(Beresford and Willey, 2019)		*(IAEA, 2006)*
plant category	*number of records to calculate conversion factor*	*plant conversion factor*	*plant conversion factor*
grass	103	1.0	1.0
cereals	52	1.2	0.22
maize	8	0.44	–
rice	2	0.23	–
leafy vegetables	163	2.3	2
non-leafy vegetables	41	0.73	–
leguminous vegetables	91	2.5	1.1
root crops	43	3.0	0.67
tubers	4	1.2	0.90
fruits	11	0.92	1.1
herbs	194	5.0	–
medicinal plants	162	6.7	–
other crops	16	0.96	–

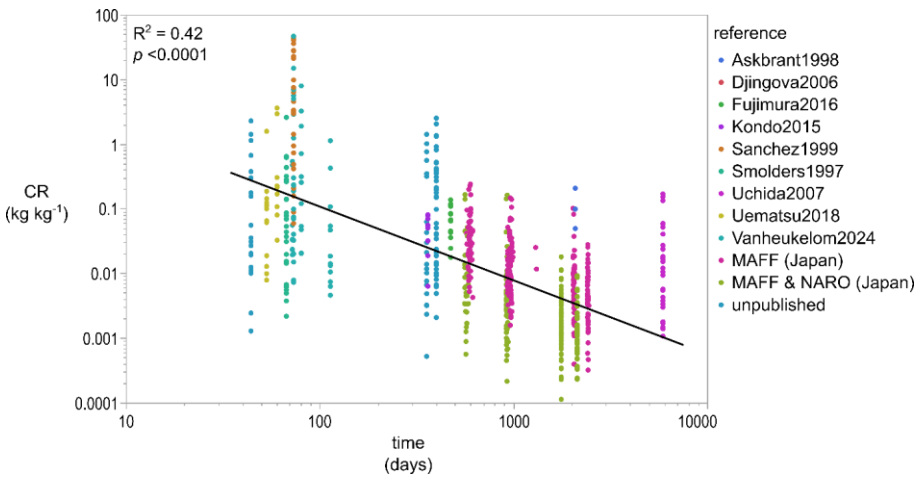

Figure II.6. The CR related to time of contact between soil and radiocaesium shows for this selection of data (N = 836) the grouping of *time* per *reference* (or source document, N_{ref} = 12).

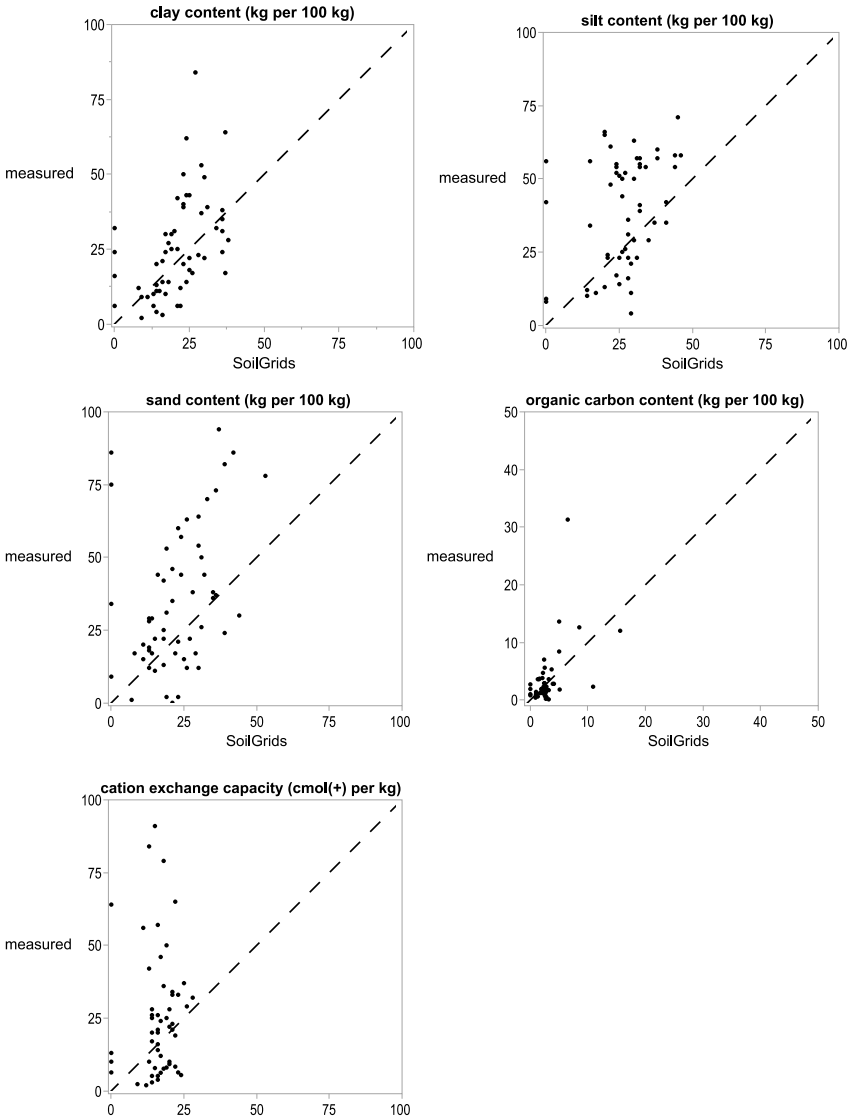

Figure II.7. Comparison of soil variables measured (Gilis and Sweeck, 2019; Chapter 4) and corresponding values obtained by SoilGrids using coordinates (*N* = 57) showing the underestimation at higher measured values. For some variables (*N* = 4), there were no values available in SoilGrids.

Appendix III
Quantitative clay mineralogy predicts radiocaesium bioavailability to ryegrass grown on clay-sand mixtures

The RIP of reference illite du Puy is 4,397 mmol kg^{-1} (and standard deviation 88 mmol kg^{-1}) and the CEC is 18.0 $cmol_c$ kg^{-1} (and standard deviation 0.5 $cmol_c$ kg^{-1}).

The group of 2:1 structure phyllosilicates consists both of the very selective, non-expanding and less selective, expanding minerals. As suggested by Zeelmaekers (2011), we quantify the 2:1 phyllosilicates and group them together, however XRD cannot detect FES and hence, 2:1 phyllosilicates refer to high and low RIP clays. The reason for this is because it is challenging to distinguish the 2:1 phyllosilicates with XRD. The XRD technique relies on the identification of the mineral interlayer spaces, which in case of the phyllosilicates have a closely matching distance so that characteristic peaks often overlap. By isolating the phyllosilicates, the type 2:1 phyllosilicates can be distinguished. However, this additional information is often too laborious to obtain in a routine manner. The isolation of the phyllosilicates prior to the XRD analysis was done following the standardized procedure suggested by Zeelmaekers (2011) as given below.

The fraction smaller than 2 µm was isolated after chemical removal of aggregate forming particles and centrifugation (modified after Jackson, 1975; Zeelmaekers, 2011). The clays were chemically treated to remove cements that hold clay particles in a matrix. Carbonates were removed by a pH 5 buffer solution of Na-acetate and acetic acid. The organic matter was oxidized by a 7% H_2O_2 solution. Free iron (hydr)oxides were removed by a citrate-bicarbonate-dithionite solution. The clays were ultrasonically treated to loosen the aggregates between each treatment. The 2 µm fraction was separated by centrifuging the clays at 305 *g* for 2 min. The interlayers were saturated by calcium ions by dissolving the clays in a 1 mol L^{-1} $CaCl_2$ solution to ensure interlayer conditions were similar. Excess chloride ions were removed by placing the clays in a dialysis membrane (VISKING®, MWCO 12 kDa to 14 kDa) in deionized water which was refreshed twice a day for 5 days. Afterwards the clays were dried in the oven (60°C) overnight.

The 00*l* reflections of the phyllosilicate minerals were enhanced by depositing the isolated phyllosilicates on a glass slide prior to XRD measurements. The oven-dry clays were dispersed in deionized water after ultrasonic treatment.

About 10 mg of clay per cm^2 was deposited on the glass slide (Moore and Reynolds, 1997). The slides were recorded with XRD in two states: air-dry and solvated in ethylene glycol. After the air-dried slide was measured, the slide was inserted in a desiccator with ethylene glycol bath in an oven (60°C) overnight. The slides in two states were measured with the same diffractometer as described above, but with a scanning range from 2 °2θ to 47 °2θ.

The minerals in the isolated 2 µm fraction were identified and quantified using SYBILLA (© Chevron ETC). The SYBILLA software, based on the multispecimen method, fits the model on the XRD record in two states (Zeelmaekers, 2011). The quantified phase results were accepted if the model fit in the ethylene glycol state agreed with the model in the air-dry state.

The VER pattern of the isolated clay fraction was impossible to quantify with the SYBILLA software. It is known that vermiculite and vermiculite-chlorite mixed minerals are present in VER (Thiry, 1997). However, the vermiculite and chlorite minerals were quantified in the bulk sample, so it did not affect the final conclusion based on 2:1 and 2:1:1 groups of summed mineral phases.

The results from both bulk rock analysis and the isolated clay fraction were combined as explained by Zeelmaekers (2011). The isolated clay results were integrated by splitting the bulk-rock quantity for the 2:1 type group into proportions of illite, smectite and mixed-layered illite-smectite according to their relative proportions in the isolated 2 µm fraction. After the identified mineral phases were quantified, the results were normalized.

Table III.1. The mineral content (g 100 g^{-1}) of the quantified mineral phases after XRD analysis. The group of Al-rich dioctahedral 2:1 phyllosilicates is split up in illite, illite-smectite mixed layered and smectite mineral contents. The data are arithmetic means if replicates in the bulk powder method were measured (*n* = 1, 3 or 4, see below). The limit of detection is 0.1 g 100 g^{-1}.

minerals	BEN[g]	BIO[g]	ILL[g]	VER[g]	BC[h]	CC[i]	IC[i]	RFC[h]	RL[h]	WC[h]
illite	<0.1	<0.1	42.5	<0.1	4.0	5.1	5.7	6.9	2.4	9.3
illite-smectite	<0.1	<0.1	24.5[j]	<0.1	14.1[j]	14.0[j]	8.8[j]	7.6[j]	9.1[j]	6.4[k]
smectite	92.6	<0.1	<0.1	<0.1	27.2	9.3	40.6	11.0	11.3	<0.1
Fe-rich dioctahedral 2:1 phyllosilicates	<0.1	<0.1	<0.1	<0.1	<0.1	<0.1	<0.1	<0.1	<0.1	<0.1
Fe-rich trioctahedral 2:1 phyllosilicates	<0.1	97.3	<0.1	86.0	<0.1	<0.1	<0.1	<0.1	<0.1	<0.1
kaolinite	<0.1	<0.1	1.0	<0.1	6.2	3.4	4.4	1.3	1.1	18.0
kaolinite-smectite	<0.1	<0.1	<0.1	<0.1	4.2	3.5	2.0	2.4	1.9	<0.1
chloritic minerals	<0.1	<0.1	1.0	9.0	2.0	3.3	2.9	2.7	2.0	<0.1
quartz	3.0	<0.1	21.0	<0.1	28.8	52.1	22.5	58.5	53.0	64.2
K-feldspar	3.0	<0.1	8.0	<0.1	7.7	5.0	6.6	4.7	8.3	1.5
plagioclase	1.0	<0.1	<0.1	<0.1	2.7	2.8	3.5	5.0	9.3	<0.1
augite	<0.1	<0.1	<0.1	4.0	<0.1	<0.1	<0.1	<0.1	<0.1	<0.1
carbonate minerals	0.4	<0.1	2.0	1.0	<0.1	<0.1	0.8	<0.1	1.7	<0.1
gypsum	<0.1	<0.1	<0.1	<0.1	0.8	0.9	0.6	<0.1	<0.1	<0.1
apatite	<0.1	2.7	<0.1	<0.1	<0.1	<0.1	<0.1	<0.1	<0.1	<0.1
pyrite	<0.1	<0.1	<0.1	<0.1	1.7	0.3	1.0	<0.1	<0.1	<0.1
anatase	<0.1	<0.1	<0.1	<0.1	0.6	0.3	0.7	<0.1	<0.1	<0.1
rutile	<0.1	<0.1	<0.1	<0.1	<0.1	<0.1	<0.1	<0.1	<0.1	0.7

[g] *n* = 1; [h] *n* = 3; [i] *n* = 4; [j] randomly mixed-layered; [k] regularly mixed-layered

The *CEC calculated* of the sand-clay mixtures was calculated as for the RIP calculated (Section 2.2.2).The agreement of the CEC measured on the clays and the mixtures shows the CEC additivity (N = 20, R^2 = 0.92***, RMSE = 0.13) (Figure III.1). In mineral substrates, residual CEC is negligible. However, in soils where there is organic matter, this can be a large part of the non-selective adsorption.

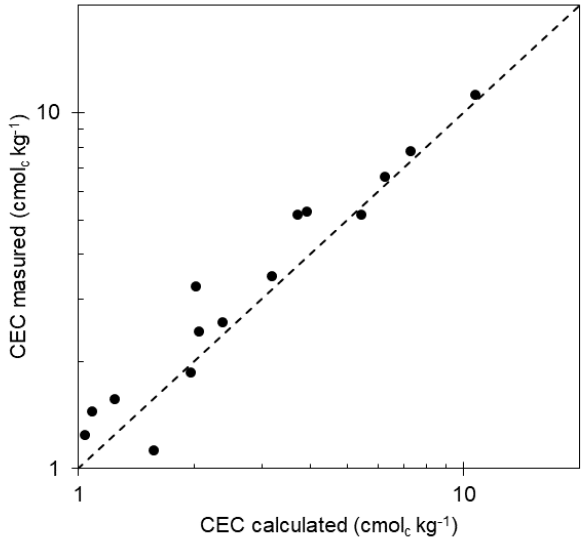

Figure III.1. The cation exchange capacity (CEC) (cmol$_c$ kg^{-1}) measured on the clay-sand mixture before plant growth (x-axis) and calculated as the sum of the CEC of its component clay and sand (y-axis). The dashed line shows the 1:1 line.

Data is given of the measured variables prior (Table III.2) and after (Table III.3) plant growth.

Table III.2. Properties of the substrate and grass shoots before plant growth. Data are arithmetic means and standard deviations (in parentheses) of triplicates, unless stated otherwise. The standard deviation of $RIP_{calculated}$ is calculated based on the error of the RIP_{clay} and RIP_{sand} and no covariance is assumed. The minimum, maximum and mean values are given at the bottom of the table.

code	substrate						exchangeable cations[n]									
	$CEC_{mixture}$[l,m]		moisture content		pH 0.01 M $CaCl_2$		total ^{137}Cs		^{137}Cs		K		Ca		Mg	
	$cmol_c$ kg^{-1}		g H_2O 100 g^{-1}				kBq kg^{-1}		kBq kg^{-1}		$cmol_c$ kg^{-1}		$cmol_c$ kg^{-1}		$cmol_c$ kg^{-1}	
BEN5	5.2		21.3		7.7	(0.1)	396.4	(5.9)	231	(7.0)	0.2	(<0.1)	6.0	(0.2)	2	(<0.1)
BEN10	7.8		27.2		7.6	(<0.1)	405.6	(5.9)	207	(1.8)	0.4	(<0.1)	11.5	(0.8)	3.0	(0.1)
BIO5	0.6		13.3		8.5	(<0.1)	413.0	(1.6)	90.9	(2.8)	0.2	(<0.1)	3.8	(0.1)	0.6	(<0.1)
BIO10	0.2		13.6		8.3	(0.1)	405.8	(5.0)	77.2	(0.2)	0.4	(<0.1)	8.6	(<0.1)	1.1	(<0.1)
ILL5	1.6		12.8		8.0	(<0.1)	385.2	(0.4)	115	(2.0)	0.4	(<0.1)	4.9	(<0.1)	3.0	(0.1)
ILL10	2.6		16.0		7.9	(<0.1)	378.9	(10.0)	110	(1.1)	0.7	(<0.1)	9.8	(0.1)	5.8	(<0.1)
VER5	5.2		13.4		8.0	(<0.1)	402.1	(5.9)	17.3	(0.9)	0.1	(<0.1)	4.9	(0.2)	4.1	(0.1)
VER10	11.2		13.2		7.8	(0.1)	392.1	(10.5)	11	(0.6)	0.1	(<0.1)	9.4	(0.5)	7.7	(0.3)
BC10	3.2		13.5		3.2	(<0.1)	388.3	(12.1)	176	(17.0)	0.1	(<0.1)	3.4	(0.3)	1.2	(0.1)
BC20	5.3		16.2		2.9	(0.1)	402.8	(7.5)	143	(7.8)	0.4	(<0.1)	6.6	(0.4)	2.4	(0.2)
CC10	1.4		13.3		3.0	(0.1)	394.1	(8.7)	236	(19.0)	<0.1	(<0.1)	1.9	(0.2)	0.3	(<0.1)
CC20	1.1		13.5		2.9	(0.1)	391.2	(3.0)	202	(9.7)	0.1	(<0.1)	2.8	(0.1)	0.6	(<0.1)
IC10	3.5		13.1		6.8	(0.2)	370.9	(17.3)	128	(7.4)	0.5	(<0.1)	4.0	(<0.1)	2.4	(<0.1)
IC20	6.6		18.9		6.8	(0.2)	410.5	(16.2)	118	(5.2)	1.0	(<0.1)	7.2	(0.4)	4.3	(0.2)
RFC10	1.2		11.0		7.1	(0.1)	378.8	(6.6)	85.9	(10.5)	<0.1	(<0.1)	1.5	(0.2)	0.1	(<0.1)
RFC20	1.9		13.2		6.6	(0.2)	391.6	(9.2)	73.1	(5.6)	<0.1	(<0.1)	2.3	(0.1)	0.2	(<0.1)
RL10	1.4		10.7		7.6	(<0.1)	399.3	(7.1)	102	(3.0)	<0.1	(<0.1)	9.3	(0.3)	0.4	(<0.1)
RL20	2.4		10.8		7.4	(0.1)	403.9	(8.2)	98.4	(3.8)	0.1	(<0.1)	16.7	(0.6)	0.4	(<0.1)
WC10	0.5		12.0		6.6	(<0.1)	406.8	(7.2)	189	(0.8)	<0.1	(<0.1)	0.7	(<0.1)	0.2	(<0.1)
WC20	0.6		13.1		6.5	(0.1)	404.1	(4.6)	191	(2.1)	<0.1	(<0.1)	1.0	(0.1)	0.3	(<0.1)
min	0.2		10.7		2.9		370.9		11		<0.1		0.7		0.1	
max	11.2		27.2		8.5		413.0		236		1.0		16.7		7.7	
median	2.2		13.3		7.2		397.9		116		0.1		4.9		1.2	

[l] n = 1; [m] cobalthexamine method; [n] ammonium acetate extraction at pH 7

Table III.2. *Continued.*

code	pore water									
	^{137}Cs		K		Ca		Mg		$RIP_{calculated}$	
	kBq L^{-1}		mmol L^{-1}		mmol L^{-1}		mmol L^{-1}		mmol kg^{-1}	
BEN5	18.3	(0.18)	5.02	(0.06)	44.32	(0.58)	13.1	(0.20)	29.5	(2.0)
BEN10	12	(0.53)	6.99	(0.13)	76.81	(1.20)	22.7	(0.40)	48.2	(3.9)
BIO5	11.1	(0.68)	9.47	(0.18)	41.62	(0.36)	14.5	(0.33)	132	(2)
BIO10	9.6	(0.27)	16.09	(0.59)	80.95	(2.16)	26.5	(0.66)	253	(4)
ILL5	1.69	(0.08)	6.58	(0.11)	32.78	(0.51)	9.69	(0.18)	430	(73)
ILL10	1.34	(0.03)	9.14	(0.12)	51.53	(0.59)	17.6	(0.58)	850	(145)
VER5	2.34	(0.45)	1.44	(0.06)	21.39	(1.09)	11.1	(0.45)	36.4	(2.4)
VER10	1.24	(0.29)	3.65	(0.09)	72.76	(1.13)	44.2	(0.23)	62.0	(4.7)
BC10	1.45	(0.13)	5.90	(0.17)	13.56	(0.13)	21.4	(0.83)	567	(10)
BC20	0.75	(0.04)	6.24	(0.15)	13.23	(0.06)	26.9	(0.74)	1120	(20)
CC10	1.19	(0.01)	0.67	(0.06)	13.97	(0.19)	6.75	(1.09)	266	(17)
CC20	0.55	(0.01)	0.28	(0.02)	12.50	(0.04)	12.2	(0.34)	520	(34)
IC10	0.95	(0.11)	6.11	(0.17)	15.42	(0.30)	13.3	(0.80)	581	(17)
IC20	0.55	(0.04)	6.58	(0.12)	15.63	(0.25)	13.7	(1.16)	1150	(30)
RFC10	0.1	(0.01)	0.12	(<0.01)	4.42	(0.08)	0.66	(0.01)	347	(20)
RFC20	0.05	(0.02)	0.07	(<0.01)	4.45	(0.07)	0.59	(<0.01)	684	(41)
RL10	0.06	(0.01)	0.08	(<0.01)	4.31	(0.16)	0.35	(0.01)	357	(15)
RL20	0.05	(0.01)	0.06	(<0.01)	4.75	(0.05)	0.32	(0.01)	704	(29)
WC10	2.21	(0.11)	1.45	(0.02)	8.09	(0.23)	2.44	(0.05)	100	(2)
WC20	0.78	(0.05)	1.28	(0.02)	11.40	(0.44)	3.76	(0.07)	189	(3)
min	0.05		0.06		4.31		0.32		29.5	
max	18.33		16.09		80.95		44.2		1150	
median	1.22		4.34		14.70		12.7		352	

Table III.3. Properties of the substrate and grass shoots after 30 days of plant growth. Data are arithmetic means and standard deviations (in parentheses) of triplicates. The CF is calculated based on data of non-corresponding replicates. Therefore, standard deviations of the CF is calculated based on the error of the nominator and the error of the denominator because the sampling is unpaired and no covariance is assumed. The minimum, maximum and mean values are given at the bottom of the table. If no data have been obtained, a "-" is noted.

code	pore water										grass shoot							
	^{137}Cs		K		Ca		Mg		yield		^{137}Cs		K		Ca		Mg	
	kBq L-1		mmol L^{-1}		mmol L^{-1}		mmol L^{-1}		g		kBq kg^{-1}		g kg^{-1}		g kg^{-1}		g kg^{-1}	
BEN5	0.57	(0.04)	2.15	(0.04)	39.26	(0.51)	10.67	(0.20)	0.85	(0.07)	247.9	(14.5)	21.3	(0.7)	15.1	(1.2)	2.2	(0.1)
BEN10	0.98	(0.01)	5.22	(0.11)	70.68	(2.45)	20.35	(0.46)	0.72	(0.08)	150.5	(8.0)	30.7	(0.6)	19.9	(4.8)	2.8	(0.6)
BIO5	1.68	(0.05)	3.64	(0.04)	30.14	(0.11)	9.85	(0.12)	0.70	(0.09)	121.4	(12.0)	24.8	(2.3)	16.9	(0.6)	2.7	(0.1)
BIO10	3.96	(0.08)	13.05	(0.74)	82.49	(3.28)	28.93	(1.79)	0.36	(0.01)	142.4	(15.1)	31.2	(2.2)	22.2	(4.3)	3.3	(0.3)
ILL5	0.61	(0.02)	2.94	(0.02)	24.62	(0.02)	7.64	(0.05)	0.74	(0.03)	20.2	(0.6)	25.6	(1.4)	14.8	(1.5)	2.5	(0.1)
ILL10	0.46	(0.05)	5.68	(0.10)	42.06	(0.67)	13.43	(0.08)	0.71	(0.02)	16.5	(0.8)	26.4	(1.0)	17.2	(1.2)	2.5	(0.1)
VER5	1.92	(0.05)	1.23	(0.03)	25.72	(0.18)	16.03	(0.10)	0.60	(0.03)	133.9	(5.4)	25.5	(2.0)	19.1	(1.0)	4.1	(0.2)
VER10	1.09	(0.03)	2.26	(0.04)	62.01	(0.62)	39.33	(0.60)	0.34	(0.06)	71.8	(4.6)	30.1	(2.1)	28.0	(1.4)	6.1	(0.3)
BC10	-	-	-	-	-	-	-	-	-	-	-	-	-	-	-	-	-	-
BC20	-	-	-	-	-	-	-	-	-	-	-	-	-	-	-	-	-	-
CC10	-	-	-	-	-	-	-	-	-	-	-	-	-	-	-	-	-	-
CC20	-	-	-	-	-	-	-	-	-	-	-	-	-	-	-	-	-	-
IC10	0.35	(0.02)	4.28	(0.10)	15.05	(0.47)	11.58	(0.27)	0.72	(0.02)	12.0	(1.1)	19.4	(2.1)	5.7	(0.4)	2.8	(0.2)
IC20	0.25	(0.01)	5.42	(0.31)	15.30	(0.25)	13.98	(0.67)	0.86	(0.04)	6.2	(1.4)	20.2	(3.0)	5.0	(0.6)	2.8	(0.2)
RFC10	0.03	(<0.01)	0.03	(<0.01)	2.02	(0.03)	0.20	(0.01)	0.57	(0.04)	242.7	(12.4)	11.6	(0.4)	14.5	(0.2)	2.8	(0.2)
RFC20	0.07	(0.01)	0.03	(<0.01)	2.15	(0.05)	0.20	(0.01)	0.76	(0.04)	104.9	(1.5)	13.7	(0.6)	12.7	(0.3)	2.4	(0.1)
RL10	0.04	(0.01)	0.04	(<0.01)	2.27	(0.06)	0.12	(0.01)	0.57	(0.05)	147.4	(12.6)	8.7	(0.7)	8.9	(0.3)	1.5	(0.1)
RL20	0.03	(0.01)	0.04	(0.01)	2.24	(0.02)	0.11	(0.02)	0.65	(0.01)	68.1	(3.9)	11.8	(0.9)	9.5	(0.5)	1.7	(0.2)
WC10	0.09	(0.01)	0.05	(<0.01)	5.78	(0.19)	1.64	(0.08)	0.72	(0.03)	891.7	(8.8)	14.3	(0.8)	10.2	(0.2)	2.5	(<0.1)
WC20	0.46	(0.08)	0.19	(0.01)	9.34	(0.40)	3.10	(0.08)	0.72	(0.04)	380.1	(15.3)	17.1	(1.0)	9.4	(0.3)	2.3	(0.2)
min	0.03		0.03		2.02		0.11		0.34		6.2		8.7		5.0		1.5	
max	3.96		13.05		82.49		39.33		0.86		891.7		31.2		28.0		6.1	
median	0.46		2.20		19.96		10.26		0.72		127.7		20.8		14.7		2.6	

Table III.3. *Continued.*

code	$RIP_{mixture}$		CF	
	mmol kg^{-1}		L kg^{-1}	
BEN5	23	(1)	435	(38)
BEN10	39	(2)	153	(8)
BIO5	420	(40)	72.1	(7.4)
BIO10	837	(33)	35.9	(3.9)
ILL5	689	(48)	33.2	(1.4)
ILL10	1097	(82)	35.6	(4.5)
VER5	28	(2)	69.8	(3.4)
VER10	54	(1)	65.7	(4.5)
BC10	830	(41)	-	-
BC20	1307	(123)	-	-
CC10	372	(13)	-	-
CC20	715	(17)	-	-
IC10	528	(12)	34.0	(3.9)
IC20	975	(61)	25.0	(5.6)
RFC10	318.9	(<1)	9250	(1630)
RFC20	620	(73)	1530	(310)
RL10	299	(15)	3790	(1100)
RL20	761	(14)	2020	(730)
WC10	144	(19)	9940	(860)
WC20	240	(8)	821	(145)
min	23		25.0	
max	1307		9940	
median	474		112	

The K concentrations in pore water were similar before and after plant growth (Figure III.2). The concentrations of ^{137}Cs were reduced during the pot experiment. The large ^{137}Cs concentration changes in the pore water of BEN and BIO substrates cannot be ascribed to a depletion in K ions competing for ^{137}Cs adsorption on the solid phase which can be shown by mass balance calculations. Plant uptake also cannot explain the largest concentration changes because the total estimated plant accumulation of ^{137}Cs was less than 10% of the quantify initially present in pore water if the above ground part is assumed 2/3 of the total biomass. This agrees with what was found earlier (Smolders et al., 1997) after which it was concluded that both pore water cation concentrations before or after plant growth could be used to demonstrate relationships such as the influence of pore water composition on ^{137}Cs availability.

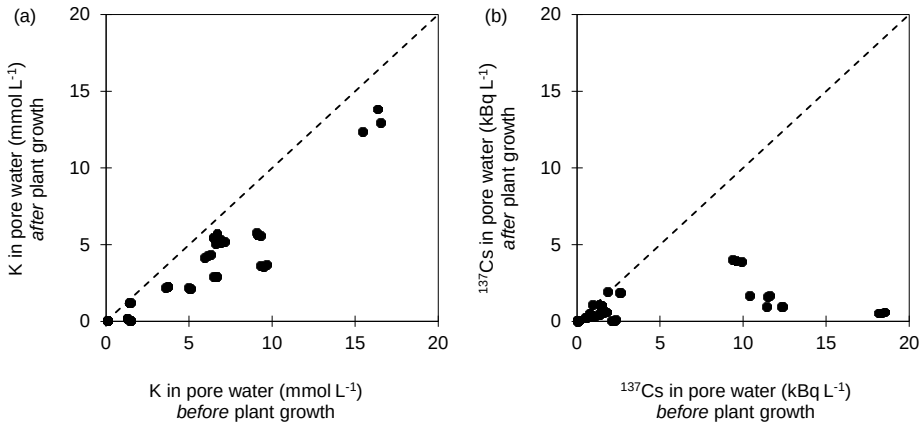

Figure III.2. The change in pore water concentrations before (x-axis) and after (y-axis) plant growth for (a) K and (b) ^{137}Cs. Replicate values are shown. The dashed line shows the 1:1 line.

It is expected that the large ^{137}Cs concentration changes in pore water is due to a low capacity to selectively bind ^{137}Cs. However, although BEN with the lowest RIP of all substrates explains the ^{137}Cs depletion in the pore water, this is not the case for the BIO substrate which has a larger RIP that increases during the pot experiment. The change in both the available ^{137}Cs in the pore water and the selective adsorption of ^{137}Cs onto the solid phase has implications on the assumption that the ^{137}Cs soil-pore water ratio, that is the solid-liquid distribution coefficient K_D, may be considered constant during the

course of the experiment, although this is only for two exceptional cases BEN and BIO substrates.

The behavior of Cs in the soil-plant system is described by a sorption-desorption process between soil and solution, quantified by K_D, and an ion uptake process from solution to plant, quantified by CF. The K_D is expected to be positively correlated with RIP and the 2:1 phyllosilicate content. However, this is not the case (Table III.4). The K_D is strongly negatively correlated with K concentrations. As expected, the CF correlates most strongly to cation composition of pore water, and especially with K concentration. The CR correlates negatively with 2:1 phyllosilicate content and very strongly with exchangeable K content. This shows that the influence of K is predominant in these substrate-plant systems.

Table III.4. The Pearson correlation coefficients estimated by row-wise method between K_D, CF and CR based on pore water concentrations after growth and the substrate or plant mean values (N = 16) after log-transformation, except for the pH. The RIP was measured on the substrates after plant growth. Significant correlations are in bold with *** $p < 0.001$; ** $p < 0.01$; * $p < 0.05$.

		K_D	CF	CR
substrate				
	2:1 minerals	**-0.56***	**-0.75*****	**-0.57***
	RIP	0.28	-0.11	**-0.51***
	CEC	-0.04	-0.29	-0.43
	pH	**-0.60***	-0.48	-0.09
exchangeable				
	^{137}Cs	0.26	0.25	0.10
	K	**-0.63****	**-0.92*****	**-0.76*****
pore water *before*				
	^{137}Cs	**-0.83*****	**-0.52***	0.12
	K	**-0.84*****	**-0.80*****	-0.32
pore water *after*				
	^{137}Cs	-	-	-0.11
	K	**-0.86*****	**-0.93*****	**-0.51***
plant				
	yield	0.28	0.10	-0.17
	^{137}Cs	0.12	-	-
	K	**-0.93*****	**-0.83*****	-0.27

Appendix IV
Highly weathered mineral soils have highest transfer risk of radiocaesium contamination after a nuclear accident: a global soil-plant study

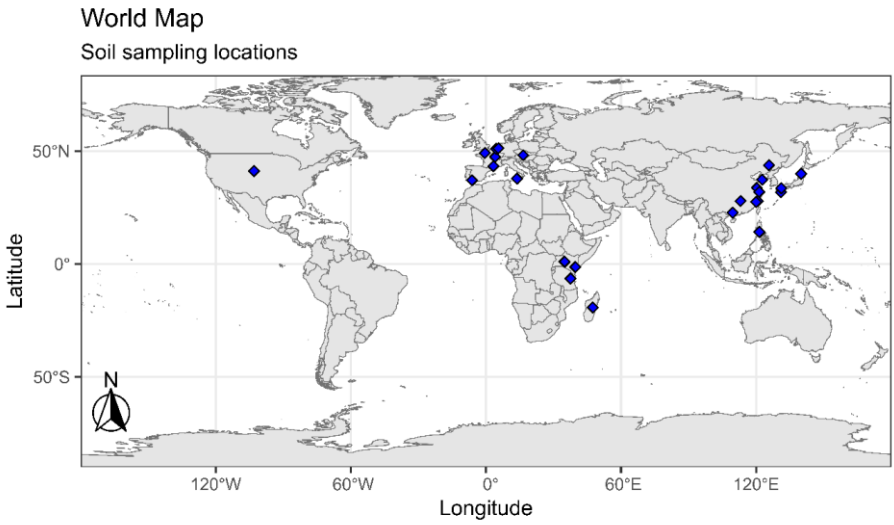

Figure IV.1. World map of soil sampling locations (WGS84 geographic coordinate reference system).

Table IV.1. Coordinates of soil sampling locations. Contact authors for missing coordinates: (Dengra i Grau, 2020; Neugschwandtner et al., 2020; Saracanlao et al., 2022; Six et al., 2012). Numbers in brackets discriminate soil sampling locations.

soil sampling origin	coordinates	
city, country	latitude	longitude
Miyakonojo, Japan	–	–
Mount Elgon, Kenya (1)	1°7'59.0" N	34°40'46.4" E
Sidney, United States	41°14'8" N	102°59'38" W
Gross Enzersdorf, Austria	–	–
Changchun, China	43°47'28" N	125°41'26" E
Yancheng, China	33°45'16" N	120°18'6" E
Nantong, China	31°58'36" N	121°22'12" E
Weihai, China	37°24'33" N	122°40'25" E
Ogata, Japan	–	–
Kitale, Kenya (1)	0°57'58.1" N	34°59'7.8" E
Rots, France (1)	49°12'15" N	0°29'25" W
Rots, France (2)	49°12'15" N	0°29'25" W
Teso, Kenya	–	–
Mount Elgon, Kenya (2)	1°8'28.0" N	34°41'52.0" E
Mount Elgon, Kenya (3)	1°9'15.0" N	34°45'59.8" E
Sint-Katelijne-Waver, Belgium	51°4'30.7" N	4°31'28.5" E
Hamont-Achel, Belgium	51°16'43.7" N	5°30'27.6" E
Pagsanjan, Philippines (1)	14°15'45" N	121°22'0" E
Pagsanjan, Philippines (2)	14°14'8" N	121°23'29" E
Brécy, France (1)	47°29'9" N	4°2'45" E
Yoshiki, Japan	–	–
Pagsanjan, Philippines (3)	14°13'22" N	121°23'44" E
Brécy, France (2)	47°29'9" N	4°2'45" E
Montpellier, France	43°21'49" N	3°20'1" E
Aliminusa, Italy	37°52'9" N	13°47'42" E
Pagsanjan, Philippines (4)	14°15'1" N	121°25'57" E
Pagsanjan, Philippines (5)	14°15'55" N	121°27'28" E
Isla Mayor, Spain	–	–
Dakawa, Tanzania	6°23'56.6" S	37°33'47.5" E
Endebess, Kenya	1°3'58.3" N	34°54'41.8" E
Ningde, China	27°31'25" N	119°57'39" E
Wenzhou, China	27°52'50" N	120°42'28" E
Chenzhou, China	27°55'59" N	113°03'55" E
Nanning, China	22°45'32" N	109°33'21" E
Cavinti, Philippines	14°15'26" N	121°31'46" E

soil sampling origin	coordinates	
city, country	latitude	longitude
Kitale, Kenya (2)	1°5'10.4" N	34°56'33.9" E
Behenjy, Madagascar	19°12'59.3" S	47°27'10.6" E
Luisiana, Philippines	–	–

The soil collection included 26 topsoils with contrasting soil properties, along with 12 topsoils from two sequences representing various weathering stages. A clayey Andosol was sampled in Miyakonojo, a lowland paddy rice Gleysol in Ogata, and a sandy woodland Cambisol in Yoshiki, Japan. A Kastanozem (or Mollisol) was sampled from arable land in Sidney (Nebraska, USA). A silty loam Chernozem was sampled from arable land in Gross Enzersdorf (Austria) at the experimental farm of the University of Natural Resources and Life Sciences, Vienna. Two haplic Luvisols were sampled from arable land in Rots, two calcaric Cambisols from arable land in Brécy, and a chromic Cambisol from woodland in Montpellier, France. A terric Anthrosol was sampled in Sint-Katelijne-Waver at the Research Station for vegetable production, and a sandy woodland plaggic Anthrosol in Hamont-Achel, Belgium. A woodland vertic Cambisol was sampled in Aliminusa (Italy), and a Vertisol was sampled in Isla Mayor (Spain). Soils were sampled at eight locations in China representing a collection with outspoken clayey properties. A paddy soil from loess sediment and alluvial deposits was sampled in Changchun, an upland soil from coastal sediments in Yancheng, an upland soil from calcareous alluvial deposit in Nantong, an upland soil from light-colored crystalline weathered rock in Weihai, an upland soil from light-colored fine crystalline weathered rock mixed with sand and shale weathered clastic sedimentary rocks and associated metamorphic weathered rock in Ningde, an upland soil from light-colored fine crystalline weathered rock mixed with sand and shale weathered clastic sedimentary rocks and associated metamorphic weathered rock in Wenzhou, an upland soil from neutral alluvial deposits in Chenzhou, and a paddy soil from light-colored crystalline weathered rock in Nanning, China. A granitic Lixisol was sampled in Teso (Kenya), and a lowland rice Vertisol in Dakawa (Tanzania). A Ferralsol was sampled from arable land in Behenjy (Madagascar) and in Luisiana (Philippines).

A sequence of soils was collected in Kenya in 2022 at Mount Elgon (4,321 m.a.s.l.) and in the valley. Mount Elgon, a Miocene-age volcano formed 22–12 million years ago (Ballatore and Olaka, 2015), has soils developed from pyroclastic volcanic rock (Siderius and Njeru, 1976). Samples were obtained

from three locations on the northeast flank of the mountain (3,212–2,411 m.a.s.l., slope 12–5%) and three locations in the valley (1,816–1,855 m.a.s.l., slope below 4%). Average annual precipitation ranged from 1600 mm at the highest site to 1,050 mm in the valley (Ballatore and Olaka, 2015). The Andosol was collected from a shallow soil bed with grass in an open forest with coniferous trees. Humic and haplic Nitisols were collected from deeper soil beds in dense rainforest. Pellic Vertisol and mollic Gleysol were sampled from moist bottomland areas cultivated with sugar cane and maize, respectively. Rhodic Ferralsol was sampled from uplands cropped with maize and tuber.

A second sequence of soils were collected in the Philippines in 2022 east of Lake Laguna de Bai on the Caliraya plateau. The lake was formed 2.3–1.7 million years ago by volcanic and tectonic processes (Aurelio and Peña, 2010). Samples were collected from four sites in the lowlands (below 20 m.a.s.l., slope below 1%), one site at the foot of a hill (24 m.a.s.l., slope 17%) and in the uplands (300 m.a.s.l., slope 2%). Average annual precipitation ranged from 1,800 mm to 3,600 mm, with the highest rainfall values associated with more weathered soils. A “Hydrosol” soil (Cambisol) was collected near Laguna de Bai Lake, which was periodically flooded for rice cultivation (Carating et al., 2014). Further from the lake, “Markina silty clay loam” soil (Cambisol) was collected, which was cultivated with rice. “Calumpang clay” (Cambisol) soil was collected, exhibiting shrinking and swelling properties (Carating et al., 2014) and used for perennial vegetable cultivation. “Lipa loam” (Cambisol) soil was sampled, developed on volcanic tuff (Carating et al., 2014) and used for pasture. “Paete clay loam” (Cambisol) soil was sampled, derived from andesite-basalt parent materials (Carating et al., 2014), and used for coconut cultivation. On the plateau, “Luisiana clay” (Acrisol) was sampled, representing well-drained, weathered soils utilized for fruit tree cultivation despite low pH (<5) and limited nutrient content.

Table IV.2. Soil mineralogy (*N* = 38), weathering index of minerals (Jackson et al., 1948; Jackson and Sherman, 1953) and calculated weathering index of soils. Rows are ordered by increasing weathering index and grouped in reference soil groups (WRB). Qtz = quartz; 1:1 = kaolin phyllosilicates; Al-2:1 = aluminum 2:1 phyllosilicates; Fe-2:1 = iron 2:1 phyllosilicates; Fe-2:1:1 = iron chlorite phyllosilicates; Mg-2:1:1 = magnesium chlorite phyllosilicates; Ms = muscovite; Fsp = K-feldspars and plagioclase; Cal/Dol = calcite and dolomite; Po = pyrrhotite; Ant = anatase; FeOx = iron (oxy-)hydroxides; AlOx = aluminium (oxy-)hydroxides; Amp/Px = amphibole and pyroxene; a = mineral phases that appear amorphous on XRD pattern. Limit of detection is 1 g 100 g^{-1}.

reference soil group and sampling origin	Qtz	1:1	Al-2:1	Fe-2:1	Fe-2:1:1	Mg-2:1:1	Ms	Fsp	Cal/Dol	Po	Ant	FeOx	AlOx	Amp/Px	a	weathering index
city, country	g 100 g^{-1}															-
mineral weathering index:	*6*	*9*	*7*	*4*	*4*	*8*	*7*	*5*	*2*	*1*	*12*	*11*	*10*	*3*	*1*	
Andosol																
[j]Miyakonojo, Japan	4	<1	<1	<1	<1	<1	7	22	<1	<1	<1	<1	<1	<1	67	2.5
[k]Mount Elgon, Kenya (1)	3	9	6	<1	<1	7	6	7	<1	<1	<1	3	3	<1	56	3.7
Kastanozem																
[j]Sidney, United States	35	1	14	<1	<1	<1	1	24	1	<1	<1	<1	<1	1	23	4.8
[k]Sidney, United States	35	<1	11	<1	<1	<1	25	19	<1	<1	<1	<1	<1	2	8	5.7
Chernozem																
[j]Gross Enzersdorf, Austria	38	2	6	<1	5	3	12	11	22	<1	<1	<1	<1	1	<1	5.2
Phaeozem																
[k]Changchun, China	36	4	17	<1	<1	6	<1	35	2	<1	<1	<1	<1	<1	<1	5.8
Fluvisol																
[k]Yancheng, China	39	2	8	<1	<1	7	8	25	9	<1	<1	<1	<1	2	<1	5.4
[k]Nantong, China	43	<1	8	<1	<1	8	14	17	3	<1	<1	<1	<1	2	5	5.4
[k]Weihai, China	46	<1	<1	<1	<1	<1	14	38	<1	<1	<1	<1	<1	<1	2	5.6
Gleysol																
[j]Ogata, Japan	20	3	33	<1	<1	<1	<1	25	<1	<1	<1	<1	<1	<1	19	5.2
[k]Kitale, Kenya (1)	61	10	4	<1	<1	<1	3	14	<1	<1	1	1	<1	<1	6	6.1

reference soil group and sampling origin	Qtz	1:1	Al-2:1	Fe-2:1	Fe-2:1:1	Mg-2:1:1	Ms	Fsp	Cal/Dol	Po	Ant	FeOx	AlOx	Amp/Px	a	weathering index
city, country	g 100 g^{-1}															-
mineral weathering index:	*6*	*9*	*7*	*4*	*4*	*8*	*7*	*5*	*2*	*1*	*12*	*11*	*10*	*3*	*1*	
Luvisol																
[j]Rots, France (1)	67	<1	7	<1	3	<1	<1	14	9	<1	<1	<1	<1	<1	<1	5.5
[k]Rots, France (1)	65	<1	6	<1	1	<1	2	16	10	<1	<1	<1	<1	<1	<1	5.5
[j]Rots, France (2)	58	<1	13	<1	4	<1	<1	15	10	<1	<1	<1	<1	<1	<1	5.5
Lixisol																
[j]Teso, Kenya	71	6	<1	<1	<1	<1	1	22	<1	<1	<1	<1	<1	<1	<1	6.0
Nitisol																
[k]Mount Elgon, Kenya (2)	6	6	10	<1	<1	<1	12	8	<1	<1	1	13	2	<1	42	5.1
[k]Mount Elgon, Kenya (3)	10	18	16	<1	<1	<1	6	8	<1	<1	3	15	2	<1	22	6.6
Anthrosol																
[j]Sint-Katelijne-Waver, Belgium	80	3	1	5	<1	<1	<1	11	<1	<1	<1	<1	<1	<1	<1	5.9
[k]Sint-Katelijne-Waver, Belgium	86	<1	5	<1	<1	<1	2	7	<1	<1	<1	<1	<1	<1	<1	6.0
[j]Hamont-Achel, Belgium	97	<1	1	<1	<1	<1	<1	2	<1	<1	<1	<1	<1	<1	<1	6.0
[k]Hamont-Achel, Belgium	87	<1	<1	<1	<1	<1	7	6	<1	<1	<1	<1	<1	<1	<1	6.0
Cambisol																
[k]Pagsanjan, Philippines (1)	1	15	<1	<1	<1	<1	11	37	<1	1	<1	<1	<1	4	31	4.6
[k]Pagsanjan, Philippines (2)	3	15	<1	<1	<1	<1	12	45	<1	1	<1	<1	<1	2	22	5.1
[j]Brécy, France (1)	31	6	18	<1	<1	<1	21	4	19	<1	<1	<1	<1	<1	<1	5.8
[k]Yoshiki, Japan	26	11	<1	5	<1	9	19	29	<1	<1	<1	<1	<1	1	<1	6.0
[k]Pagsanjan, Philippines (3)	4	33	<1	<1	<1	<1	16	21	<1	1	<1	<1	<1	<1	25	6.0
[j]Brécy, France (2)	30	10	17	<1	<1	<1	25	2	16	<1	<1	<1	<1	<1	<1	6.1
[j]Montpellier, France	60	<1	30	<1	<1	<1	<1	10	<1	<1	<1	<1	<1	<1	<1	6.2
[j]Aliminusa, Italy	51	17	25	<1	<1	<1	<1	6	<1	<1	1	<1	<1	<1	<1	6.7

reference soil group and sampling origin	Qtz	1:1	Al-2:1	Fe-2:1	Fe-2:1:1	Mg-2:1:1	Ms	Fsp	Cal/Dol	Po	Ant	FeOx	AlOx	Amp/Px	a	weathering index
city, country	g 100 g^{-1}															-
mineral weathering index:	*6*	*9*	*7*	*4*	*4*	*8*	*7*	*5*	*2*	*1*	*12*	*11*	*10*	*3*	*1*	
[k]Aliminusa, Italy	57	22	11	<1	<1	<1	4	4	<1	<1	1	<1	<1	<1	1	7.0
[k]Pagsanjan, Philippines (4)	8	42	<1	<1	<1	<1	30	8	<1	1	<1	2	<1	<1	9	7.5
[k]Pagsanjan, Philippines (5)	6	44	<1	<1	<1	<1	30	4	<1	2	<1	4	<1	<1	10	7.6
Vertisol																
[j]Isla Mayor, Spain	16	2	43	<1	<1	6	7	11	15	<1	<1	<1	<1	<1	<1	6.0
[j]Dakawa, Tanzania	44	13	29	<1	<1	<1	<1	14	<1	<1	<1	<1	<1	<1	<1	6.6
[k]Endebess, Kenya	35	13	11	<1	<1	<1	7	13	<1	<1	1	13	2	<1	5	7.1
Acrisol																
[k]Ningde, China	65	6	10	<1	<1	<1	5	6	<1	<1	<1	1	<1	<1	7	6.1
[k]Wenzhou, China	55	9	8	<1	<1	<1	5	18	<1	<1	<1	<1	1	<1	4	6.1
[k]Chenzhou, China	37	19	15	<1	<1	10	1	<1	<1	<1	<1	6	<1	<1	12	6.4
[k]Nanning, China	36	16	18	<1	<1	7	<1	3	<1	<1	2	11	3	<1	4	7.3
[k]Cavinti, Philippines	3	68	<1	5	<1	<1	12	<1	<1	1	<1	11	<1	<1	<1	9.2
Ferralsol																
[k]Kitale, Kenya (2)	28	24	13	<1	<1	<1	7	5	<1	<1	2	15	2	<1	4	7.9
[j]Behenjy, Madagascar	25	35	<1	<1	<1	2	<1	<1	<1	<1	5	27	6	<1	<1	9.0
[k]Behenjy, Madagascar	23	22	<1	<1	<1	<1	<1	<1	<1	<1	6	19	30	<1	<1	9.4
[j]Luisiana, Philippines	2	82	<1	<1	<1	<1	<1	<1	<1	<1	<1	16	<1	<1	<1	9.3
[k]Luisiana, Philippines	2	87	<1	<1	<1	<1	<1	<1	<1	<1	<1	11	<1	<1	<1	10.0
min	1	<1	<1	<1	<1	<1	<1	<1	<1	<1	<1	<1	<1	<1	<1	2.5
max	97	82	43	5	5	10	30	45	22	2	5	27	6	4	67	9.3
geometric mean	21	4	2	<1	<1	<1	2	7	<1	<1	<1	<1	<1	<1	1	6.0

[j] measured with PW1830 (Philips) and processed using Quanta; [k] measured with D8 Advance (Bruker) and processed using Profex

The variability in results between methods of quantifying mineralogy is noteworthy. For a selection of soil samples (*N* = 7), mineralogy was determined on bulk powder samples independently using two set-ups and processing methods for comparison (Table IV.2). Mineral phases in soils with high contents (>10 wt%) were similar between methods, as such quartz had a deviation up to 15%, 55% for 2:1 phyllosilicates, 35% for 1:1 phyllosilicates and 48% for the total phyllosilicates. For mineral phases with low contents (<10 wt%), the deviation was much higher (up to a factor of 30) and at the lowest contents (<5 wt%), there was disagreement in the presence of mineral phases in the samples. Operator error in processing XRD patterns accounted for the majority of deviation in the final result. The result after the MIF method was used in the study for further data processing. The data processing relies on a library of measured reference materials with the XRD device, while the Rietveld method is based on the theoretical parameters of minerals and the XRD device. Therefore, the former method was considered more reliable, as it accounts for measurement errors.

Loss-On-Ignition was determined (Nelson and Sommers, 1996) (Table IV.3). Air-dry soil samples (*N* = 26) in triplicate were weighed in glass vials and placed in a muffle oven for a controlled temperature increment (550 °C). Samples were left to cool in a desiccator and weights were recorded using an analytical balance. The percentage of weight loss at the temperature range (105–550 °C) corresponds to the weight of organic matter.

For a selection of samples (*N* = 5) and allophane, the acid ammonium oxalate and pyrophosphate extractable Al, Fe, Mn and Si were determined (McKeague, 1967; McKeague and Day, 1966). Allophane, isolated from Japanese soil, still contained 40% impurity of ferric iron and volcanic glass after treatment with H_2O_2, ultrasonication and autoclavation (121 °C, 20 min), but no further treatments were applied. Samples of 0.4 g air-dry soil in triplicate with 20 mL of 0.2 mmol L^{-1} $(NH_4)_2C_2O_4$ and 0.2 mmol L^{-1} $(COOH)_2{\cdot}H_2O$ at pH 3 were shaken end-over-end (2 h) or 20 mL of 0.1 mmol L^{-1} $Na_4P_2O_7$ were shaken end-over-end (16 h). After centrifugation (15 min), the supernatant was filtered at 0.45 µm (Acrodisc®). The cation concentrations were measured (4200 MP-AES, Agilent Technologies). Allophane in soils was estimated from the Si extracted in acid oxalate (Parfitt and Kimble, 1989). The Al/Si molar ratio (Table IV.4) was calculated by Al extracted by oxalic acid, corrected by Al extracted by pyrophosphate and Si extracted by oxalic acid. Soil allophane

content was derived by multiplying an empirical formula of the Al/Si molar ratio (Parfitt and Kimble, 1989) and the percentage of Si extracted by oxalic acid.

Soil classification is based on diagnostic criteria based on key properties of soils to categorize soils into classes. In the case of Andosols, one of the key properties is the presence of allophane (IUSS Working Group WRB FAO, 2022). Allophane was found in the youngest soil of this study (Miyakonojo) and in the youngest soil of the Kenyan soil series (Mount Elgon) (Table IV.4). Both soils had andic properties, characteristic of Andosols, such as an oxalate extractable Al + 1/2·Fe value of >4%; high soil organic C >5%; low bulk density; and loamy texture. In Ferralsols, low-activity clay such as kaolinite is the dominant phyllosilicate in soil and it contains Fe and Al (hydr-)oxides (IUSS Working Group WRB FAO, 2022). The most weathered soils of this study were dominated by 1:1 phyllosilicates and Fe and Al oxides (Kitale; Behenjy; Luisiana) (Table IV.2). The soils had a ferralic horizon which is characterized by a high clay content (>40%); Fe and Mn nodules in lower soil layers (>20 cm); low exchange capacity of the clay fraction (<16 $cmol_c$ kg^{-1} clay); no easily weatherable minerals (2:1 phyllosilicate; 2:1:1 phyllosilicate; feldspar; dolomite) except for the soil from Kitale which contained 13% 2:1 phyllosilicates and 5% feldspars. Despite the exceptional mineralogy of the soil from Kitale that calls into question whether the soil is a Ferralsol, the soil was identified in the field as rhodic Ferralsol and the soil class, mineralogy, and other soil properties were confirmed by soil surveys (Ballatore and Olaka, 2015; Siderius and Njeru, 1976).

Table IV.3. Soil characteristics (*N* = 38) measured before soil fertilization and plant growth. Rows are ordered by increasing weathering index and grouped in reference soil groups (WRB). Values represent triplicate means and the standard deviation of RIP is given in brackets. The limits of detection are 0.1 or 1 g 100 g^{-1}.

reference soil group and sampling origin	clay	sand	clay[o]	sand[o]	SIC[p]	SOC[p]	LOI[p]	CEC[p]	RIP[p]		weathering index
city, country	g 100 g^{-1}							$cmol_c$ kg^{-1} soil	mmol kg^{-1} soil		-
Andosol											
Miyakonojo, Japan	23[n]	60	8	44	<0.10	5.6	15.0	5.1	116	(6)	2.5
Mount Elgon, Kenya (1)	10[m]	13	34	2	–	14	–	6.2	365	(15)	3.7
Kastanozem											
Sidney, United States	21[m]	22	11	21	0.19	1.4	5.2	20	6,140	(480)	4.8[j]
Chernozem											
Gross Enzersdorf, Austria	15[m]	40	18	31	3.0	1.0	4.0	13	3,600	(130)	5.2
Phaeozem											
Changchun, China	–	–	24	21	<0.10	1.4	4.8	33	4,270	(280)	5.8
Fluvisol											
Yancheng, China	–	–	12	17	1.0	0.87	3.5	79	2,870	(140)	5.4
Nantong, China	–	–	14	28	0.48	0.95	3.8	91	4,610	(310)	5.4
Weihai, China	–	–	10	54	0.10	1.0	3.0	17	2,150	(60)	5.6
Gleysol											
Ogata, Japan	32[m]	34	15	23	<0.10	1.8	7.0	32	2,000	(110)	5.2
Kitale, Kenya (1)	15[m]	57	13	44	–	1.3	–	5.4	514	(22)	6.1
Luvisol											
Rots, France (1)	10[n]	20	14	28	1.2	1.2	3.7	14	3,900	(90)	5.5[j]
Rots, France (2)	27[n]	19	16	24	1.4	1.3	4.2	20	5,320	(200)	5.5
Lixisol											
Teso, Kenya	6[n]	82	4	74	<0.10	0.45	1.9	3.0	773	(8)	6.0

reference soil group and sampling origin	clay	sand	clay[o]	sand[o]	SIC[p]	SOC[p]	LOI[p]	CEC[p]	RIP[p]		weathering index
city, country	g 100 g^{-1}							$cmol_c$ kg^{-1} soil	mmol kg^{-1} soil		-
Nitisol											
Mount Elgon, Kenya (2)	9[m]	19	42	5	–	8.4	–	46	1,680	(100)	5.1
Mount Elgon, Kenya (3)	27[m]	17	46	<1	–	5.3	–	50	5,030	(540)	6.6
Anthrosol											
Sint-Katelijne-Waver, Belgium	3[m]	88	6	70	0.19	2.9	5.6	9.2	1,080	(40)	5.9[j]
Hamont-Achel, Belgium	–	–	3	86	0.66	2.3	4.2	1.9	84.8	(1.4)	6.0[j]
Cambisol											
Pagsanjan, Philippines (1)	24[m]	22	22	4	–	1.8	–	24	1,040	(10)	4.6
Pagsanjan, Philippines (2)	17[m]	29	12	7	–	2.3	–	22	328	(6)	5.1
Brécy, France (1)	39[n]	20	28	3	1.9	1.8	7.5	24	5,250	(1,330)	5.8
Yoshiki, Japan	6[n]	86	3	75	<0.10	0.83	4.2	9.8	1,150	(130)	6.0
Pagsanjan, Philippines (3)	38[m]	12	29	4	–	1.8	–	34	863	(20)	6.0
Brécy, France (2)	37[m]	18	35	2	2.0	1.9	7.5	24	5,580	(610)	6.1
Montpellier, France	25[n]	63	17	31	<0.10	0.23	3.3	8.4	2,480	(170)	6.2
Aliminusa, Italy	49[m]	25	10	24	0.13	0.81	6.6	26	5,920	(670)	6.7
Pagsanjan, Philippines (4)	28[m]	18	32	1	–	1.8	–	23	1,190	(30)	7.0
Pagsanjan, Philippines (5)	31[m]	17	39	<1	–	1.8	–	28	658	(9)	7.5
Vertisol											
Isla Mayor, Spain	8[n]	16	39	<1	2.6	1.7	7.1	26	5,820	(700)	6.0
Dakawa, Tanzania	32[n]	12	21	32	0.15	1.2	5.9	21	1,180	(40)	6.6
Endebess, Kenya	28[m]	45	19	47	–	2.0	–	19	1,660	(30)	7.1

reference soil group and sampling origin	clay	sand	clay[o]	sand[o]	SIC[p]	SOC[p]	LOI[p]	CEC[p]	RIP[p]		weathering index
city, country	g 100 g^{-1}							$cmol_c$ kg^{-1} soil	mmol kg^{-1} soil		-
Acrisol											
Ningde, China	–	–	17	44	<0.10	1.6	5.3	42	2,650	(130)	6.1
Wenzhou, China	–	–	14	31	0.24	1.9	6.2	84	1,880	(130)	6.1
Chenzhou, China	–	–	43	2	<0.10	3.7	14	25	1,880	(90)	6.4
Nanning, China	–	–	30	38	0.23	3.6	14	56	1,620	(120)	7.3
Cavinti, Philippines	62[m]	17	45	<1	–	0.56	–	10	129	(<1)	9.2
Ferralsol											
Kitale, Kenya (2)	57[m]	24	29	29	–	1.8	–	8.3	3,630	(200)	7.9
Behenjy, Madagascar	42[m]	24	9	69	<0.10	2.9	18	2.3	13.8	(1.2)	9.0[j]
Luisiana, Philippines	83[m]	2	10	67	<0.10	0.54	13	7.6	143	(2)	9.3[j]
min	3	2	3	<1	<0.10	0.23	1.9	1.9	13.8		2.5
max	83	88	46	86	3.0	14	18	91	6,140		9.3
geometric mean	24	24	17	12	0.28	1.7	5.9	17	1,310		6.0

[m] pipet method (ISO 11277); [n] previously obtained (Buekers, 2007; De Bauw et al., 2021; Dengra i Grau, 2020; Neugschwandtner et al., 2020; Saracanlao et al., 2022; Six et al., 2012); [o] laser diffraction; [p] n = 3

Table IV.4. Acid oxalate and pyrophosphate extractable Al, Fe, Mn and Si in soils (*N* = 5) and isolated allophane. Rows are ordered by increasing weathering index and grouped in reference soil groups (WRB). Values represent triplicate means.

reference soil group and sampling origin	acid oxalate				pyrophosphate				Al/Si ratio	allophane	weathering index
	Al	Fe	Mn	Si	Al	Fe	Mn	Si			
city, country	mg kg^{-1}								–	wt%	–
isolated allophane	46,800	6,880	35.0	19,000	5,280	1,030	5.04	279	2.3	18	
Andosol											
Miyakonojo, Japan	36,500	6,530	92,800	14,800	9,310	2,250	113	290	1.9	12	2.5
Mount Elgon, Kenya (1)	30,900	19,700	1,170	3,690	24,000	17,000	669	1,270	1.9	3	3.7
Nitisol											
Mount Elgon, Kenya (2)	16,600	12,600	2,220	3,490	17,700	11,200	1,050	2,080	<1.0	0	5.1
Ferralsol											
Behenjy, Madagascar	2,610	1,330	30.4	72.6	12,100	6,850	13.1	851	<1.0	0	9.0
Luisiana, Philippines	1,970	942	132	370	1,480	325	59.7	201	1.4	0	9.3

The particle size distribution of Luisiana Ferralsol strongly depended on both the pretreatment, such as removal of cements and dispersion, and the measurement method, such as diffraction or sedimentation. All samples were treated in the same batch and measured by laser diffraction. This showed that Luisiana Ferralsol had a clay content of 10% (Table IV.3). This was in contrast to the clay yield of 83% after the pipet method. This soil was again measured by diffraction after no or (hydr)oxides removal and ultrasonic dispersion treatments where the clay content was 30–44% (Table IV.5).

Table IV.5. Particle size distributions of Ferralsol soil (Luisiana) for various dispersion treatments (with or without removal of iron by 1 mol L^{-1} oxalic acid, with an ultrasonic treatment of 20 sec, 1 min, or 2 min) before measurements by laser diffraction compared to the pipet sedimentation method (ISO 11277). Values represent means (*n* = 2 or 5; see below), and standard deviations are given in brackets.

	sedimentation (ISO 11277)	laser diffraction											
soil fraction		no oxalic acid/ 20" sonication[q]		no oxalic acid / 1' sonication[q]		no oxalic acid / 2' sonication[q]		oxalic acid/ 20" sonication[r]		oxalic acid/ 1' sonication[r]		oxalic acid/ 2' sonication[r]	
<0.002 mm	83	38	(2)	33	(6)	39	(5)	**30**	(8)	33	(13)	**44**	(6)
0.002–0.053 mm	14	56	(5)	57	(1)	55	(<1)	50	(14)	44	(17)	51	(5)
0.053–2 mm	2	6	(7)	11	(7)	6	(5)	20	(21)	23	(29)	5	(2)

[q] *n* = 2; [r] *n* = 5

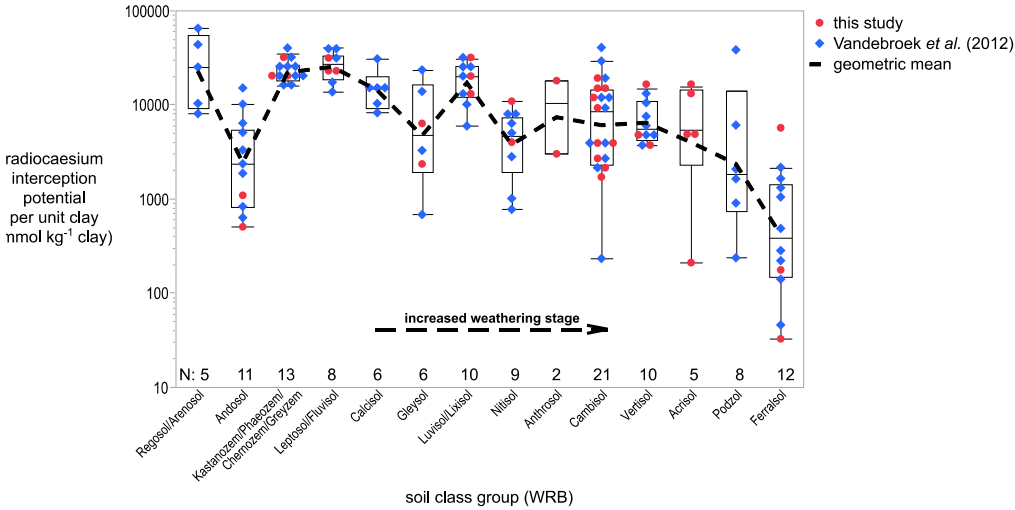

Figure IV.2. Comparison of radiocaesium interception potential of soil per unit clay (highest clay contents) in relation to soil weathering stages in this study and Vandebroek et al. (2012). The dotted line connects the geometric means of the RIP/%clay values of soil groups. The number of soils per group (*N*) are given.

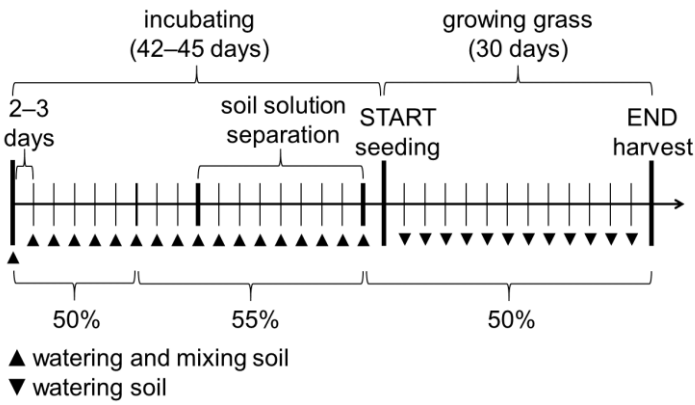

Figure IV.3. Timeline of experimental phases of incubation and growth in the pot experiment with moisture contents (%) of fully saturated soil.

Table IV.6. Soil properties measured after soil fertilization, except for the moisture content, but before plant growth (N = 53). Values represent means of triplicates, except for moisture content (n = 1). Rows are ordered by increasing weathering index and grouped in reference soil groups (WRB).

reference soil group and sampling origin	pH	moisture content	soil ^{137}Cs	soil solution						exchangeable cations					
				^{137}Cs	K	NH_4	Na	Ca	Mg	^{137}Cs	K	NH_4	Na	Ca	Mg
city, country		g H_2O g^{-1} soil	kBq kg^{-1}	kBq L^{-1}	mmol L^{-1}					kBq kg^{-1}	$cmol_c$ kg^{-1}				
Andosol															
Miyakonojo, Japan	4.8	31	377	2.2	0.50	0.27	1.3	6.2	3.0	200	0.20	0.0090	0.11	3.8	1.1
[s]Miyakonojo, Japan	4.8	-	379	4.1	2.9	0.24	1.4	7.4	3.5	200	0.56	0.0080	0.11	3.9	1.0
Mount Elgon, Kenya (1)	4.1	39	804	0.45	0.29	0.11	0.92	1.3	1.1	390	0.78	–	0.21	0.58	0.47
[s]Mount Elgon, Kenya (1)	4.1	–	798	1.1	2.0	0.12	1.1	1.6	1.3	370	1.4	–	0.21	0.58	0.45
Kastanozem															
Sidney, United States	6.4	22	374	0.21	7.3	0.19	1.7	17	4.8	170	3.6	0.010	0.14	13	2.5
Chernozem															
Gross Enzersdorf, Austria	7.4	32	341	0.017	0.26	0.016	1.2	14	2.5	95	0.50	0.010	0.13	32	2.4
Phaeozem															
Changchun, China	7.1	32	429	0.072	0.23	0.014	4.3	26	5.3	52	0.75	0.030	0.50	32	4.8
Fluvisol															
Yancheng, China	7.5	23	342	0.16	3.20	0.012	15	29	9.3	100	1.0	0.0095	0.82	31	3.2

reference soil group and sampling origin	pH	moisture content	soil ^{137}Cs	soil solution ^{137}Cs	soil solution K	soil solution NH_4	soil solution Na	soil solution Ca	soil solution Mg	exchangeable cations ^{137}Cs	exchangeable cations K	exchangeable cations NH_4	exchangeable cations Na	exchangeable cations Ca	exchangeable cations Mg
city, country		g H_2O g^{-1} soil	kBq kg^{-1}	kBq L^{-1}	mmol L^{-1}					kBq kg^{-1}	$cmol_c$ kg^{-1}				
Nantong, China	7.4	26	333	0.012	0.27	0.0071	1.2	12	2.0	44	0.37	0.0082	0.15	32	2.1
Weihai, China	4.4	13	346	0.92	0.86	3.80	2.7	7.2	2.7	41	0.30	0.24	0.12	2.4	0.74
Gleysol															
Ogata, Japan	5.1	33	365	0.073	0.11	0.16	4.8	9.6	4.6	61	0.46	0.079	1.1	17	7.1
Kitale, Kenya (1)	4.1	18	416	0.39	0.56	0.12	4.6	10	4.0	150	0.18	–	0.19	1.7	0.43
[s]Kitale, Kenya (1)	4.1	–	408	1.0	3.8	0.19	5.1	13	5.6	57	0.47	–	0.21	1.8	0.5
Luvisol															
Rots, France (1)	7.4	21	358	0.090	2.3	0.085	2.2	37	1.6	160	0.76	0.0090	0.11	30	0.66
Rots, France (2)	7.4	22	358	0.080	1.5	0.029	2.7	26	1.6	130	1.0	0.012	0.21	33	1.0
Lixisol															
Teso, Kenya	5.0	11	336	12	2.0	9.0	2.5	7.4	4.1	240	0.18	0.29	0.070	1.2	0.38
Nitisol															
Mount Elgon, Kenya (2)	5.4	33	520	0.16	1.80	0.0086	0.48	14	6.3	210	2.4	–	0.13	16	4.1
[s]Mount Elgon, Kenya (2)	5.4	–	509	0.24	2.7	0.0041	0.53	15	7.0	210	2.8	–	0.12	16	3.9
Mount Elgon, Kenya (3)	5.2	26	502	0.13	2.0	0.015	0.60	11	4.6	220	2.6	–	0.12	12	2.6
[s]Mount Elgon, Kenya (3)	5.2	–	505	0.15	3.1	0.0084	0.66	13	5.8	220	2.9	–	0.12	12	2.5

reference soil group and sampling origin	pH	moisture content	soil ^{137}Cs	soil solution						exchangeable cations					
				^{137}Cs	K	NH_4	Na	Ca	Mg	^{137}Cs	K	NH_4	Na	Ca	Mg
city, country		g H_2O g^{-1} soil	kBq kg^{-1}	kBq L^{-1}	mmol L^{-1}					kBq kg^{-1}	$cmol_c$ kg^{-1}				
Anthrosol															
Sint-Katelijne-Waver, Belgium	5.1	22	350	0.16	0.69	0.013	2.1	18	6.9	110	0.29	0.0086	0.12	6.9	1.6
Hamont-Achel, Belgium	3.0	16	334	20	0.80	13	2.3	0.62	2.0	39	0.049	0.27	0.060	0.25	0.14
[s]Hamont-Achel, Belgium	3.0	-	330	27	11	16	2.7	1.2	3.1	47	0.39	0.27	0.069	0.27	0.17
Cambisol															
Pagsanjan, Philippines (1)	5.9	45	406	0.14	0.29	0.072	1.2	1.0	0.89	180	0.91	–	0.54	7.4	4.5
[s]Pagsanjan, Philippines (1)	5.9	–	408	0.19	0.80	0.045	1.8	2.6	2.3	160	1.2	–	0.53	7.6	4.6
Pagsanjan, Philippines (2)	5.3	54	535	0.54	0.26	0.15	1.4	2.1	2.2	260	0.67	–	0.48	6.5	4.8
[s]Pagsanjan, Philippines (2)	5.4	–	522	0.69	0.63	0.18	1.8	3.0	3.1	160	0.99	–	0.48	6.6	4.8
Brécy, France (1)	7.4	30	385	0.025	0.78	0.024	0.76	8.0	0.49	74	1.2	0.014	0.14	38	1.1
Yoshiki, Japan	5.2	23	357	0.18	0.25	0.74	1.4	9.7	3.3	13	0.15	0.049	0.11	5.5	1.3
Pagsanjan, Philippines (3)	5.6	46	437	0.036	0.17	0.013	0.89	2.3	1.7	180	0.83	–	0.52	11	5.7
[s]Pagsanjan, Philippines (3)	5.5	–	438	0.065	0.57	0.017	1.6	6.0	4.5	160	1.2	–	0.55	11	5.9
Brécy, France (2)	7.4	38	391	0.062	0.67	0.47	0.59	3.5	3.10	73	1.3	0.035	0.13	36	1.1

reference soil group and sampling origin	pH	moisture content	soil ^{137}Cs	soil solution ^{137}Cs	K	NH_4	Na	Ca	Mg	exchangeable cations ^{137}Cs	K	NH_4	Na	Ca	Mg
city, country		g H_2O g^{-1} soil	kBq kg^{-1}	kBq L^{-1}	mmol L^{-1}					kBq kg^{-1}	$cmol_c$ kg^{-1}				
Montpellier, France	4.1	22	456	0.24	0.33	0.67	3.4	2.1	3.4	110	0.45	0.13	0.29	3.8	4.3
Aliminusa, Italy	5.8	25	407	0.067	0.27	0.34	2.50	1.4	0.90	100	0.79	0.088	0.47	12	5.8
Pagsanjan, Philippines (4)	4.3	31	439	0.24	0.47	0.17	1.0	5.8	4.8	160	0.74	–	0.20	6.4	3.9
[s]Pagsanjan, Philippines (4)	4.4	–	436	0.35	0.88	0.37	1.0	5.3	4.5	99	1.1	–	0.20	6.5	3.9
Pagsanjan, Philippines (5)	4.8	40	432	0.14	0.056	0.34	0.82	1.2	0.88	44	0.26	–	0.33	7.3	4.0
[s]Pagsanjan, Philippines (5)	4.8	–	438	0.10	0.28	0.57	1.2	3.2	2.3	29	0.63	–	0.33	7.7	4.1
Vertisol															
Isla Mayor, Spain	7.8	43	364	0.021	0.54	0.0084	13	3.4	4.4	71	1.8	0.013	2.2	36	15
Dakawa, Tanzania	5.7	30	395	0.059	0.36	0.070	3.8	2.8	2.4	130	0.79	0.021	0.66	13	9.3
Endebess, Kenya	4.5	21	403	0.26	0.21	0.049	0.76	3.6	2.6	160	0.69	–	0.21	5.0	2.5
[s]Endebess, Kenya	4.5	–	410	0.15	1.4	0.011	2.0	11	7.9	140	0.93	–	0.21	4.9	2.5
Acrisol															
Ningde, China	6.3	8.0	356	0.20	2.6	0.010	2.1	20	7.2	160	1.1	0.0085	0.15	8.0	2.2
Wenzhou, China	5.4	5.9	341	1.5	0.91	3.6	1.6	13	1.6	93	0.32	0.24	0.10	5.9	0.63
Chenzhou, China	6.5	19	378	0.027	0.21	0.017	1.4	27	9.3	110	0.46	0.022	0.15	19	5.3
Nanning, China	6.6	17	350	0.036	0.24	0.0091	1.6	27	9.1	89	0.43	0.022	0.16	17	5.0

reference soil group and sampling origin	pH	moisture content	soil ^{137}Cs	soil solution ^{137}Cs	soil solution K	soil solution NH_4	soil solution Na	soil solution Ca	soil solution Mg	exchangeable cations ^{137}Cs	exchangeable cations K	exchangeable cations NH_4	exchangeable cations Na	exchangeable cations Ca	exchangeable cations Mg
city, country		g H_2O g^{-1} soil	kBq kg^{-1}	kBq L^{-1}	mmol L^{-1}					kBq kg^{-1}	$cmol_c$ kg^{-1}				
Cavinti, Philippines	3.8	38	429	0.53	0.021	0.22	0.56	0.15	0.15	360	0.058	–	0.23	0.41	0.33
[s]Cavinti, Philippines	3.8	–	425	1.0	0.17	0.40	1.0	0.30	0.31	330	0.40	–	0.22	0.46	0.33
Ferralsol															
Kitale, Kenya (2)	3.8	28	404	0.19	2.2	0.030	1.1	5.4	3.8	220	1.2	–	0.087	1.2	0.63
[s]Kitale, Kenya (2)	3.9	–	401	0.19	3.8	0.038	1.2	6.8	5.0	220	1.6	–	0.10	1.3	0.71
Behenjy, Madagascar	4.2	18	434	64	0.24	7.4	1.0	0.13	0.40	380	0.054	0.36	0.069	0.23	0.14
[s]Behenjy, Madagascar	4.2	–	439	97	4.8	9.5	1.0	0.19	0.58	370	0.46	0.42	0.059	0.17	0.14
Luisiana, Philippines	4.3	47	362	0.56	0.033	0.28	1.2	0.59	0.31	300	0.11	0.14	0.31	1.8	0.76
min	3.0	11	333	0.012	0.021	0.0041	0.48	0.13	0.15	13	0.049	0.0061	0.059	0.17	0.13
max	7.8	54	804	97	11	16	15	37	9.3	390	3.6	0.41	2.2	38	15
geometric mean	5.1	26	411	0.29	0.65	0.11	1.6	4.6	2.4	130	0.60	0.030	0.20	5.2	1.6

[s] K treated soils

Table IV.7. Soil (*N* = 24) and plant (*N* = 53) properties measured after plant growth. Values represent means of triplicates with SD in parentheses. Rows are ordered by increasing weathering index and grouped in reference soil groups (WRB). Letters indicate significant differences among ^{137}Cs soil-grass concentration ratios per soil type (Tukey-Kramer HSD, p <0.05, n = 3).

reference soil group and sampling origin	exchangeable cations					grass								
	^{137}Cs	K	Na	Ca	Mg	yield	^{137}Cs	K	Na	Ca	Mg	CR		
city, country	kBq kg^{-1}	cmol$_c$ kg^{-1}				g	kBq kg^{-1}	g kg^{-1}				kg kg^{-1}		
Andosol														
Miyakonojo, Japan	–	–	–	–	–	0.14	470	44	7.7	13	5.5	1.25	(0.24)	e,f,g,h
^{s}Miyakonojo, Japan	–	–	–	–	–	0.16	88	57	4.7	9.9	3.9	0.232	(0.032)	j,k,l,m
Mount Elgon, Kenya (1)	470	0.28	0.078	0.31	0.21	0.56	360	10	7.3	5.2	2.9	0.430	(0.023)	h,i,j,k,l
^{s}Mount Elgon, Kenya (1)	450	0.48	0.12	0.37	0.22	0.65	87	24	4.6	3.3	1.9	0.109	(0.008)	l,m,n,o
Kastanozem														
Sidney, United States	–	–	–	–	–	1.32	7.6	58	7.0	10	2.5	0.0204	(0.0140)	p,q,r,s,t
Chernozem														
Gross Enzersdorf, Austria	–	–	–	–	–	0.25	11	47	6.9	14	3.6	0.0328	(0.0078)	o,p,q,r
Phaeozem														
Changchun, China	–	–	–	–	–	0.63	15	38	14	15	3.3	0.0341	(0.0184)	o,p,q,r
Fluvisol														
Yancheng, China	–	–	–	–	–	1.07	8.2	49	13	10	3.4	0.0239	(0.0048)	p,q,r,s
Nantong, China	–	–	–	–	–	0.68	19	31	13	13	2.8	0.0564	(0.0288)	n,o,p,q

reference soil group and sampling origin		exchangeable cations				grass							
	^{137}Cs	K	Na	Ca	Mg	yield	^{137}Cs	K	Na	Ca	Mg	CR		
city, country	kBq kg^{-1}	cmol$_c$ kg^{-1}				g	kBq kg^{-1}	g kg^{-1}				kg kg^{-1}		
Weihai, China	–	–	–	–	–	0.73	190	32	15	7.3	3.6	0.546	(0.049)	g,h,i,j
Gleysol														
Ogata, Japan	–	–	–	–	–	0.80	87	31	18	11	4.2	0.238	(0.045)	j,k,l,m
Kitale, Kenya (1)	160	0.068	0.067	1.2	0.33	1.84	470	13	7.9	6.4	3.5	1.14	(0.06)	e,f,g,h,i
[s]Kitale, Kenya (1)	58	0.18	0.12	1.2	0.32	1.73	19	29	3.5	5.9	2.4	0.0473	(0.0066)	n,o,p,q
Luvisol														
Rots, France (1)	–	–	–	–	–	1.40	25	46	6.3	15	1.7	0.0707	(0.0236)	m,n,o,p
Rots, France (2)	–	–	–	–	–	0.38	5.4	51	4.9	13	1.6	0.0152	(0.0028)	q,r,s,t
Lixisol														
Teso, Kenya	–	–	–	–	–	0.77	1,900	32	12	11	4.5	5.70	(0.34)	b,c,d
Nitisol														
Mount Elgon, Kenya (2)	250	1.4	0.081	11	2.9	1.16	3.9	31	3.7	6.7	3.5	0.00749	(0.00046)	s,t
[s]Mount Elgon, Kenya (2)	200	1.8	0.083	11	3.0	1.14	5.4	31	3.9	6.2	3.1	0.0107	(0.0011)	r,s,t
Mount Elgon, Kenya (3)	230	1.6	0.068	8.1	1.9	1.39	2.3	36	3.5	6.5	3.8	0.00466	(0.00068)	t
[s]Mount Elgon, Kenya (3)	230	1.9	0.070	8.6	2.0	1.30	3.2	33	3.4	6.1	3.2	0.00636	(0.00158)	s,t

reference soil group and sampling origin	exchangeable cations					grass								
	^{137}Cs	K	Na	Ca	Mg	yield	^{137}Cs	K	Na	Ca	Mg	CR		
city, country	kBq kg^{-1}	cmol$_c$ kg^{-1}				g	kBq kg^{-1}	g kg^{-1}				kg kg^{-1}		
Anthrosol														
Sint-Katelijne-Waver, Belgium	–	–	–	–	–	0.98	67	32	11	13	4.7	0.190	(0.053)	j,k,l,m,n
Hamont-Achel, Belgium	–	–	–	–	–	0.19	1,700	12	12	0.81	2.0	5.07	(0.34)	b,c,d
[s]Hamont-Achel, Belgium	–	–	–	–	–	0.04	960	42	11	0.81	1.5	2.92	(0.61)	c,d,e,f
Cambisol														
Pagsanjan, Philippines (1)	190	0.55	0.29	5.0	3.2	0.58	8.5	15	4.3	3.3	1.9	0.0209	(0.0028)	p,q,r,s
[s]Pagsanjan, Philippines (1)	140	0.80	0.34	5.1	3.3	0.52	8.4	24	3.8	4.4	2.2	0.0205	(0.0008)	p,q,r,s
Pagsanjan, Philippines (2)	240	0.25	0.26	4.3	3.3	1.79	390	15	2.3	2.8	2.0	0.722	(0.116)	f,g,h,i,j
[s]Pagsanjan, Philippines (2)	170	0.40	0.28	4.4	3.4	1.78	130	23	1.8	3.7	2.4	0.258	(0.044)	j,k,l,m
Brécy, France (1)	–	–	–	–	–	0.57	29	19	13	7.5	1.1	0.0752	(0.0581)	n,o,p,q
Yoshiki, Japan	–	–	–	–	–	0.33	110	44	9.0	14	4.4	0.304	(0.049)	i,j,k,l
Pagsanjan, Philippines (3)	180	0.37	0.27	7.5	4.0	1.66	53	15	2.1	3.0	1.4	0.122	(0.023)	k,l,m,n,o
[s]Pagsanjan, Philippines (3)	150	0.55	0.27	7.5	4.2	2.14	24	20	1.6	3.3	1.5	0.0543	(0.0068)	n,o,p,q
Brécy, France (2)	–	–	–	–	–	0.39	2.9	35	6.2	8.7	1.3	0.00738	(0.00285)	s,t
Montpellier, France	–	–	–	–	–	0.43	110	34	11	6.4	3.9	0.242	(0.046)	j,k,l,m

reference soil group and sampling origin	exchangeable cations					grass								
	^{137}Cs	K	Na	Ca	Mg	yield	^{137}Cs	K	Na	Ca	Mg	CR		
city, country	kBq kg^{-1}	cmol$_c$ kg^{-1}				g	kBq kg^{-1}	g kg^{-1}				kg kg^{-1}		
Aliminusa, Italy	–	–	–	–	–	0.13	17	54	8.0	7.7	3.1	0.0409	(0.0255)	o,p,q,r
Pagsanjan, Philippines (4)	150	0.32	0.11	4.4	2.8	1.66	140	25	3.2	5.2	2.9	0.318	(0.028)	h,i,j,k,l
[s]Pagsanjan, Philippines (4)	99	0.55	0.11	4.4	2.9	1.50	21	30	3.7	5.5	2.6	0.0482	(0.0368)	o,p,q,r
Pagsanjan, Philippines (5)	45	0.15	0.17	5.2	2.9	1.55	830	12	5.5	5.7	3.0	1.91	(0.03)	d,e,f,g
[s]Pagsanjan, Philippines (5)	30	0.36	0.23	5.1	3.0	1.43	140	22	3.1	5.3	2.4	0.317	(0.054)	h,i,j,k,l
Vertisol														
Isla Mayor, Spain	–	–	–	–	–	0.38	2.9	30	6.6	3.0	1.9	0.00797	(0.00583)	s,t
Dakawa, Tanzania	–	–	–	–	–	0.55	39	25	7.6	4.3	1.9	0.0997	(0.1488)	o,p,q,r
Endebess, Kenya	200	0.37	0.12	3.6	1.9	0.95	22	29	5.2	7.0	4.2	0.0546	(0.0048)	n,o,p,q
[s]Endebess, Kenya	99	0.55	0.11	4.4	2.9	1.22	5.8	30	4.1	6.0	3.3	0.0143	(0.0021)	q,r,s,t
Acrisol														
Ningde, China	–	–	–	–	–	0.77	7.0	59	6.8	13	4.1	0.0196	(0.0014)	p,q,r,s
Wenzhou, China	–	–	–	–	–	0.52	160	43	13	11	2.6	0.479	(0.076)	g,h,i,j,k
Chenzhou, China	–	–	–	–	–	0.15	8.8	51	6.3	13	4.8	0.0234	(0.0046)	p,q,r,s
Nanning, China	–	–	–	–	–	0.20	12	54	6.1	12	4.9	0.0333	(0.0028)	o,p,q,r
Cavinti, Philippines	370	0.035	0.072	2.9	0.29	1.64	3,500	0.79	10	4.6	2.6	8.03	(2.25)	b,c

reference soil group and sampling origin	exchangeable cations					grass								
	^{137}Cs	K	Na	Ca	Mg	yield	^{137}Cs	K	Na	Ca	Mg	CR		
city, country	kBq kg^{-1}	cmol$_c$ kg^{-1}				g	kBq kg^{-1}	g kg^{-1}				kg kg^{-1}		
[s]Cavinti, Philippines	340	0.11	0.084	1.3	0.26	2.36	1,400	13	6.1	4.4	1.6	3.27	(0.58)	c,d,e
Ferralsol														
Kitale, Kenya (2)	250	0.51	0.076	3.0	0.57	2.88	7.6	29	3.6	6.3	3.5	0.0187	(0.0560)	p,q,r,s,t
[s]Kitale, Kenya (2)	230	0.72	0.083	0.27	0.56	2.81	5.4	34	3.7	6.0	3.0	0.0134	(0.0009)	q,r,s,t
Behenjy, Madagascar	–	–	–	–	–	0.86	20,000	2.1	18	6.7	3.5	47.1	(2.3)	a
[s]Behenjy, Madagascar	–	–	–	–	–	0.87	6,600	44	15	5.4	2.6	15.0	(2.0)	a,b
Luisiana, Philippines	–	–	–	–	–	0.49	2,600	7.7	32	9.9	3.6	0.25	(0.95)	b,c,d
min	30	0.035	0.067	0.31	0.21	0.04	2.3	0.79	1.6	0.81	1.1	0.00466		
max	470	1.9	0.34	11	4.2	2.88	20,000	59	32	15	5.5	47.1		
geometric mean	170	0.40	0.13	3.4	1.4	0.73	56	26	6.4	6.5	2.8	0.137		

[s] K treated soils

The experiment results were reproducible because the variation in ^{137}Cs concentration in grass shoots for the triplicate pots was generally limited (CV <50%, except for 8 of 53 soils or soil treatments). The CV of ^{137}Cs in grass shoots was >100% for Dakawa (Tanzania), where the ^{137}Cs concentration of one pot was over 10-fold higher than the other replicate pots. Contamination of grass shoots with ^{137}Cs from splashed soil particles during the pot experiment was checked for all pots by measuring concentrations of soil element Ti in the grass shoots, but no trends with grass shoot ^{137}Cs concentrations were found (data not shown).

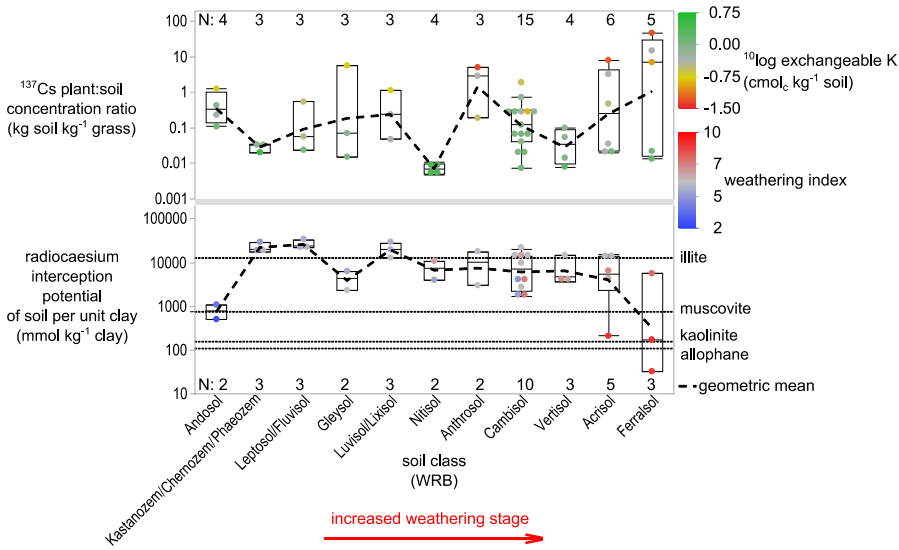

Figure IV.4. Top: grass-soil ^{137}Cs concentrations ratios (log scale) in relation to WRB soil classification. Data from soil studies with and without K fertilizer treatment are combined. Points on the graph are arithmetic mean CR values (n = 3) and are colored depending on exchangeable K content in soils (note log scale). Bottom: RIP of soil per unit clay (highest clay content) as soil weathering increases and are colored depending on a calculated weathering index based on mineralogy with youngest (Andosols) equal to 2.5 (blue) and oldest (Ferralsols) equal to 9.3 (red). The number of soils per group (N) are given. The dotted lines are RIP of allophane (111 mmol kg^{-1}), illite (10,000–16,000 mmol kg^{-1}; de Koning et al., 2007; Wauters et al., 1996c), muscovite (740 mmol kg^{-1}; De Preter, 1990) and kaolinite (6–310 mmol kg^{-1}; Nakao et al., 2008; Ogasawara et al., 2013). The dashed line connects the geometric means of the CR and RIP values of soil groups.

Table IV.8. Pearson correlation coefficients estimated by row-wise method between ^{137}Cs K_D, CF, CR, and measured variables (N = 53) after log-transformation, except for pH. Significant correlations are *** p <0.001; ** p <0.01; * p <0.05; and not significant (n.s.) if p >0.05.

	K_D	CF	CR
soil			
pH	0.63***	n.s.	-0.57***
%clay^{t}	0.61***	n.s.	-0.50***
%clay^{u}	0.37**	n.s.	n.s.
%SOC	n.s.	-0.39**	n.s.
CEC	0.75***	n.s.	-0.66***
RIP	0.79***	n.s.	-0.83***
soil solution			
^{137}Cs	–	–	0.72***
K	-0.29*	-0.83***	-0.33*
NH_4	-0.80***	n.s.	0.76***
exchangeable			
^{137}Cs	n.s.	n.s.	n.s.
K	0.51***	-0.54***	-0.82***
NH_4^{v}	-0.68***	n.s.	0.75***
grass			
yield	n.s.	n.s.	n.s.
^{137}Cs	-0.72***	–	–
K	n.s.	-0.52***	-0.56***

^{t} clay content by laser diffraction; ^{u} clay content data of highest clay yield; ^{v} N = 29

Table IV.9. Pearson correlation coefficients estimated by row-wise method between measured variables (N = 53) after log-transformation, except for pH. Significant correlations are *** p <0.001; ** p <0.01; * p <0.05; and not significant (n.s.) if p >0.05.

	soil						*soil solution*			*exchangeable*			*grass*	
	pH	%clay[w]	%clay[x]	%SOC	CEC	RIP	^{137}Cs	K	NH_4	^{137}Cs	K	NH_4[y]	yield	^{137}Cs
soil														
pH	–													
%clay[w]	n.s.	–												
%clay[x]	n.s.	0.78***	–											
%SOC	n.s.	n.s.	n.s.	–										
CEC	0.62***	0.56***	n.s.	n.s.	–									
RIP	0.63***	0.39**	n.s.	n.s.	0.70***	–								
soil solution														
^{137}Cs	-0.66***	-0.57***	-0.34*	n.s.	-0.75***	-0.81***	–							
K	n.s.	n.s.	n.s.	0.30*	n.s.	n.s.	0.29*	–						
NH_4	-0.54***	-0.57***	-0.38**	n.s.	-0.65***	-0.60***	0.78***	n.s.	–					
exchangeable														
^{137}Cs	n.s.	n.s.	0.40**	n.s.	n.s.	-0.32*	0.30*	n.s.	n.s.	–				
K	0.40**	0.54***	0.34*	0.35**	0.54***	0.61***	-0.48***	0.50***	-0.59***	n.s.	–			
NH_4[y]	-0.73***	-0.39*	n.s.	n.s.	-0.50**	-0.53**	0.69***	n.s.	0.86***	n.s.	-0.58**	–		
grass														
yield	n.s.	0.40**	0.32*	n.s.	n.s.	n.s.	n.s.	n.s.	n.s.	n.s.	n.s.	n.s.	–	
^{137}Cs	-0.59***	-0.46***	n.s.	n.s.	-0.66***	-0.84***	0.73***	-0.34*	0.75***	n.s.	-0.80***	0.75***	n.s.	–
K	0.40**	n.s.	n.s.	n.s.	0.28*	0.52***	n.s.	0.57***	n.s.	-0.29*	0.52***	-0.45*	-0.30*	-0.58***

[w] clay content by laser diffraction; [x] clay content data of highest clay yield; [y] N = 29

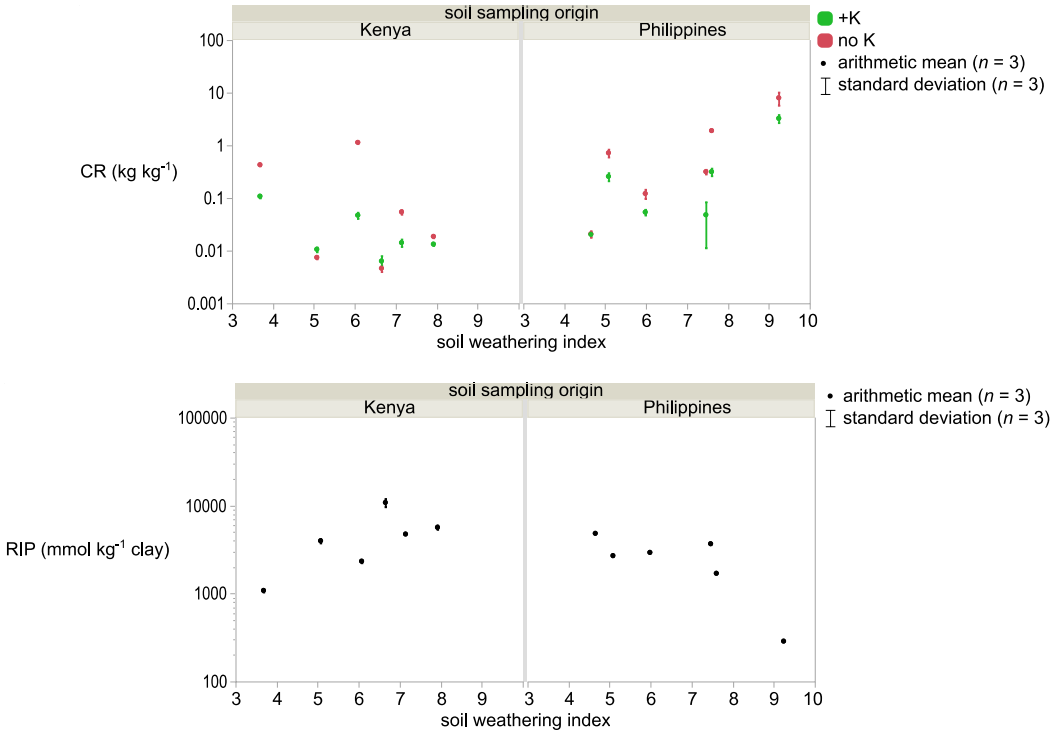

Figure IV.5. Top: grass-soil ^{137}Cs concentrations ratios (log scale) in relation to calculated weathering index based on mineralogy showing a decrease in ^{137}Cs bioavailability in the Kenyan sequence and an increase in the Philippine sequence with increasing weathering. Points on the graph are colored depending on the treatment with and without K fertilizer. Bottom: RIP of soil per unit clay (highest clay content) in relation to weathering index showing an increase in ^{137}Cs adsorption in the Kenyan sequence and a decrease in the Philippine sequence with increasing weathering.

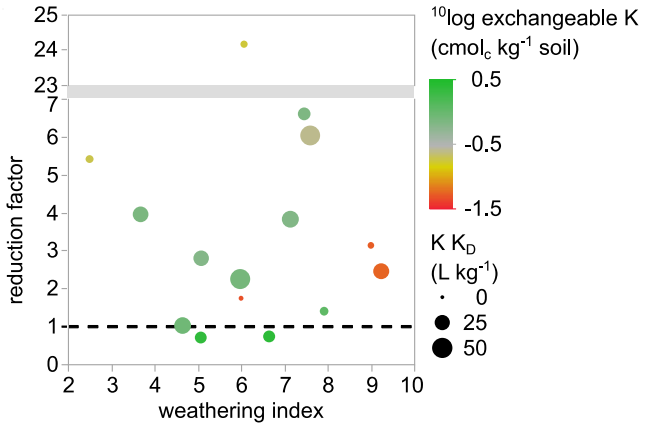

Figure IV.6. Effects of fertilizer K addition on the grass-soil ^{137}Cs concentration ratio in soils from three reference soil groups (*N* = 3) and soil sequences (*N* = 12). Points on the graph are reduction factors: the ratio of CR of non-K-treated soil and CR of K-treated soil. Point size is the K K_D, calculated as the ratio of exchangeable K content and K in soil solution in non-K-treated soil and color is the log-transformed exchangeable K content in non-K-treated soil.

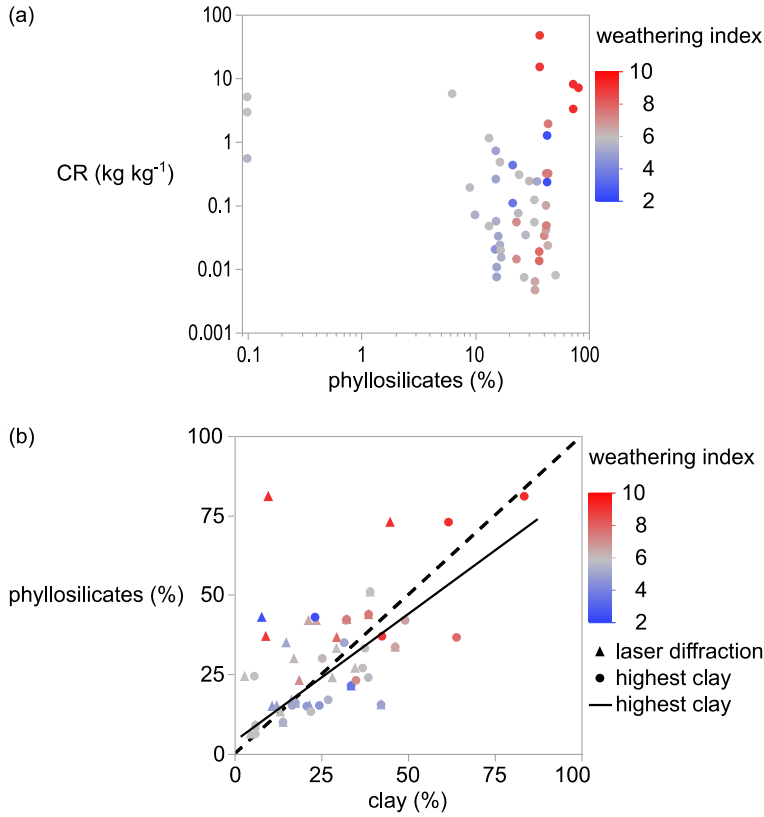

Figure IV.7. (a) Content of 1:1, 2:1 and 2:1:1 phyllosilicates quantified by XRD and unrelated to the grass-soil ^{137}Cs concentration ratio (CR) (p >0.05, N = 53). (b) Comparison of clay contents determined by laser diffraction (n.s., N = 29) and highest clay content determined by various methods (R^2 = 0.62***, RMSE = 11, N = 29) as an estimate for phyllosilicates content. Points on the graph are mean values (n = 3) and are colored depending on a calculated weathering index, with the youngest (Andosols) equal to 2.5 (blue) and the oldest (Ferralsols) equal to 9.3 (red). The full line is the regression line and the broken line is the 1:1 line.

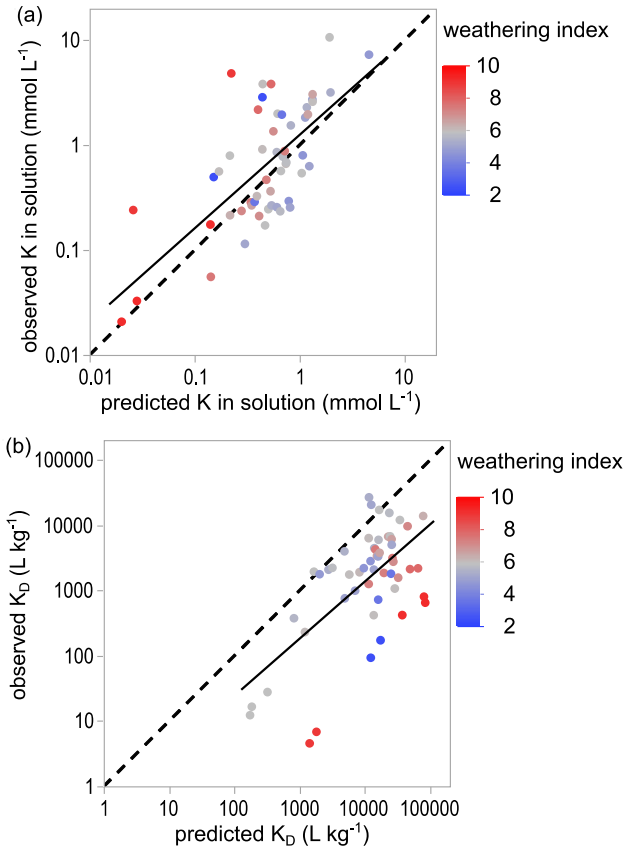

Figure IV.8. (a) Predictions of K in solution with the Tarsitano 2011 model compared with observed values (R^2 = 0.47***, RMSE = 0.42, *N* = 53). (b) Predictions of ^{137}Cs K_D with the Tarsitano 2011 model compared with observed values (R^2 = 0.41***, RMSE = 0.67, *N* = 53). Points on the graph are mean values (*n* = 3) and are colored depending on a calculated weathering index based on mineralogy, with the youngest (Andosols) equal to 2.5 (blue) and the oldest (Ferralsols) equal to 9.3 (red). The full line is the regression line and the broken line is the 1:1 line.

Appendix V
The clay mineralogy rather than the clay content determines radiocaesium adsorption in soils

The method to isolate 0–2 µm and 2–50 µm fractions using Na^+-resin (Rouiller et al., 1972) was validated by comparing it to a standardized pipet method for particle size analysis (ISO, 1998) with reference soils. The internal reference soil from the Division of Soil and Water Management (KU Leuven, Belgium) was sampled in Leuven, Belgium (50°52'42"N 4°39'24"E), was used as arable land (rotation wheat and peas) and was classified as Haplic Luvisol (IUSS Working Group WRB FAO, 2022). The soil was air-dried and milled to pass a 2 mm sieve. The interlaboratory reference soils from Wageningen Evaluating Programmes for Analytical Laboratories (WEPAL) of the International Soil-analytical Exchange program included clayey soil from Ivory Coast (reference 883), sandy soil from Droevendaal, Netherlands (reference 997), and organic Ferralsol from Sumatra Barat, Indonesia (reference 998). The soils were oven-dried (40 °C), milled to pass a 0.5 mm sieve, and sampled using an automatic sample divider. Each reference sample had mean values and statistics of soil characteristics (2010 and 2012 reports).

Particle distribution analyzed by resin method included mechanical disaggregation of soil particles by sonication, dispersion by a Na^+-resin, and isolation of the 0–2 µm fraction by siphoning. In contrast, the ISO 11277 method included chemical disaggregation of soil particles by removing organic matter and salts (optional removal of iron oxides and carbonates), dispersion by a hexametaphosphate, and sampling the 0–2 µm fraction by pipet. In short, following the ISO 11277 method, 10–20 g of air-dry soil was milled to pass a 2 mm sieve. The soils were suspended in deionized water (250 mL) and treated with hydrogen peroxide (15%) to remove organic matter, followed by removing soluble salts with deionized water. Between each step, suspended soils were centrifuged (15 min, 2000 *g*), and clear supernatant was removed by decanting. The dispersing agent was made by dissolving 33 g of sodium hexametaphosphate (HMP) and 7 g of anhydrous sodium carbonate in 1 L of water. The sand fractions were separated by wet sieving (63 µm sieve). The remaining fractions were put in cylinders (500 mL) in a water bath (30°C), in which they equilibrated overnight (16 h). The contents of the cylinders were agitated using a plunger at a speed of 30 times per minute for 2 min.

According to Stoke's law, after 6 h 9 min 45 sec, a sample (20 mL) was taken with a pipet 10 cm below the surface. All subsamples were oven-dried (105 °C, minimum two days), cooled to room temperature in a desiccator, and weighed analytically (accuracy 0.0001 g, OHAUS Adventurer™ AR2140). Corrections were made for moisture (105 °C) and the weight of HMP salt to calculate the weight of each fraction. Most results fell within an acceptable range of variation (Table V.1), indicating that the resin method was reliable for particle size distributions. A representative 0–2 µm fraction was successfully isolated in this study using this method.

Table V.1. Validation of the particle size analysis method following ISO 11277 and procedure with a Na^+-resin (used in this study to isolate the 0–2 µm and 2–50 µm fractions) by comparing results of reference soil samples. Number of measurements are given (*N*), mean values, and standard deviations.

	ISO 11277 method				resin method		
location	*N*	<2 µm	*N*	>63 µm	<2 µm	>50 µm	recovery
city, country		g 100 g^{-1}		g 100 g^{-1}	g 100 g^{-1}	g 100 g^{-1}	%
Leuven, Belgium	29	7 ± 2	4	13 ± 3	15	13	100
Ivory Coast	30	9 ± 1	18	77 ± 2	8	78	99
Droevendaal, Netherlands	125	4 ± 1	70	80 ± 5	4	82	99
Sumatra Barat, Indonesia	35	83 ± 8	19	5 ± 1	82	8	94

Table V.2. Mineralogy of the bulk soils previously determined (Chapter 4). Soils are ordered by increasing WI and grouped as young (WI = 2.5–4.7), intermediate (WI = 4.7–7.0), or weathered (WI = 7.0–9.2). qtz = quartz; mica = mica minerals; Al-2:1 = aluminium 2:1 phyllosilicates; Fe-2:1 = iron 2:1 phyllosilicates; Fe-2:1:1 = iron chlorite phyllosilicates; Mg-2:1:1 = magnesium chlorite phyllosilicates; 1:1 = kaolin phyllosilicates; fsp = K-feldspars and plagioclase; cal/dol = calcite and dolomite; po = pyrrhotite; Ant = anatase; FeOx = iron (oxy-)hydroxides; AlOx = aluminium (oxy-)hydroxides; amp/px = amphibole and pyroxene; a = mineral phases that appear amorphous on XRD patterns. The limit of detection is 1 g 100 g^{-1}.

	mineralogy bulk soil															weathering index
location	qtz	mica	Al-2:1	Fe-2:1	Fe-2:1:1	Mg-2:1:1	1:1	fsp	cal/dol	po	ant	Fe Ox	Al Ox	amp/px	a	
city, country	g 100 g^{-1}															-
mineral weathering index:	*6*	*7*	*7*	*4*	*4*	*8*	*9*	*5*	*2*	*1*	*12*	*11*	*10*	*3*	*1*	
young																
Miyakonojo, Japan	4	7	<1	<1	<1	<1	<1	22	<1	<1	<1	<1	<1	<1	67	2.5
Mount Elgon, Kenya (1)	3	6	6	<1	<1	7	9	7	<1	<1	<1	3	3	<1	56	3.7
Pagsanjan, Philippines (1)	1	11	<1	<1	<1	<1	15	37	<1	1	<1	<1	<1	4	31	4.6
intermediate																
Sidney, United States	35	1	14	<1	<1	<1	1	24	1	<1	<1	<1	<1	1	23	4.8
Mount Elgon, Kenya (2)	6	12	10	<1	<1	<1	6	8	<1	1	13	2	<1	<1	42	5.1
Pagsanjan, Philippines (2)	3	12	<1	<1	<1	<1	15	45	<1	1	<1	<1	<1	2	22	5.1
Gross Enzersdorf, Austria	38	12	6	<1	5	3	2	11	22	<1	<1	<1	<1	1	<1	5.2
Ogata, Japan	20	<1	33	<1	<1	<1	3	25	<1	<1	<1	<1	<1	<1	19	5.2
Mount Elgon, Kenya (3)	8	7	13	<1	<1	<1	13	5	<1	<1	2	11	1	<1	40	5.4
Rots, France	58	<1	13	<1	4	<1	<1	15	10	<1	<1	<1	<1	<1	<1	5.5
Changchun, China	36	<1	17	<1	<1	6	4	35	2	<1	<1	<1	<1	<1	<1	5.8

location	mineralogy bulk soil															weathering index
	qtz	mica	Al-2:1	Fe-2:1	Fe-2:1:1	Mg-2:1:1	1:1	fsp	cal/dol	po	ant	Fe Ox	Al Ox	amp/px	a	
city, country	g 100 g^{-1}															-
mineral weathering index:	*6*	*7*	*7*	*4*	*4*	*8*	*9*	*5*	*2*	*1*	*12*	*11*	*10*	*3*	*1*	
Pagsanjan, Philippines (3)	4	16	<1	<1	<1	<1	33	21	<1	1	<1	<1	<1	<1	25	6.0
Isla Mayor, Spain	16	7	43	<1	<1	6	2	11	15	<1	<1	<1	<1	<1	<1	6.0
Yoshiki, Japan	26	19	5	<1	<1	9	11	29	<1	<1	<1	<1	<1	1	<1	6.0
Kitale, Kenya (1)	61	3	4	<1	<1	<1	10	14	<1	<1	1	1	<1	<1	6	6.1
Mount Elgon, Kenya (4)	10	6	16	<1	<1	<1	18	8	<1	<1	3	15	2	<1	22	6.6
Aliminusa, Italy	51	<1	25	<1	<1	<1	17	6	<1	<1	1	<1	<1	<1	<1	6.7
weathered																
Endebess, Kenya	35	7	11	<1	<1	<1	13	13	<1	<1	1	13	2	<1	5	7.1
Pagsanjan, Philippines (4)	8	30	<1	<1	<1	<1	42	8	<1	1	<1	2	<1	<1	9	7.5
Pagsanjan, Philippines (5)	6	30	<1	<1	<1	<1	44	4	<1	2	<1	4	<1	<1	10	7.6
Kitale, Kenya (2)	28	7	13	<1	<1	<1	24	5	<1	<1	2	15	2	<1	4	7.9
Kitale, Kenya (3)	35	2	12	<1	<1	<1	23	8	<1	<1	<1	18	2	<1	<1	7.9
Behenjy, Madagascar	25	<1	<1	<1	<1	2	35	<1	<1	<1	5	27	6	<1	<1	9.0
Cavinti, Philippines	3	12	5	<1	<1	<1	68	<1	<1	1	<1	11	<1	<1	<1	9.2

Table V.3. Properties of the bulk soil previously determined (Chapter 4). Soils are ordered by increasing WI and grouped as young (WI = 2.5–4.7), intermediate (WI = 4.7–7.0), or weathered (WI = 7.0–9.2). More details on soil origin can be found elsewhere (Chapter 4).

		particle size distribution						RIP	
location	WRB[a] soil class	<2 µm	2–50 µm	50–2000 µm	organic C	pH	CEC	bulk soil	weathering index
city, country		g 100 g^{-1}					$cmol_c$ kg^{-1} soil	mmol kg^{-1} soil	
young									
Miyakonojo, Japan	Andosol	20	42	38	5.6	4.8	5.1	120	2.5
Mount Elgon, Kenya (1)	Andosol	29	62	9	14	4.1	6.2	360	3.7
Pagsanjan, Philippines (1)	Cambisol	31	39	30	1.8	5.9	24	1,000	4.6
intermediate									
Sidney, United States	Kastanozem	27	45	28	1.4	6.4	20	6,100	4.8
Mount Elgon, Kenya (2)	Nitisol	54	39	7	8.4	5.4	45	1,700	5.1
Pagsanjan, Philippines (2)	Cambisol	18	38	44	2.3	5.3	22	330	5.1
Gross Enzersdorf, Austria	Chernozem	26	42	32	1.0	7.4	13	3,600	5.2
Ogata, Japan	Gleysol	44	31	25	1.8	5.1	32	2,000	5.2
Mount Elgon, Kenya (3)	Nitisol	65	28	7	7.9	6.3	41	1,900	5.4
Rots, France	Luvisol	27	54	19	1.3	7.4	20	5,300	5.5
Changchun, China	Phaeozem	36	38	26	1.4	7.1	33	4,300	5.8
Pagsanjan, Philippines (3)	Cambisol	48	31	21	1.8	5.6	34	860	6.0
Isla Mayor, Spain	Vertisol	59	38	3	1.7	7.8	26	5,800	6.0
Yoshiki, Japan	Cambisol	8	19	73	0.83	5.2	9.8	1,100	6.0
Kitale, Kenya (1)	Gleysol	18	27	55	1.3	4.1	5.4	510	6.1
Mount Elgon, Kenya (4)	Nitisol	58	35	7	5.3	5.2	50	5,000	6.6

location	WRB[a] soil class	particle size distribution			organic C	pH	CEC	RIP	weathering index
		<2 µm	2–50 µm	50–2000 µm				bulk soil	
city, country		g 100 g^{-1}					$cmol_c$ kg^{-1} soil	mmol kg^{-1} soil	
Aliminusa, Italy	Cambisol	56	19	25	0.81	5.8	26	5,900	6.7
weathered									
Endebess, Kenya	Vertisol	38	21	41	2.0	4.5	19	1,700	7.1
Pagsanjan, Philippines (4)	Cambisol	36	34	30	1.8	4.3	23	1,200	7.5
Pagsanjan, Philippines (5)	Cambisol	48	28	24	1.8	4.8	28	660	7.6
Kitale, Kenya (2)	Ferralsol	56	21	23	1.8	3.8	8.3	3,600	7.9
Kitale, Kenya (3)	Ferralsol	44	19	37	1.8	4.8	8.1	2,200	7.9
Behenjy, Madagascar	Ferralsol	68	12	20	2.9	4.2	2.3	14	9.0
Cavinti, Philippines	Acrisol	25	7	68	0.56	3.8	9.9	130	9.2

[a] (IUSS Working Group WRB FAO, 2022)

The identification of phyllosilicate mineral phases in X-ray diffraction (XRD) patterns of isolated 0–2 µm and 2–50 µm fractions from soils was performed following the procedure of Moore and Reynolds (1997). The patterns were shifted to position the quartz peak around 3.34 Å. A mineral phase was identified based on the peak position, corresponding to the largest peak in the XRD pattern. The smaller peaks were located to confirm its presence, and these peaks were subsequently discarded from consideration. This iterative process was continued by examining the remaining peaks to identify additional mineral phases, repeating the steps until all observable peaks were attributed to specific minerals. Mineral phases not included in the Sybilla software library were identified using tables in Brindley and Brown (1980). However, some difficulties were encountered due to high background noise and overlapping peaks of different mineral phases. These interferences made it challenging to identify specific minerals, leaving some peaks unassigned, such as in Figure V.3.

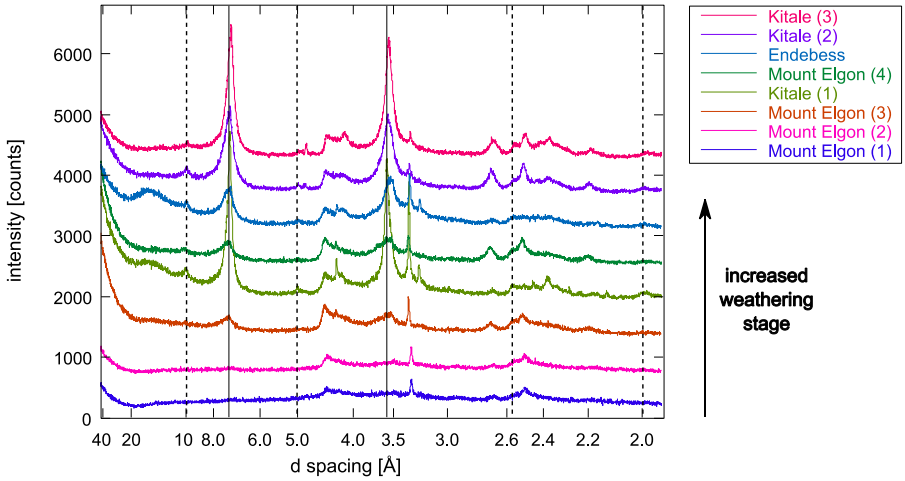

Figure V.1. Comparison of the oriented clay fractions in air-dried, Ca-saturated soils from Kenya. Full lines indicate peak positions of kaolinite at 7.17 Å and 3.58 Å, and dotted lines indicate peak positions of illitic mineral phases at 10 Å, 5.0 Å, 3.36 Å, 2.56 Å, and 2.00 Å.

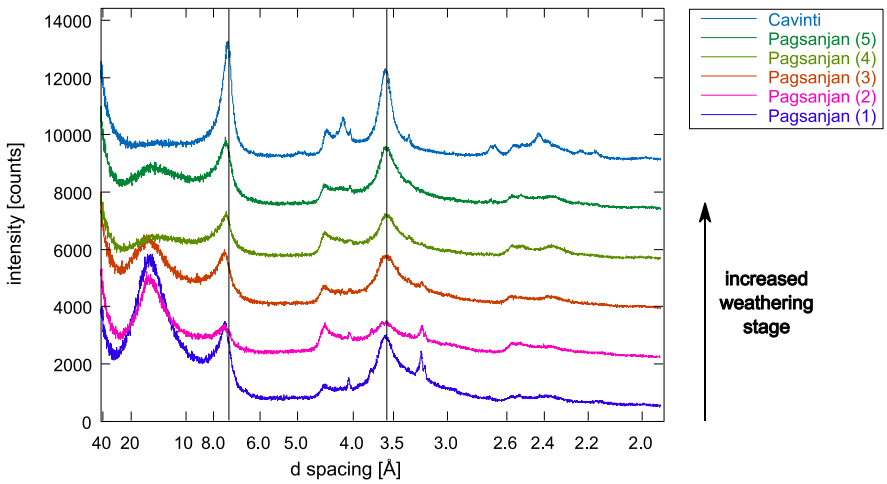

Figure V.2. Comparison of the oriented clay fractions in air-dried, Ca-saturated soils from the Philippines. The XRD patterns shown here were measured with variable slit but converted to fixed slit. Full lines indicate peak positions of kaolinite at 7.17 Å and 3.58 Å.

The quantification of phyllosilicate mineral phases in XRD patterns of isolated 0–2 µm fractions from soils was performed following the procedure of Zeelmaekers (2011). Mineral phases were quantified using Sybilla software (© Chevron ETC) by fitting the model of operator-selected mineral models to the experimental XRD pattern in both air-dried Ca-form and ethylene glycol solvated states. The background was removed using a linear function. The patterns were shifted to position the kaolinite peak around 7.15 Å, which was clear and unaffected by ethylene glycol. To facilitate model calculations, the step size was increased from 0.02 °2θ to 0.05 °2θ, which was acceptable given the wide peaks of the phyllosilicates. Parts of the experimental XRD pattern that could not be modeled, such as quartz peaks or background at low angles (2–5 °2θ), were excluded from the fitting process. In the software library, kaolinite and chlorite were available as discrete mineral phases, while illite and smectite were fitted as mixed-layered mineral phases. Mixed-layered mineral phases with expandable layers, such as illite-smectite (high-charge), were fitted with two types of smectic layers: regular and high-charge. The high-charge layers with smaller d-spacings compared to regular smectite were used to model vermiculite-like swelling behavior. The proportions of the layers varied between 0 and 100%. For example, in Figure V.5, randomly mixed-layered kaolinite-smectite (high charge) with proportions 50:30:20 had a 50% kaolinite layer, 30% regular smectite, and 20% high-charge smectite. In this study, regular and high-charge smectite contents were summed together as expandable mineral phase. The quantified mineral phase results were accepted if the model fit for the ethylene glycol state agreed with the model for the air-dry state. The mineral phase contents were calculated as averages of the results of the two states.

Calcite was observed in many soils (Figure V.6, Figure V.9, Figure V.10, Figure V.12, Figure V.13, Figure V.15, Figure V.19, and Figure V.25) except the sequence soils. In the bulk soils, calcite was observed by XRD analysis (Table V.2), which varied between <1–22 g 100 g^{-1}. In addition, inorganic carbon was previously measured in these soils, which varied between <0.10–3.0% inorganic carbon (Chapter 4). However, this was not expected for the more weathered soil of Behenjy (Figure V.25), in which inorganic carbon was not measured. Moreover, the pH (4.2) was lower than pKa (9.0), so calcite in the soil would probably have dissolved. It is assumed that the calcite in the soil is a precipitation product due to significant pH changes during the experimental procedure. The use of Na^+-resin (>500 µm, Amberlite® IR-120

(H), Supelco®) facilitated the exchange of H^+ ions for Na^+ ions, leading to a substantial increase in pH. When the soil was exposed to 1 mol L^{-1} $CaCl_2$, the increased pH promoted the formation of carbonate ions (CO_3^{2-}) from bicarbonate (HCO_3^-). The pH was 8.3 for Behenjy (Madagascar), measured in 0.2 g of 0–2 µm fraction in 2 mL purified water (Hanna HI 2002-02). This high concentration of Ca^{2+} and CO_3^{2-} ions resulted in the precipitation of $CaCO_3$ as calcite. Thus, the calcite peaks observed in XRD are probably the result of these experimental conditions rather than the presence of calcite in the original soil sample. No calcite was observed in the soil sequences, probably because the soil buffered the pH more. In the soil from Kitale (Kenya 1), the pH of the 0–2 µm fraction was 7.6.

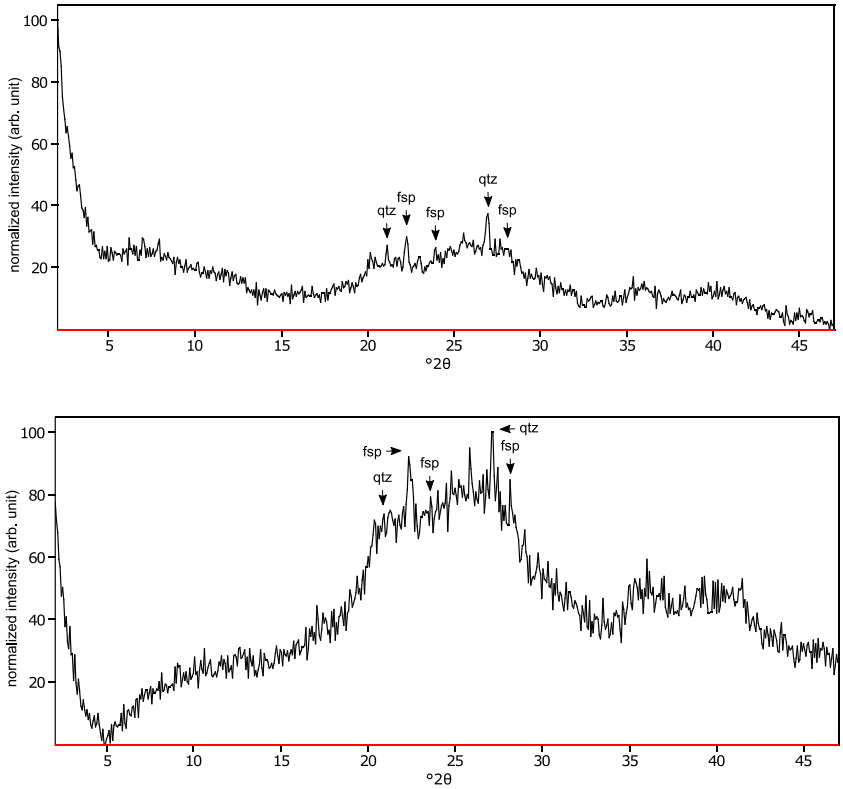

Figure V.3. The oriented clay fraction of soil from Miyakonojo (Japan). Top: experimental XRD patterns in air-dried, Ca-saturated state (black), and no pattern was modeled because no phyllosilicate could be identified; Bottom: experimental XRD patterns in ethylene glycol solvated, Ca-saturated state (black) and no pattern was modeled because no phyllosilicate could be identified. The arrows indicate quartz (qtz) and feldspar (fsp) peaks. Allophane shows broad peaks at 3.50 Å (25.45 °2θ) and 2.50 Å (35.90 °2θ).

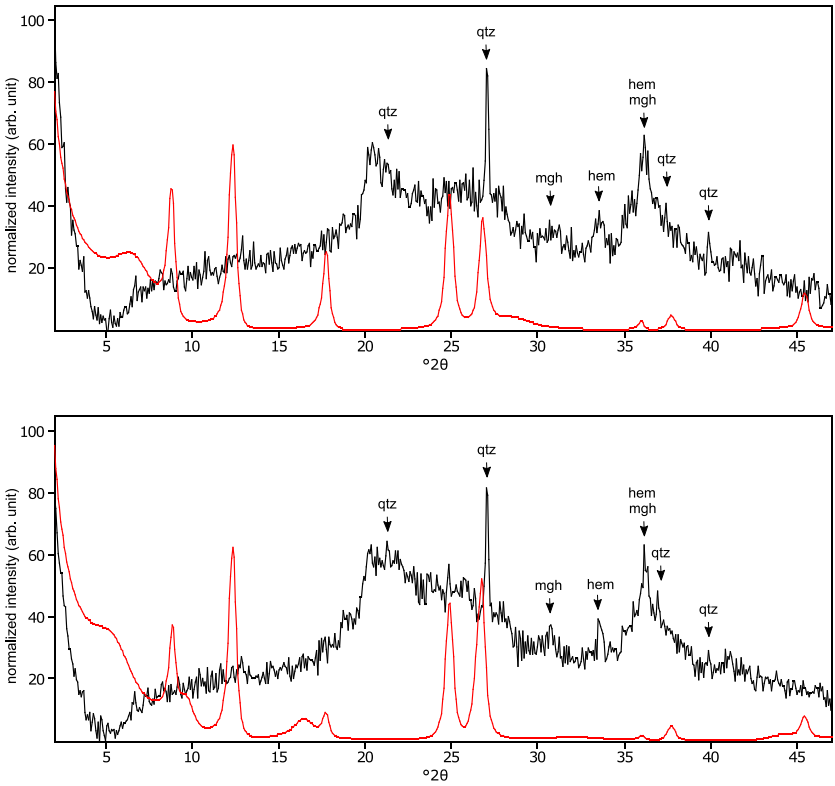

Figure V.4. The oriented clay fraction of soil from Mount Elgon (Kenya 1). Top: experimental XRD patterns in air-dried, Ca-saturated state (black) and the modeled pattern (red) of 30% kaolinite, 45% randomly mixed-layered illite-smectite (97:3), and 25% randomly mixed-layered illite-smectite (60:40); Bottom: experimental XRD patterns in ethylene glycol solvated, Ca-saturated state (black) and the modeled pattern (red) of 27% kaolinite, 24% randomly mixed-layered illite-smectite (97:3), and 49% randomly mixed-layered illite-smectite (60:40). The arrows indicate quartz (qtz), maghemite (mgh), and hematite (hem) peaks. Allophane shows broad peaks at 3.52 Å (25.29 °2θ) and 2.50 Å (35.85 °2θ).

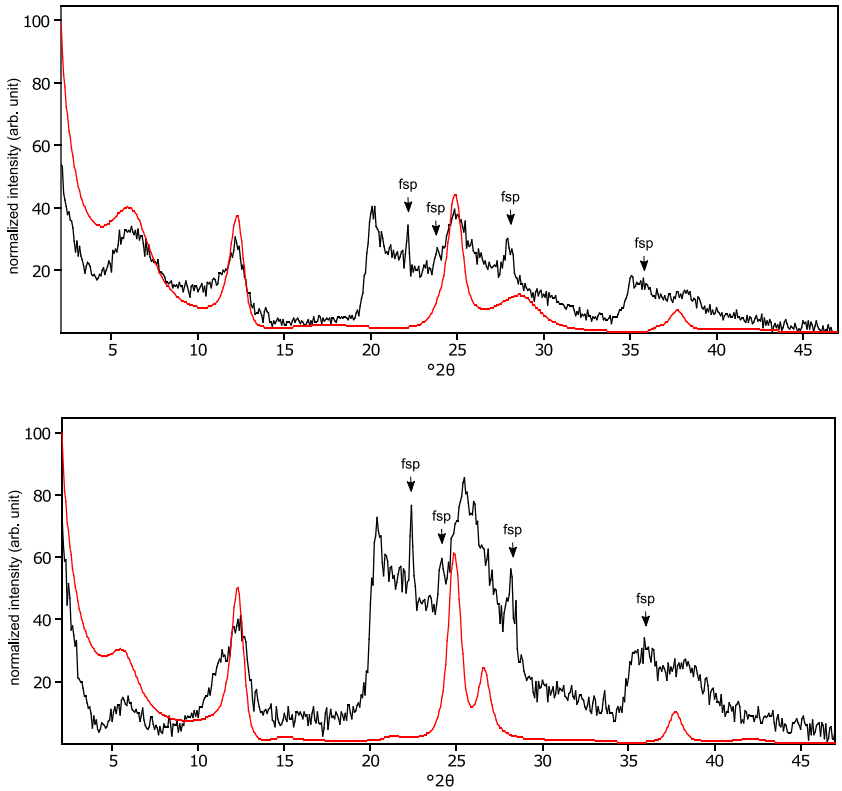

Figure V.5. The oriented clay fraction of soil from Pagsanjan (Philippines 1). Top: experimental XRD patterns in air-dried, Ca-saturated state (black) and the modeled pattern (red) of 30% kaolinite and 70% randomly mixed-layered kaolinite-smectite (high charge) (50:30:20); Bottom: experimental XRD patterns in ethylene glycol solvated, Ca-saturated state (black) and the modeled pattern (red) of 30% kaolinite, and 70% randomly mixed-layered kaolinite-smectite (high charge) (50:30:20). The arrows indicate feldspar (fsp) peaks.

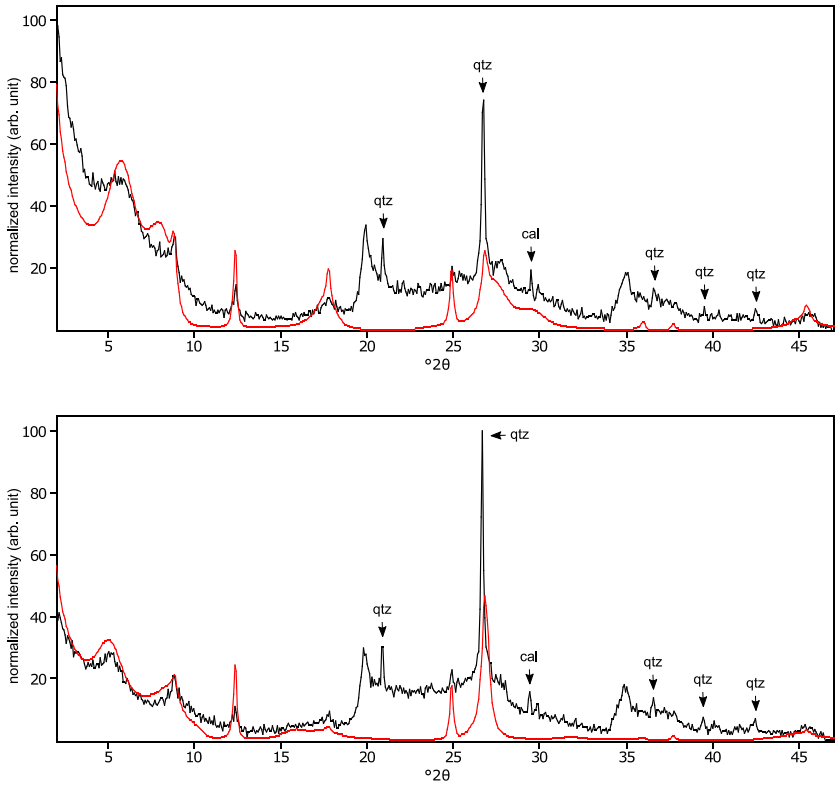

Figure V.6. The oriented clay fraction of soil from Sidney (United States). Top: experimental XRD patterns in air-dried, Ca-saturated state (black) and the modeled pattern (red) of 6% kaolinite, 16% randomly mixed-layered illite-smectite (97:3), 59% randomly mixed-layered illite-smectite (high charge) (72:14:14), and 19% randomly mixed-layered illite-smectite (20:80); Bottom: experimental XRD patterns in ethylene glycol solvated, Ca-saturated state (black) and the modeled pattern (red) of 8% kaolinite, 6% randomly mixed-layered illite-smectite (97:3), 66% randomly mixed-layered illite-smectite (high charge) (72:14:14), and 20% randomly mixed-layered illite-smectite (20:80). The arrows indicate quartz (qtz), and calcite (cal) peaks.

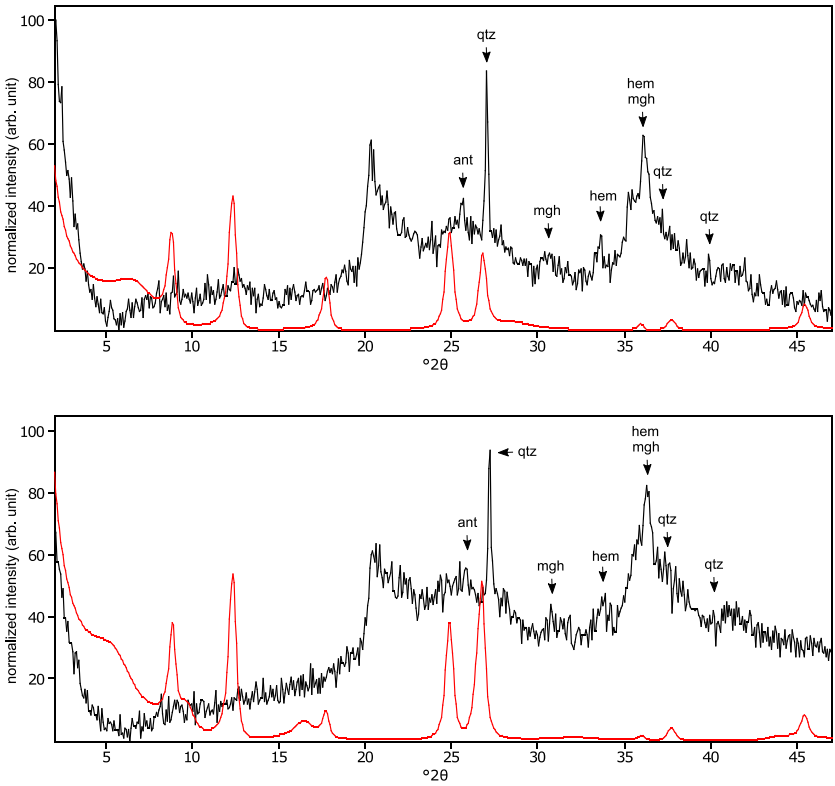

Figure V.7. The oriented clay fraction of soil from Mount Elgon (Kenya 2). Top: experimental XRD patterns in air-dried, Ca-saturated state (black) and the modeled pattern (red) of 31% kaolinite, 45% randomly mixed-layered illite-smectite (97:3), and 24% randomly mixed-layered illite-smectite (60:40); Bottom: experimental XRD patterns in ethylene glycol solvated, Ca-saturated state (black) and the modeled pattern (red) of 26% kaolinite, 28% randomly mixed-layered illite-smectite (97:3), and 46% randomly mixed-layered illite-smectite (60:40). The arrows indicate quartz (qtz), anatase (ant), maghemite (mgh), and hematite (hem) peaks.

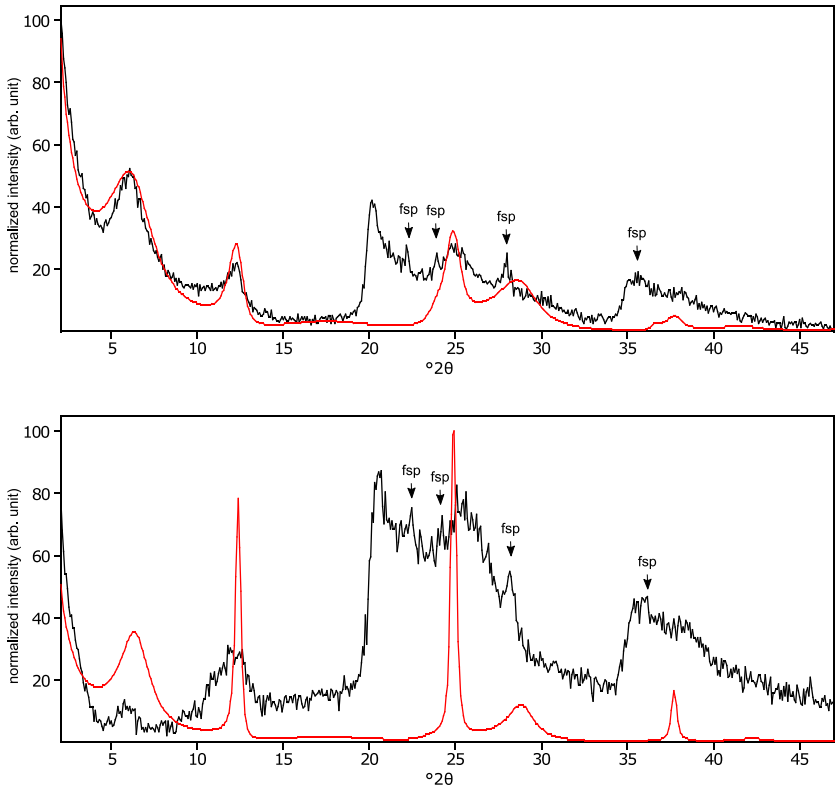

Figure V.8. The oriented clay fraction of soil from Pagsanjan (Philippines 2). Top: experimental XRD patterns in air-dried, Ca-saturated state (black) and the modeled pattern (red) of 16% kaolinite and 84% randomly mixed-layered kaolinite-smectite (high charge) (50:30:20); Bottom: experimental XRD patterns in ethylene glycol solvated, Ca-saturated state (black) and the modeled pattern (red) of 16% kaolinite, and 84% randomly mixed-layered kaolinite-smectite (high charge) (50:30:20). The arrows indicate feldspar (fsp) peaks.

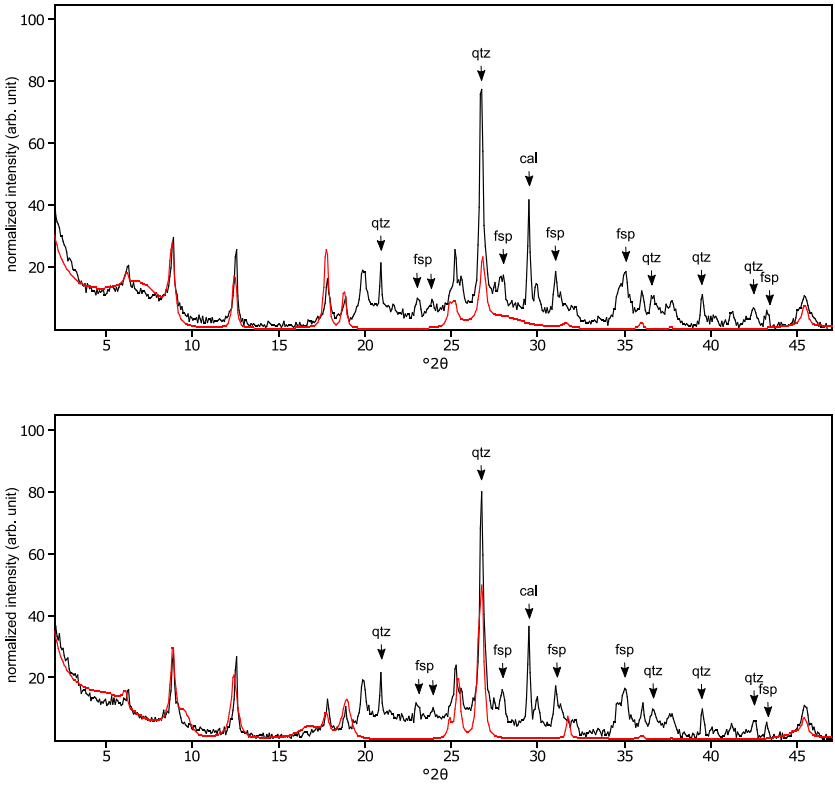

Figure V.9. The oriented clay fraction of soil from Gross Enzersdorf (Austria). Top: experimental XRD patterns in air-dried, Ca-saturated state (black) and the modeled pattern (red) of 3% kaolinite, 38% randomly mixed-layered illite-smectite (97:3), 48% randomly mixed-layered illite-smectite (68:32), and 11% randomly mixed-layered chlorite-smectite (90:10); Bottom: experimental XRD patterns in ethylene glycol solvated, Ca-saturated state (black) and the modeled pattern (red) 3% kaolinite, 27% randomly mixed-layered illite-smectite (97:3), 50% randomly mixed-layered illite-smectite (68:32), and 20% randomly mixed-layered chlorite-smectite (90:10). The arrows indicate quartz (qtz), feldspar (fsp), and calcite (cal) peaks.

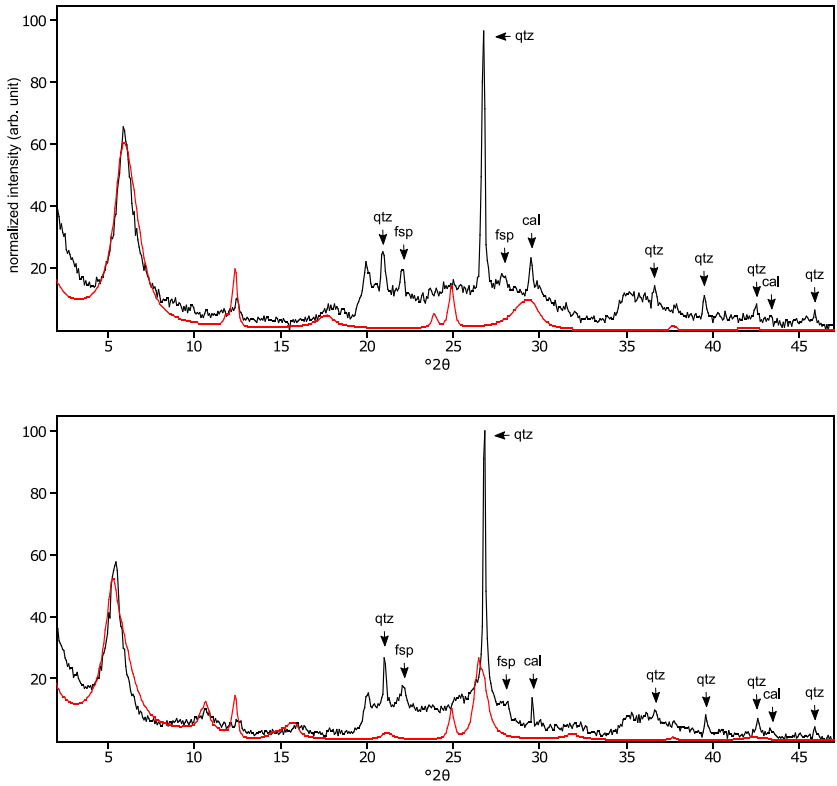

Figure V.10. The oriented clay fraction of soil from Ogata (Japan). Top: experimental XRD patterns in air-dried, Ca-saturated state (black) and the modeled pattern (red) of 15% kaolinite, 46% randomly mixed-layered kaolinite-smectite (high charge) (25:37:38), 39% randomly mixed-layered kaolinite-smectite (regular) (25:75), and 1% randomly mixed-layered illite-smectite (15:85); Bottom: experimental XRD patterns in ethylene glycol solvated, Ca-saturated state (black) and the modeled pattern (red) of 8% kaolinite, 65% randomly mixed-layered kaolinite-smectite (high charge) (25:37:38), 19% randomly mixed-layered kaolinite-smectite (regular) (25:75), and 8% randomly mixed-layered illite-smectite (15:85). The arrows indicate quartz (qtz), feldspar (fsp), and calcite (cal) peaks.

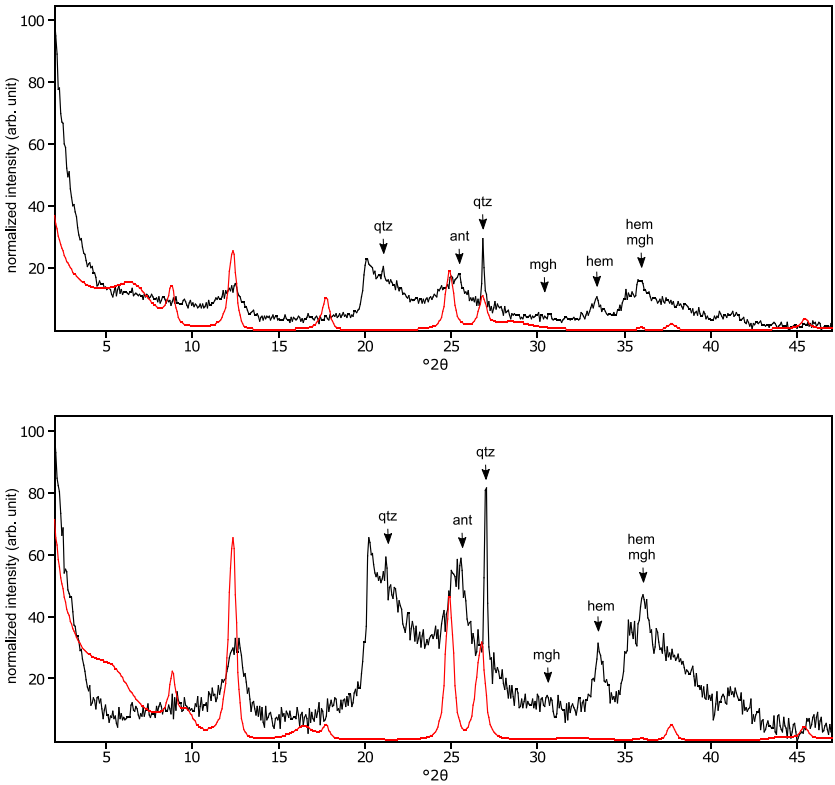

Figure V.11. The oriented clay fraction of soil from Mount Elgon (Kenya 3). Top: experimental XRD patterns in air-dried, Ca-saturated state (black) and the modeled pattern (red) of 29% kaolinite, 29% randomly mixed-layered illite-smectite (97:3), and 42% randomly mixed-layered illite-smectite (60:40); Bottom: experimental XRD patterns in ethylene glycol solvated, Ca-saturated state (black) and the modeled pattern (red) of 39% kaolinite, 17% randomly mixed-layered illite-smectite (97:3), and 44% randomly mixed-layered illite-smectite (60:40). The arrows indicate quartz (qtz), anatase (ant), maghemite (mgh), and hematite (hem) peaks.

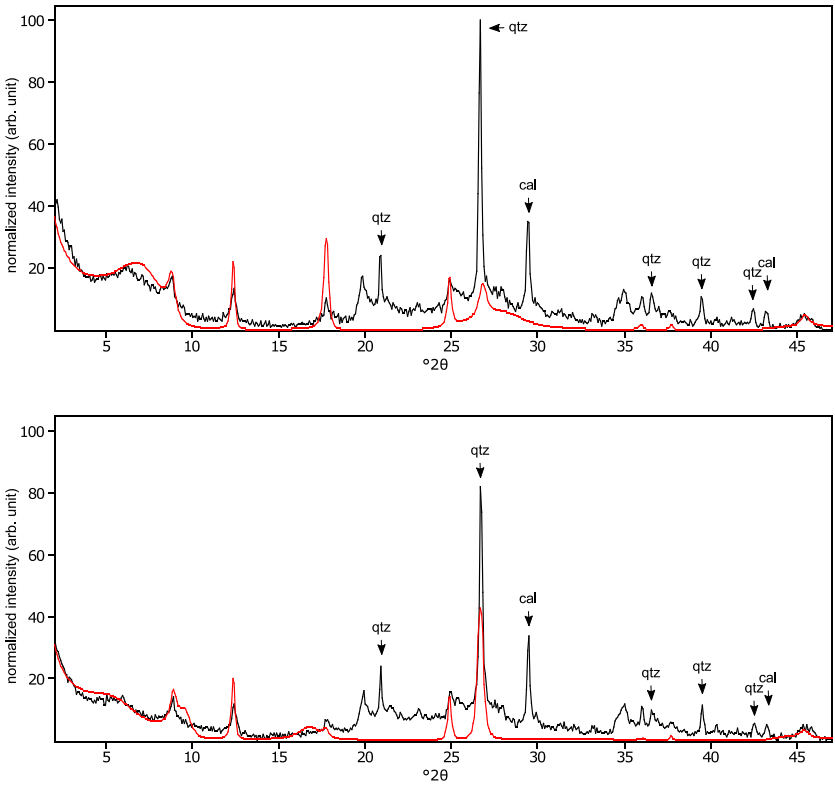

Figure V.12. The oriented clay fraction of soil from Rots (France). Top: experimental XRD patterns in air-dried, Ca-saturated state (black) and the modeled pattern (red) of 9% kaolinite, 26% randomly mixed-layered illite-smectite (95:5), and 65% randomly mixed-layered illite-smectite (68:32); Bottom: experimental XRD patterns in ethylene glycol solvated, Ca-saturated state (black) and the modeled pattern (red) of 9% kaolinite, 19% randomly mixed-layered illite-smectite (95:5), and 72% randomly mixed-layered illite-smectite (68:32). The arrows indicate quartz (qtz), and calcite (cal) peaks.

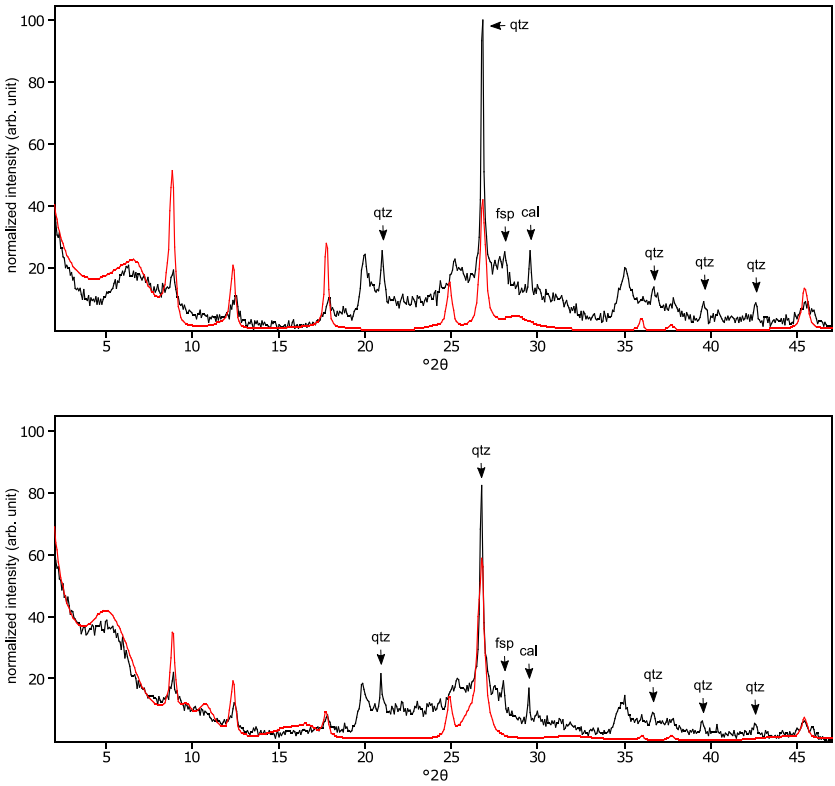

Figure V.13. The oriented clay fraction of soil from Changchun (China). Top: experimental XRD patterns in air-dried, Ca-saturated state (black) and the modeled pattern (red) of 9% kaolinite, 11% randomly mixed-layered kaolinite-smectite (regular) (50:50), 11% randomly mixed-layered illite-smectite (high charge) (33:33:34), 60% randomly mixed-layered illite-smectite (97:3), and 9% randomly mixed-layered illite-smectite (63:37); Bottom: experimental XRD patterns in ethylene glycol solvated, Ca-saturated state (black) and the modeled pattern (red) of 6% kaolinite, 24% randomly mixed-layered kaolinite-smectite (regular) (50:50), 17% randomly mixed-layered illite-smectite (high charge) (33:33:34), 22% randomly mixed-layered illite-smectite (97:3), and 31% randomly mixed-layered illite-smectite (63:37). The arrows indicate quartz (qtz), feldspar peak (fsp), and calcite (cal) peaks.

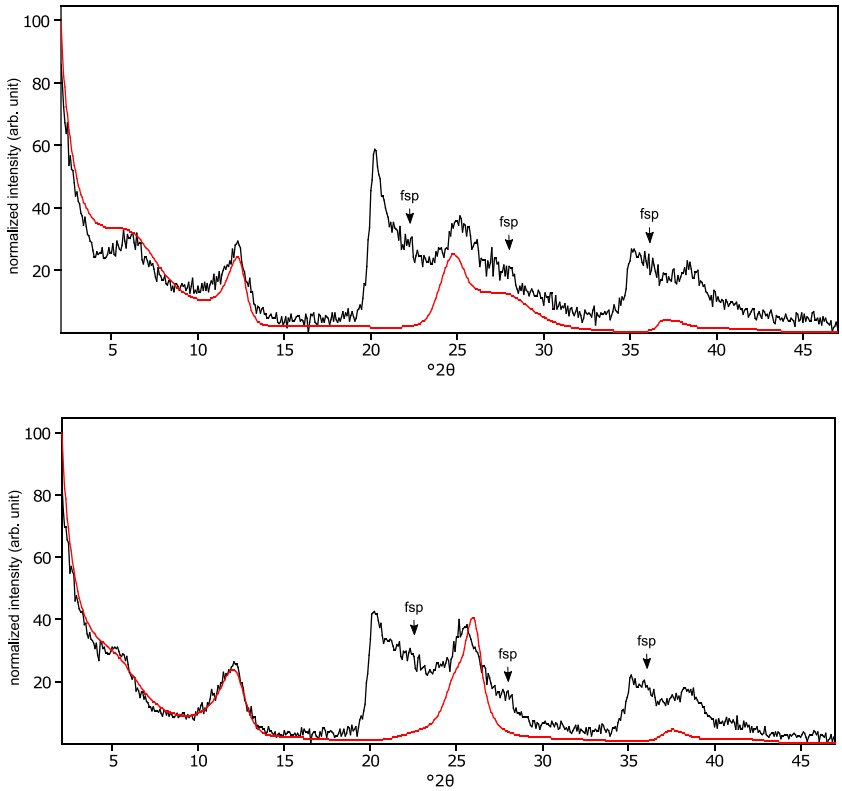

Figure V.14. The oriented clay fraction of soil from Pagsanjan (Philippines 3). Top: experimental XRD patterns in air-dried, Ca-saturated state (black) and the modeled pattern (red) of 10% kaolinite, and 90% randomly mixed-layered kaolinite-smectite (high charge) (66:17:17); Bottom: experimental XRD patterns in ethylene glycol solvated, Ca-saturated state (black) and the modeled pattern (red) of 10% kaolinite, and 90% randomly mixed-layered kaolinite-smectite (high charge) (66:17:17). The arrows indicate feldspar (fsp) peaks.

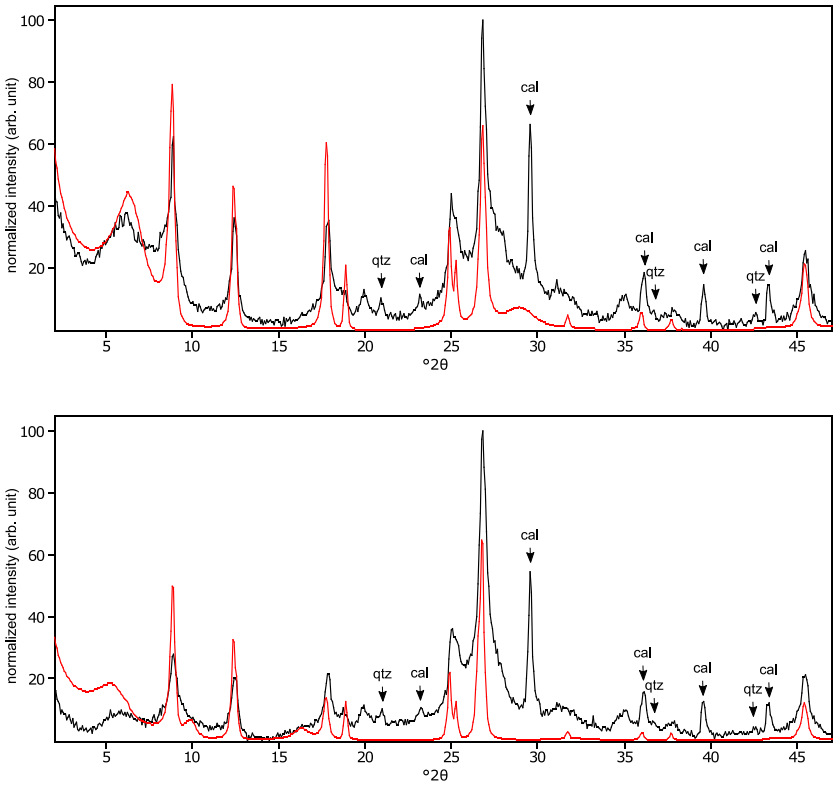

Figure V.15. The oriented clay fraction of soil from Isla Mayor (Spain). Top: experimental XRD patterns in air-dried, Ca-saturated state (black) and the modeled pattern (red) of 9% kaolinite, 54% randomly mixed-layered illite-smectite (97:3), 31% randomly mixed-layered illite-smectite (50:50), and 6% chlorite; Bottom: experimental XRD patterns in ethylene glycol solvated, Ca-saturated state (black) and the modeled pattern (red) of 10% kaolinite, 51% randomly mixed-layered illite-smectite (97:3), 33% randomly mixed-layered illite-smectite (50:50), and 6% chlorite. The arrows indicate quartz (qtz) and calcite (cal) peaks.

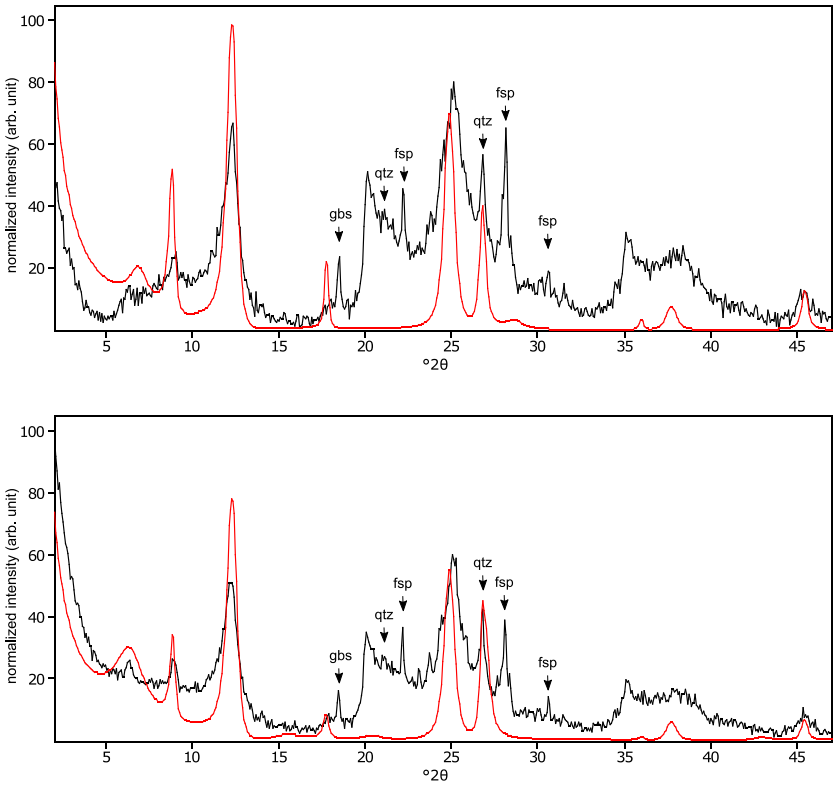

Figure V.16. The oriented clay fraction of soil from Yoshiki (Japan). Top: experimental XRD patterns in air-dried, Ca-saturated state (black) and the modeled pattern (red) of 56% kaolinite, 6% randomly mixed-layered illite-smectite (high charge) (29:28:43), and 38% randomly mixed-layered illite-smectite (97:3); Bottom: experimental XRD patterns in ethylene glycol solvated, Ca-saturated state (black) and the modeled pattern (red) of 48% kaolinite, 31% randomly mixed-layered illite-smectite (high charge) (29:28:43), and 21% randomly mixed-layered illite-smectite (97:3). The arrows indicate quartz (qtz), feldspar (fsp), and peak (gbs) peaks.

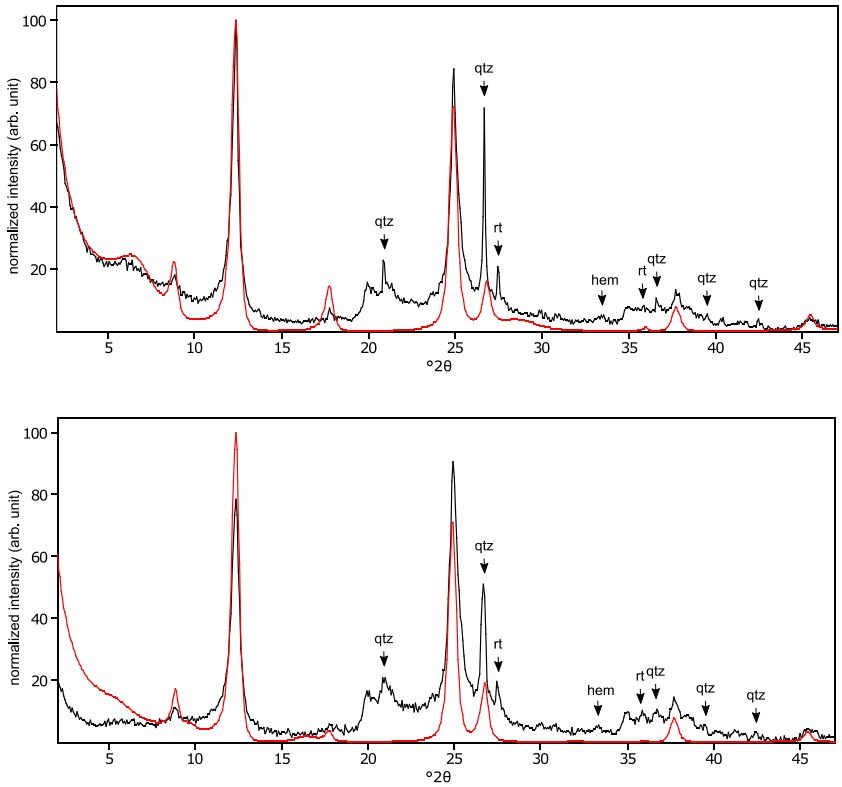

Figure V.17. The oriented clay fraction of soil from Kitale (Kenya 1). Top: experimental XRD patterns in air-dried, Ca-saturated state (black) and the modeled pattern (red) of 53% kaolinite, 19% randomly mixed-layered illite-smectite (97:3), and 28% randomly mixed-layered illite-smectite (60:40); Bottom: experimental XRD patterns in ethylene glycol solvated, Ca-saturated state (black) and the modeled pattern (red) of 65% kaolinite, 16% randomly mixed-layered illite-smectite (97:3), and 19% randomly mixed-layered illite-smectite (60:40). The arrows indicate quartz (qtz), rutile (rt), and hematite (hem) peaks.

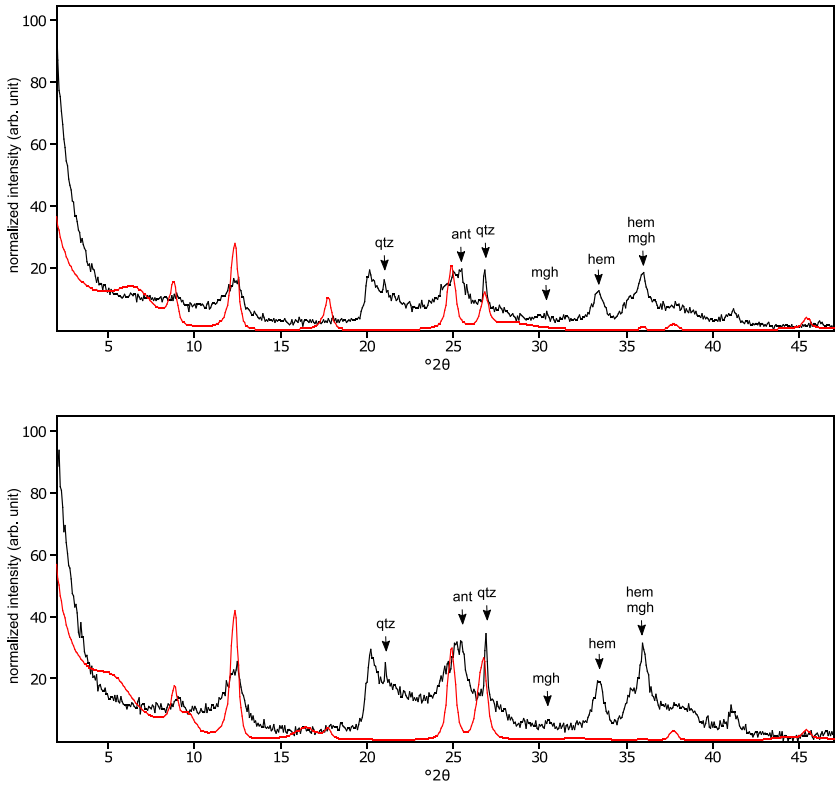

Figure V.18. The oriented clay fraction of soil from Mount Elgon (Kenya 4). Top: experimental XRD patterns in air-dried, Ca-saturated state (black) and the modeled pattern (red) of 31% kaolinite, 32% randomly mixed-layered illite-smectite (97:3), and 37% randomly mixed-layered illite-smectite (60:40); Bottom: experimental XRD patterns in ethylene glycol solvated, Ca-saturated state (black) and the modeled pattern (red) of 32% kaolinite, 17% randomly mixed-layered illite-smectite (97:3), and 51% randomly mixed-layered illite-smectite (60:40). The arrows indicate quartz (qtz), anatase (ant), maghemite (mgh), and hematite (hem) peaks.

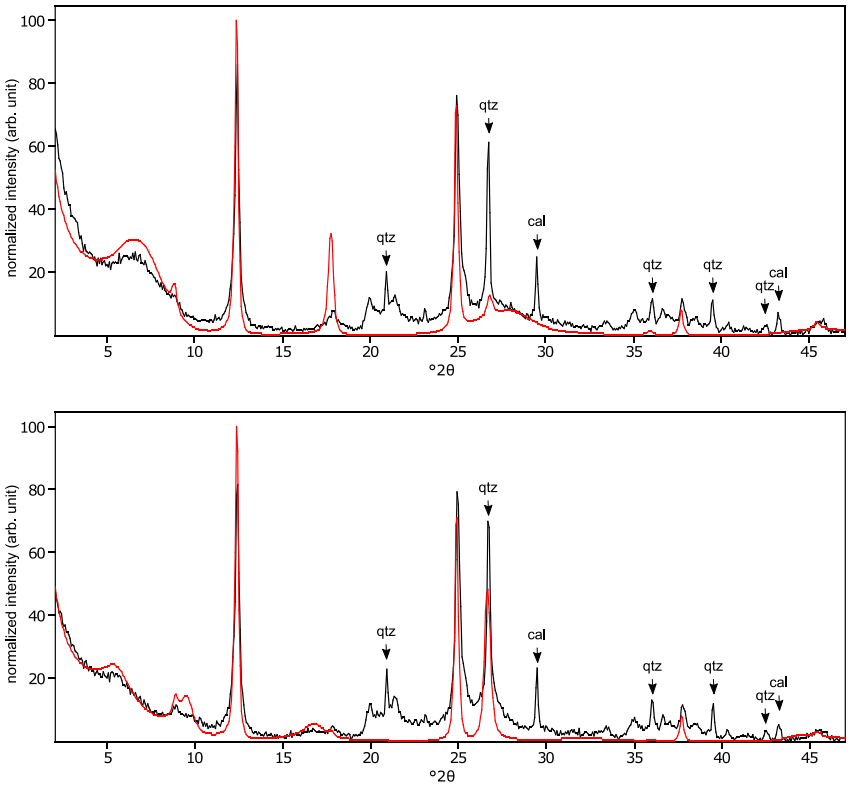

Figure V.19. The oriented clay fraction of soil from Aliminusa (Italy). Top: experimental XRD patterns in air-dried, Ca-saturated state (black) and the modeled pattern (red) of 28% kaolinite, 8% randomly mixed-layered illite-smectite (97:3), 61% randomly mixed-layered illite-smectite (68:32), and 3% smectite; Bottom: experimental XRD patterns in ethylene glycol solvated, Ca-saturated state (black) and the modeled pattern (red) of 28% kaolinite, 5% randomly mixed-layered illite-smectite (97:3), 55% randomly mixed-layered illite-smectite (68:32), and 12% smectite. The arrows indicate quartz (qtz) and calcite (cal) peaks.

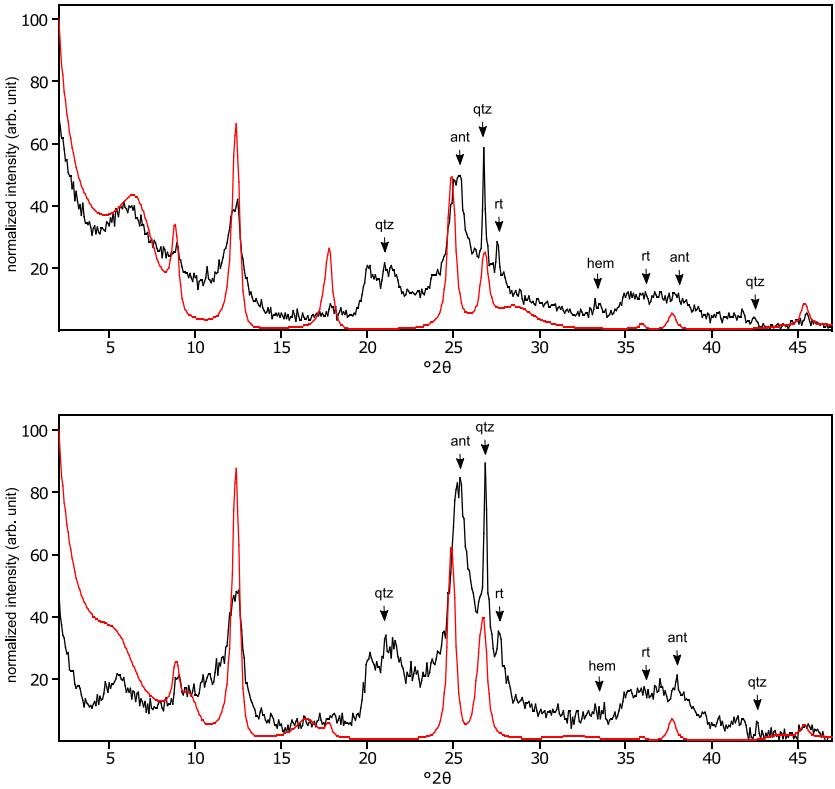

Figure V.20. The oriented clay fraction of soil from Endebess (Kenya). Top: experimental XRD patterns in air-dried, Ca-saturated state (black) and the modeled pattern (red) of 29% kaolinite, 25% randomly mixed-layered illite-smectite (97:3), and 46% randomly mixed-layered illite-smectite (60:40); Bottom: experimental XRD patterns in ethylene glycol solvated, Ca-saturated state (black) and the modeled pattern (red) of 38% kaolinite, 13% randomly mixed-layered illite-smectite (97:3), and 49% randomly mixed-layered illite-smectite (60:40). The arrows indicate quartz (qtz), anatase (ant), rutile (rt), and hematite (hem) peaks.

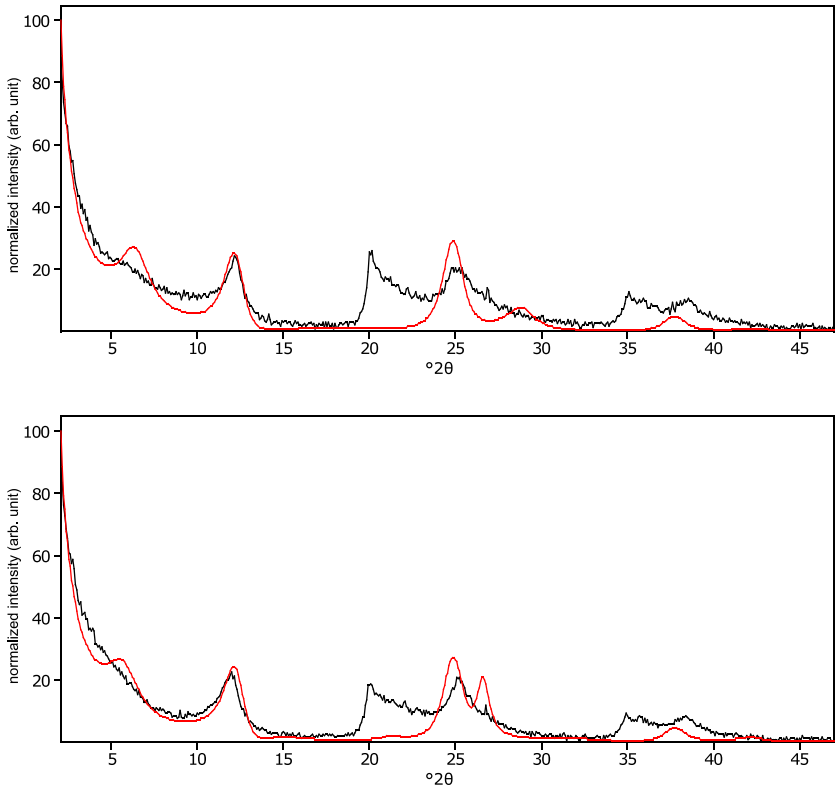

Figure V.21. The oriented clay fraction of soil from Pagsanjan (Philippines 4). Top: experimental XRD patterns in air-dried, Ca-saturated state (black) and the modeled pattern (red) of 52% kaolinite and 48% randomly mixed-layered kaolinite-smectite (high charge) (33:33:34); Bottom: experimental XRD patterns in ethylene glycol solvated, Ca-saturated state (black) and the modeled pattern (red) of 41% kaolinite, and 59% randomly mixed-layered kaolinite-smectite (high charge) (33:33:34).

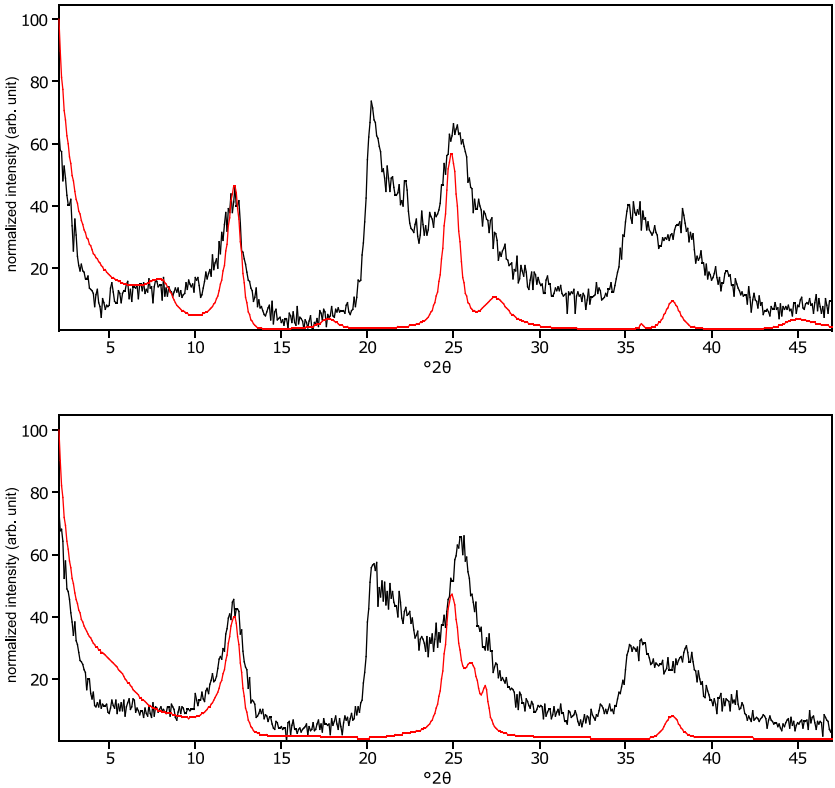

Figure V.22. The oriented clay fraction of soil from Pagsanjan (Philippines 5). Top: experimental XRD patterns in air-dried, Ca-saturated state (black) and the modeled pattern (red) of 66% kaolinite, 2% randomly mixed-layered kaolinite-smectite (high charge) (60:24:16), and 32% randomly mixed-layered illite-smectite (high charge) (70:15:15); Bottom: experimental XRD patterns in ethylene glycol solvated, Ca-saturated state (black) and the modeled pattern (red) of 36% kaolinite, 58% randomly mixed-layered kaolinite-smectite (high charge) (60:24:16) and 6% randomly mixed-layered illite-smectite (high charge) (70:15:15).

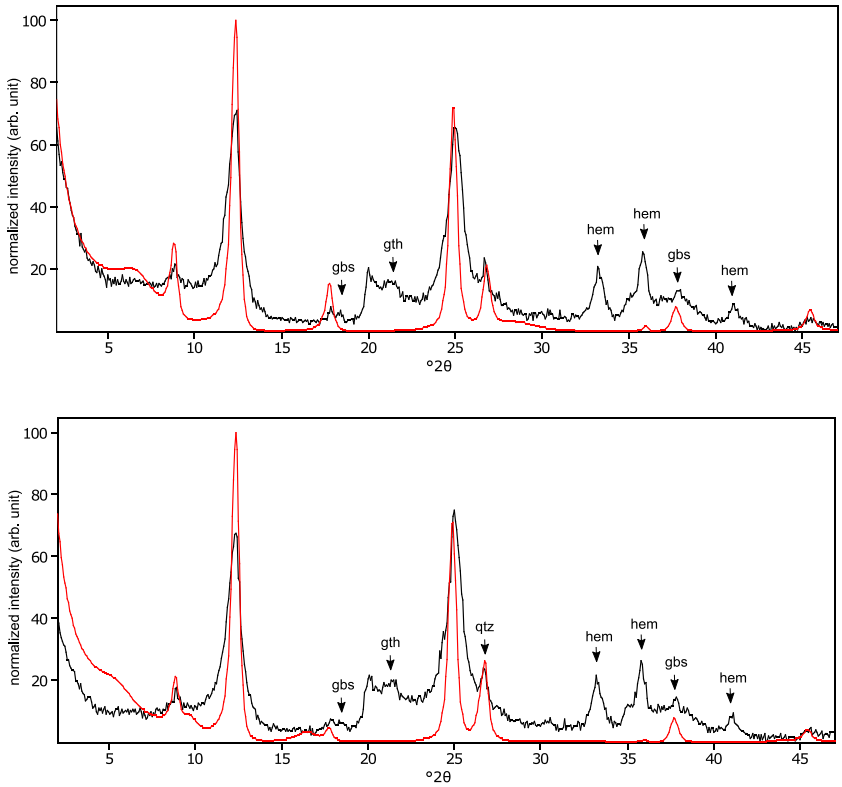

Figure V.23. The oriented clay fraction of soil from Kitale (Kenya 2). Top: experimental XRD patterns in air-dried, Ca-saturated state (black) and the modeled pattern (red) of 53% kaolinite, 27% randomly mixed-layered illite-smectite (97:3), and 20% randomly mixed-layered illite-smectite (60:40); Bottom: experimental XRD patterns in ethylene glycol solvated, Ca-saturated state (black) and the modeled pattern (red) of 55% kaolinite, 16% randomly mixed-layered illite-smectite (97:3), and 29% randomly mixed-layered illite-smectite (60:40). The arrows indicate gibbsite (gbs), goethite (gth), and hematite (hem) peaks.

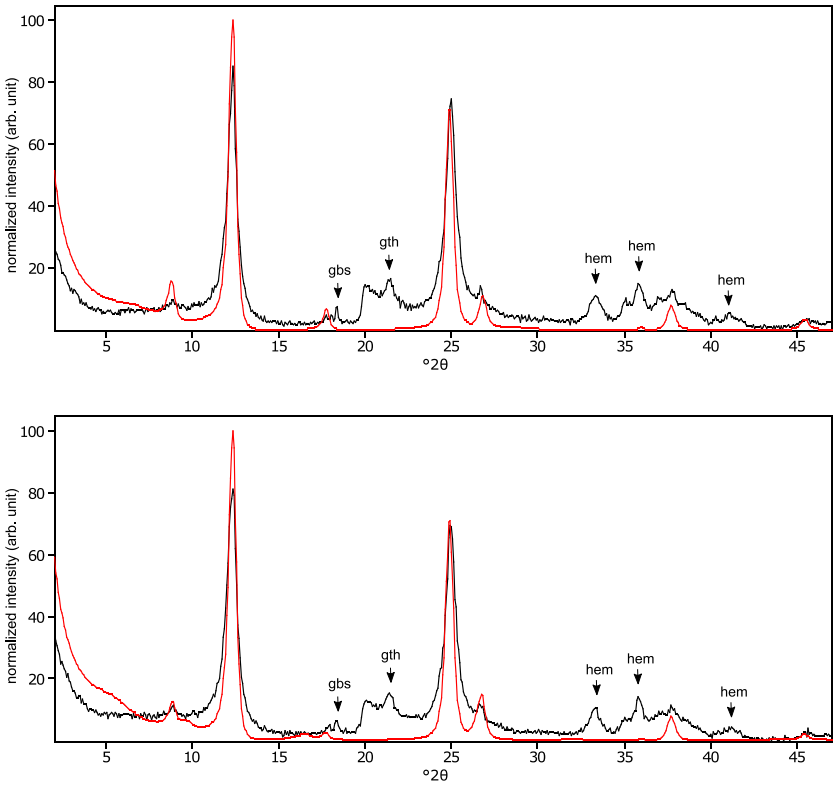

Figure V.24. The oriented clay fraction of soil from Kitale (Kenya 3). Top: experimental XRD patterns in air-dried, Ca-saturated state (black) and the modeled pattern (red) of 73% kaolinite, 20% randomly mixed-layered illite-smectite (97:3), and 7% randomly mixed-layered illite-smectite (60:40); Bottom: experimental XRD patterns in ethylene glycol solvated, Ca-saturated state (black) and the modeled pattern (red) of 68% kaolinite, 10% randomly mixed-layered illite-smectite (97:3), and 22% randomly mixed-layered illite-smectite (60:40). The arrows indicate gibbsite (gbs), goethite (gth), and hematite (hem) peaks.

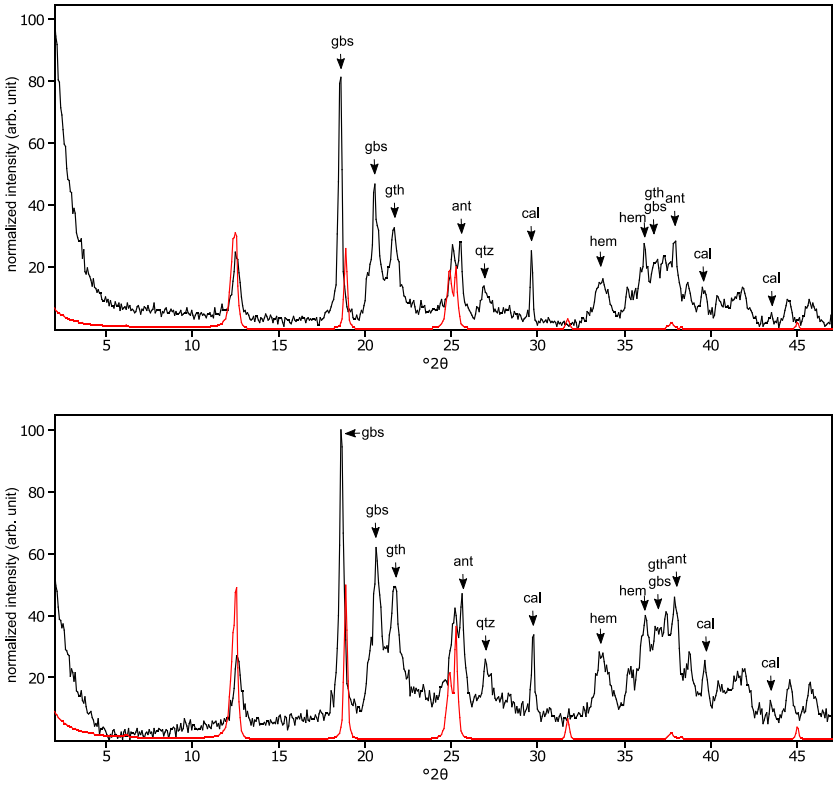

Figure V.25. The oriented clay fraction of soil from Behenjy (Madagascar). Top: experimental XRD patterns in air-dried, Ca-saturated state (black) and the modeled pattern (red) of 54% kaolinite and 46% chlorite; Bottom: experimental XRD patterns in ethylene glycol solvated, Ca-saturated state (black) and the modeled pattern (red) of 40% kaolinite, and 60% chlorite. The arrows indicate quartz (qtz), gibbsite (gbs), goethite (gth), anatase (ant), hematite (hem), and calcite (cal) peaks.

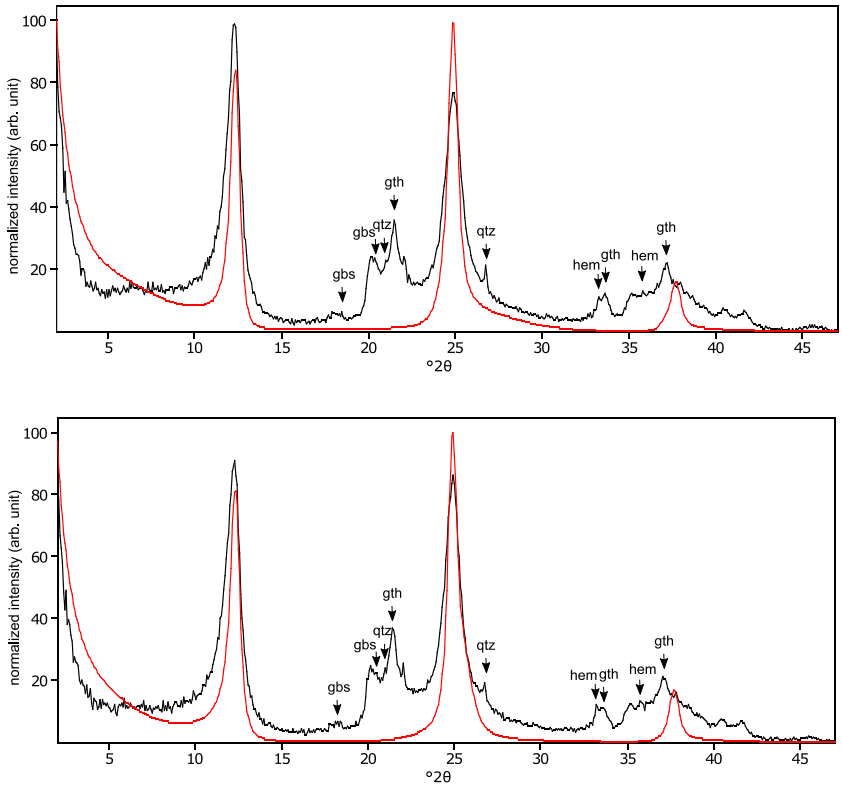

Figure V.26. The oriented clay fraction of soil from Cavinti (Philippines). Top: experimental XRD patterns in air-dried, Ca-saturated state (black) and the modeled pattern (red) of 38% kaolinite, and 62% randomly mixed-layered kaolinite-smectite (high charge) (80:10:10); Bottom: experimental XRD patterns in ethylene glycol solvated, Ca-saturated state (black) and the modeled pattern (red) of 42% kaolinite, and 58% randomly mixed-layered kaolinite-smectite (high charge) (80:10:10). The arrows indicate quartz (qtz), gibbsite (gbs), goethite (gth), and hematite (hem) peaks.

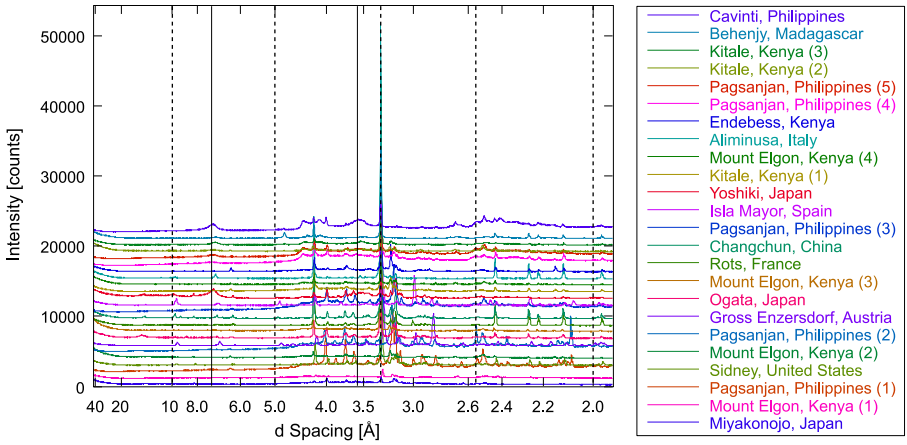

Figure V.27. Comparison of the oriented silt fractions in air-dried, Ca-saturated state of all soils in this study ordered from bottom to top by increased weathering stage. Full lines indicate peak positions of kaolinite at 7.17 Å and 3.58 Å, and dotted lines indicate peak positions of mica at 10 Å, 5.0 Å, 3.36 Å, 2.56 Å, and 2.00 Å. Quartz peaks are at 3.34 Å, 4.26 Å, and 2.46 Å.

Table V.4. Mineralogy of the <2 µm fraction of soils. Soils are ordered by increasing WI and grouped as young (WI = 2.5–4.7), intermediate (WI = 4.7–7.0), or weathered (WI = 7.0–9.2). K = kaolinite; I = illite; S = regular smectite; S^b = high-charge smectite, i.e., expandable layers with vermiculite-like swelling behavior; C = chlorite. Combinations are randomly mixed-layered (i.e., mixed-layered) mineral phases. Illite is modeled as mixed-layered illite-smectite with 3–5% smectite (IS^c) to match the illite peaks better. Ratios show the percentage of the mineral phase. Note: Mineral phases quantified are limited to illite, vermiculite, smectite, kaolinite, chlorite, and their mixed layers; other phases (e.g., allophane, mica, feldspars) were not included in the analysis.

location	K	KSS	ratio KSS			KS	ratio KS		ISS	ratio ISS			IS^c	ratio IS^c		IS	ratio IS		SS	C	CS	ratio CS	
city, country	g 100 g^{-1}	g 100 g^{-1}	%K	%S	%S^b	g 100 g^{-1}	%K	%S	g 100 g^{-1}	%I	%S	%S^b	g 100 g^{-1}	%I	%S	g 100 g^{-1}	%I	%S	g 100 g^{-1}	g 100 g^{-1}	g 100 g^{-1}	%C	%S
young																							
Miyakonojo, Japan	<0.5	<0.5				<0.5			<0.5				<0.5			<0.5			<0.5	<0.5	<0.5		
Mount Elgon, Kenya (1)	28.5	<0.5				<0.5			<0.5				34.5	97	3	37.0	60	40	<0.5	<0.5	<0.5		
Pagsanjan, Philippines (1)	30.0	70.0	50	30	20	<0.5			<0.5				<0.5			<0.5			<0.5	<0.5	<0.5		
intermediate																							
Sidney, United States	7.0	<0.5				<0.5			62.5	72	14	14	11.0	97	3	19.5	20	80	<0.5	<0.5	<0.5		
Mount Elgon, Kenya (2)	28.5	<0.5				<0.5			<0.5				36.5	97	3	35.0	60	40	<0.5	<0.5	<0.5		
Pagsanjan, Philippines (2)	16.0	84.0	50	30	20	<0.5			<0.5				<0.5			<0.5			<0.5	<0.5	<0.5		
Gross Enzersdorf, Austria	3.0	<0.5				<0.5			<0.5				32.5	97	3	49.0	68	32	<0.5	<0.5	15.5	90	10

location	K	KSS	ratio KSS			KS	ratio KS		ISS	ratio ISS			IS[c]	ratio IS[c]		IS	ratio IS		SS	C	CS	ratio CS	
city, country	g 100 g^{-1}	g 100 g^{-1}	%K	%S	%S[b]	g 100 g^{-1}	%K	%S	g 100 g^{-1}	%I	%S	%S[b]	g 100 g^{-1}	%I	%S	g 100 g^{-1}	%I	%S	g 100 g^{-1}	g 100 g^{-1}	g 100 g^{-1}	%C	%S
Ogata, Japan	11.5	55.5	25	37	38	29.0	25	75	<0.5				<0.5			4.5	15	85	<0.5	<0.5	<0.5		
Mount Elgon, Kenya (3)	34.0	<0.5				<0.5			<0.5				23.0	97	3	43.0	60	40	<0.5	<0.5	<0.5		
Rots, France	9.0	<0.5				<0.5			<0.5				22.5	95	5	68.5	68	32	<0.5	<0.5	<0.5		
Changchun, China	7.5	<0.5				17.5	50	50	14.0	33	33	34	41.0	97	3	20.0	63	37	<0.5	<0.5	<0.5		
Pagsanjan, Philippines (3)	10.0	90.0	66	17	17	<0.5			<0.5				<0.5			<0.5			<0.5	<0.5	<0.5		
Isla Mayor, Spain	9.5	<0.5				<0.5			<0.5				52.5	97	3	32.0	50	50	<0.5	6.0	<0.5		
Yoshiki, Japan	52.0	<0.5				<0.5			18.5	29	28	43	29.5	97	3	<0.5			<0.5	<0.5	<0.5		
Kitale, Kenya (1)	59.0	<0.5				<0.5			<0.5				17.5	97	3	23.5	60	40	<0.5	<0.5	<0.5		
Mount Elgon, Kenya (4)	31.5	<0.5				<0.5			<0.5				24.5	97	3	44.0	60	40	<0.5	<0.5	<0.5		
Aliminusa, Italy	28.0	<0.5				<0.5			<0.5				6.5	97	3	58.0	68	32	7.5	<0.5	<0.5		
weathered																							
Endebess, Kenya	33.5	<0.5				<0.5			<0.5				19.0	97	3	47.5	60	40	<0.5	<0.5	<0.5		
Pagsanjan, Philippines (4)	46.5	53.5	33	33	34	<0.5			<0.5				<0.5			<0.5			<0.5	<0.5	<0.5		

location	K	KSS	ratio KSS			KS	ratio KS		ISS	ratio ISS			IS[c]	ratio IS[c]		IS	ratio IS		SS	C	CS	ratio CS	
city, country	g 100 g^{-1}	g 100 g^{-1}	%K	%S	%S[b]	g 100 g^{-1}	%K	%S	g 100 g^{-1}	%I	%S	%S[b]	g 100 g^{-1}	%I	%S	g 100 g^{-1}	%I	%S	g 100 g^{-1}	g 100 g^{-1}	g 100 g^{-1}	%C	%S
Pagsanjan, Philippines (5)	51.0	30.0	60	24	16	<0.5			19.0	70	15	15	<0.5			<0.5			<0.5	<0.5	<0.5		
Kitale, Kenya (2)	54.0	<0.5				<0.5			<0.5				21.5	97	3	24.5	60	40	<0.5	<0.5	<0.5		
Kitale, Kenya (3)	70.5	<0.5				<0.5			<0.5				15.0	97	3	14.5	60	40	<0.5	<0.5	<0.5		
Behenjy, Madagascar	47.0	<0.5				<0.5			<0.5				<0.5			<0.5			<0.5	53.0	<0.5		
Cavinti, Philippines	40.0	60.0	80	10	10	<0.5			<0.5				<0.5			<0.5			<0.5	<0.5	<0.5		

Table V.5. Pearson correlation coefficients estimated by pairwise method between measured variables (N = 24) and the illite equivalent clay. Significant correlations are *** p <0.001; ** p <0.01; * p <0.05; and not significant (n.s.) if p >0.05. I = illite; S = expanding phyllosilicate (regular and high-charge smectite); C = chlorite; K = kaolinite.

	0–2000 µm							*2–50 µm*	*<2 µm*				
	RIP_{soil}[e]	<2 µm[d]	2–50 µm[d]	50–2000 µm[d]	^{10}log(%C organic)[e]	pH[e]	CEC[e]	RIP_{silt}[d]	RIP_{clay}[d]	%I[d]	%S[d]	%C[d]	%K[d]
0–2000 µm													
RIP_{soil}	-												
<2 µm	n.s.	-											
2–50 µm	n.s.	n.s.	-										
50–2000 µm	n.s.	-0.73***	-0.47*	-									
^{10}log(%C organic)	n.s.	n.s.	0.45*	-0.61**	-								
pH	0.66***	n.s.	0.45*	n.s.	n.s.	-							
CEC	n.s.	0.46*	n.s.	-0.55**	n.s.	n.s.	-						
2–50 µm													
RIP_{silt}	n.s.	n.s.	n.s.	n.s.	n.s.	n.s.	n.s.	-					
0–2 µm													
RIP_{clay}	0.83***	n.s.	n.s.	n.s.	-0.45*	0.67***	n.s.	n.s.	-				
%I	0.72***	n.s.	0.42*	n.s.	n.s.	0.57**	n.s.	n.s.	0.65***	-			
%S	n.s.	n.s.	n.s.	n.s.	n.s.	n.s.	0.42*	n.s.	n.s.	n.s.	-		
%C	n.s.	n.s.	n.s.	n.s.	n.s.	n.s.	n.s.	n.s.	n.s.	n.s.	n.s.	-	
%K	-0.58**	n.s.	-0.59**	0.43*	n.s.	-0.63**	n.s.	n.s.	-0.51*	-0.67***	n.s.	n.s.	-
%IEC	0.72***	n.s.	0.42*	n.s.	n.s.	0.57**	n.s.	n.s.	0.65***	1.00***	n.s.	n.s.	-0.67***

[d] n = 1; [e] n = 3

Appendix VI
Advancing global radiocaesium soil-to-plant transfer predictions: Feasibility, modeling, mapping, and future challenges

Table VI.1. Coordinates of soil sampling locations. Numbers in brackets discriminate soil sampling locations.

soil sampling origin (city, country)	coordinates (latitude)	(longitude)
Cantal, France (1)	45°10'26.976" N	2°37'43.7802" E
Volcano San Pedro, Guatemala (1)	14°39'29.739" N	91°15'50.2374" W
Volcano San Pedro, Guatemala (2)	14°39'51.2274" N	91°16'2.0352" W
Volcano San Pedro, Guatemala (3)	14°39'41.9754" N	91°15'59.1984" W
Volcano San Pedro, Guatemala (4)	14°40'34.6404" N	91°16'18.0402" W
Volcano San Pedro, Guatemala (5)	14°39'59.1582" N	91°16'5.8758" W
Volcano San Pedro, Guatemala (6)	14°40'23.808" N	91°16'18.4332" W
Volcano San Pedro, Guatemala (7)	14°40'15.0018" N	91°16'13.9296" W
Volcano San Pedro, Guatemala (8)	14°40'7.6614" N	91°16'7.6728" W
Fukushima, Japan (1)	-	-
Senbonmatsu, Nasushiobara, Tochigi, Japan	-	-
Morioka, Iwate, Japan	-	-
Chiltern, United Kingdom	51°37'12" N	1°1'48" E
Corney, United Kingdom	-	-
Brusand, Rogaland, Norway (1)	-	-
Brusand, Rogaland, Norway (2)	-	-
North Wales, United Kingdom	-	-
Volcano San Pedro, Guatemala (9)	14°41'10.43" N	91°16'35.09" W
Cantal, France (2)	45°14'36.76" N	2°33'15.55" E
Cantal, France (3)	45°11'10.6" N	2°37'4.22" E
Volcano San Pedro, Guatemala (10)	14°40'10.77" N	91°16'9.5" W
Volcano San Pedro, Guatemala (11)	14°40'25.5" N	91°16'18.98" W
Cantal, France (4)	45°12'3.75" N	2°36'11.1" E
Sparkbridge, United Kingdom	-	-
Córdoba, Spain (1)		
Cantal, France (5)	45°16'49.93" N	2°32'0.18" E
Cajón del Maipo, Chile (1)	33°45'43" S	70°16'54.8" W
Cajón del Maipo, Chile (2)	33°45'45.6" S	70°16'52.2" W
Cajón del Maipo, Chile (3)	33°45'43.7" S	70°16'58.2" W
Cajón del Maipo, Chile (4)	33°45'49.1" S	70°16'57.2" W
Cantal, France (6)	45°18'12.27" N	2°30'40.67" E
Fukushima, Japan (2)	-	-
Kalmthout, Belgium	-	-
Cantal, France (7)	45°17'17.8" N	2°31'35.11" E
Matsukawa, Japan	-	-
Cajón del Maipo, Chile (5)	33°45'41.9" S	70°16'46.2" W

soil sampling origin (city, country)	coordinates (latitude)	(longitude)
Meldert, Belgium	-	-
Bromyard, United Kingdom	-	-
Da Loan, Vietnam (1)	-	-
Da Loan, Vietnam (2)	-	-
Oudenburg, Belgium	-	-
Alveringem, Belgium	-	-
Wingene, Belgium	-	-
Fukushima, Japan (3)	-	-
Fukushima, Japan (4)	-	-
Fukushima, Japan (5)	-	-
Da Loan, Vietnam (3)	-	-
Valero, Spain	-	-
Córdoba, Spain (2)	37°42'21.6" N	5°0'1.14" W
Córdoba, Spain (3)	37°45'38.46" N	5°5'47.52" W
Casar de Cáceres, Spain	-	-
Bazagona, Spain	-	-
Bierbeek, Belgium	-	-
Córdoba, Spain (4)	37°42'24.42" N	5°0'0.78" W
Córdoba, Spain (5)	37°50'31.26" N	4°56'27.0" W
Córdoba, Spain (6)	37°51'34.56" N	4°51'12.96" W
Brimstone, United Kingdom	51°39' 0" N	1° 38' 24" W
Monfragüe, Spain	-	-
Retortillo, Spain	-	-
Torreorgaz, Spain	-	-
Mount Elgon, Kenya	01°09'08.2" N	34°43'42.6" E
Iablang, Vietnam	-	-
Fukushima, Japan (6)	-	-
Fukushima, Japan (7)	-	-
Da Loan, Vietnam (4)	-	-
Xuan Loc, Vietnam	-	-
Kitale, Kenya	0°58'01.9" N	34°58'44.1" E
Da Loan, Vietnam (5)	-	-
Dak Nhau, Vietnam	-	-

The new data came from a soil collection consisting of 69 topsoils samples, including 39 soils from soil sequences and 30 from different global locations with contrasting properties. Soil sequences were sampled in Chile, France, Guatemala, Kenya, Spain and Vietnam.

The Chile, France, Guatemala, and Kenya sequences were collected from volcanic mountains. The sequence from Chile was sampled in Cajón del Maipo, where underlying geological layers of the Farellones Formation contain basalt parent material. Soil samples were taken in a sclerophyll forest. The sequence from France was sampled on the Planèze de Trizac basalt plateau from the Cantal volcano in the Massif Central. In Guatemala, soils were collected from San Pedro Volcano, a stratovolcano next to Lake Atitlán, near the active Atitlán Volcano. Soil samples were collected in tropical forest (samples 1, 2, 3, 5, 7, 8), coffee plantations (samples 4, 6, 11), and maize-cropped fields (samples 9, 10). The sequence from Kenya, described in Chapter 4, included two additional soils: a Nitisol from Mount Elgon tropical forest and a Ferralsol from a maize field in Kitale.

The sequences from Spain and Vietnam, previously studied (Buekers et al., 2007; Torrent et al., 1980), were sampled to link Fe mineralogy to metal and phosphorus adsorption in soils. In Spain, a river terrace sequence (N = 6) near the Guadalquivir River in Córdoba was collected. In Vietnam, a toposequence (N = 5) from Da Loan, representing various weathering stages, was sampled, along with three tropical soils from Xuan Loc, Dak Nhau, and Iablang regions. Soils were characterized and Fe extractable with oxalate (Fe_o) and dithionite (Fe_d) was measured as an indicator of soil weathering stages, with a decreasing Fe_o/Fe_d ratio indicating more weathered soils due to a decreasing content of amorphous relative to crystalline oxides.

Compared, the Fe_o/Fe_d ratio does not always agree with the weathering indices based on (XRD) mineralogy as proposed in this study. The Fe_o/Fe_d ratio decreased with increasing mineralogical weathering indices in the Vietnam sequence, and the opposite was found for the Spanish sequence, but the relations were not significant (p >0.05, Figure VI.1). As expected for both sequences, the Fe_o/Fe_d ratio increased with increasing RIP/%clay, but again, the relations were not significant.

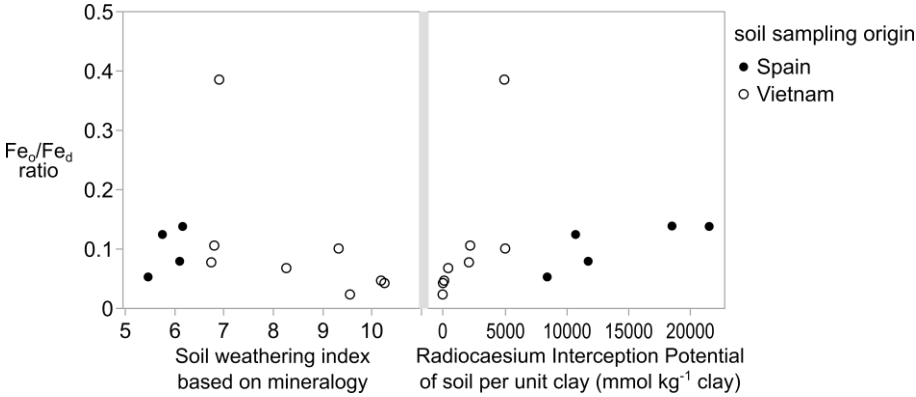

Figure VI.1. Comparison of Fe oxide ratios in Spain (*N* = 6) and Vietnam (*N* = 8) sequences, showing amorphous vs. crystalline oxide fractions against (left) weathering stage based on soil mineralogy; and (right) radiocaesium interception potential corrected for (highest) clay content.

Soils with contrasting soil properties (*N* = 20) were sampled in Belgium, Norway, Spain, and United Kingdom and characterized for the CONFIDENCE project. One of the project goals was to improve radio-ecological models of the human food chain, including the semi-mechanistic radiocaesium transfer model from soil to plant (Absalom et al., 2001).

Additionally, soils (*N* = 10) were sampled in Japan for a study to assess the vulnerability of soils in the Fukushima affected area for soil-to-crop radiocaesium transfer (Uematsu et al., 2018, 2015). Samples included grassland (*N* = 6), paddy fields (*N* = 3), and forest (*N* = 1) from Fukushima and Tochigi Prefectures, collected 1 to 2 years post-accident.

Table VI.2. Soil mineralogy (*N* = 69), weathering index of minerals (Jackson et al., 1948; Jackson and Sherman, 1953) and calculated weathering index of soils. Rows are ordered by increasing weathering index and grouped in reference soil groups (WRB). Qtz = quartz; 1:1 = kaolin phyllosilicates; Al-2:1 = aluminum 2:1 phyllosilicates; Fe-2:1 = iron 2:1 phyllosilicates; Tri-2:1 = trioctahedral 2:1 phyllosilicates; Fe-2:1:1 = iron chlorite phyllosilicates; Mg-2:1:1 = magnesium chlorite phyllosilicates; Ms = muscovite; Fsp = K-feldspars and plagioclase; Cal/Dol = calcite and dolomite; Sulf/Salt = sulfides and salts; Ant = anatase; FeOx = iron (oxy-)hydroxides; AlOx = aluminium (oxy-)hydroxides; Amp/Px = amphibole and pyroxene; a = mineral phases that appear amorphous on XRD pattern. The limit of detection is 1 g 100 g^{-1}.

soil classification and sampling origin	Qtz	1:1	Al-2:1	Fe-2:1	Tri-2:1	Fe-2:1:1	Mg-2:1:1	Ms	Fsp	Cal/Dol	Sulf/Salt	Ant	FeOx	AlOx	Amp/Px	a	weathering index
(city, country)	g 100 g^{-1}																-
weathering index mineral	*6*	*9*	*7*	*4*	*4*	*4*	*8*	*7*	*5*	*2*	*1*	*12*	*11*	*10*	*3*	*1*	
Andosol																	
[b]Cantal, France (1)	2	<1	2	<1	<1	<1	<1	7	5	1	<1	<1	4	<1	22	57	2.6
[b]Volcano San Pedro, Guatemala (1)	2	<1	<1	<1	1	<1	<1	5	35	<1	1	<1	<1	<1	7	49	3.0
[b]Volcano San Pedro, Guatemala (2)	2	<1	<1	<1	1	<1	<1	5	43	<1	2	<1	<1	<1	7	40	3.3
[b]Volcano San Pedro, Guatemala (3)	2	<1	<1	<1	1	<1	<1	6	46	<1	1	<1	<1	<1	8	36	3.5
[b]Volcano San Pedro, Guatemala (4)	2	<1	2	<1	<1	<1	<1	7	44	<1	1	<1	<1	<1	8	36	3.6
[b]Volcano San Pedro, Guatemala (5)	1	<1	<1	<1	1	<1	<1	4	57	<1	1	<1	<1	<1	10	26	3.8
[b]Volcano San Pedro, Guatemala (6)	1	<1	4	<1	<1	<1	<1	10	49	<1	<1	<1	<1	<1	8	28	4.0
[b]Volcano San Pedro, Guatemala (7)	2	<1	2	<1	<1	<1	<1	6	57	<1	<1	<1	<1	<1	11	22	4.0
[b]Volcano San Pedro, Guatemala (8)	1	<1	<1	<1	1	<1	<1	11	54	<1	<1	<1	<1	<1	11	22	4.1
[b]Fukushima, Japan (1)	16	9	10	<1	<1	<1	<1	3	27	<1	<1	<1	<1	5	20	10	5.3
[b]Senbonmatsu, Nasushiobara, Tochigi, Japan	36	9	11	<1	<1	<1	7	8	17	<1	<1	<1	<1	3	2	7	6.0

soil classification and sampling origin	Qtz	1:1	Al-2:1	Fe-2:1	Tri-2:1	Fe-2:1:1	Mg-2:1:1	Ms	Fsp	Cal/Dol	Sulf/Salt	Ant	FeOx	AlOx	Amp/Px	a	weathering index
(city, country)	g 100 g^{-1}																-
weathering index mineral	*6*	*9*	*7*	*4*	*4*	*4*	*8*	*7*	*5*	*2*	*1*	*12*	*11*	*10*	*3*	*1*	
[b]Morioka, Iwate, Japan	26	10	15	<1	<1	<1	10	10	7	<1	<1	<1	3	5	8	6	6.1
Leptosol																	
[a]Chiltern, United Kingdom	12	1	<1	<1	<1	<1	<1	4	2	81	<1	<1	<1	<1	<1	<1	2.8
Podzol																	
[a]Corney, United Kingdom	27	<1	<1	<1	<1	<1	<1	7	8	<1	<1	<1	<1	<1	58	<1	3.1
[b]Brusand, Rogaland, Norway (1)	36	<1	<1	<1	<1	<1	2	3	55	<1	<1	<1	<1	<1	4	<1	5.3
[b]Brusand, Rogaland, Norway (2)	39	<1	<1	<1	<1	<1	3	4	52	<1	<1	<1	<1	<1	2	<1	5.4
[b]North Wales, United Kingdom	88	<1	5	<1	<1	<1	<1	<1	2	<1	<1	<1	<1	<1	<1	5	5.8
Cambisol																	
[b]Volcano San Pedro, Guatemala (9)	3	<1	<1	<1	2	<1	<1	8	41	<1	1	<1	<1	<1	5	40	3.4
[b]Cantal, France (2)	3	6	6	<1	<1	<1	<1	7	8	<1	<1	<1	3	<1	14	53	3.4
[b]Cantal, France (3)	2	8	9	<1	<1	<1	<1	7	2	1	<1	<1	7	<1	6	58	3.7
[b]Volcano San Pedro, Guatemala (10)	2	7	<1	<1	<1	<1	<1	9	36	<1	2	<1	<1	1	9	34	4.0
[b]Volcano San Pedro, Guatemala (11)	2	7	<1	<1	<1	<1	<1	6	42	<1	2	<1	<1	2	12	27	4.2
[b]Cantal, France (4)	4	12	9	<1	<1	<1	<1	11	9	1	<1	<1	2	<1	13	39	4.3
[a]Sparkbridge, United Kingdom	34	<1	1	14	<1	7	<1	7	10	<1	<1	<1	3	<1	<1	24	4.5
[a]Córdoba, Spain (1)	34	5	12	<1	<1	<1	<1	7	3	39	<1	<1	<1	<1	<1	<1	4.8
[b]Cantal, France (5)	18	7	<1	<1	2	<1	<1	9	24	<1	<1	<1	5	<1	13	22	4.8
[b]Cajón del Maipo, Chile (1)	16	8	12	<1	<1	<1	6	3	27	<1	1	<1	2	<1	<1	25	4.9
[b]Cajón del Maipo, Chile (2)	15	8	15	<1	<1	<1	6	3	27	<1	1	<1	2	<1	<1	23	5.0
[b]Cajón del Maipo, Chile (3)	17	10	15	<1	<1	<1	7	5	17	<1	2	<1	2	<1	<1	25	5.1
[b]Cajón del Maipo, Chile (4)	16	9	15	<1	<1	<1	7	4	25	<1	<1	<1	3	<1	<1	19	5.3
[b]Cantal, France (6)	35	5	7	<1	<1	<1	7	6	29	<1	<1	<1	<1	<1	2	9	5.4

soil classification and sampling origin	Qtz	1:1	Al-2:1	Fe-2:1	Tri-2:1	Fe-2:1:1	Mg-2:1:1	Ms	Fsp	Cal/Dol	Sulf/Salt	Ant	FeOx	AlOx	Amp/Px	a	weathering index
(city, country)	g 100 g^{-1}																-
weathering index mineral	*6*	*9*	*7*	*4*	*4*	*4*	*8*	*7*	*5*	*2*	*1*	*12*	*11*	*10*	*3*	*1*	
[b]Fukushima, Japan (2)	24	6	9	<1	6	<1	<1	<1	47	<1	<1	<1	<1	<1	8	<1	5.5
[b]Kalmthout, Belgium	91	<1	2	<1	<1	<1	<1	1	6	<1	<1	<1	<1	<1	<1	<1	6.0
[b]Cantal, France (7)	34	5	11	<1	<1	<1	10	17	22	<1	<1	<1	<1	<1	1	<1	6.0
[b]Matsukawa, Japan	27	13	16	<1	6	<1	11	<1	25	<1	<1	<1	<1	<1	2	<1	6.0
[b]Cajón del Maipo, Chile (5)	19	12	18	<1	<1	<1	8	4	28	<1	2	<1	3	<1	<1	6	6.0
[b]Meldert, Belgium	45	6	17	<1	<1	<1	7	8	14	<1	<1	<1	<1	<1	<1	3	6.0
[a]Bromyard, United Kingdom	31	3	57	<1	<1	3	<1	<1	6	<1	<1	<1	<1	<1	<1	<1	6.6
[b]Da Loan, Vietnam (1)	71	10	6	<1	<1	<1	<1	9	<1	<1	<1	3	1	<1	<1	<1	6.8
[b]Da Loan, Vietnam (2)	44	44	2	<1	<1	<1	<1	<1	<1	<1	<1	3	7	<1	<1	<1	8.3
Fluvisol																	
[b]Oudenburg, Belgium	62	2	10	<1	<1	<1	2	3	15	4	<1	<1	<1	<1	<1	2	5.8
[b]Alveringem, Belgium	72	<1	8	<1	<1	<1	3	3	12	2	<1	<1	<1	<1	<1	<1	5.9
[b]Wingene, Belgium	87	<1	2	<1	<1	<1	1	1	9	<1	<1	<1	<1	<1	<1	<1	5.9
Gleysol																	
[b]Fukushima, Japan (3)	23	9	15	<1	<1	<1	<1	6	26	<1	<1	<1	<1	<1	8	12	5.5
[b]Fukushima, Japan (4)	31	13	<1	<1	5	<1	9	<1	37	<1	<1	<1	<1	<1	5	<1	5.7
[b]Fukushima, Japan (5)	13	20	<1	<1	4	<1	13	<1	43	<1	<1	<1	<1	<1	6	1	5.8
[b]Da Loan, Vietnam (3)	58	15	8	<1	<1	<1	<1	17	<1	<1	<1	1	1	<1	<1	<1	7.0
Luvisol																	
Valero, Spain	-	-	-	-	-	-	-	-	-	-	-	-	-	-	-	-	-
[b]Córdoba, Spain (2)	58	7	14	<1	<1	<1	<1	<1	2	6	<1	<1	<1	<1	<1	13	5.5
[a]Córdoba, Spain (3)	61	5	12	<1	<1	<1	<1	6	3	8	<1	<1	<1	<1	<1	5	5.8
[a]Casar de Cáceres, Spain	34	7	11	<1	3	<1	<1	3	42	<1	<1	<1	<1	<1	<1	<1	5.9
[a]Bazagona, Spain	52	4	<1	<1	<1	<1	<1	10	34	<1	<1	<1	<1	<1	<1	<1	5.9
[b]Bierbeek, Belgium	65	3	8	<1	<1	<1	4	4	16	<1	<1	<1	<1	<1	<1	<1	6.0

soil classification and sampling origin	Qtz	1:1	Al-2:1	Fe-2:1	Tri-2:1	Fe-2:1:1	Mg-2:1:1	Ms	Fsp	Cal/Dol	Sulf/Salt	Ant	FeOx	AlOx	Amp/Px	a	weathering index
(city, country)	g 100 g^{-1}																-
weathering index mineral	*6*	*9*	*7*	*4*	*4*	*4*	*8*	*7*	*5*	*2*	*1*	*12*	*11*	*10*	*3*	*1*	
[a]Córdoba, Spain (4)	89	3	5	<1	<1	<1	<1		3	<1	<1	<1	<1	<1	<1	<1	6.1
[a]Córdoba, Spain (5)	45	5	7	<1	<1	<1	<1	18	25	<1	<1	<1	<1	<1	<1	<1	6.2
[a]Córdoba, Spain (6)	78	4	8	<1	<1	<1	<1	5	5	<1	<1	<1	<1	<1	<1	<1	6.2
[a]Brimstone, United Kingdom	43	5	13	11	<1	2	7	8	10	<1	<1	<1	1	<1	<1	<1	6.2
[a]Monfragüe, Spain	53	13	20	<1	<1	1	<1	5	6	<1	<1	<1	2	<1	<1	<1	6.7
[a]Retortillo, Spain	42	29	4	2	<1	<1	<1	17	4	2	<1	<1	<1	<1	<1	<1	7.0
Vertisol																	
[a]Torreorgaz, Spain	45	5	12	<1	<1	7	2	14	14	<1	<1	<1	1	<1	<1	<1	6.2
Nitisol																	
[b]Mount Elgon, Kenya	8	13	13	<1	<1	<1	<1	7	5	<1	<1	2	11	1	<1	40	5.4
[b]Iablang, Vietnam	5	63	<1	<1	<1	<1	<1	<1	<1	<1	<1	17	10	5	<1	<1	10.2
Acrisol																	
[b]Fukushima, Japan (6)	29	7	<1	<1	<1	<1	8	9	39	<1	<1	<1	<1	<1	8	<1	5.6
[b]Fukushima, Japan (7)	28	6	10	<1	<1	<1	7	<1	45	<1	<1	<1	<1	<1	4	<1	5.6
[b]Da Loan, Vietnam (4)	54	15	19	<1	<1	<1	<1	<1	<1	<1	<1	3	3	<1	<1	6	6.8
Lixisol																	
[b]Xuan Loc, Vietnam	12	50	7	<1	<1	<1	<1	8	<1	<1	<1	10	13	<1	<1	<1	9.4
Ferralsol																	
[b]Kitale, Kenya	35	23	12	<1	<1	<1	<1	2	5	3	<1	<1	18	2	<1	<1	7.9
[b]Da Loan, Vietnam (5)	17	65	<1	<1	<1	<1	<1	<1	<1	<1	<1	8	10	<1	<1	<1	9.6
[b]Dak Nhau, Vietnam	<1	73	<1	<1	<1	<1	<1	<1	<1	<1	<1	8	15	4	<1	<1	10.3

[a] measured with PW1830 (Philips) and processed using Quanta; [b] measured with D8 Advance (Bruker) and processed using Profex

Table VI.3. Soil characteristics (*N* = 69). Rows are ordered by increasing weathering index and grouped in reference soil groups (WRB). Values represent triplicate means and the standard deviation of RIP is given in brackets. The limits of detection are 0.1 or 1 g 100 g^{-1}.

soil classification and sampling origin	pH	clay[c]	sand[c]	clay[d]	sand[d]	SIC	SOC	LOI	CEC	RIP	weathering index
(city, country)	-	g 100 g^{-1}							$cmol_c$ kg^{-1} soil	mmol kg^{-1} soil	-
Andosol											
Cantal, France (1)	4.2	-	-	23	10	-	18	-	16	209	2.6
Volcano San Pedro, Guatemala (1)	4.6	-	-	15	23	-	15	-	25	45.3	3.0
Volcano San Pedro, Guatemala (2)	6.3	-	-	11	37	-	8.7	-	39	98	3.3
Volcano San Pedro, Guatemala (3)	6.1	-	-	9	51	-	7.0	-	27	59.1	3.5
Volcano San Pedro, Guatemala (4)	5.8	-	-	13	36	-	5.0	-	23	436	3.6
Volcano San Pedro, Guatemala (5)	5.9	-	-	9	46	-	3.6	-	15	68.4	3.8
Volcano San Pedro, Guatemala (6)	5.4	-	-	14	35	-	2.5	-	11	382	4.0
Volcano San Pedro, Guatemala (7)	5.6	-	-	12	37	-	4.4	-	18	328	4.0
Volcano San Pedro, Guatemala (8)	6.0	-	-	12	44	-	3.9	-	18	438	4.1
[e]Fukushima, Japan (1)	5.4	23	36	-	-	-	6.1	17	20	685	5.3
[e]Senbonmatsu, Nasushiobara, Tochigi, Japan	5.3	25	37	-	-	-	8.0	19	17	383	6.0
[e]Morioka, Iwate, Japan	4.9	27	30	-	-	-	2.1	11	23	1,080	6.1
Leptosol											
Chiltern, United Kingdom	8.0[e]	-	-	43	<1	9.0	2.8	6.7	36	2,550[e]	2.8
Podzol											
Corney, United Kingdom	5.0[e]	-	-	10	38	<0.10	31	26	65	806[e]	3.1
Brusand, Rogaland, Norway (1)	-	1[e]	95[e]	2	87	<0.10	4.0	10	9.0	81.8[e]	5.3
Brusand, Rogaland, Norway (2)	-	1[e]	94[e]	2	94	<0.10	2.3	4.9	6.3	103[e]	5.4
North Wales, United Kingdom	5.4[e]	13[e]	64[e]	12	41	<0.10	12	23	29	625[e]	5.8

Cambisol											
Volcano San Pedro, Guatemala (9)	5.8	-	-	12	37	-	1.2	-	8.2	637	3.4
Cantal, France (2)	5.1	-	-	28	1	-	11	-	23	201	3.4
Cantal, France (3)	4.2	-	-	38	<1	-	16	-	16	184	3.7
Volcano San Pedro, Guatemala (10)	5.6	-	-	13	32	-	1.7	-	15	181	4.0
Volcano San Pedro, Guatemala (11)	5.6	-	-	16	33	-	1.0	-	12	161	4.2
Cantal, France (4)	4.8	-	-	31	<1	-	8.4	-	14	198	4.3
Sparkbridge, United Kingdom	6.4[e]	-	-	20	36	<0.10	13.0	22	37	2,140[e]	4.5
Córdoba, Spain (1)	7.6[e]	55[e]	23[e]	46	<1	5.1	1.1	6.1	35[e]	4,100	4.8
Cantal, France (5)	4.9	-	-	23	9	-	9.2	-	9.2	185	4.8
Cajón del Maipo, Chile (1)	6.8	-	-	12	54	-	3.3	-	18	4,370	4.9
Cajón del Maipo, Chile (2)	6.9	-	-	22	29	-	4.1	-	24	5,490	5.0
Cajón del Maipo, Chile (3)	7.4	-	-	24	28	-	4.2	-	40	7,850	5.1
Cajón del Maipo, Chile (4)	6.7	-	-	17	34	-	3.70	-	19	3,900	5.3
Cantal, France (6)	4.3	-	-	16	11	-	6.00	-	5.1	217	5.4
[e]Fukushima, Japan (2)	4.4	7	72	-	-	-	1.1	4.1	10	2,300	5.5
Kalmthout, Belgium	4.6[e]	12[e]	78[e]	4	75	<0.10	3.6	5.8	7.8	794[e]	6.0
Cantal, France (7)	4.5	-	-	10	44	-	4.8	-	7.7	689	6.0
[e]Matsukawa, Japan	5.1	15	59	-	-	-	1.6	7.2	15	4,730	6.0
Cajón del Maipo, Chile (5)	7.4	-	-	16	39	-	1.4	-	18	5,290	6.0
Meldert, Belgium	6.2[e]	16[e]	46[e]	31	13	0.18	4.7	13	57	10,500[e]	6.0
Bromyard, United Kingdom	6.9	32	9	26	4	0.19	2.7	9.5	6.4	10,400	6.6
Da Loan, Vietnam (1)	3.9[e]	19[e]	45[e]	14	41	<0.10	1.8	-	2.1[e]	428	6.8
Da Loan, Vietnam (2)	3.9[e]	51[e]	22[e]	49	<1	<0.10	2.0	-	4.7[e]	304	8.3
Fluvisol											
Oudenburg, Belgium	6.9[e]	25[e]	46[e]	12	49	0.54	2.8	6.7	33	4,580[e]	5.8
Alveringem, Belgium	7.3[e]	20[e]	57[e]	8	47	0.57	1.3	3.5	21	3,640[e]	5.9
Wingene, Belgium	5.7[e]	16[e]	75[e]	2	85	0.39	1.9	4.2	6.3	897[e]	5.9

Gleysol											
[e]Fukushima, Japan (3)	5.8	20	40	-	-	-	1.8	7.1	27	3,130	5.5
[e]Fukushima, Japan (4)	4.1	7	67	-	-	-	1.9	6.6	11	831	5.7
[e]Fukushima, Japan (5)	5.2	18	47	-	-	-	2.3	10	30	1,760	5.8
Da Loan, Vietnam (3)	4.0[e]	25[e]	26[e]	20	17	<0.10	2.3	-	4.2[e]	1,260	7.0
Luvisol											
[e]Valero, Spain	6.5	6	44	-	-	-	-	-	5.1	929	-
Córdoba, Spain (2)	7.6[e]	41	35	17	53	4.9	0.86	5.8	26[e]	3,520	5.5
Córdoba, Spain (3)	7.6[e]	37[e]	29[e]	24	36	4.6	0.63	5.2	31[e]	4,050	5.8
Casar de Cáceres, Spain	7.8[e]	2[e]	58[e]	9	50	<0.10	3.8	8.4	26	2,690[e]	5.9
Bazagona, Spain	5.2[e]	1[e]	88[e]	4	73	<0.10	0.57	1.7	3.8	982[e]	5.9
Bierbeek, Belgium	6.3[e]	30	35	15	30	<0.10	7.0	15	28	8,090[e]	6.0
Córdoba, Spain (4)	5.5[e]	14[e]	68[e]	9	58	2.0	0.40	2.4	6.8[e]	1,740	6.1
Córdoba, Spain (5)	5.8[e]	18[e]	30[e]	15	31	3.2	0.66	3.8	8.5[e]	4,030	6.2
Córdoba, Spain (6)	6.4[e]	18[e]	44[e]	15	38	2.4	0.52	3.0	6.8[e]	3,290	6.2
Brimstone, United Kingdom	8.0[e]	53[e]	11[e]	13	15	<0.10	1.7	5.6	20	8,750[e]	6.2
Monfragüe, Spain	6.6[e]	2[e]	46[e]	11	37	<0.10	3.6	9.3	16	1,960[e]	6.7
Retortillo, Spain	7.1[e]	3[e]	41[e]	9	30	<0.10	1.1	5.0	12	4,930[e]	7.0
Vertisol											
Torreorgaz, Spain	5.9[e]	3[e]	45[e]	11	26	<0.10	1.2	4.7	10	4,180[e]	6.2
Nitisol											
Mount Elgon, Kenya	6.3	25	10	47	<1	-	7.9	-	41	1,940	5.4
Iablang, Vietnam	4.7[e]	39[e]	22[e]	66	<1	<0.10	2.4	-	6.9[e]	177	10.2
Acrisol											
[e]Fukushima, Japan (6)	3.9	11	61	-	-	-	3.7	13	11	420	5.6
[e]Fukushima, Japan (7)	3.6	13	56	-	-	-	4.4	11	13	460	5.6
Da Loan, Vietnam (4)	3.8[e]	41[e]	25[e]	33	3	<0.10	2.8	-	5.0[e]	982	6.8
Lixisol											
Xuan Loc, Vietnam	4.8[e]	59[e]	12[e]	59	<1	<0.10	1.8	-	13[e]	3,090	9.4

Ferralsol											
Kitale, Kenya	4.8	48	37	26	36	-	1.8	-	8.1	2,250	7.9
Da Loan, Vietnam (5)	4.0[e]	55[e]	14[e]	67	<1	<0.10	2.5	-	3.8[e]	95.1	9.6
Dak Nhau, Vietnam	4.1[e]	81[e]	2[e]	70	<1	<0.10	2.5	-	8.0[e]	137	10.3

[c] pipet method (ISO 11277); [d] laser diffraction; [e] previously obtained (Buekers, 2007; Gilis and Sweeck, 2019; Uematsu et al., 2018)

Project output

Published articles:

Vanheukelom, M., Sweeck, L., Almahayni, T., De Bruyn, M., Steegmans, P., Fondu, L., Van Gompel, A., Van Hees, M., Wannijn, J., Smolders, E., 2024. Highly weathered mineral soils have highest transfer risk of radiocaesium contamination after a nuclear accident: A global soil-plant study. Sci. Total Environ. 173583.
https://doi.org/https://doi.org/10.1016/j.scitotenv.2024.173583

Vanheukelom, M., Sweeck, L., Van Hees, M., Weyns, N., Van Orshoven, J., Smolders, E., 2023. Quantitative clay mineralogy predicts radiocesium bioavailability to ryegrass grown on reconstituted soils. Sci. Total Environ. 873, 162372. https://doi.org/10.1016/J.SCITOTENV.2023.162372

Articles to be published:

Chapter 5 (submitted):
Vanheukelom, M., Haenen, N., Almahayni, T., Sweeck, L., Weyns, N., Van Hees, M., Smolders, E., 2024. The clay mineralogy rather than the clay content determines radiocaesium adsorption in soils.

Chapter 2:
Vanheukelom, M., Mng'ong'o, M., Abrams, F., Gupta, S., Sweeck, L., Almahayni, T., Van Orshoven, J., Smolders, E., 2025. A database for predicting radiocaesium soil-to-plant transfer on a global scale. (draft title)

Published book chapter:

Lourenço, J., Mothersill, C., Arena, C., Oughton, D., Vanheukelom, M., Pereira, R., Mendo, S., De Micco, V., 2023. Environmental Radiobiology BT - Radiobiology Textbook, in: Baatout, S. (Ed.). Springer International Publishing, Cham, pp. 469–501.
https://doi.org/10.1007/978-3-031-18810-7_9

Published blogpost:

Vanheukelom, M., 2023. Laat het gras maar groeien ... op radioactieve bodems. EOS Blogs Natuur & Milieu.
https://www.eoswetenschap.eu/natuur-milieu/laat-het-gras-maar-groeien-op-radioactieve-bodems

Use of Generative AI

I did use the generative AI assistance tool ChatGPT.

ChatGPT was used for generating programming code. More specifically, For Chapter 2 to create code for data cleaning, data introduction, modeling, a histogram, violin plot and for solving errors in the code.

The text/images in this thesis are my own (unless otherwise specified) and generative AI has only been used in accordance with the KU Leuven guidelines and appropriate references have been added. I have reviewed and edited the content as needed and I take full responsibility for the content of the thesis.